

SIMULATING AND CONTROLLING NON-ADIABATIC  
EFFECTS IN ULTRAFAST PHOTOCHEMISTRY

by

THOMAS JAMES PENFOLD

A thesis submitted to  
the University of Birmingham  
for the examination of  
DOCTOR OF PHILOSOPHY

School of Chemistry  
University of Birmingham  
2009

UNIVERSITY OF  
BIRMINGHAM

**University of Birmingham Research Archive**

**e-theses repository**

This unpublished thesis/dissertation is copyright of the author and/or third parties. The intellectual property rights of the author or third parties in respect of this work are as defined by The Copyright Designs and Patents Act 1988 or as modified by any successor legislation.

Any use made of information contained in this thesis/dissertation must be in accordance with that legislation and must be properly acknowledged. Further distribution or reproduction in any format is prohibited without the permission of the copyright holder.

# Abstract

Photochemistry plays a critical role in many fundamental processes. These reactions necessarily involve excited states and therefore the breakdown of the Born-Oppenheimer approximation means that many photochemical processes are dominated by non-adiabatic effects, such as conical intersections. The study of such reactions is therefore vital to our understanding of many fundamental processes and the interesting topological features which cause them.

The photophysics and photochemistry of benzene is a classic example of the richness of competing pathways available to a molecule after photoexcitation. Computer simulations are one way to provide a molecular picture for the dynamics behind the experimental observations. We develop a Vibronic Coupling Hamiltonian previously published [G.A.Worth, *J. Photochem. Photobio.* 190:190-199,2007]. Using CASPT2 we add dynamic correlation to the description of the excited states, improving their accuracy dramatically. Seven coupled states and all vibrational mode are included in the model and the parameters are obtained by fitting to points provided by the quantum chemistry calculations. The model is shown to be a good fit of the adiabatic surfaces and its accuracy is demonstrated by the calculation of three absorption bands, which compare favourably with the experimentally obtained spectra.

Using the calculated Hamiltonian we investigate the ultrafast dynamics of benzene of electronically and vibrationally excited benzene. We observe ultrafast decay which is a result of internal conversion occurring at the  $S_1/S_0$  conical intersection at a prefulvene geometry. These results are able to describe most of the dynamical features seen experimentally.

Spin orbit coupling is generally a small, but sometimes a vital perturbation to the Hamiltonian. It is often ignored in hydrocarbons due to the size of the static coupling at equilibrium. However these static couplings ignore the vibrational effects

which can occur, and which can be important in describing fine details on spectroscopic measurements. A detailed analysis of spin orbit coupling in cyclobutadiene and benzene is presented. Spin orbit coupling values are presented along the important normal modes, which promote the strength of the coupling. The effect of conical intersections on the strength of spin orbit coupling are presented by plotting the vector in normal mode space from equilibrium geometry to the  $S_1/S_0$  conical intersection.

We further investigate the ultrafast dynamics of benzene by including the triplet manifold and spin orbit coupling to the Hamiltonian. Ultrafast intersystem crossing is observed between  $S_1$  and  $T_2$ , which are degenerate along the important prefulvene reaction coordinate. These results challenge the accepted view that ultrafast intersystem crossing cannot occur in hydrocarbons due to the size of spin orbit coupling.

Coherent control uses shaped laser pulses to control the outcome of chemical reactions. Local control calculates a pulse as a function of the instantaneous dynamics of the system at each time step. By defining some operator, the field is calculated to ensure an increase or decrease in its expectation value. We present the initial implementation of this method within MCTDH quantum dynamics package. Using models of cyclobutadiene, pyrazine and ammonia we demonstrate that this method is effective in controlling chemical reactions and extremely efficient. The simplicity of this approach means that the calculated fields are very easy to relate to the dynamics of each system providing detailed understanding of the processes involved.

*For Dad*

# Acknowledgements

This thesis would not have been possible without the contribution of a few important people. Most importantly I would like to thank my supervisor Graham. His knowledge and patience has been fundamental to the success and enjoyment of my PhD. The last four years have been a steep learning curve, but well Worth it.

For enjoyable and fruitful collaborations during my PhD I would like to extend my upmost thanks to the Fielding group: Helen, Dorian and Russell. Their experimental results have provided much of the inspiration behind this work.

I would also like to thank Chris Meier for a very meritorious and rewarding collaboration on the implementation of Local Control Theory. My 4 weeks in Toulouse were superb, apart from the weather!

I would also like to thank the whole of the Worth group and the rest of floor 2 for many hours of fun in the last 3 years. In particular Andy Bennett, for the Pennett, Adam and Dan for cricket conversations and most importantly Kousik for teaching me why we study quantum chemistry: "because once we have  $\Psi$  we have everything, earth, the gods and the heavens."

I am also greatly indebted to my parents for an infinite number of things, especially their help and encouragement. I would not have done a PhD if Mum hadn't persuaded me to stay for the MSci and I wouldn't be as impatient and such a geek if it wasn't for Dad's genes!

Finally I would like to thank my wife Charlotte. I am so thankful for her unfaltering support, belief in me and for her patience especially when I try and draw her pictures of potential energy surfaces.

This thesis and the work described in it are entirely my own, except where I have acknowledged *either* help from a named person *or* a reference is given to a published source or a thesis. Text taken from another source will be enclosed in quotation marks and a reference will be given.

February 17, 2010

# List of Publications

1. Parker, D. S. N. and Minns, R. S. and Penfold, T. J. and Worth, G. A. and Fielding, H. H. *Ultrafast dynamics of the  $S_1$  excited state of benzene*, Chemical Physics Letters, 2009,**469**:43:47.
2. Penfold, T. J. and Worth, G. A. *A model Hamiltonian to simulate the complex photochemistry of benzene II*, Journal of Chemical Physics, 2009,**131**.
3. Penfold, T. J. and Worth, G. A. *Spin Orbit Coupling in Small Hydrocarbons* (in preparation)
4. Parker, D. S. N. and Minns, R. S. and Penfold, T. J. and Worth, G. A. and Fielding, H. H. *Benzene photochemistry: The role of triplet states in ultrafast dynamics*. (in preparation)
5. Penfold, T. J. and Parker, D. S. N. and Minns, R. S. and Fielding, H. H. and Worth, G. A. *Quantum dynamics of the complex photochemistry of benzene*. (in preparation)
6. Penfold, T. J. and Meier, C. and Worth G. A. *Coherent Control of multidimensional systems: Implementation of Local Control Theory into the MCTDH*. (in preparation)



# Contents

<b>List of Figures</b>	<b>xix</b>
<b>List of Tables</b>	<b>xxv</b>
<b>Glossary</b>	<b>xxviii</b>
<b>1 Introduction</b>	<b>1</b>
<b>2 Theory</b>	<b>12</b>
2.1 The Schrödinger Equation . . . . .	12
2.2 Born-Oppenheimer Approximation . . . . .	14
2.3 Adiabatic to Diabatic Representation via Non-Adiabatic corrections . .	16
2.3.1 Adiabatic Representation . . . . .	16
2.3.2 Conical Intersections . . . . .	17
2.3.3 Non-Adiabatic Corrections . . . . .	18
2.3.4 Diabatic Representation . . . . .	19
2.4 The Vibronic Coupling Model Hamiltonian . . . . .	20
2.5 Coherent Control . . . . .	23
2.5.1 Light and Matter Interaction . . . . .	23
2.5.2 The Essence of Controllability . . . . .	24
2.5.3 Local Control Theory . . . . .	25
<b>3 Computation and Methodology</b>	<b>27</b>

## Contents

---

3.1	Hartree-Fock (HF) theory . . . . .	28
3.2	Complete Active Space Self Consistent Field (CASSCF) theory . . . . .	30
3.3	Complete Active Space with 2 <sup>nd</sup> Order Perturbation (CASPT2) Theory . . . . .	32
3.4	Spin Orbit Coupling . . . . .	35
3.5	Multi-Configuration Time Dependent Hartree (MCTDH) method . . . . .	37
3.5.1	General Formulation . . . . .	37
3.5.2	Efficiency and Memory . . . . .	40
3.5.3	DVR Functions . . . . .	40
3.5.4	Autocorrelation Functions and Calculation of Spectra . . . . .	41
<b>4</b>	<b>Benzene</b>	<b>43</b>
4.1	The Model Hamiltonian . . . . .	46
4.1.1	First Order Parameters . . . . .	51
4.1.2	Morse Parameters . . . . .	54
4.1.3	Second Order Parameters . . . . .	56
4.2	Cuts Through The Potential Energy Surfaces . . . . .	59
4.2.1	Along The Normal Modes . . . . .	59
4.2.2	Combination Modes . . . . .	63
4.3	The Prefulvene Vector and S <sub>0</sub> /S <sub>1</sub> Conical Intersection . . . . .	65
4.4	The Absorption Spectra . . . . .	67
4.5	Quantum Dynamics Calculations . . . . .	69
4.5.1	Experimental Data . . . . .	69
4.5.2	5 State Diabatic Model . . . . .	74
4.5.3	2 State Adiabatic Model . . . . .	81
4.6	Conclusion . . . . .	92

## Contents

---

<b>5</b>	<b>Spin Orbit Coupling</b>	<b>99</b>
5.1	Introduction . . . . .	99
5.2	Methodology and Computation . . . . .	103
5.3	Results . . . . .	103
5.3.1	Cyclo-Butadiene . . . . .	103
5.3.2	Benzene . . . . .	111
5.3.3	Spin Orbit Coupling at the Intersection . . . . .	114
5.4	Conclusion . . . . .	119
<b>6</b>	<b>Ultrafast Intersystem Crossing Dynamics in Benzene</b>	<b>121</b>
6.1	The Model Hamiltonian . . . . .	122
6.1.1	First Order Parameters . . . . .	123
6.1.2	Second Order Parameters . . . . .	124
6.1.3	Cuts Through The Potential Energy Surfaces . . . . .	126
6.1.4	Spin Orbit Coupling Parameters . . . . .	128
6.1.5	Effective Couplings . . . . .	129
6.2	The Dynamics . . . . .	132
6.3	Conclusion . . . . .	137
<b>7</b>	<b>Coherent Control</b>	<b>143</b>
7.1	Methodology and Computation . . . . .	145
7.2	Results . . . . .	145
7.2.1	Neutral cyclobutadiene . . . . .	145
7.2.2	Cyclobutadiene Radical Cation . . . . .	151
7.2.3	Pyrazine . . . . .	159
7.2.4	Ammonia . . . . .	165
7.3	Conclusion . . . . .	170
<b>8</b>	<b>Conclusion</b>	<b>176</b>

## Contents

---

Bibliography

183

# List of Figures

1.1	Model potential energy surface of the cis/trans-isomerisation of retinal in Rhodopsin. At the Franck-Condon point the energy gap between the states is equivalent to the frequency of visible light, this results in efficient excitation. The gradient in the excited state leads to the $S_1/S_0$ surface crossing resulting in the formation of either the trans form or the regeneration of the cis ground state. Figure adapted from [2] . . . . .	2
1.2	Typical types of conical intersection. (a) Symmetry induced sloped (b) $E \times \epsilon$ linear Jahn-Teller. Figure taken from [10]. . . . .	4
1.3	Femtochemistry of ICN: (a) A schematic of the potential energy surface and the motion of the wavepacket along the I-CN coordinate following excitation into $\tilde{A}$ . (b) Experimental results probing the CN fragment via LIF signal as a function of time with probe wavelengths of $\lambda=388.9\text{nm}$ , $389.8\text{nm}$ , $390.4\text{nm}$ and $391.4\text{nm}$ . Figure taken from [15,16]. . . . .	6
1.4	Dissociation of NaI: (a) A schematic of the potential energy surface including the ground state, first excited state and second excited state. (b) Experimental results plotting the Na fragment as a function of time. The upper plot on figure (b) shows an increasing signal of the free Na, the lower plot shows the oscillatory behaviour of the transition state. Figure taken from [15,16]. . . . .	7

---

## List of Figures

---

1.5	In the Brumer-Shapiro approach coherent control can be achieved by manipulating interfering pathways of two pulses connecting an initial state to a final state [23]. . . . .	8
1.6	A schematic for the Tannor, Rice and Kosloff pump-dump approach. An initial pump pulse creates a wavepacket on an excited state. This is then allowed to evolve on the excited state field free. At some time after $t_0$ a dump pulse transfers the wavepacket down to the ground, into the desired minima. Figure adapted from [27]. . . . .	9
4.1	The $\pi$ valence orbitals in benzene. The lowest three are doubly occupied in the ground state determinant. The unoccupied $\pi^*$ orbitals ( $e_{2u}$ and $b_{1g}$ ) are occupied in the most important excited determinants and therefore are required to provide the electron correlation required to give a good energetic description of the excited states. . . . .	44
4.2	Ground state minimum energy geometry structure of (a) fulvene (b) benzvalene and (c) dewar benzene. . . . .	45
4.3	Cuts through the adiabatic potential energy surfaces for benzene, including the ground states and 6 excited states. In order of energy at $\mathbf{Q}=0$ these states are $\tilde{X} A_{1g}$ , $\tilde{A} B_{2u}$ , $\tilde{B} B_{1u}$ , $\tilde{C} E_{1u}$ , $\tilde{D} E_{2g}$ . (a) $\nu_1$ ( $1a_{1g}$ ), the breathing mode, (b) $\nu_4$ ( $1b_{2g}$ ), the chair mode, (c) $\nu_{6a}$ ( $1e_{2g}$ ), the quinoid mode . . . . .	60
4.4	Cuts through the adiabatic potential energy surfaces for benzene, including the ground states and 6 excited states. In order of energy at $\mathbf{Q}=0$ these states are $\tilde{X} A_{1g}$ , $\tilde{A} B_{2u}$ , $\tilde{B} B_{1u}$ , $\tilde{C} E_{1u}$ , $\tilde{D} E_{2g}$ . (a) $\nu_{16a}$ ( $1e_{2u}$ ), the boat mode, (b) $\nu_{10a}$ ( $1e_{1g}$ ) (c) $\nu_{11}$ ( $1a_{2u}$ ). . . . .	61

## List of Figures

---

4.5	Cuts through the adiabatic potential energy surfaces for benzene, including the ground states and 6 excited states. In order of energy at $\mathbf{Q}=0$ these states are $\tilde{X} A_{1g}$ , $\tilde{A} B_{2u}$ , $\tilde{B} B_{1u}$ , $\tilde{C} E_{1u}$ , $\tilde{D} E_{2g}$ . (a) $\nu_{12}$ ( $1b_{1u}$ ) (b) $\nu_{13}$ ( $2b_{1u}$ ) (c) $\nu_{17a}$ ( $2e_{2u}$ ). . . . .	61
4.6	Cuts through the adiabatic potential energy surfaces for benzene, including the ground states and 6 excited states. In order of energy at $\mathbf{Q}=0$ these states are $\tilde{X} A_{1g}$ , $\tilde{A} B_{2u}$ , $\tilde{B} B_{1u}$ , $\tilde{C} E_{1u}$ , $\tilde{D} E_{2g}$ . (a) $\nu_{18a}$ ( $1e_{1u}$ ) (b) $\nu_{19a}$ ( $2e_{1u}$ ) (c) $\nu_{20a}$ ( $3e_{1u}$ ). . . . .	62
4.7	Cuts through the adiabatic potential energy surfaces for benzene, including the ground states and 6 excited states. In order of energy at $\mathbf{Q}=0$ these states are $\tilde{X} A_{1g}$ , $\tilde{A} B_{2u}$ , $\tilde{B} B_{1u}$ , $\tilde{C} E_{1u}$ , $\tilde{D} E_{2g}$ . (a) $\nu_{7a}$ ( $4e_{2g}$ ) (b) $\nu_{8a}$ ( $3e_{2g}$ ) (c) $\nu_{9a}$ ( $2e_{2g}$ ). . . . .	62
4.8	Cuts through the adiabatic potential energy surfaces for benzene, including the ground states and 4 excited states. In order of energy at $\mathbf{Q}=0$ these states are $\tilde{X} A_{1g}$ , $\tilde{A} B_{2u}$ , $\tilde{B} B_{1u}$ and $\tilde{C} E_{1u}$ . (a) $\nu_{4+16a}$ (b) $\nu_{1+16a}$ (c) $\nu_{6a+16a}$ . . . . .	64
4.9	Cuts through the adiabatic potential energy surfaces for benzene, including the ground states and 4 excited states. In order of energy at $\mathbf{Q}=0$ these states are $\tilde{X} A_{1g}$ , $\tilde{A} B_{2u}$ , $\tilde{B} B_{1u}$ and $\tilde{C} E_{1u}$ . (a) $\nu_{1+6a}$ (b) $\nu_{4+6a}$	65
4.10	Cuts along the vector for the prefulvene $S_1/S_0$ minimum energy CI and the minimum barrier height leading to the $S_1/S_0$ CI. (a) The prefulvene $S_1/S_0$ minimum energy CI along $Q_{CoIn}$ , using parameters up to second order. (b) Including the third order parameters. (c) Fit of the minimum barrier height along $Q_{barrier}$ including third order parameters. The <i>ab-initio</i> points were calculated at PT2(6,6) level. . . . .	66

**List of Figures**

---

- 4.11 The experimental spectra [90,113]. (a) The  ${}^1B_{2u} \leftarrow \tilde{X}$  spectra. The four major peaks are a breathing mode progression coupled with  $6_0^1$  to make it allowed transition. One can also see  $6_0^1 6_1^1$  and  $6_1^2$  hotbands. (b) The  ${}^1E_{1u} \leftarrow \tilde{X}$  absorption spectra, with the  ${}^1B_{1u} \leftarrow \tilde{X}$  spectra inset. The  ${}^1E_{1u} \leftarrow \tilde{X}$  transition is an allowed transition and therefore produces a broad and structureless band. . . . . 69
- 4.12 (a) The  ${}^1B_{2u} \leftarrow \tilde{X}$  absorption spectra. This shows agreement with the experimental spectra. The spectra includes the main breathing mode progression and the  $6_0^1 6_1^1$  and  $6_1^2$  hotbands. (b) The  ${}^1B_{1u} \leftarrow \tilde{X}$  absorption spectra. Main progression in the spectra is a breathing mode progression with mode  $9_0^1$ . . . . . 70
- 4.13 The  ${}^1E_{1u} \leftarrow \tilde{X}$  absorption spectra. This allowed transition produces an broad, intense and structureless band. The tail structure (enlarged inset) is the  ${}^1B_{1u} \leftarrow \tilde{X}$  spectra arising from intensity borrowing of the allowed transition as a result of the vibronic coupling which exists between the two states. . . . . 70
- 4.14 (a) Experimental decay curves, detecting the photoelectron yield as a function of probe delay of hot wavepacket following excitation into  $S_1$ . The pump pulse was 243nm and the probe pulse 235nm (blue) and 254nm (red). (b) The ratio of the amplitude of the slow component to the amplitude of the fast component is plotted as a function of the probe wavelength. The step at 250nm is a signature of a new ionisation pathway opening. Figure reproduced with the permission of Prof. H. Fielding, UCL, London. [19]. . . . . 72



## List of Figures

---

4.15 Intensity of kinetic energies of the expelled photoelectrons as a function of pump-probe delay, the exponential decay has been removed. (a) Photoelectron kinetic energies following a Franck-Condon excitation of the hot wavepacket into $S_1$ (b) Photoelectron kinetic energy following a Franck-Condon excitation of the cold wavepacket into $S_1$ . Figure reproduced with the permission of Prof. H. Fielding, UCL, London. [19]. . . . .	73
4.16 Integrated intensities of photoelectrons as a function of pump-probe delay with the exponential decay removed. The open circles correspond to integration over the range $\varepsilon_{1a}$ and $\varepsilon_{1b}$ . The closed circles correspond to integration over the range $\varepsilon_2$ and the filled triangles correspond to integration over the range $\varepsilon_3$ . $\varepsilon_{1a}=1.25-1.35\text{eV}$ , $\varepsilon_{1b}=1.13-1.23\text{eV}$ , $\varepsilon_2=0.75-0.95\text{eV}$ and $\varepsilon_3=0.35-0.45\text{eV}$ . Figure reproduced with the permission of Prof. H. Fielding, UCL, London. [19]. . . . .	73
4.17 (a) Diabatic state populations of $\tilde{A}$ (blue) and $\tilde{A}+\tilde{C}$ (red) following a excitation of the hot wavepacket into the Franck-Condon point on $\tilde{A}$ . (b) Diabatic populations of $\tilde{A}$ (red) and $\tilde{A}+\tilde{C}$ (blue) following excitation of the cold packet into Franck-Condon point on $\tilde{A}$ . . . . .	76
4.18 Expectation values of the position of the hot wavepacket during propagation for the first 2000fs. (a) $\langle q \rangle$ of $\nu_4$ (green) and $\nu_{16}$ (red) on $S_0$ . (b) $\langle q \rangle$ of $\nu_1$ (purple) and $\nu_6$ (blue) on $S_0$ . (c) $\langle q \rangle$ of $\nu_4$ (green) and $\nu_{16}$ (red) on $S_1$ . (d) $\langle q \rangle$ of $\nu_1$ (purple) and $\nu_6$ (blue) on $S_1$ . (e) $\langle q \rangle$ of $\nu_4$ (green) and $\nu_{16}$ (red) on $S_3$ . (f) $\langle q \rangle$ of $\nu_1$ (purple) and $\nu_6$ (blue) on $S_3$ . . . . .	79

---

## List of Figures

---

4.19	Expectation values of the width of the hot wavepacket during propagation for the first 2000fs. (a) $\langle dq \rangle$ of $\nu_4$ (green) and $\nu_{16}$ (red) on $S_0$ . (b) $\langle dq \rangle$ of $\nu_1$ (purple) and $\nu_6$ (blue) on $S_0$ . (c) $\langle dq \rangle$ of $\nu_4$ (green) and $\nu_{16}$ (red) on $S_1$ . (d) $\langle dq \rangle$ of $\nu_1$ (purple) and $\nu_6$ (blue) on $S_1$ . (e) $\langle dq \rangle$ of $\nu_4$ (green) and $\nu_{16}$ (red) on $S_3$ . (f) $\langle dq \rangle$ of $\nu_1$ (purple) and $\nu_6$ (blue) on $S_3$ . . . . .	80
4.20	The wavefunction density on $\tilde{X}$ in benzene along $\nu_4$ and $\nu_{16a}$ . (a) 0fs (b) 50fs (c) 100fs (d) 150fs (e) 200fs (f) 250fs (g) 350fs (h) 450fs (i) 550fs (j) 1000fs. . . . .	82
4.21	The wavefunction density on $\tilde{A}$ in benzene along $\nu_4$ and $\nu_{16a}$ . (a) 0fs (b) 50fs (c) 100fs (d) 150fs (e) 200fs (f) 250fs (g) 350fs (h) 450fs (i) 550fs (j) 1000fs. . . . .	83
4.22	The wavefunction density on $\tilde{C}$ in benzene along $\nu_4$ and $\nu_{16a}$ . (a) 0fs (b) 50fs (c) 100fs (d) 150fs (e) 200fs (f) 250fs (g) 350fs (h) 450fs (i) 550fs (j) 1000fs. . . . .	84
4.23	The wavefunction density on $\tilde{X}$ in benzene along $\nu_1$ and $\nu_{6a}$ . (a) 0fs (b) 50fs (c) 100fs (d) 150fs (e) 200fs (f) 250fs (g) 350fs (h) 450fs (i) 550fs (j) 1000fs. . . . .	85
4.24	The wavefunction density on $\tilde{A}$ in benzene along $\nu_1$ and $\nu_{6a}$ . (a) 0fs (b) 50fs (c) 100fs (d) 150fs (e) 200fs (f) 250fs (g) 350fs (h) 450fs (i) 550fs (j) 1000fs. . . . .	86
4.25	The wavefunction density on $\tilde{C}$ in benzene along $\nu_1$ and $\nu_{6a}$ . (a) 0fs (b) 50fs (c) 100fs (d) 150fs (e) 200fs (f) 250fs (g) 350fs (h) 450fs (i) 550fs (j) 1000fs. . . . .	87

## List of Figures

---

4.26 (a) Diabatic state population of $\tilde{A}$ (green) and $\tilde{A}$ minus population on the CI side of the barrier (red) for the two state model Hamiltonian following excitation of the hot wavepacket into $\tilde{A}$ . (b) Diabatic state population of $\tilde{A}$ (green) and $\tilde{A}$ minus population on the CI side of the barrier (red) following excitation of the cold wavepacket into $\tilde{A}$ . . . . .	89
4.27 Expectation values of the position of the hot wavepacket during propagations for first 2000fs. (a) $\langle q \rangle$ of $\nu_4$ (green) and $\nu_{16}$ (red) on $S_0$ . (b) $\langle q \rangle$ of $\nu_1$ (purple) and $\nu_6$ (blue) on $S_0$ . (c) $\langle q \rangle$ of $\nu_4$ (green) and $\nu_{16}$ (red) on $S_1$ . (d) $\langle q \rangle$ of $\nu_1$ (purple) and $\nu_6$ (blue) on $S_1$ . . . . .	90
4.28 Expectation values of the width of the hot wavepacket during propagations for first 2000fs. (a) $\langle q \rangle$ of $\nu_4$ (green) and $\nu_{16}$ (red) on $S_0$ . (b) $\langle q \rangle$ of $\nu_1$ (purple) and $\nu_6$ (blue) on $S_0$ . (c) $\langle q \rangle$ of $\nu_4$ (green) and $\nu_{16}$ (red) on $S_1$ . (d) $\langle q \rangle$ of $\nu_1$ (purple) and $\nu_6$ (blue) on $S_1$ . . . . .	91
4.29 The wavefunction density on $S_0$ in benzene along $\nu_4$ and $\nu_{16a}$ . (a) 0fs (b) 50fs (c) 100fs (d) 150fs (e) 200fs (f) 250fs (g) 350fs (h) 450fs (i) 550fs (j) 1000fs. . . . .	93
4.30 The wavefunction density on $S_0$ in benzene along $\nu_1$ and $\nu_{6a}$ . (a) 0fs (b) 50fs (c) 100fs (d) 150fs (e) 200fs (f) 250fs (g) 350fs (h) 450fs (i) 550fs (j) 1000fs. . . . .	94
4.31 The wavefunction density on $S_1$ in benzene along $\nu_4$ and $\nu_{16a}$ . (a) 0fs (b) 50fs (c) 100fs (d) 150fs (e) 200fs (f) 250fs (g) 350fs (h) 450fs (i) 550fs (j) 1000fs. . . . .	95
4.32 The wavefunction density on $S_1$ in benzene along $\nu_1$ and $\nu_{6a}$ . (a) 0fs (b) 50fs (c) 100fs (d) 150fs (e) 200fs (f) 250fs (g) 350fs (h) 450fs (i) 550fs (j) 1000fs. . . . .	96

---

## List of Figures

---

5.1	(a) The HOMO and LUMO orbitals of ethylene and the spin flip involved in a $\pi\pi^*$ transition from $S_0$ to $T_1$ . There is no possible change in angular momentum and hence the spin-flip is forbidden. (b) The electron one-centre jump involved in $S_0$ to $T_3$ transition (HOMO and LUMO+1). The change in angular momentum involved in a jump from a $p_z$ to $p_y$ is match exactly by the change in angular momentum associated with a spin-flip, conserving angular momentum and making this an allowed transition. . . . .	101
5.2	The pure p orbital is able to mix when an out of plane C-H bend occurs. This create an $sp^n$ orbital and the mixing between $\sigma$ and $\pi$ states provides a mechanism for spin orbit coupling. . . . .	102
5.3	Optimised structures of cyclobutadiene using a CAS(4,4)/6-31g* basis. (a) $D_{2h}$ rectangular form (b) $D_{4h}$ square planar form. Bond lengths are in Å. . . . .	104
5.4	Changes in spin orbit coupling values along selected normal modes of cyclobutadiene: (a) $\nu_1$ ( $1a_u$ ) (b) $\nu_2$ ( $1b_{2g}$ ) (c) $\nu_3$ ( $1b_{3u}$ ) (d) $\nu_4$ ( $2a_u$ ). In all cases the green line is spin orbit coupling between $2^1A_{1g}/^3B_{1g}$ . The red curve is spin orbit coupling between $1^1A_{1g}/^3B_{1g}$ . . . . .	109
5.5	The $\pi$ valence orbitals of cyclobutadiene. (a) Equilibrium geometry (b) Distorted along $\nu_3$ , an out of the plane C-H bend. At this point the hydrogen atom is bent $63^\circ$ out of plane of the molecule. The orbitals show $sp^n$ character responsible for a mechanism for spin orbit coupling. . . . .	110
5.6	Changes in spin orbit coupling values along the important vibrational modes of benzene: (a) $\nu_4$ ( $1b_{2g}$ ), (b) $\nu_5$ ( $2b_{2g}$ ), (c) $\nu_{10}$ ( $1e_{1g}$ ), (d) $\nu_{11}$ ( $1a_{2u}$ ), (e) $\nu_{16}$ ( $1e_{2u}$ ), (f) $\nu_{17}$ ( $2e_{2u}$ ) . . . . .	115

---

**List of Figures**

---

5.7	The $\pi$ valence orbitals (without the degenerate pairs) of benzene. (a) Equilibrium geometry (b) Distorted along $\nu_5$ , an out of the plane C-H bend. The orbitals clearly show $sp^n$ character responsible for a mechanism for spin orbit coupling. (c) Distorted along the Jahn-Teller mode $\nu_6$ . Although the orbitals are distorted there is no out of plane C-H motion and no $sp^n$ character. Therefore despite being a very important coupling mode in both the triplet and singlet manifold it is not responsible for linking the two. . . . .	116
5.8	The potential energy surface cuts along the vector from the Franck-Condon point to the $S_1/S_0$ conical intersection and corresponding spin orbit coupling values. (a) Cyclo-butadiene: States at $\mathbf{Q}_0$ are ordered $S_0$ , $T_1$ , $S_1$ and $T_2$ at equilibrium. (b) Benzene: States at $\mathbf{Q}_0$ are ordered $S_0$ , $T_1$ , $T_2$ , $x$ , $T_2$ , $y$ and $S_2$ at equilibrium. (c) Spin orbit coupling between $2^1A_{1g}/1^3B_{1g}$ (green) and $1^1A_{1g}/1^3B_{1g}$ (red) towards the $S_1/S_0$ conical intersection for cyclobutadiene. (d) Spin orbit coupling between $1^1B_{2u}/1^3B_{1u}$ towards the $S_1/S_0$ conical intersection for benzene . . . . .	118
5.9	The $\pi$ valence orbitals (without the degenerate pairs) at the conical intersection of (a) cyclobutadiene and (b) benzene . . . . .	118
6.1	Cuts along the normal modes for the triplet potential energy surfaces in benzene. In order of energy at $\mathbf{Q}=0$ these states are $T_1$ ( $B_{1u}$ ) and $T_2$ ( $E_{1u}$ ). (a) $\nu_1$ ( $1a_{1g}$ ), the breathing mode, (b) $\nu_4$ ( $1b_{2g}$ ), the chair mode, (c) $\nu_{6a}$ ( $1e_{2g}$ ), the quinoid mode (d) $\nu_{16a}$ ( $1e_{2u}$ ), the boat mode, (e) $\nu_{8a}$ ( $3e_{1g}$ ) (f) $\nu_{9a}$ ( $2e_{1g}$ ) . . . . .	127
6.2	Cut along the prefulvene combination mode ( $\nu_4 + \nu_{16a}$ ) for the triplet potential energy surfaces in benzene. In order of energy at $\mathbf{Q}=0$ these states are $T_1$ ( $B_{1u}$ ) and $T_2$ ( $E_{1u}$ ). . . . .	128

---

## List of Figures

---

- 6.3 (a) Diabatic state populations of benzene during the first 2000fs following excitation of the hot wavepacket into  $S_1$ . The blue line is the population of  $S_1$  minus the population which is over the barrier to the  $S_1/S_0$  population. This corresponds to the photoelectron data using the 254nm probe wavelength. The red line is the population of  $S_1$  plus the triplet populations corresponding the photoelectron data using the 235nm probe wavelength. (b) Diabatic state populations of the benzene triplet states during the first 2000fs following excitation of the hot wavepacket into  $S_1$ .  $T_1$  (red),  $T_{2,x}$  (green) and the sum of all of the triplets (blue). . . . . 134
- 6.4 Expectation values of the position of the hot wavepacket in the triplet states during propagations for first 2000fs. (a)  $\langle q \rangle$  of  $\nu_4$  (green) and  $\nu_{16}$  (red) on  $T_1$ . (b)  $\langle q \rangle$  of  $\nu_1$  (purple) and  $\nu_6$  (blue) on  $T_1$ . (c)  $\langle q \rangle$  of  $\nu_4$  (green) and  $\nu_{16}$  (red) on  $T_{2,x}$ . (d)  $\langle q \rangle$  of  $\nu_1$  (purple) and  $\nu_6$  (blue) on  $T_{2,x}$ . . . . . 135
- 6.5 Expectation values of the width of the hot wavepacket in the triplet states during propagations for first 2000fs. (a)  $\langle q \rangle$  of  $\nu_4$  (green) and  $\nu_{16}$  (red) on  $T_1$ . (b)  $\langle q \rangle$  of  $\nu_1$  (purple) and  $\nu_6$  (blue) on  $T_1$ . (c)  $\langle q \rangle$  of  $\nu_4$  (green) and  $\nu_{16}$  (red) on  $T_{2,x}$ . (d)  $\langle q \rangle$  of  $\nu_1$  (purple) and  $\nu_6$  (blue) on  $T_{2,x}$ . . . . . 136
- 6.6 The wavefunction density on  $T_1$  in benzene along  $\nu_4$  and  $\nu_{16a}$ . (a) 0fs (b) 50fs (c) 100fs (d) 150fs (e) 200fs (f) 250fs (g) 350fs (h) 450fs (i) 550fs (j) 1000fs. . . . . 138
- 6.7 The wavefunction density on  $T_1$  in benzene along  $\nu_1$  and  $\nu_{6a}$ . (a) 0fs (b) 50fs (c) 100fs (d) 150fs (e) 200fs (f) 250fs (g) 350fs (h) 450fs (i) 550fs (j) 1000fs. . . . . 139

List of Figures

---

6.8	The wavefunction density on $T_{2,x}$ in benzene along $\nu_4$ and $\nu_{16a}$ . (a) 0fs (b) 50fs (c) 100fs (d) 150fs (e) 200fs (f) 250fs (g) 350fs (h) 450fs (i) 550fs (j) 1000fs. . . . .	140
6.9	The wavefunction density on $T_{2,x}$ in benzene along $\nu_1$ and $\nu_{6a}$ . (a) 0fs (b) 50fs (c) 100fs (d) 150fs (e) 200fs (f) 250fs (g) 350fs (h) 450fs (i) 550fs (j) 1000fs. . . . .	141
7.1	“Cuts through potential energy surface for the lowest 3 singlet states $\tilde{X}^1B_{1g}$ , $\tilde{A}^1A_g$ , and $\tilde{B}^1B_{2g}$ of neutral cyclobutadiene along the $D_{4h}$ normal vibrational modes (a) $\nu_1(1a_g)$ , (b) $\nu_4(2b_{1g})$ and (c) $\nu_6(1b_{2g})$ . Points are energies calculated using SA-CAS(4,4)/6-31G*, lines are from the Vibronic Coupling Hamiltonian.” Figure used with permission of Dr G. Worth, taken from [129]. . . . .	147
7.2	“ Contour plots of the potential energy surface for the lowest adiabatic singlet state, $\tilde{X}^1B_{1g}$ , of neutral cyclobutadiene in the space of (b), (d) the $b_{1g}$ modes, $\nu_4$ and $\nu_5$ , and (a), (c) the strongest vibronically coupled modes, $\nu_4$ and $\nu_6$ . Surfaces are from the vibronic coupling model Hamiltonian fitted to SA-CAS(4,4)/6-31G* data: (a) and (b) include only linear coupling, (c) and (d) including second-order terms.” Figure used with permission of Dr G. Worth, taken from [129] . . . . .	147
7.3	The diabatic state populations for 50fs of the lowest three singlet states, $\tilde{X}^1B_{1g}$ (red), $\tilde{A}^1A_g$ (green), and $\tilde{B}^1B_{2g}$ (blue) in neutral cyclobutadiene, without an external field following a vertical excitation into $\tilde{A}$ . . . . .	149
7.4	(a) The diabatic state populations of of the lowest three singlet states, $\tilde{X}^1B_{1g}$ (red), $\tilde{A}^1A_g$ (green), and $\tilde{B}^1B_{2g}$ (blue) in neutral cyclobutadiene for 100fs of controlled dynamics to populate $S_0$ , $\lambda=0.25$ . (b) Electric field calculated by the local control algorithm. . . . .	149

---

## List of Figures

---

7.5	(a) The diabatic state populations of of the lowest three singlet states, $\tilde{X}^1B_{1g}$ (red), $\tilde{A}^1A_g$ (green), and $\tilde{B}^1B_{2g}$ (blue) in neutral cyclobutadiene for 200fs of the controlled dynamics to populate $S_0$ , $\lambda=0.01$ . (b) Electric field calculated by the local control algorithm. . . . .	149
7.6	Fourier transform of the pulse calculated to the control the dynamics of population transfer between $S_1$ and $S_0$ of neutral cyclobutadiene: (a) $\lambda=0.25$ (b) $\lambda=0.01$ . . . . .	150
7.7	Snapshot of wavepacket on $S_0$ for neutral cyclobutadiene during the control of $S_1$ and $S_0$ population after 100fs: (a) $\lambda=0.01$ (b) $\lambda=0.25$ . . .	151
7.8	(a) The diabatic state populations of of the lowest three singlet states, $\tilde{X}^1B_{1g}$ (red), $\tilde{A}^1A_g$ (green), and $\tilde{B}^1B_{2g}$ (blue) in neutral cyclobutadiene over 100fs for the control of population to $S_2$ , $\lambda=0.25$ . (b) Electric field calculated by the local control algorithm. . . . .	151
7.9	(a) The diabatic state populations of of the lowest three singlet states, $\tilde{X}^1B_{1g}$ (red), $\tilde{A}^1A_g$ (green), and $\tilde{B}^1B_{2g}$ (blue) in neutral cyclobutadiene over 100fs for the controlled population of $S_2$ , $\lambda=0.01$ . (b) Electric field calculated by the local control algorithm. . . . .	152
7.10	Fourier transform of calculated pulse for the control of populations from $S_1$ to $S_2$ of neutral cyclobutadiene using (a) $\lambda=0.25$ (b) $\lambda=0.01$ . . . . .	152
7.11	Snapshot of the wavepacket on $S_2$ of neutral cyclobutadiene after 65fs for control of $S_1$ and $S_2$ population: (a) $\lambda=0.01$ (b) $\lambda=0.25$ . . . . .	152
7.12	The diabatic PES of the ${}^2E_{2g}$ state along $\nu_4$ ( $b_{1g}$ ) and $\nu_6$ ( $b_{2g}$ ) modes of the radical cationic cyclobutadiene. The two minima represent the rectangular structures, while the transition state is the square planar geometry. . . . .	153



---

## List of Figures

---

7.13	The diabatic state populations of the lowest doubly degenerate ${}^2E_{2g}$ state, ${}^2E_{2g,x}$ (red) and ${}^2E_{2g,y}$ (green) of radical cation cyclobutadiene for 8ps. . . . .	154
7.14	(a) The diabatic state populations of the lowest doubly degenerate ${}^2E_{2g}$ state, ${}^2E_{2g,x}$ (red) and ${}^2E_{2g,y}$ (green) of radical cation cyclobutadiene for 8ps using the control field (b). . . . .	154
7.15	The wavefunction density on $D_{0,x}$ and $D_{0,y}$ in the radical cation cyclobutadiene along $\nu_4$ and $\nu_6$ (a)/(b) 0fs, (c)/(d) 1000fs (e)/(f) 1800fs (g)/(h) 4000fs and (i)/(j) 4700fs. . . . .	156
7.16	(a) $\langle q_4 \rangle$ for $D_{0,x}$ and $D_{0,y}$ . (b) $\langle dq_4 \rangle$ for $D_{0,x}$ and $D_{0,y}$ . In both cases red represents $D_{0,x}$ and green represents $D_{0,y}$ . . . . .	157
7.17	Fourier transform of the calculated pulses for the radical cation cyclobutadiene. (a) Unfiltered (b) Filtered. . . . .	158
7.18	Controlled dynamics performed with the filtered field. (a) Controlled diabatic state populations, ${}^2E_{2g,x}$ (red) and ${}^2E_{2g,y}$ (green). (b) Filtered control pulse. This pulse contains only the four main frequencies highlighted from the first control. . . . .	158
7.19	The diabatic potential energy surface for pyrazine along $\nu_{6a}$ and $\nu_{10a}$ showing the conical intersection which is located close to the Franck-Condon point on $S_2$ . . . . .	161
7.20	(a) The diabatic state populations of pyrazine over 500fs under the influence of the field shown in (b). In this control the coupling between $S_1$ and $S_2$ has been ignored. $S_0$ (blue) and $S_2$ (green) . . . . .	162
7.21	Fourier transform of the electric field for pyrazine control, selectively populating $S_2$ in the absence of vibronic coupling between $S_1$ - $S_2$ . . . . .	162
7.22	The wavefunction density on $S_0$ and $S_2$ in pyrazine along $\nu_{6a}$ and $\nu_{10a}$ (a)/(b) 0fs, (c)/(d) 30fs (e)/(f) 45fs (g)/(h) 60fs and (i)/(j) 75fs. . . . .	163

---

## List of Figures

---

7.23	Control to maximise the $S_2$ population (a) The diabatic state populations of pyrazine over 45fs under the influence shown of the field shown in (b). The coupling between $S_1$ and $S_2$ is included. $S_0$ (blue), $S_1$ (red) and $S_2$ (green). . . . .	164
7.24	Control to maximise the $S_1$ population (a) The diabatic state populations of pyrazine over 200fs under the influence shown of the field shown in (b). The coupling between $S_1$ and $S_2$ is included. $S_0$ (blue), $S_1$ (red) and $S_2$ (green). . . . .	165
7.25	2D $\text{NH}_3$ model with DOF $R$ and $\theta$ defining the umbrella mode by the motion of one proton relative to a fixed $\text{NH}_2$ group [169]. . . . .	166
7.26	Lowest two excited states ( $\tilde{X}^1A'$ and $\tilde{A}^1A''$ ) of ammonia . The two coordinates are expressed in terms of the dissociating H atom where $R$ is the distance between H and the centre of mass of the $\text{NH}_2$ , and $\theta$ is the angle that $R$ makes with the plane of the $\text{NH}_2$ . . . . .	168
7.27	Calculated transition dipole surfaces between $\tilde{X}^1A'$ and $\tilde{A}^1A''$ for ammonia (a) $x$ component (b) $z$ component. Calculated at MRCI level. . .	169
7.28	The diabatic state populations for the lowest singlet state ( $\tilde{X}^1A'$ and $\tilde{A}^1A''$ ) of ammonia in an unperturbed system. $\tilde{X}^1A'$ (green) and $\tilde{A}^1A''$ (red). . . . .	169
7.29	(a) The diabatic state populations for the lowest singlet state ( $\tilde{X}^1A'$ and $\tilde{A}^1A''$ ) of ammonia under the influence shown of the field shown in (b). $\tilde{X}^1A'$ (green) and $\tilde{A}^1A''$ (red). . . . .	169
7.30	Fourier transform of the control pulse obtained from the local control calculation of ammonia. . . . .	170
7.31	Wavefunction density plots for $S_0$ and $S_1$ for ammonia with no pulse applied along $r_d$ and $\theta$ . (a)/(b) 0fs, (c)/(d) 5fs (e)/(f) 10fs (g)/(h) 20fs and (i)/(j) 30fs. . . . .	171

## List of Figures

---

7.32 Wavefunction density plots for $S_0$ and $S_1$ for ammonia with pulse applied along $r_d$ and $\theta$ . (a)/(b) 0fs, (c)/(d) 5fs (e)/(f) 10fs (g)/(h) 20fs and (i)/(j) 30fs. . . . .	172
--	-----

# List of Tables

4.1	Mode symmetry and vibration energies (in eV) for the gerade normal modes of benzene, using Wilson numbering. Calculated using a CAS(6,6) active space and 6-31g* basis set. . . . .	47
4.2	Mode symmetry and vibration energies (in eV) for the ungerade normal modes of benzene, using Wilson numbering. Calculated using a CAS(6,6) active space and 6-31g* basis set. . . . .	48
4.3	Vertical excitation energies (in eV) of six singlet excited states of benzene, calculated at equilibrium geometry. The SA-CAS(6,6) used a 6-31g* basis and is averaged over all 6 states plus the ground state. The PT2(6,6) and PT2(6,10) uses a Molpro specific Roos(3s2p1d/2s) basis. . . . .	49
4.4	On-diagonal linear coupling constants, $\kappa_\alpha$ , for the normal modes of benzene (in eV). Obtained by fitting a Vibronic Coupling Hamiltonian to the adiabatic potential energy surface at the CASPT2(6,6) level. There are no values for $v_{7a}$ because they are so small they can be considered negligible. . . . .	52
4.5	Off-diagonal linear coupling constants, $\lambda_\alpha$ , for the normal modes of benzene (in eV). Obtained by fitting a Vibronic Model Hamiltonian to the adiabatic potential energy surface at the CASPT2(6,6) level. The columns and rows are the different states, subscripts denote the normal modes providing the coupling. The $E_{1u,y}$ and $E_{2g,y}$ columns are not included as they symmetrically replicate the $x$ component data. . . . .	53

---

List of Tables

---

4.6	The parameters for the Morse potentials in atomic units (au) for the modes which exhibit a lot of antisymmetric behaviour. Obtained by fitting a Vibronic Coupling Hamiltonian to the adiabatic potential energy surface at the CASPT2(6,6) level. . . . .	55
4.7	On-diagonal second order coupling constants, $\gamma_\alpha$ for the normal modes of benzene (in eV). Obtained by fitting a Vibronic Coupling Hamiltonian to the adiabatic potential energy surface at CASPT2(6,6) level. . . . .	57
4.8	Off-diagonal intrastate second order coupling constants, $\gamma_{\alpha\beta}$ for the normal modes of benzene (in eV). Obtained by fitting a Vibronic Coupling Hamiltonian to the adiabatic potential energy surface at CASPT2(6,6) level. . . . .	58
4.9	Off-diagonal inter state second-order coupling terms $\mu_{\alpha\beta}$ (see equation 2.41) for the normal modes of benzene (in eV). Obtained by fitting a Vibronic Coupling Hamiltonian to the adiabatic potential energy surface at PT2(6,6) level. The $\tilde{D}E_{2g}$ state is not included in this table because there were no significant parameters for this state required. . . . .	58
4.10	On-diagonal quartic coupling constants, $\epsilon_\alpha$ (see equation 2.44) for the normal modes of benzene (in eV). Obtained by fitting a Vibronic Coupling Hamiltonian to the adiabatic potential energy surface at CASPT2(6,6) level. . . . .	59
4.11	Computational details for the quantum dynamics simulations for the calculation of the absorption spectra. $N_i, N_j$ are the no. of primitive Harmonic oscillator DVR basis functions used to describe each mode [78]. $n_i$ are the number of single-particle functions used for the wavepacket on each state. CPU time for the $B_{2u}$ spectra was just over 2hrs, for the other two spectra ( $B_{1u}$ and $E_{1u}$ ) the CPU was just under 30mins, as these calculations required fewer modes. . . . .	68

---

List of Tables

---

4.12	Computational details for the quantum dynamics simulations for the diabatic 5 state model. $N_i, N_j$ are the number of primitive Harmonic oscillator DVR basis functions used to describe each mode [78]. $n_i$ are the number of single-particle functions used for the wavepacket on each state. This ensured convergence for 1000fs in the hot wavepacket case and for the full 2000fs in the cold wavepacket case. The CPU time was 780hrs. . . . .	74
4.13	Computational details for the quantum dynamics simulations using the 2 state model Hamiltonian. $N_i$ is the no. of primitive Harmonic oscillator DVR basis functions used to describe each mode [78]. $n_i$ are the number of single-particle functions used for the wavepacket on each state. This ensured full convergence on $S_1$ for 2000fs and on $S_0$ for 1000fs. The CPU time was 380hrs. . . . .	88
5.1	Mode symmetry and vibration energies (in eV) for the lowest 14 normal modes of cyclobutadiene. Calculated using MP2 and 6-31g* basis set. The last 4 high frequency vibrational modes not included because they play no role in this study but can be found in [129]. . . . .	105
5.2	Vertical excitation energies (in eV) and spin orbit coupling (in $\text{cm}^{-1}$ ) of 3 singlet and 1 triplet states of cyclobutadiene, calculated at $D_{2h}$ equilibrium geometry. Two active spaces and 3 basis sets are used. The Roos basis is a Roos(3s2p1d/2s) basis which uses an ANO basis truncated to 6-31g* size. CASSCF is used except in the final columns for each active space which uses MRCI with a Roos basis. . . . .	107
5.3	Vertical excitation for benzene singlet and triplet excited states (in eV) and spin orbit coupling calculations (in $\text{cm}^{-1}$ ) at $D_{6h}$ equilibrium geometry.	112

---

**List of Tables**

---

6.1	Vertical excitation energies (in eV) of lowest three triplet states of benzene relative to the benzene singlet ground state, calculated at equilibrium geometry. The SA-CAS(6,6) used a 6-31g* basis and are averaged over three states. The PT2(6,6) and PT2(6,10) uses a Molpro specific Roos(3s2p1d/2s) basis. . . . .	122
6.2	On-diagonal linear coupling constants, $\kappa_\alpha$ (in eV), for the important normal modes of benzene in the triplet manifold. Obtained by fitting a Vibronic Coupling Hamiltonian to the adiabatic potential energy surfaces at the CASPT2(6,6) level. . . . .	123
6.3	Off-diagonal linear coupling constants, $\lambda_\alpha$ (in eV), for the important normal modes of benzene in the triplet manifold. Obtained by fitting a Vibronic Coupling Hamiltonian to the adiabatic potential energy surfaces at the CASPT2(6,6) level. The columns and rows are the different states, subscripts denote the normal modes providing the coupling. The $E_{1u,y}$ column is not included as it would symmetrically replicate the $x$ component data. . . . .	124
6.4	On-diagonal second order coupling constants (in eV), $\gamma_\alpha$ , for the important normal modes of benzene in the triplet manifold. Obtained by fitting a Vibronic Coupling Hamiltonian to the adiabatic potential energy surfaces at CASPT2(6,6) level. . . . .	125
6.5	Off-diagonal intrastate second order coupling constants (in eV), $\gamma_{\alpha\beta}$ for the important normal modes of benzene in the triplet manifold. Obtained by fitting a Vibronic Coupling Hamiltonian to the adiabatic potential energy surfaces at CASPT2(6,6) level. . . . .	125
6.6	On-diagonal quartic coupling constants, $\epsilon_\alpha$ (in eV) for the normal modes of benzene. Obtained by fitting a vibronic Hamiltonian to the adiabatic potential energy surfaces at CASPT2(6,6) level. . . . .	126

---

List of Tables

---

6.7	First order vibrational spin orbit coupling terms. Calculations performed with (6,6) active space and Molpro specific Roos(3s2p1d/2s) basis.	129
6.8	Second order vibrational spin orbit coupling terms. Values above the middle double line are on-diagonal terms and below are off-diagonal. Calculations performed with (6,6) active space and Molpro specific Roos(3s2p1d/2s) basis. . . . .	130
6.9	Computational details for the quantum dynamics simulations using the Intersystem crossing model Hamiltonian. $N_i$ is the number of primitive Harmonic oscillator DVR basis functions used to describe each mode [78]. $n_i$ are the number of single-particle functions used for the wavepacket on each state. The modes are combined to produce 4 2D singlet particle functions, to reduce the computational expense. The CPU was 620 hours . . . . .	133
7.1	Computational details of the quantum dynamics simulations for the control of cyclobutadiene. $N_i$ is the no. of primitive Harmonic oscillator DVR basis functions used to describe each mode [78]. $n_i$ are the number of singlet particle functions used for the wavepacket on each state. $\lambda$ denotes the strength parameter of the pulse. Note that some of the variation in the CPU is because of different $T_{final}$ . . . . .	146
7.2	Computational details for the quantum dynamics simulations for control of the radical cation of cyclobutadiene for 8ps. $N_i$ is the no. of primitive Harmonic oscillator DVR basis functions used to describe each mode [78]. $n_i$ are the number of SPF used for the wavepacket on each state. .	153



## List of Tables

---

7.3	Computational details for the quantum dynamics simulations for pyrazine. $N_i$ is the no. of primitive Harmonic oscillator DVR basis functions used to describe each mode [78]. $n_i$ are the number of single-particle functions used for the wavepacket on each state. NIC stands for No internal conversion. . . . .	160
7.4	Computational details of the quantum dynamics simulations for ammonia. $N_i$ is the no. of primitive Harmonic oscillator DVR basis functions used to describe each mode [78]. $n_i$ are the number of SPF used for the wavepacket on each state. . . . .	167

# Glossary

$$\hbar \frac{h}{2\pi}$$

$\langle dq_i \rangle$   $[\langle q_i^2 \rangle - \langle q_i \rangle^2]^{1/2}$ : Width of wavepacket for mode  $i$ .

$\langle q_i \rangle$   $\langle \Psi | \hat{q}_i | \Psi \rangle$ : Position of wavepacket for mode  $i$ .

**ANO** Atomic Natural Orbitals

**AU** Atomic Units

**BOA** Born-Oppenheimer Approximation

**BS** Brumer-Shapiro

**C(t)** Time Autocorrelation Function

**CAP** Complex Absorbing Potential

**CASPT2** Complete Active Space with 2<sup>nd</sup> Order Perturbation

**CASSCF** Complete Active Space Self Consistent Field

**CI** Conical Intersection

**CSF** Configuration State Functions

**DOF** Degrees Of Freedom

**DVR** Discrete Variable Representation

**FBR** Finite Basis Representation

**FC** Franck-Condon

**FFT** Fast Fourier Transform

**FS** Femtosecond

**FT** Fourier Transform

**Hamiltonian Operator**  $\hat{H} = -\frac{\hbar^2}{2m} \frac{\partial^2}{\partial r^2} + V(r)$

**HF** Hartree Fock

**i**  $\sqrt{-1}$

**IC** Internal Conversion

**ISC** Intersystem Crossing

**IVR** Inter Vibration Redistribution

**JT** Jahn-Teller

**LCAO** Linear Combination of Atomic Orbitals

**LCT** Local Control Theory

**LIF** Laser Induced Fluorescence

**MCSCF** Multi-Configuration Self Consistent Field

**MCTDH** Multi Configuration Time Dependent Hartree

**MRCI** Multireference Configuration Interaction

**OCT** Optimal Control Theory

**PES** Potential Energy Surface

**PJT** Pseudo Jahn-Teller

**RMSD** Root Mean Standard Deviation

**SCF** Self Consistent Field

**SOC** Spin Orbit Coupling

**SPF** Single Particle Functions

**TDH** Time Dependent Hartree

**TDSE**  $-i\hbar\frac{\partial\Psi(r,t)}{\partial t} = \hat{H}\Psi(r,t)$  (Time Dependent Schrödinger Equation)

**TISE**  $-\frac{\hbar^2}{2m}\frac{\partial^2\psi}{\partial r^2} + V(r)\psi = E\psi$  (Time Independent Schrödinger Equation)

**TRK** Tannor-Rice-Kosloff

**UV** Ultra Violet

# Chapter 1

## Introduction

Photochemistry is the study of chemical reactions which are initiated by light. In the simplest scenario light interacts with a molecule resulting in the formation of an excited species. Each excited state has a definite energy and lifetime, which are exclusively dependent upon the electronic and nuclear structure of that state. Photochemistry should therefore simply be considered as the study of the time evolution of the nuclear and electronic coordinates following perturbation by the radiation field.

Each day the sun provides the earth  $100\text{k cal cm}^{-2}$  of radiant energy, it is therefore unsurprising that photochemical processes, such as photosynthesis, play such a critical part in life as we know it. Understanding these processes is therefore not only critical to our understanding of many natural processes, but also to developing systems which are able to utilise this energy as efficiently or more so than nature.

There is a multitude of photochemical reactions which play an important role in chemistry, physics and biology [1]. Photosynthesis is the most obvious example. In this reaction the pigment chlorophyll absorbs one photon and loses one electron, initiating a chain reaction to form Nicotinamide adenine dinucleotide phosphate (NADPH). Photosynthesis is a very complex process which involves a multiple step mechanism, however there are many examples of other fundamental processes which are remarkably simple. A prime example of this is the cis/trans-isomerisation of the retinal chromophore of the Rhodopsin protein (figure 1.1) [2–4].

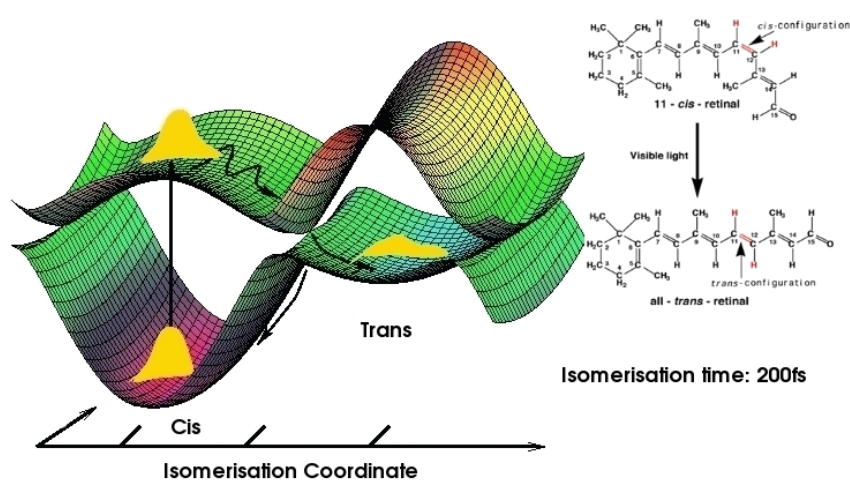


Fig. 1.1: Model potential energy surface of the cis/trans-isomerisation of retinal in Rhodopsin. At the Franck-Condon point the energy gap between the states is equivalent to the frequency of visible light, this results in efficient excitation. The gradient in the excited state leads to the  $S_1/S_0$  surface crossing resulting in the formation of either the trans form or the regeneration of the cis ground state. Figure adapted from [2]

Rhodopsin is a pigment of the retina that is responsible for the formation of the photoreceptor cells, the first events in the perception of light. Upon interaction with light, the system is efficiently excited to the  $S_1$ , because the energy gap at the Franck-Condon (FC) point is equivalent to the frequency of light. The isomerisation then occurs on a timescale of approximately 200fs, this is shown in figure 1.1. Other fundamental examples can be found in [5–7].

As illustrated in retinal the dynamics immediately proceeding excitation can often describe the ultimate outcome of the reaction and reveal detailed information about the behaviour of a chemical system. Driven by the manipulation of the electronic distribution in a molecule, changes occur on the femtosecond (fs) to the nanosecond (ns) time frame. Quantum dynamics in which a chemical system is represented in a multi-dimensional model is a powerful method for elucidating dynamical information about chemical systems on these ultrafast timescales. A wavefunction is propagated

under the Hamiltonian operator according to the time dependent Schrödinger equation (TDSE) :

$$i\hbar\frac{\partial\Psi(r,t)}{\partial t} = \hat{H}\Psi(r,t) \quad (1.1)$$

The solution of the TDSE is a superposition of eigenstates of the quantum system, this superposition is called a wavepacket and will evolve with time over a potential energy surface (PES) according to the Hamiltonian operator  $\hat{H}$ . Therefore one can see that in order to obtain a good description of the dynamics the PES must be accurately described, especially in low energy regions most often visited by the wavepacket.

$$\hat{H} = -\frac{\hbar^2}{2m}\frac{\partial^2}{\partial r^2} + V(r) \quad (1.2)$$

The potential,  $V(r)$ , which is generally time independent, can be obtained using *ab-initio* calculations. By calculating points at various geometries on the PES it is possible to perform a fit to these points, and thus obtain parameters which will accurately describe the surface. This obviously becomes increasingly difficult in multi-dimensional surfaces as the number of points required to obtain a good fit increases.

In all but the simplest cases it is impossible to solve the Schrödinger equation exactly, therefore approximations must be used. A fundamental approximation is the Born-Oppenheimer approximation (BOA) [8]. By utilising the mass difference between the nuclei and electrons we can consider the nuclei as stationary with respect to electronic motion and therefore represent the nuclei as point masses moving over a PES, provided by the electrons. This approximation allows separation of the nuclear and electronic wavefunctions in the form:

$$\Psi(r; R, t) = \psi(r; R, t)\chi(R) \quad (1.3)$$

where  $r$  is the nuclear coordinates,  $R$  is the electronic coordinates,  $\psi$  is the nuclear wavefunction and  $\chi$  is the electronic wavefunction. By neglecting the coupling that can exist, we significantly simplify the overall wavefunction. This approximation works very well when nuclear vibrations are small.

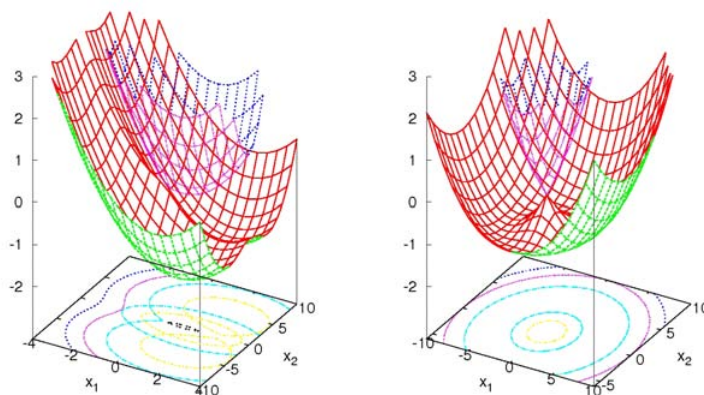


Fig. 1.2: Typical types of conical intersection. (a) Symmetry induced sloped (b)  $E \times \epsilon$  linear Jahn-Teller. Figure taken from [10].

Photochemical processes, like the isomerisation of Rhodopsin, necessarily involve excited electronic states. In this scenario fast nuclear vibrations means that the BOA is no longer valid. The coupling between nuclear and electronic motion can no longer be considered negligible and can cause the PES to cross resulting in the formation of a topology called a conical intersection (CI).

First derived in 1929 by Neumann and Wigner [9] CI provide an ultrafast and highly efficient radiationless transition between electronic states. Since their discovery such topological features have been shown to play a key role in many photochemical reactions. Figure 1.2 shows two classic examples of CI. Figure 1.2(a) is a sloped intersection which is formed because the gradient of the upper state is smaller than the lower state, causing the glancing interaction of the two surfaces. Figure 1.2(b) is a special case, a Jahn-Teller (JT) CI [11], these occur from the splitting of a degenerate state along a doubly degenerate mode.

A vital tool for understanding photochemical processes is spectroscopy. Detection of emission products following radiation of a molecular species naturally lends itself to photochemistry. In order to accurately probe a process in a time resolved manner



the radiation source must: (1) Operate typically an order of magnitude faster than the event, (2) be highly tunable and (3) have a small bandwidth of frequencies to obtain processable signal.

The development of lasers in the 1950's accelerated understanding photochemical reactions. The lasers were able to produce pulses on reaction timescales making it possible to probe reactions in real time. However it was not until the 1980's when huge developments in technologies resulted in lasers which could obtain a subpicosecond pulse width. This made it possible to probe photochemical processes in the femtosecond regime, the timescale on which molecules vibrate and bonds break [12, 13].

Culminating in the 1999 Nobel prize, femtosecond work was pioneered by Ahmed Zewail [14]. Ultrafast lasers produced pulses on the order of  $10^{-15}$ s meaning that they were an order of magnitude faster than a vibrational period ( $10^{-14}$  to  $10^{-13}$ s). This made it possible to create wavepackets focused upon a section of a vibrational motion enabling the observation of chemical reactions in real time.

The first example showing the progress of ultrafast events is the dynamics of the I-CN bond cleavage (PES shown in figure 1.3(a)) [15]. Excitation into the  $\tilde{A}$  continuum leads to dissociation along two channels producing ground or excited state iodine, however importantly for both channels the CN fragment is produced in the ground state. An initial pump pulse prepares the molecule in the  $\tilde{A}$  continuum and a delayed secondary pulse excites the wavepacket into a higher electronic excited state, which yields an excited CN fragment. The fluorescence signal from the excited CN is detected by a Laser Induced Fluorescence (LIF). Because the PES for the two continua are not parallel by altering the wavelength of the probe pulse the resonance position on the PES may be moved along the reaction coordinate. Figure 1.3(b) shows results when the probe wavelengths are 388.9nm, 389.8nm, 390.4nm and 391.4nm. In the lower three plots the wavepacket passes through resonance and progresses along the reaction coordinate, shown by the rise and fall of the LIF signal. When  $\lambda=388.9$ nm

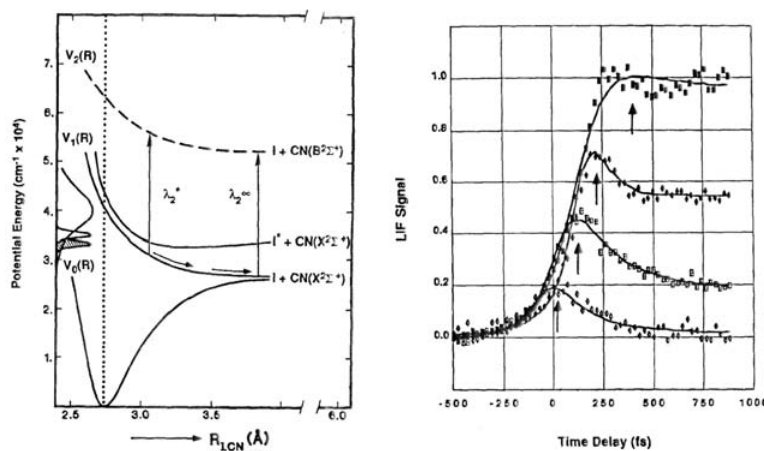


Fig. 1.3: Femochemistry of ICN: (a) A schematic of the potential energy surface and the motion of the wavepacket along the I-CN coordinate following excitation into  $\tilde{A}$ . (b) Experimental results probing the CN fragment via LIF signal as a function of time with probe wavelengths of  $\lambda=388.9\text{nm}$ ,  $389.8\text{nm}$ ,  $390.4\text{nm}$  and  $391.4\text{nm}$ . Figure taken from [15, 16].

the molecule is dissociated and therefore the wavelength is on resonant with the CN product fluorescence and therefore no decay in the signal is observed.

This pump-probe approach was also applied to the study of the dissociation of NaI (figure 1.4) [17]. This showed that upon initial excitation the wavepacket is promoted to the covalent state which corresponds to  $\text{Na} + \text{I}$ . The wavepacket proceeds along the dissociative coordinate whereupon it encounters a crossing between the covalent and ionic states, at  $\mathbf{R} = 6.93\text{\AA}$ . At this point a small portion of the wavepacket continues along the covalent curve, via the avoided crossing and dissociates to produce  $\text{Na} + \text{I}$ . The larger portion of the wavepacket follows the ionic potential, but does not have enough energy to produce  $\text{Na}^+ + \text{I}^-$  and so oscillates back and forth along the dissociative mode, with a small portion of the wavepacket yielding  $\text{Na} + \text{I}$  each time it encounters the crossing [18]. The oscillations of the wavepacket in the well is shown in figure 1.4(b). Each peak on the lower plot corresponds to the wavepacket returning to its initial position and as the dissociation progresses there is a decay in the oscillations as more  $\text{Na} + \text{I}$  is produced. The upper plot (figure 1.4(b)) is a measure of the amount

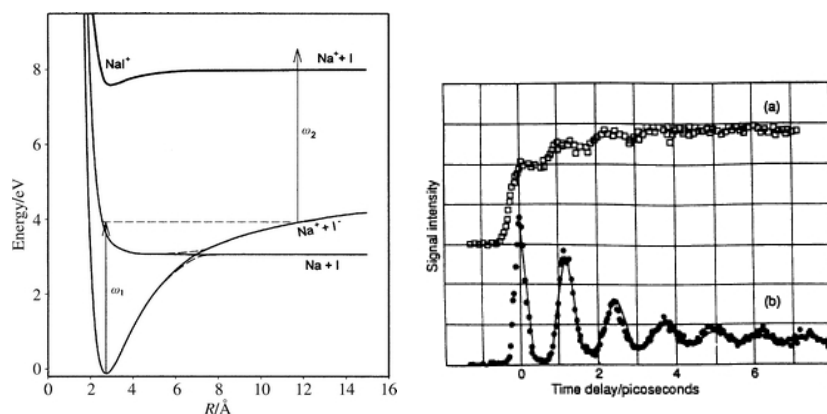


Fig. 1.4: Dissociation of NaI: (a) A schematic of the potential energy surface including the ground state, first excited state and second excited state. (b) Experimental results plotting the Na fragment as a function of time. The upper plot on figure (b) shows an increasing signal of the free Na, the lower plot shows the oscillatory behaviour of the transition state. Figure taken from [15, 16].

of neutral Na produced over time and of course this increases as the reaction proceeds.

This seminal work has been the basis for a huge number of investigations into the short time dynamics of a large range of important chemical systems [16, 19]. The use of ultrafast lasers has made it possible to observe reactions in real time. This naturally lead to the question: If we can use lasers to watch reactions, can we also use them to control them?

Initial attempts to control reactions were simple and focused upon using force. They typically used monochromatic light to deposit increasing amounts of energy into a chemical bond or vibrational mode [20–22]. One initial notable success was the dissociation of semi deuterated water. By altering the frequency of the light it is possible to selectively break either the OH or OD bond.



This control is a two step process. Initially by varying the wavelength of the first pulse ( $\nu_{OH}=3735.21\text{cm}^{-1}$  and  $\nu_{OD}=2720.9\text{cm}^{-1}$ ) it is possible to selectively excite one

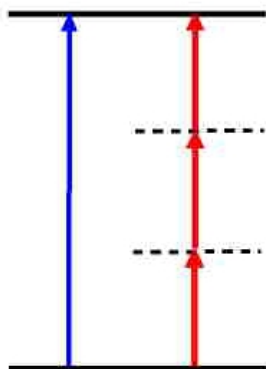


Fig. 1.5: In the Brumer-Shapiro approach coherent control can be achieved by manipulating interfering pathways of two pulses connecting an initial state to a final state [23].

of the OH or OD bonds. The second ultra violet (UV) pulse is then used to break the vibrationally excited bond, leading to the products selected by the initial radiation. Although conceptually a realistic and simple approach, in more complex systems the energy focused on a bond is spread around the entire system by inter-vibration redistribution (IVR) . Increasing the energy only results in the breaking of the weakest bond. This early approach for controlling chemical reactions ignored the benefits which could be obtained by utilising the wavelength and interference properties of light.

Femtosecond lasers and pulse shapers made it possible to introduce more sophisticated ideas for controlling chemical reactions. By altering the amplitude, time delay (phase) and frequencies of the pulses it becomes possible to create a superposition which would excite particular eigenstates of interest and hence more selectively control the wavepacket.

The most well known of these methods are the Brumer-Shapiro (BS) [24] and the Tannor-Rice-Kosloff (TRK) method [25,26]. The former (shown in figure 1.5) proved that by altering the relative phase between two pulses which couple to the final state allows control of the outcome. The TRK method (shown in figure 1.6) uses a time dependent picture. By timing the ultrashort pulse correctly is it possible to drive the wavepacket into a desired channel. The use of the excited state to access the desired

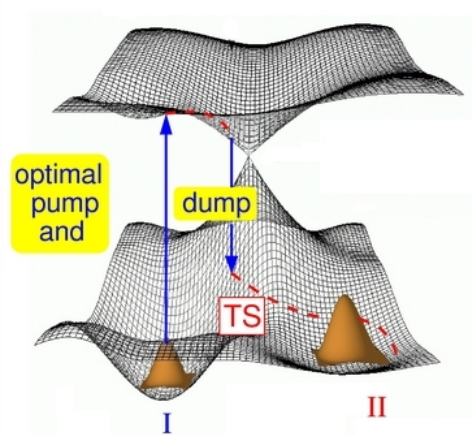


Fig. 1.6: A schematic for the Tannor, Rice and Kosloff pump-dump approach. An initial pump pulse creates a wavepacket on an excited state. This is then allowed to evolve on the excited state field free. At some time after  $t_0$  a dump pulse transfers the wavepacket down to the ground, into the desired minima. Figure adapted from [27].

minima on the ground state lead to this method being referred to as the pump-dump approach. Both of these techniques proved successful for a variety of chemical systems, but more importantly exhibited the strong time and frequency dependence required for controlling chemical reactions.

Theoretical calculations have been very important in advancing understanding of coherent control. There are numerous examples and methods throughout the literature [28–30]. One of the most commonly used methods is optimal control theory (OCT). First proposed by Judson and Rabitz [31] this technique uses the variational principle and an iterative process of forward and backward propagations to construct a field which guides the wavefunction towards a predefined target wavefunction. This method has been shown to be extremely successful in both theoretical and experimental calculations [32, 33]. Despite the successes of this method, in theoretical calculations there exist two main drawbacks of this approach. The nature of the iterative process means that this method can be extremely computationally expensive. Also the optimisation of a field using a ‘global picture’ can make them very complex and hard to relate the calculated fields to the atomic/molecular dynamics.

Local control theory (LCT) first appeared in the formulation of OCT. Introduced by Kosloff it has been extensively developed since then [34, 35]. This method moves away from the picture of a global target, instead LCT produces a control field which is calculated as a function of the instantaneous dynamics of the system at each time step. By defining an operator such as electronic population, vibrational state population or nuclear motion, the field is calculated to ensure an increase or decrease in its expectation value.

During this thesis the scientific advances we have made during my PhD are presented. In chapter 2 the fundamental theory surrounding this topic is shown, this is developed in a practical sense in chapter 3 as the methods used are discussed in detail.

In chapter 4 a detailed study of the early time dynamics of benzene is discussed. Benzene and its derivatives form a basic structure for a vast range of organic compounds in nature, and is a primary example of a photochemically rich molecule, with a number of competing pathways that can result after photoexcitation. Much of the behaviour has been characterised however a number of questions, especially in the higher vibrational states of the  $B_{2u}$  ( $S_1$ ) state remain unanswered. In this study a Vibronic Coupling Hamiltonian is set up by obtaining parameters from a fit, up to 4<sup>th</sup> order, to *ab-initio* points calculated along the important normal modes. The main three absorption spectra of benzene are calculated to test the validity of the models produced. In the final section of this chapter a detailed analysis of the short time dynamics is provided and compared with experimental data.

In chapter 5 we discuss the nature of spin orbit coupling (SOC) in some simple hydrocarbons. The triplet manifold is often ignored in hydrocarbons due to the size of SOC which is usually very small. In this chapter we give a detailed analysis of SOC in benzene and cyclobutadiene, with particular interest in the vibrational effects along the normal modes and the vector leading to the  $S_1/S_0$  CI.

In chapter 6, the triplet manifold is included into the benzene model Hamiltonian

calculated in chapter 4. By including the SOC parameters obtained from chapter 5 we are able to present dynamics of a benzene model including both singlet and triplet states. These calculations are related to recent experimental work done by the Fielding group at University College London.

Chapter 7 details the work on coherent control. Since the development of femtosecond lasers coherent control has become an important tool for both understanding and controlling chemical reactions. Various control strategies exist, one of which is LCT. In this approach the objective is to increase some predefined observable. By integrating this method into the Heidelberg Multi-configuration time dependent Hartree method (MCTDH) quantum dynamics package (see chapter 3), we show the effectiveness of this method in designing laser pulses to control ultrafast processes, especially on multi-dimensional PES. In this chapter we present control calculations for model systems of cyclobutadiene, pyrazine and ammonia. This chapter represents a stepping stone to progress to larger systems with more complicated operators.

# Chapter 2

## Theory

In this chapter a detailed description of the fundamental theory and important approximations used in this thesis are discussed. The core equation for the whole of this work is of course the Schrödinger equation, in both the time independent and time dependent forms. Time independent methods, known as *ab initio* calculations are used to treat the electronic problem and calculate the potential energy at nuclear geometries to form a PES. Time dependent methods, in which a wavepacket is propagated over the calculated PES then allow us to accurately describe the nuclear dynamics of a chemical system.

Due to the size of the wavefunction and Hamiltonian it is impossible to solve the Schrödinger equation exactly for systems much larger than  $\text{H}_2$ . The requirements of basis set size and configuration space become too large especially when more complex systems contain a large number of degrees of freedom (DOF). Therefore approximations, such as the BOA, are critical to quantum mechanics calculations

### 2.1 The Schrödinger Equation

Developed by Erwin Schrödinger and first published in 1926 [36], the Schrödinger equation is one of the single most important equations in physical sciences and is the basis of modern quantum mechanics. The partial differential equation describes each



chemical system as a wavefunction which evolves in time:

$$i\hbar \frac{\partial \Psi(r, t)}{\partial t} = \hat{H} \Psi(r, t) \quad (2.1)$$

the Hamiltonian operator ( $\hat{H}$ ) is written:

$$\hat{H} = -\frac{\hbar^2}{2\mu_i} \nabla_i^2 + V(r) \quad (2.2)$$

$i$  is  $\sqrt{-1}$  and  $\hbar$  is Planck's constant divided by  $2\pi$  and  $\mu$  is the reduced mass.

One method of solving equation 2.1 is by using separation of variables. This is done by expressing the full adiabatic wavefunction  $\Psi(r, t)$  as a product of the spatial and temporal parts [37]:

$$\Psi(r, t) = \psi(r)T(t) \quad (2.3)$$

where  $\psi(r)$  is the spatial wavefunction and  $T(t)$  is the temporal part. Substituting equation 2.3 into equation 2.1 and dividing by the overall wavefunction we obtain two equations:

$$i\hbar \frac{\partial T(t)}{\partial t} = ET(t) \quad (2.4a)$$

$$\hat{H}\psi(r) = E\psi(r) \quad (2.4b)$$

Equation 2.4b is the time independent Schrödinger equation. This equation is an example of an eigenvalue equation.  $E$  is the eigenvalue and can take on certain discrete values depending on the eigenfunction  $\psi$  and linear operator  $\hat{H}$ . Equation 2.4a can be developed to give the solution:

$$T(t) = T_0 \exp^{-iEt/\hbar} \quad (2.5)$$

We may now write the TDSE as

$$\Psi(x, t) = \psi(r)T_0 \exp^{-iEt/\hbar} \quad (2.6)$$

This describes the time evolution of the wavefunction.  $T_0$  is the initial temporal wavefunction which can be absorbed into  $\psi(r)$ .

## 2.2 Born-Oppenheimer Approximation

The Hamiltonian, as described in equation 2.2, is comprised of a kinetic energy and potential energy part. This may be written in terms of electronic and nuclear components:

$$H = T_e + T_N + V_e + V_N + V_{eN} \quad (2.7a)$$

$$H = \sum_i -\frac{\hbar^2}{2m} \frac{\partial^2}{\partial^2 r_i} + \sum_i -\frac{\hbar^2}{2M_i} \frac{\partial^2}{\partial^2 R_i} + \sum_{j>i} \frac{e^2}{|r_i - r_j|} + \sum_{j>i} \frac{Z_i Z_j e^2}{|R_i - R_j|} - \sum_{ij} \frac{Z_j e^2}{|r_i - R_j|} \quad (2.7b)$$

$T_e$  and  $T_N$  are the kinetic energy terms for the electrons and nuclei,  $V_e$  and  $V_N$  are the potential energy terms for the electrons and nuclei and  $V_{eN}$  is the nuclear-electronic potential coupling term.  $R_i$ ,  $\frac{\partial^2}{\partial^2 R_i}$  is the nuclear position and momenta,  $Z_i$  is the nuclear charge and  $r_i$ ,  $\frac{\partial^2}{\partial^2 r_i}$  is the electronic position and momenta.

Equation 2.7b shows that even in the simplest molecule, it is very difficult to solve the Schrödinger equation analytically due to the large number of terms. This is overcome by utilising the huge difference in mass between the electrons and the nuclei [8]. The mass difference means that the position of the electrons will change instantaneously in conjunction with any change in the nuclear geometry. Therefore we may consider the nuclei fixed and solve only for the electrons at a fixed nuclear geometry. This can be shown by expressing the full wavefunction as:

$$\Psi(r; R) = \psi(r; R)\chi(R) \quad (2.8)$$

a product of the electronic ( $\psi$ ) wavefunction and nuclear ( $\chi$ ) wavefunction. The electronic wavefunction is dependent on the coordinates of the electrons,  $\mathbf{r}$  and the position of interacting nuclei,  $\mathbf{R}$ . The nuclear wavefunction is only dependent on  $\mathbf{R}$ . Substituting equation 2.8 into equation 2.4b with the Hamiltonian in equation 2.7b we obtain:

$$[\hat{T}_N(R) + \hat{T}_e(r) + \hat{V}_{eN}(r, R) + \hat{V}_{NN}(R) + \hat{V}_{ee}(r)]\psi(r; R)\chi(R) = E\psi(r; R)\chi(R) \quad (2.9)$$

since  $\hat{T}_e$  contains no  $\mathbf{R}$  dependence, we can write:

$$\hat{T}_e\psi(r; R)\chi(R) = \chi\hat{T}_e\psi \quad (2.10)$$

However the same cannot be assumed for the nuclear kinetic energy term because it is dependent on  $\mathbf{R}$ . Hence equation 2.11a cannot be written and must be expressed, using the product rule, as 2.11b:

$$\hat{T}_N\psi(r; R)\chi(R) = \psi\hat{T}_N\chi \quad (2.11a)$$

$$\frac{\partial^2}{\partial R^2}\psi(r; R)\chi(R) = \psi\frac{\partial^2}{\partial R^2}\chi + 2\frac{\partial}{\partial R}\psi\frac{\partial}{\partial R}\chi + \chi\frac{\partial^2}{\partial R^2}\psi \quad (2.11b)$$

This is more commonly written:

$$H\psi\chi = T_e\psi\chi + V_e\psi\chi + V_N\psi\chi + V_{eN}\psi\chi + W = E\psi\chi \quad (2.12a)$$

$$W = -\sum_j \frac{\hbar^2}{2m} \left( \psi \frac{\partial^2}{\partial R^2} \chi + 2 \frac{\partial}{\partial R} \psi(r; R) \frac{\partial}{\partial R} \chi(R) + \chi \frac{\partial^2}{\partial R^2} \psi \right) \quad (2.12b)$$

In equation 2.12b the last two terms involve derivatives of the electronic wavefunction, with respect to nuclear coordinates, however both of these terms are proportional to the mass ratio between electrons and nuclei, and hence due to the massive difference in size these terms can be ignored [37–39]. This means the Schrödinger equation in the BOA is written:

$$\psi T_N \chi + (T_e \psi + V_e \psi + V_N \psi + V_{eN} \psi) \chi = E \psi \chi \quad (2.13)$$

we may multiply on the left by  $\psi^*$  to yield the nuclear Schrödinger equation:

$$(T_N + V) \chi = E \chi \quad (2.14)$$

From equation 2.12b it is possible to deduce the limit of this approximation. In excited states fast nuclear vibrations means that the two terms neglected can no longer be ignored. This results in the coupling between nuclear and electronic motion and some interesting and important dynamical features.

## 2.3 Adiabatic to Diabatic Representation via Non-Adiabatic corrections

### 2.3.1 Adiabatic Representation

The adiabatic representation is based upon the BOA. This method is fundamental to much of our understanding of modern science. Spectroscopy relies heavily on the adiabatic picture, each individual state is represented by a spectral band, whose structure and shape is defined by the motion of nuclei on a PES [10].

In this representation we go beyond the BOA by writing the exact solution in the adiabatic basis as:

$$\Psi(r; R) = \sum_{n=0}^{\infty} \psi_n(r; R) \chi_n(r; R) \quad (2.15)$$

Strictly, this sum spans only bound electronic states and for completeness one needs to include an integral over the unbound states, but this is ignored for simplicity. Substituting equation 2.15 in equation 2.12a and projecting from the left with  $\psi_m(r; R)$  leads to:

$$\sum_n \{ (T_N + E_n(R) + V_N(R)) \delta_{nm} + 2T_{mn}^{(1)}(R) \nabla + T_{mn}^{(2)}(R) \} \chi_n(R) = E \chi_m(R) \quad (2.16a)$$

$$T_{mn}^{(1)}(R) = \langle \psi_m | \nabla \psi_n \rangle \quad (2.16b)$$

$$T_{mn}^{(2)}(R) = \langle \psi_m | \nabla^2 \psi_n \rangle \quad (2.16c)$$

Note that  $T_{mn}^{(1)}$  is a vector the number of whose components is equal to the number of vibrational DOF.  $T_{mn}^{(2)}$  is scalar.

When nuclear and electronic coupling is small we keep just the diagonal elements of equation 2.16a. We can therefore write the Schrödinger equation in the form expressed in equation 2.14 with an additional small but non-vanishing  $T_{nn}^{(2)}$ .

$$\sum_n (T_N + E_n + V_N + T_{nn}^{(2)}) \chi_n = E \chi_n \quad (2.17)$$

However in the case where non-adiabatic couplings are large (avoided crossing) the off diagonal elements cannot be ignored and can be inconvenient to calculate.

### 2.3.2 Conical Intersections

The BOA and adiabatic approximation holds for the vast majority of chemical situations. However in the presence of fast nuclear vibrations the electrons are unable to instantaneously adapt to the rapid changes in nuclear positions, this leads to significant coupling between nuclear and electronic motion called vibronic coupling [10]. This coupling is ultimately responsible for the breakdown of the adiabatic picture and the interesting topological features, such as CI that can result.

First proved in 1929 by Neumann and Wigner [9], the existence of intersecting electronic states can be shown by considering two adiabatic electronic states  $\psi_1$  and  $\psi_2$ . The adiabatic potential surfaces may be expanded into a diabatic basis ( $\phi$ , discussed in section 2.3.4) and therefore for a two state system may be written [10]:

$$\psi_1 = c_{11}\phi + c_{12}\phi \tag{2.18a}$$

$$\psi_2 = c_{21}\phi + c_{22}\phi \tag{2.18b}$$

The Hamiltonian matrix is written:

$$W(t) = \begin{pmatrix} W_{11} & W_{12} \\ W_{21} & W_{22} \end{pmatrix} \tag{2.19}$$

where  $W_{ij} = \langle \phi_i | \hat{H} | \phi_j \rangle$ . The eigenvalues are therefore written:

$$V_{\pm} = \bar{W} \pm \sqrt{\Delta W^2 + W_{12}^2} \tag{2.20}$$

where  $\bar{W} = \frac{1}{2}(W_{11} + W_{22})$  and  $\Delta W = \frac{1}{2}(W_{22} - W_{11})$ . From inspection it is easy to see that the eigenvalues of the matrix will be degenerate when  $W_{22} - W_{11} = 0$  and  $W_{12} = 0$  and therefore the PES may cross. This assumes that there are either two or more DOF or that  $\phi_{11}$  and  $\phi_{22}$  are different symmetries.

CI may take a wide variety of forms, of which two are shown in figure 1.2. Symmetry plays a critical role in the nature of a CI. The off-diagonal coupling and gradient difference terms are only non-zero if the product of symmetries of the two states and

nuclear coordinate involved is totally symmetric:

$$\Gamma_i \otimes \Gamma_j \otimes \Gamma_\alpha \supset A_g \quad (2.21)$$

where  $\Gamma_i$  and  $\Gamma_j$  are the two coupled states and  $\Gamma_\alpha$  is the coordinate. From this we can deduce that for the first order gradient difference ( $\Delta W$  from equation 2.20) terms will only be non-zero for totally symmetric modes or when degenerate states are involved. Conversely first order linear coupling elements ( $W_{12}$  from equation 2.20) will be non-zero for non-totally symmetric modes, assuming the intersecting states have different symmetry [10].

A special case occurs when the states involved are degenerate (i.e belonging to E or T representation). The most well known example is when two fold degenerate E terms couple, as a result of JT effect [40–42] in which degeneracy of a doubly degenerate state is lifted by a doubly degenerate vibration resulting in a lowering of symmetry. This forms a Mexican hat intersection shown in figure 1.2(b). This was first described by Van Vleck in 1939 [43] and properly characterised in the 1960’s following extensive work by Longuet-Higgins, Bersuker and O’Brian [44].

Most molecular systems in nature have little or no symmetry. CI can still exist in these cases and are simply termed accidental CI. Locating such intersections is harder due to the lack of symmetry for guidance. The earliest example of such an intersection was found in ozone. In this case two minima (of differing symmetry) are separated by a transition state which lies near an intersection between the  $1^1A_1$  and  $2^1A_1$  states [45].

### 2.3.3 Non-Adiabatic Corrections

It is possible to rewrite equation 2.16a so that the evolving wavefunction is written:

$$\left(\hat{T}_N + V_i\right) |\Psi_i\rangle - \sum_j \Lambda_{ij} |\Psi_j\rangle = i\hbar \frac{\partial}{\partial t} |\Psi_i\rangle \quad (2.22)$$

where  $i$  and  $j$  represent the two states, and  $\Lambda_{ij}$  is the non-adiabatic coupling which is expressed:

$$\Lambda_{ij} = \frac{1}{2M} (G_{ij} + 2F_{ij} \nabla) \quad (2.23)$$

$G_{ij}$  represents a matrix of numbers which can be further broken down into the form

$$G_{ij} = \langle \Psi_i | \nabla^2 \Psi_j \rangle \quad (2.24)$$

Showing that the force matrix  $F_{ij}$  is the defining quantity in the strength of the non-adiabatic coupling, which itself is dependent on the energy gap between the two states:

$$F_{ij} = \langle \Psi_i | \nabla \Psi_j \rangle \quad (2.25a)$$

$$F_{ij} = \frac{\langle \Psi_i | \partial \tilde{H}_{el} | \Psi_j \rangle}{V_j - V_i} \quad (2.25b)$$

$V_j - V_i$  is the gap between the two states.

### 2.3.4 Diabatic Representation

Equation 2.25b highlights the limit of the adiabatic picture. This picture breaks down when the energy gap between states tends to zero, ( $F_{ij} \rightarrow \infty$  as  $V_j - V_i \rightarrow 0$ ). It is therefore desirable to switch to a diabatic representation.

Diabatization, in which the adiabatic coupling terms are replaced with a diabatic coupling matrix containing the whole potential is the natural choice, especially for systems which contain CI. The diabatic representation is the natural choice for systems containing large non-adiabatic effects because it removes singularities created as  $V_j - V_i \rightarrow 0$ , and creates a smooth, simple surface without such phenomena as CI [10]. The Schrödinger equation in this basis is now expressed:

$$\tilde{T}_N |\Psi_i\rangle + \sum_j W_{ij} |\Psi_j\rangle = i\hbar \frac{\partial}{\partial t} |\chi_i\rangle \quad (2.26)$$

where  $W_{ij}$  represents the potential matrix, coupling is now achieved by the off-diagonal elements.  $W_{ij}$  can be expressed as:

$$W_{ij} = \langle \Phi_i | \tilde{H}_{el} | \Phi_j \rangle \quad (2.27)$$

Practically the diabatic states of a system are usually obtained by a unitary transformation on the adiabatic states. The orthogonal matrix,  $S$  transforms the operator

from adiabatic to diabatic:

$$(|\Phi_1\rangle|\Phi_2\rangle) = S (|\phi_1\rangle|\phi_2\rangle) \quad (2.28)$$

In two state space the matrix,  $S$  can be written as a  $\mathbf{R}$  dependent rotation:

$$S(R) = \begin{pmatrix} \cos\theta(R) & -\sin\theta(R) \\ \sin\theta(R) & \cos\theta(R) \end{pmatrix} \quad (2.29)$$

Where  $\theta$  is the mixing angle between the two diabatic states. From equation 2.29 we can write:

$$W^{11} = \langle \Phi_1 | \hat{H}_{el} | \Phi_1 \rangle = V_1 \cos^2 \theta + V_2 \sin^2 \theta \quad (2.30)$$

$$W^{22} = \langle \Phi_2 | \hat{H}_{el} | \Phi_2 \rangle = V_1 \sin^2 \theta + V_2 \cos^2 \theta \quad (2.31)$$

for the on-diagonal terms. For the off-diagonal terms we write:

$$W_{12} = \langle \Phi_1 | \hat{H}_{el} | \Phi_2 \rangle = (V_1 - V_2) \cos \theta \sin \theta \quad (2.32)$$

$V_{1,2}$  are the adiabatic energies,  $W_{11}$  and  $W_{22}$  are the diabatic potential energies and  $W_{12}$  is the coupling.

## 2.4 The Vibronic Coupling Model Hamiltonian

In order to describe a molecular system containing vibronic coupling, it is essential that the appropriate Hamiltonian is used. First described by Cederbaum *et al* [46] the Vibronic Coupling Hamiltonian is a diabatic expression of the PES around the area of interest. This method has been successfully used to describe many systems where coupling between states exists [10, 47–49].

The Hamiltonian can be written as a sum of a zeroth order Hamiltonian ( $\mathbf{H}^{(0)}$ ) and a set of diabatic coupling matrices ( $\mathbf{W}^{(i)}$ ):

$$\mathbf{H} = \mathbf{H}^{(0)} + \mathbf{W}^{(0)} + \mathbf{W}^{(1)} + \dots \quad (2.33)$$



The zeroth order Hamiltonian is simply expressed using, for example a ground state harmonic oscillator approximation:

$$H^{(0)} = \sum_{\alpha} \frac{\omega_{\alpha}}{2} \left( \frac{\partial^2}{\partial Q_{\alpha}^2} + Q_{\alpha}^2 \right) \quad (2.34)$$

with the vibrational frequencies  $\omega_{\alpha}$ . The zeroth order coupling matrix contains the adiabatic state energies at  $\mathbf{Q}_0$ . The adiabatic PES are equal to the diabatic surfaces at this point, so  $\mathbf{W}^{(0)}$  is diagonal.

The first order coupling matrix elements contain linear terms and are expressed:

$$W_{ii}^{(1)} = \sum_{\alpha} \kappa_{\alpha}^{(i)} Q_{\alpha} \quad (2.35)$$

$$W_{ij}^{(1)} = \sum_{\alpha} \lambda_{\alpha}^{(i,j)} Q_{\alpha} \quad (2.36)$$

The on-diagonal terms  $\kappa_{\alpha}^{(i)}$  are related to the derivative of the adiabatic PES with respect to the coordinates and represent the forces on the diabatic surface. The off-diagonal  $\lambda_{\alpha}^{(i,j)}$  terms are the non-adiabatic couplings between states:

$$\kappa_{\alpha}^{(i)} = \left\langle \phi_i \left| \frac{\partial H_{el}}{\partial Q_{\alpha}} \right| \phi_i \right\rangle \quad (2.37)$$

$$\lambda_{\alpha}^{(i,j)} = \left\langle \phi_i \left| \frac{\partial H_{el}}{\partial Q_{\alpha}} \right| \phi_j \right\rangle \quad (2.38)$$

where  $\phi_i$  are the diabatic electronic wavefunctions at  $\mathbf{Q}_0$ . Second order coupling matrices follow the same pattern, the second order terms can be expressed:

$$W_{ii}^{(2)} = \frac{1}{2} \sum_{\alpha,\beta} \gamma_{\alpha,\beta}^{(i)} Q_{\alpha} Q_{\beta} \quad (2.39)$$

$$W_{ij}^{(2)} = \frac{1}{2} \sum_{\alpha,\beta} \mu_{\alpha,\beta}^{(i,j)} Q_{\alpha} Q_{\beta} \quad (2.40)$$

where  $\gamma_{\alpha,\beta}^{(i)}$  are second order derivatives of the adiabatic PES at  $\mathbf{Q}_0$  and  $\mu_{\alpha,\beta}^{(i,j)}$  are second order non-adiabatic derivatives.

Symmetry is important in obtaining the Vibronic Coupling Hamiltonian. Many parameters can be considered zero due to symmetry, as described in equation 2.21.

However the Vibronic Coupling Hamiltonian is complicated when degenerate states are present in the system. For example in the  $D_{6h}$  point group,  $E_{1g} \otimes E_{1g} = A_{1g} + E_{2g} + A_{2g}$ , therefore modes with  $e_{2g}$  symmetry can be either on-diagonal, or off-diagonal coupling terms. But which? The easiest way to answer this question is to look at the symmetries of the states and modes using the  $D_{2h}$  point group. This is the largest Abelian point-group, that is a subset of  $D_{6h}$ . If a coefficient must be zero at  $D_{2h}$  it must also be zero at  $D_{6h}$ . The lower symmetry however means that potentially non-zero coefficients at  $D_{2h}$  may be zero at the higher symmetry. At  $D_{2h}$  an  $e_{2g}$  mode goes to  $a_g + b_{3g}$ . The component that goes to  $a_g$  thus enters on the diagonal of the coupling matrix, while the  $b_{3g}$  component goes on the off-diagonal. This is an example of the  $E \otimes e$  JT effect in which degeneracy of a doubly degenerate state is lifted by a doubly degenerate vibration resulting in a lowering of symmetry. The linear coupling matrices in the  $E \otimes e$  JT interaction have 2x2 blocks for the states  $i, i+1$ :

$$W_{i,i+1}^{(1)} = \sum_{\alpha} \begin{pmatrix} \kappa_{\alpha}^{(i)} Q_{\alpha,x} & \lambda_{\alpha}^{(i,i+1)} Q_{\alpha,y} \\ \lambda_{\alpha}^{(i,i+1)} Q_{\alpha,y} & \kappa_{\alpha}^{(i+1)} Q_{\alpha,x} \end{pmatrix} \quad (2.41)$$

$$\kappa_{\alpha}^{(i)} = -\kappa_{\alpha}^{(i+1)} = \lambda_{\alpha}^{(i,i+1)} \quad (2.42)$$

where  $x, y$  denote the 2 components of the doubly degenerate mode  $Q_{\alpha}$ . A rigorous method for obtaining the relationship between the coupling parameters is found in [48, 50].

In some coordinates it is important to add fourth order terms to the potential to model symmetric anharmonic effects at large displacements. For these modes, in place of Equation 2.34, the diabatic surfaces for state  $i$  are defined as:

$$V_{\alpha}^{(i)} = \frac{\omega_{\alpha}}{2} Q_{\alpha}^2 + \frac{\gamma_{\alpha\alpha}^{(i)}}{2} Q_{\alpha}^2 + \frac{\epsilon_{\alpha}^{(i)}}{24} Q_{\alpha}^4 \quad (2.43)$$

It should be noted that adding higher order terms for degenerate modes in systems involving JT and PJT is non-trivial. For an analysis of the correct symmetry retaining relationship see [51].

In a few modes, particularly the totally symmetric modes the surfaces can be asymmetrically anharmonic that a Morse potential of the form below was used [52]:

$$V_{\alpha}^{(i)} = D_0[\exp(\beta(Q_{\alpha} - Q_{i\alpha}) - 1)]^2 \quad (2.44)$$

$$D_0 = k_1 \quad (2.45)$$

$$\beta = \sqrt{\frac{\omega + k_2}{2D_0}} \quad (2.46)$$

$$Q_{i\alpha} = k_3 \quad (2.47)$$

Where  $k_1, k_2$  and  $k_3$  are the parameters for fitting.

## 2.5 Coherent Control

### 2.5.1 Light and Matter Interaction

The Hamiltonian written in equation 2.2 describes an isolated system with no external forces ( $H_{sys}$ ). Upon interaction with light the Hamiltonian is perturbed and must be written in the form:

$$H = H_{sys} + H_{rad} \quad (2.48)$$

$H_{rad}$  is the Hamiltonian to describe the effect of the external field. The full radiative Hamiltonian is written:

$$H = \frac{1}{2m}(\vec{p} - e\vec{A})^2 - e\phi + V' \quad (2.49)$$

in which  $\vec{p}$  is the momentum of the electrons,  $e$  is the electric charge  $\vec{A}$  is the vector of the applied potential,  $\phi$  is the scalar potential and  $V'$  is the static electric potential [53].

Expanding equation 2.49 gives:

$$H_{sys} = -\frac{\hbar}{2\mu}\nabla^2 + V \quad (2.50a)$$

$$H_{rad} = \frac{e}{2\mu}[2i\hbar\nabla + i\hbar(\nabla \cdot \vec{A}) + e\vec{A} \cdot \vec{A}] \quad (2.50b)$$

where we have let  $V = -e\phi + V'$ . From here it is possible to differentiate between two limits, the weak and strong field limits. In the weak field limit,  $|\vec{p}| \gg |e\vec{A}|$ , and

therefore only the first term in equation 2.50b needs to be considered and we therefore seek solutions to the Schrödinger equation which are perturbations to wavefunctions which are eigenstates of  $H_{sys}$ . We can therefore write the perturbed Hamiltonian as:

$$H = H_0 + W(R, t) \quad (2.51)$$

where  $H_0$  is the unperturbed Hamiltonian and  $W$  is the field written as:

$$W(R, t) = -\mu(R)E(t) \quad (2.52)$$

where  $\mu$  is the dipole moment and  $E$  is the energy. Within this thesis we work exclusively in the weak field limit.

## 2.5.2 The Essence of Controllability

The fundamental concept behind coherent control is the aim to maximise a desired state within a chemical system. Expressed mathematically this is simply written:

$$J \equiv \lim_{t \rightarrow \infty} \langle \psi(t) | P_\alpha | \psi(t) \rangle \quad (2.53)$$

where  $P_\alpha$  is a projection operator describing the target scenario. The yield  $J$  is defined in the limit  $t \rightarrow \infty$ , this represents the time for the wavepacket to reach its asymptotic arrangement. In a system perturbed by an external field, it is clear that the yield ( $J$ ) is a function of the field ( $\varepsilon(t)$ ), and hence equation 2.53 is rewritten as:

$$J[\varepsilon(t)] \equiv \lim_{t \rightarrow \infty} \langle \psi([\varepsilon(t)], t) | P_\alpha | \psi([\varepsilon(t)], t) \rangle \quad (2.54)$$

This describes coherent control in the simplest form. In the perturbative regime it is necessary to add a constraint on the field strength, to ensure that the field doesn't become too strong in attempts to obtain better control. This is written [37]:

$$E \equiv \int_0^t dt |\varepsilon(t)|^2 \quad (2.55)$$

The main objective functional is now written

$$J = \lim_{t \rightarrow \infty} \langle \psi(t) | P_\alpha | \psi(t) \rangle - \lambda \int_0^t dt |\varepsilon(t)|^2 \quad (2.56)$$

where  $\lambda$  is a lagrange multiplier. This functional may be maximised using calculus of variations and is the fundamental process behind OCT [37], and in many ways in the most intuitive method for control.

### 2.5.3 Local Control Theory

LCT provides a different approach to coherent control. In this approach there is no target wavefunction and therefore no functional to optimise making it a simpler method to implement. The aim of local control is to create a control field at each time step to ensure the desired change in the expectation value of some observable.

The time evolution of an operator  $A$  is written:

$$\frac{d\langle A \rangle_t}{dt} = \frac{d}{dt} \langle \psi(t) | A | \psi(t) \rangle = \frac{i}{\hbar} \langle \psi(t) | [H_0, A] | \psi(t) \rangle + \frac{i}{\hbar} \langle \psi(t) | [W, A] | \psi(t) \rangle \quad (2.57)$$

$[X, Y] = XY - YX$  denotes the commutator of operators  $X$  and  $Y$ .  $W$  denotes the interaction, and therefore the electric field  $E(t)$ . This equation shows that if  $W$  and  $A$  do not commute it is possible to influence the changes in the expectation of  $A$  with a shaped external field.

Assuming that  $H_0$  commutes with any operator,  $A$ , which is true for any Hamiltonian in the adiabatic picture equation 2.57 can be written:

$$\frac{d\langle A \rangle_t}{dt} = -E(t) \frac{i}{\hbar} \langle \psi(t) | [\mu(R), A] | \psi(t) \rangle \quad (2.58)$$

and therefore the control is achieved by changing the temporal evolution of  $E$ .

LCT has been used for a wide range of operators and opens the possibility of the use of sequential operators. Two of main operators are discussed below [35].

#### Heating and Cooling

The simplest approach to LCT is by controlling the amount of energy in the system which is achieved by using the unperturbed Hamiltonian ( $H_0$ ) as the control operator. In this case the time evolution of the expectation values is written:

$$\frac{d\langle H_0 \rangle_t}{dt} = \frac{i}{\hbar} \langle \psi(t) | [H_0, H_0] | \psi(t) \rangle + \frac{i}{\hbar} \langle \psi(t) | [W, H_0] | \psi(t) \rangle \quad (2.59)$$

This can be simplified to:

$$\frac{d\langle H_0 \rangle_t}{dt} = -E(t) \frac{i}{\hbar} \langle \psi(t) | [\mu(R), T(P)] | \psi(t) \rangle \quad (2.60)$$

The control field is therefore a function of the momentum and is written:

$$E(t) = \pm \lambda \langle \psi | [\mu(R), T(P)] | \psi \rangle \quad (2.61)$$

By choosing either + or - the system can be heated or cooled respectively. This particular operator can be very effective in surmounting barriers on the potential surfaces and exciting selected vibrational modes [54, 55].

### Electronic and Vibrational Transfer

To control the transfer to a particular electronic state,  $k$ , the projector operator:  $|k\rangle\langle k|$  is chosen. The time evolution is now written:

$$\frac{d\langle k \rangle_t}{dt} = \frac{i}{\hbar} \langle \psi(t) | [H_0, |k\rangle\langle k|] | \psi(t) \rangle + \frac{i}{\hbar} \langle \psi(t) | [W, |k\rangle\langle k|] | \psi(t) \rangle \quad (2.62)$$

The projector commutes with the unperturbed Hamiltonian the remaining expression is written:

$$\frac{d\langle k \rangle_t}{dt} = -2E(t) \sum_m \text{Im} \langle \psi_m | \mu_{mk} | \psi_k \rangle \quad (2.63)$$

where  $E(t)$  is the electric field and  $\mu_{mk}$  is the transition dipole between states  $m$  and  $k$ . From this equation it is simple to write:

$$E_k(t) = \pm \lambda \sum_m \text{Im} \langle \psi_m | \mu_{mk} | \psi_k \rangle \quad (2.64)$$

$\lambda$  is a strength parameter and the sign controls the direction of the population transfer.

By replacing the projector of state  $k$  with a projector of vibrational state(s) a pulse can be found to ensure the increase of population in a vibrational level:

$$E_k(t) = \pm \lambda \sum_m \text{Im} \langle \psi | \mu | \varphi_k \rangle \langle \varphi_k | \psi \rangle \quad (2.65)$$

Where  $|\varphi_k\rangle\langle\varphi_k|$  is the vibrational state projector. This approach is particularly useful for locating a specific region on a PES [35, 55].

# Chapter 3

## Computation and Methodology

The methods used in this thesis can be split into two distinct groups, time independent and time dependent. The electronic structure methods which are time independent are performed at a wide selection of nuclear geometries allowing us to accurately describe the PES. Time dependent dynamic methods are used to describe the movement of a wavepacket on the calculated PES.

A variety of electronic structure methods are used in this thesis. Each develops the treatment of electron-electron repulsion (correlation) which represents the limiting factor for most *ab-initio* calculations. Hartree-Fock (HF) is the starting point for most *ab-initio* calculations and treats the electron-electron repulsion using an averaged field approach. Therefore the effects of electron correlation are neglected. Complete active space self consistent field (CASSCF) uses multiple excited electronic configurations in a determinant to account for static correlation. Complete active space with  $2^{nd}$  order perturbation (CASPT2) includes a second order perturbation to also include dynamic correlation associate with the spatial arrangement of electrons in an orbital [38,39,56].

Dynamics are performed exclusively with the MCTDH method. Based upon the time dependent Hartree (TDH) method, this multiconfigurational approach provides important correlation between the motion along the various coordinates, which is not correctly described in the mean field TDH method. This is akin to the correlation described above in the electronic structure methods. This approach has proved suc-

successful in numerous situations and is able to perform calculations beyond many time dependent approaches [57–59].

### 3.1 Hartree-Fock (HF) theory

HF is the starting point for most *ab-initio* electronic structure methods. The HF approach treats the electron-electron repulsion in an average manner. Each electron is considered to move under the effect of a field created by (n-1) electrons. Ignoring the electron-electron repulsion term enables the wavefunction to be expressed as a product of one electron wavefunctions:

$$\psi = \psi_a(1)\psi_b(2)\psi_c(3)\dots\psi_z(n) \quad (3.1)$$

where electron one is described by  $\psi_a$ , electron two by  $\psi_b$  and so on. This wavefunction ( $\psi$ ) depends on the coordinates of each electron and therefore also the positions of the nuclei. However writing the wavefunction in this manner does not take into account the spin of the electron and therefore the requirement to fulfil the Pauli principle. To do this the product wavefunction must be expressed as a Slater determinant [38,39,56]:

$$\psi(\mathbf{x};\mathbf{R}) = (n!)^{-1/2} \det | \phi_a(1)\phi_b(2)\dots\phi_z(n) | \quad (3.2)$$

$\phi_a(i)$  represents a spinorbital for an electron with coordinate  $\mathbf{x}$ , and nuclear arrangement  $\mathbf{R}$ . The spinorbitals which give the best wavefunction are found by using the variational theory to minimise the Rayleigh ratio of the determinant:

$$\varepsilon_{hf} = \frac{\langle \psi(\mathbf{x};\mathbf{R}) | \hat{H} | \psi(\mathbf{x};\mathbf{R}) \rangle}{\langle \psi(\mathbf{x};\mathbf{R}) | \psi(\mathbf{x};\mathbf{R}) \rangle} \quad (3.3)$$

$\varepsilon_{hf}$  is the energy of the ground state in nuclear configuration  $\mathbf{R}$ . In doing this minimisation one obtains an expression for the best (HF) orbitals, this is written:

$$f_1\psi_a(1) = \varepsilon_a\psi_a(1) \quad (3.4a)$$

$$f_1 = h_1 + \sum_u J_u(1) - K_u(1) \quad (3.4b)$$



$f_1$  is the Fock operator,  $h_1$  is the core Hamiltonian for one electron, which is added to the sum over all the spinorbitals of the Coulomb operator,  $J_b$  and exchange operator,  $K_b$ . For any electron  $\phi_u$  interacting with electron  $\phi_a$  these are defined:

$$J_u(1)\phi_a(1) = j_0 \left\langle \phi_u(2) \left| \frac{1}{r_1 - r_2} \right| \phi_u(2) \right\rangle |\phi_a(1)\rangle \quad (3.5a)$$

$$K_u(1)\phi_a(1) = j_0 \left\langle \phi_u(2) \left| \frac{1}{r_1 - r_2} \right| \phi_a(2) \right\rangle |\phi_u(1)\rangle \quad (3.5b)$$

where  $j_0$  is:

$$j_0 = \frac{e^2}{4\pi\epsilon_0}$$

Physically the Coulomb operator describes the repulsion between electrons and the exchange operator describes the modification of the energy due to the effects of the Pauli principle.

To solve equation 3.4a and obtain the best energy is computationally complex for molecular systems. In 1951 Roothaan and Hall [60] independently suggested expanding the spinorbitals in a known basis set of the form:

$$\phi_i = \sum_{\alpha}^M c_{\alpha i} \chi_{\alpha} \quad (3.6)$$

This defines the molecular orbitals using a linear combination of atomic orbitals (LCAO), where  $\chi_{\alpha}$  are the basis functions and  $c_{\alpha i}$  are the coefficients which are calculated by the self-consistent field (SCF) method. This SCF approach transforms the problem of the wavefunction to that of calculating coefficients. When expanded into equation 3.4a we can write:

$$f_1 \sum_{j=1}^M c_{ja} \chi(1) = \epsilon_a \sum_{j=1}^M c_{ja} \chi(1) \quad (3.7)$$

By multiplying by  $\chi_i(1)^*$  and integrating over the spin space we obtain:

$$\mathbf{F}c = \mathbf{S}c\epsilon \quad (3.8)$$

where  $\mathbf{S}$  is the overlap matrix  $\langle \chi_a | \chi_b \rangle$  and  $\mathbf{F}$  is the fock matrix,  $\langle \chi_a | f_1 | \chi_b \rangle$ . This equation only has a non-trivial solution if the following equation is satisfied:

$$\det|\mathbf{F} - \epsilon_a \mathbf{S}| = 0 \quad (3.9)$$

This equation cannot be solved directly because the matrix elements of  $\mathbf{F}$  involve integrals over the Coulomb and exchange operators which themselves are dependent on the spatial wavefunctions. Therefore it must be solved by taking an initial guess of the coefficients in equation 3.6. Equation 3.9 is then solved by using this guess to give new values. This continues in an iterative manner until a predefined convergence criteria is reached.

The HF ground state wavefunction accounts for  $\sim 99\%$  of the total energy of a system. The remaining 1% can be very important, especially when describing systems that contain significant quantum phenomena. To improve upon the HF ground state wavefunction electron correlation must be calculated more accurately.

## 3.2 Complete Active Space Self Consistent Field (CASSCF) theory

The HF method uses averaged effects and does not consider instantaneous Coulombic interactions between electrons. It also does not take into account the numerous quantum effects that rely on electronic distribution. As discussed in the previous section the HF method yields a set of spinorbitals forming a Slater determinant in which the lowest  $n$  orbitals are occupied by  $2n$  electrons. Clearly many more determinants can be described by occupying the virtual orbitals.

The exact ground state or excited state wavefunction can be describe as a linear combination of all the possible determinants written:

$$\Psi = C_0\Psi_0 + \sum_{a,p} C_a^p \phi_a^p + \sum_{a<b,p<q} C_{ab}^{pq} \phi_{ab}^{pq} + \sum_{a<b<c,p<q<r} C_{abc}^{pqr} \phi_{abc}^{pqr} + \dots \quad (3.10)$$

Where the first term is the ground state determinant, the second is a single excited determinant arising from excitation of an electron from orbital  $a$  to  $p$  and the third term is a doubly excited determinant containing excitation from orbital  $a$  to  $p$  and from  $b$  to  $q$ , when  $a < b$  and  $p < q$ . Unfortunately even in calculations involving small molecular species the number of possible determinants is extremely large and

therefore the wavefunctions are usually truncated at doubly excited determinants. The wavefunction (in equation 3.10) can therefore be expressed in a simpler form as a linear combination of a finite set of determinants:

$$\Psi_s = \sum_{J=1}^L C_{Js} \Phi_J \quad (3.11)$$

where the sum is over L determinants,  $\Phi_J$ , multiplied by the coefficients  $C_{Js}$  for state s.

Configuration Interaction methods optimise the basis set coefficients,  $c_{ji}$ , arising from the Roothaan equation [60] during the initial HF calculations (equation 3.8). These are held fixed during the optimisation of  $C_{Js}$  in the subsequent configuration interaction calculation. However in Multi Configuration Self Consistent Field (MCSCF) methods, these are optimised simultaneously. This is computationally more expensive but it enables more accurate results with fewer configuration state functions (CSF).

One such MCSCF approach is CASSCF theory. In this scheme the spinorbitals are split into three classes:

- Inactive orbitals: The lower energy spinorbitals which remain doubly occupied in all determinants.
- Virtual orbitals: The higher energy spinorbitals which remain unoccupied in all determinants.
- Active orbitals: The intermediate energy spinorbitals which are involved in the CSF which are most important in obtaining an accurate wavefunction. The configuration of the electrons within these active orbitals is calculated from the determinants possible within the active space.

By selecting the most important orbitals this method allows a complete set of the important determinants to be described accurately, while the reduced configuration space limits the computational expense. The selection of the active space is critical to

the accuracy of the calculations. The active space must contain sufficient spinorbitals to describe the appropriate determinants, however the number of CSF rises rapidly with the number of active orbitals, making calculations harder to execute [61].

### 3.3 Complete Active Space with 2<sup>nd</sup> Order Perturbation (CASPT2) Theory

Static correlation which is described as the preferential occupation of certain determinants is included by the MCSCF methods. This improves the description of  $\Psi$ . However dynamic correlation in which the spatial conditions of the electrons are taken into account are not included. This can be very important, especially in excited states which display a lot of ionic character. One method for including this is CASPT2 [62,63].

The basis of the CASPT2 approach is to partition the Hamiltonian into a zeroth order part ( $H_0$ ) and perturbation,  $V$ :

$$H = H_0 + \lambda V \tag{3.12}$$

$H_0$  is the zeroth order approximation, in this case the CASSCF Hamiltonian,  $V$  is the perturbed Hamiltonian and  $\lambda$  is the perturbation factor. The TISE in this regime is expressed [64]:

$$H|\Phi_i\rangle = (H_0 + V)|\Phi_i\rangle = \varepsilon_i|\Phi_i\rangle \tag{3.13}$$

We know the eigenfunction and eigenvalue of  $H_0$  is:

$$H_0|\Psi_i^{(0)}\rangle = E_i^{(0)}|\Psi_i^{(0)}\rangle \tag{3.14}$$

Therefore if the perturbation is small we can expect  $|\Phi_i\rangle$  and  $\varepsilon_i$  to be reasonably close to  $|\Psi_i^{(0)}\rangle$  and  $E_i^{(0)}$  and hence we wish to systematically improve the eigenvalues of  $H_0$  to converge onto the total Hamiltonian,  $H$ . This is done using the perturbation factor ( $\lambda$ ) in equation 3.12.

The exact eigenfunctions and eigenvalues are expanded in a power series in  $\lambda$ , so that:

$$\varepsilon_i = E_n^{(0)} + \lambda E^{(1)} + \lambda^2 E^{(2)} + \dots \quad (3.15a)$$

$$|\Phi_i\rangle = |\Psi_i^{(0)}\rangle + \lambda |\Psi_i^{(1)}\rangle + \lambda^2 |\Psi_i^{(2)}\rangle + \dots \quad (3.15b)$$

Substituting 3.15a and 3.15b into equation 3.13 up to a first order perturbation we obtain:

$$(H_0 + \lambda V)(|\Psi_i^{(0)}\rangle + \lambda |\Psi_i^{(1)}\rangle + \dots) = (E_i^{(0)} + \lambda E_i^{(1)} + \dots)(|\Psi_i^{(0)}\rangle + \lambda |\Psi_i^{(1)}\rangle + \dots) \quad (3.16)$$

Collating the powers we write:

$$H_0 |\Psi_i^{(0)}\rangle = E_i^{(0)} |\Psi_i^{(0)}\rangle, \quad n=0 \quad (3.17a)$$

$$H_0 |\Psi_i^{(1)}\rangle + V |\Psi_i^{(0)}\rangle = E_i^{(0)} |\Psi_i^{(1)}\rangle + E_i^{(1)} |\Psi_i^{(0)}\rangle, \quad n=1 \quad (3.17b)$$

$$H_0 |\Psi_i^{(2)}\rangle + V |\Psi_i^{(1)}\rangle = E_i^{(0)} |\Psi_i^{(2)}\rangle + E_i^{(1)} |\Psi_i^{(1)}\rangle + E_i^{(2)} |\Psi_i^{(0)}\rangle, \quad n=2 \quad (3.17c)$$

$$H_0 |\Psi_i^{(3)}\rangle + V |\Psi_i^{(2)}\rangle = E_i^{(0)} |\Psi_i^{(3)}\rangle + E_i^{(1)} |\Psi_i^{(2)}\rangle + E_i^{(2)} |\Psi_i^{(1)}\rangle + E_i^{(3)} |\Psi_i^{(0)}\rangle, \quad n=3 \quad (3.17d)$$

and therefore expressions for the  $n^{th}$  order energies can be written:

$$E_i^{(0)} = \langle \Psi_i^{(0)} | H_0 | \Psi_i^{(0)} \rangle \quad (3.18a)$$

$$E_i^{(1)} = \langle \Psi_i^{(0)} | V | \Psi_i^{(0)} \rangle \quad (3.18b)$$

$$E_i^{(2)} = \langle \Psi_i^{(0)} | V | \Psi_i^{(1)} \rangle \quad (3.18c)$$

$$E_i^{(3)} = \langle \Psi_i^{(0)} | V | \Psi_i^{(2)} \rangle \quad (3.18d)$$

Therefore to determine the  $n^{th}$  order energy we are required to solve equation 3.17a, 3.17b, 3.17c and 3.17d for  $|\Psi_i^{(n)}\rangle$ . Consider equation 3.17b for a first order perturbation, this can be rearranged:

$$(E_i^{(0)} - H_0) |\Psi_i^{(1)}\rangle = (V - E_i^{(1)}) |\Psi_i^{(0)}\rangle \quad (3.19)$$

This equation is no longer an eigenvalue, but a differential. To solve this we expand  $|\Psi_i^{(1)}\rangle$  in terms of eigenvalues of  $H_0$ :

$$|\Psi_i^{(1)}\rangle = \sum_n c_n^{(1)} |n\rangle \quad (3.20)$$

By multiplying equation 3.19 by  $\langle n|$ , and using the fact that the zeroth order wavefunctions are orthogonal we have:

$$(E_i^{(0)} - E_n^{(0)}) \langle n | \Psi_i^{(1)} \rangle = \langle n | V | \Psi_i^0 \rangle \quad (3.21)$$

and using  $|\Psi_i^{(i)}\rangle = \sum_n |n\rangle \langle n | \Psi_i^{(i)} \rangle$  with equation 3.18b we derive:

$$E_i^{(2)} = \sum_n \langle \Psi_i^0 | V | n \rangle \langle n | \Psi_i^{(1)} \rangle \quad (3.22)$$

and finally using equation 3.21 we arrive at:

$$E_i^{(2)} = \sum_n \frac{\langle \Psi_i^0 | V | n \rangle \langle n | V | \Psi_i^0 \rangle}{E_i^{(0)} - E_n^{(0)}} = \sum_n \frac{|\langle \Psi_i^0 | V | n \rangle|^2}{E_i^{(0)} - E_n^{(0)}} \quad (3.23)$$

The CASPT2 method calculates the energies in a molecular system very accurately. However problems can arise when two states are very close together or when intruder states occur (spurious states arising from a situation when the energy of the perturbation is a similar magnitude to the energy associated to the zero order wavefunction). For these problems Roos *et al* [65] have developed a method in which the energy levels are positively shifted and recalculated removing this interference. In a shift calculation the Hamiltonian takes the form:

$$H_0 = H_0 + \zeta P_e \quad (3.24)$$

$\zeta$  is a small positive shift value and  $P_e$  is a projection operator on the interacting space. Following the same procedure as above that the first order perturbation is expressed in the form of equation 3.19 and 3.20, we can write that :

$$\tilde{E}_2 = - \sum_n \frac{|\langle n | \hat{H} | \Psi_0 \rangle|^2}{\epsilon_n - E_0 + \zeta} \quad (3.25)$$

where  $\epsilon_n$  is the eigenvalues of  $H_0$ . Assuming that the inequality  $\epsilon_n - E_0 \gg \zeta$  is maintained we can write:

$$E_2 \simeq \hat{E}_2 - \zeta \left( \frac{1}{\omega} - 1 \right) \equiv E_2^{LS} \quad (3.26)$$

$\omega$  is the weighted reference CASSCF wavefunction. This method successful removes the intruder states, and allows calculation of almost degenerate levels, without shifting the relative energy of the states, and was first shown on the  $\text{Cr}(\text{CO})_5$  molecule [62, 65–67].

### 3.4 Spin Orbit Coupling

In first order approximations transitions between pure singlet and pure triplet states are forbidden due to the orthonormality of the spin wavefunctions. However SOC arising from the interaction between spin and orbital angular momentum allows mixing between the singlet and triplet manifold providing a mechanism for intersystem crossing.

The strength of SOC has been shown to be strongly dependent on (a) nuclear charge, (b) the availability of transitions between orthogonal orbitals and (c) spatial proximity of the two orbitals. In singlet transitions  $\pi^2 \rightarrow n, \pi$  transitions possess a much greater oscillator strength. However in spin forbidden transitions it is  $n^2 \rightarrow n, \pi$  which play a more important role, because the change momentum is conserved by the change in spin angular momentum change associated with a  $\alpha\beta \rightarrow \alpha\alpha$  spin flip. For non-zero SOC matrix values the two interacting states must obey El-Sayed's rule. This says that angular momentum must be conserved. Therefore the product of the two states symmetry must be part be a subset of one of the rotational symmetries in that group.

The SOC Hamiltonian ( $H_{so}$ ) acts as a small, but sometimes vital element to the Hamiltonian of the whole system [39]. Providing that the coupling is small, the spin orbit interaction can be treated as a perturbation of a non-relativistic spin pure wave-

function and written:

$$H = H_{el} + H_{so} \quad (3.27)$$

In the most accurate regime the spin orbit matrix elements are calculated from two interacting configuration interaction wavefunctions using the Briet-Pauli (BP) Hamiltonian operator:

$$H_{SO} = \sum_{\alpha} \sum_i [\hat{h}_{\alpha}(i) \cdot \hat{s}_{\alpha}(i) + \sum_{i \neq j} \hat{g}_{\alpha}(i, j) \cdot \hat{s}_{\alpha}(i)] \quad (3.28)$$

where the one electron ( $\hat{h}_{\alpha}(i)$ ) and two electron ( $\hat{g}_{\alpha}(i, j)$ ) parts are written:

$$\hat{h}_{\alpha}(i) = \frac{1}{2c^2} \sum_K \frac{Z_K [\mathbf{r}_{iK} \times \hat{\mathbf{p}}(i)]_{\alpha}}{r_{iK}^3} \quad (3.29a)$$

$$\hat{g}_{\alpha}(i, j) = -[2\hat{g}_{o\alpha}(i, j) + \hat{g}_{s\alpha}(i, j)] \quad (3.29b)$$

$$\hat{g}_{o\alpha}(i, j) = \frac{[\mathbf{r}_{ij} \times \hat{\mathbf{p}}(j)]_{\alpha}}{2c^2 r_{ij}^3} \quad (3.29c)$$

$$\hat{g}_{s\alpha}(i, j) = \frac{[\mathbf{r}_{ji} \times \hat{\mathbf{p}}(i)]_{\alpha}}{2c^2 r_{ij}^3} \quad (3.29d)$$

$\mathbf{r}_{iK}$  is the distance between electron  $i$  and nuclei  $K$ ,  $\mathbf{p}(i)$  is the momentum of electron  $i$  and  $\alpha$  is the spin. The terms  $\hat{g}_{s\alpha}$  and  $\hat{g}_{o\alpha}$  represent the spin-same orbit and spin-other orbit components of the Hamiltonian.  $\hat{s}_{\alpha}$  in equation 3.28 is a spin operator which is able to change the spin part of the electronic wavefunction on which it operates and enables mixing of wavefunctions with different multiplicities.

The matrix elements of  $\hat{H}_{so}$  between two states are evaluated by:

$$E_{so} = \langle \Psi_1 | \hat{H}_{so} | \Psi_2 \rangle \quad (3.30)$$

This is split into a simple schematic:

$$H_{so} = H_{act-act}^{1e} + H_{core-act}^{2e} + H_{act-act}^{2e} \quad (3.31)$$

where  $H_{act-act}^{1e}$  is the one electron Hamiltonian between the active orbitals,  $H_{core-act}^{2e}$  is the two electron Hamiltonian between the core and active orbitals and  $H_{act-act}^{2e}$  is



the two electron Hamiltonian between active orbitals. In some cases the one electron approach is enough to describe SOC, however in many cases the two electron terms are required for a complete description. A detailed analysis and derivation can be found in [68, 69].

## 3.5 Multi-Configuration Time Dependent Hartree (MCTDH) method

### 3.5.1 General Formulation

The molecular dynamics method was first introduced by Alder and Wainwright in the late 1950's [70, 71] to study the interactions of hard spheres. Many important insights concerning the behaviour of simple liquids emerged from their studies. The next major advance was in 1964, when Rahman carried out the first simulation using a realistic potential for liquid argon [72]. These early approaches focused upon classical methods in which a swarm of classical particles were propagated over a PES.

To recover some of the error lost using classical methods, semi-classical methods were developed. The most important of these was proposed by Heller [73] and used gaussian wavepackets. This developed many of the ideas now used as standard.

The first full quantum dynamics simulation was reported by McCullough and Wyatt in 1969 on the H+H<sub>2</sub> exchange reaction [74, 75]. The introduction of grid based methods, particularly the Fast Fourier Transform (FFT) method by Kosloff [76] and the discrete variable representation (DVR) method of Light [77] in the 1980's, provided exact simulations with efficient and accurate routines for general calculations [78].

The standard approach for solving the TDSE using a propagating wavepacket is to express the wavefunction in a time independent basis with time dependent coefficients written:

$$\Psi(Q_1, \dots, Q_f, t) = \sum_{j_1=1}^{N_1} \dots \sum_{j_f=1}^{N_f} C_{j_1 \dots j_f}(t) \prod_{k=1}^f \chi_{j_k}^{(k)}(Q_k) \quad (3.32)$$

$f$  specifies the number of degrees of freedom,  $Q_1, \dots, Q_f$  are the nuclear coordinates,

$C_{j_1 \dots j_f}$  are the time dependent coefficients,  $\chi_{j_k}^{(k)}$  are the time independent basis functions and  $N_f$  is the number of basis functions employed for the  $f^{th}$  DOF. Scaling is a major problem with this approach, computational effort grows exponentially with the number of DOF. For a calculation with  $N$  basis functions and  $f$  degrees of freedom there are  $N^f$  coefficients.

In order to negate the scaling difficulties approximate methods for solving the time dependent Schrödinger equation must be implemented. One such example is the TDH approach (also known as time dependent self consistent field due to similarities with HF). In this approximation the wavefunction is expressed:

$$\Psi(Q_1, \dots, Q_f, t) = a(t) \varphi_1(Q_1, t) \cdots \varphi_f(Q_f, t) \quad (3.33)$$

Where  $a(t)$  is a time dependent complex number and  $\varphi$  are one dimensional functions. These are time dependent, unlike in the standard approach. The product  $\varphi_1 \varphi_2$  is the Hartree product.

The performance of the TDH approach is often poor due to the lack of correlation, especially in situations when the energy of the potential changes appreciably over the width of the wavepacket [78]. Therefore, as in electronic structure methods, it seems logical to extend the approach to account for multiple configurations. In the MCTDH method the general equation 3.32 is written as a function of a linear combination of Hartree products:

$$\Psi(Q_1, \dots, Q_f, t) = \sum_{j_1=1}^{N_1} \cdots \sum_{j_f=1}^{N_f} A_{j_1 \dots j_f}(t) \prod_{k=1}^f \varphi_{j_k}^{(k)}(Q_k, t) \quad (3.34a)$$

$$\Psi(Q_1, \dots, Q_f, t) = \sum_J A_J \Phi_J \quad (3.34b)$$

As above  $Q_1, \dots, Q_f$  are the nuclear coordinates, but now  $A_{j_1 \dots j_f}$  denotes the MCTDH expansion coefficient and  $\varphi_{j_k}^{(k)}$  are expansion functions for each  $k$  DOF known as single particle functions (SPF). The number of configurations represented in the wavefunction is  $n_k$  and thus it is can be easily seen that by setting the number of configurations to 1,

equation 3.34a becomes the TDH wavefunction. Equation 3.34b defines the composite index,  $\Phi_J$  is the Hartree product.

The wavefunction expressed in Equation 3.34a can be used in conjunction with the Dirac-Frenkel variational principle to obtain a set of coupled equations of motion, one for the expansion coefficients and the other for each set of SPF:

$$i\dot{A}_J = \sum_I \mathcal{K}_{JI} A_I \quad (3.35a)$$

$$i\dot{\varphi}^{(k)} = (1 - P^{(k)})(\rho^{(k)})^{-1} \mathcal{H}^k \varphi^{(k)} \quad (3.35b)$$

$A_J$  uses a composite index representing  $A_{j_1 \dots j_f}$ ,  $\mathcal{K}_{JI}$  is the matrix element of the Hamiltonian operator between two Hartree products.  $\rho^{(k)}$  is the density matrix,  $P^{(k)}$  is a projector onto the SPF space and  $\mathcal{H}^k$  is the mean field operator. The matrix  $\mathcal{K}_{JI}$  is the the matrix element of the Hamiltonian operator in the Hartree basis:

$$\mathcal{K}_{JI} = \langle \Phi_J | H | \Phi_I \rangle \quad (3.36)$$

The operator  $(1 - P^{(k)})$  where:

$$P_j^{(k)} = |\varphi_j^{(k)}\rangle\langle\varphi_j^{(k)}| \quad (3.37)$$

ensures that the time derivative of the SPF retain the orthogonality. When the basis is complete, i.e  $1 - P = 0$ , the SPF become time independent and the equations of motion are identical to the standard method [78,79].  $H^{(k)}$  the mean field operator and  $\rho^{(k)}$  the density matrix are expressed:

$$\langle H \rangle_{ab}^{(k)} = \langle \Psi_a^{(k)} | H | \Psi_b^{(k)} \rangle \quad (3.38)$$

$$\rho_{ab}^{(k)} = \langle \Psi_a^{(k)} | \Psi_b^{(k)} \rangle \quad (3.39)$$

where the single hole functions  $\Psi_a^{(k)}$  ignore the SPF of the  $k^{th}$  mode,  $\varphi_a^{(k)}$  and the integration is over all the DOF except  $k$ . The mean field operators represent the correlation between two different sets of SPF ( $J$  and  $L$ ). See reference [78] for details.

### 3.5.2 Efficiency and Memory

Standard dynamics, using an *ansatz* in the form written in equation 3.32 have severe scaling problems. For a system with  $f$  DOF and  $N$  basis functions there will be  $N^f$  expansion coefficients to calculate. This exponential problem is highlighted in the memory requirements for a typical system with  $N=50$  basis functions. Even for a simple 4 dimensional system the memory required is 100MB just to store one wavefunction, however for a 5 dimensional system it is already 4.8GB [78]. The memory requirement for the MCTDH method is written:

$$memory \sim n^p + pnN^d \quad (3.40)$$

where  $n$  is the number of SPF for  $p$  particles, which can contain more than one DOF. The first term in this expression is the number of A coefficients and the second term is the representation of the SPF through the primitive basis functions which arise from expansion of the SPF using a set of DVR functions written:

$$\varphi_j^{(k)}(Q_k) = \sum_{k=1}^{N_k} a_{kj}^{(k)} \chi_k^{(k)}(Q_k) \quad (3.41)$$

Although there is still exponential scaling  $n < N$  and  $p < d$  and therefore the scaling problem is significantly reduced.

### 3.5.3 DVR Functions

The DVR is a grid representation which is used for representing wavefunctions and operators. It has become a widely used method for quantum dynamics simulations because it solves the problem of having to evaluate complex integrals [77, 80–82]. The time independent basis of the DVR functions can exist in various forms, including harmonic, Legendre and exponential.

In order to solve the equations of motion, equation 3.35a and 3.35b, we are required to evaluate the elements of the Hamiltonian matrix  $\mathcal{K}$ :

$$\langle \varphi_{j_1}^{(p)} \dots \varphi_{j_p}^{(p)} | H | \varphi_{j_1}^{(p)} \dots \varphi_{j_p}^{(p)} \rangle = \langle \varphi_{j_1}^{(p)} \dots \varphi_{j_p}^{(p)} | T + V | \varphi_{j_1}^{(p)} \dots \varphi_{j_p}^{(p)} \rangle \quad (3.42)$$

In a spectral basis this would require multi dimensional integrals and would be a complicated process. However in a pseudo-spectral basis, such as DVR, where the functions are represented on grids this is straight forward. A set of DVR functions ( $\chi^{(v)}(q_v)$ ) along coordinate  $q_v$  has a diagonal position operation, therefore:

$$\langle \chi_i^{(v)} | q_v | \chi_j^{(v)} \rangle = q_v^{(v)} \delta_{ij} \quad (3.43)$$

and the values  $q_v$  provide a grid of points related to the DVR functions. Hence if there are enough grid points the potential energy operator can be considered diagonal in this basis and the integral is obtained by evaluating the potential energy only at the grid point  $q_{j1}^{(1)}, \dots, q_{jf}^{(1)}$

The kinetic energy operator usually acts on one coordinate, and therefore matrix elements are evaluated in the related finite basis representation (FBR) . This can then be transformed using the FBR-DVR transformation. Detailed reviews can be found in [59, 78, 83–85]

### 3.5.4 Autocorrelation Functions and Calculation of Spectra

Spectra are calculated by performing a Fourier transform (FT) of an autocorrelation function, obtained using a quantum dynamics simulation. A time autocorrelation function,  $C(t)$ , indicates how a physical variable, in this case a wavepacket overlaps to its initial value. In the case of a wavepacket it is a representation of the overlap of the wavepacket at  $t$  with the initial wavepacket at  $t = 0$

$$C(t) = \langle \psi(0) | \psi(t) \rangle. \quad (3.44)$$

The absorption spectrum,  $I(\omega)$ , for a particular molecule is generated by Fourier transform of  $C(t)$  to the frequency domain [86]

$$I(\omega) \sim \int_{-\infty}^{\infty} C(t) e^{-i\omega t} dt \quad (3.45)$$

Before the autocorrelation function is transformed, it is modified slightly. To reduce the artifacts associated with the Gibbs phenomenon, overshooting of the fourier sum

at a discontinuity jump, the autocorrelation function is multiplied by  $\cos^2(n\pi t/2T)$ , where  $n=1,2..$  and  $T$  denotes the final time (plus one time step) of the autocorrelation function. To introduce a damping, i.e. Lorentzian or Gaussian broadening, the autocorrelation function is further multiplied with  $\exp(-|t|/\tau)^i$  where  $\tau$  and  $i$  are parameters set when calculating the spectrum.

# Chapter 4

## Benzene

Benzene and its derivatives form a basic structure for a vast range of organic compounds in nature, and can therefore be considered a model compound for a wide variety of hydrocarbons. Despite being a relatively simple molecule, benzene is a primary example of a photochemically rich molecule, with a number of competing pathways that can result after photoexcitation. Much of the behaviour has been characterised by extensive theoretical [63,87–91] and experimental [92–97] studies. However a number of questions, especially in the higher vibrational states of the  $B_{2u}$  state remain unanswered.

The ground state configuration of benzene (ignoring the inner-core) is:

$$(2a_{1g})^2(2e_{1u})^4(2e_{2g})^4(3a_{1g})^2(2b_{1u})^2(1b_{2u})^2(3e_{1u})^4(1a_{2u})^2(3e_{2g})^4(1e_{1g})^4 \quad (4.1)$$

The  $\pi$ -orbitals, formed from the 6 carbon  $2p_z$  orbitals contain 6 valence electrons giving  $(a_{2u})^2(e_{1g})^4(e_{2u})^0(b_{2g})^0$ . This is shown in figure 4.1. The initial  $\pi \rightarrow \pi^*$  transition,  $(a_{2u})^2(e_{1g})^3(e_{2u})^1(b_{2g})^0$ , leads to three singlet excited states seen in the absorption spectrum between 4.5-8eV [94], they are assigned  $\tilde{A}^1B_{2u}$ ,  $\tilde{B}^1B_{1u}$  and  $\tilde{C}^1E_{1u}$ . The  $\tilde{D}^1E_{2g}$  band has a different origin, with doubly excited configurations. The  $\tilde{X} \rightarrow \tilde{A}$  and  $\tilde{B}$  transitions are electronically forbidden and as a result give fairly weak absorption bands,  $\tilde{X} \rightarrow \tilde{C}$  is allowed and gives an intense, structureless band.

At low excess energy in the first excited state, ( $\tilde{A}^1B_{2u}$ ), fluorescence (channel 1) is observed with a quantum yield of  $\simeq 0.2$  and any non-radiative decay is attributed to

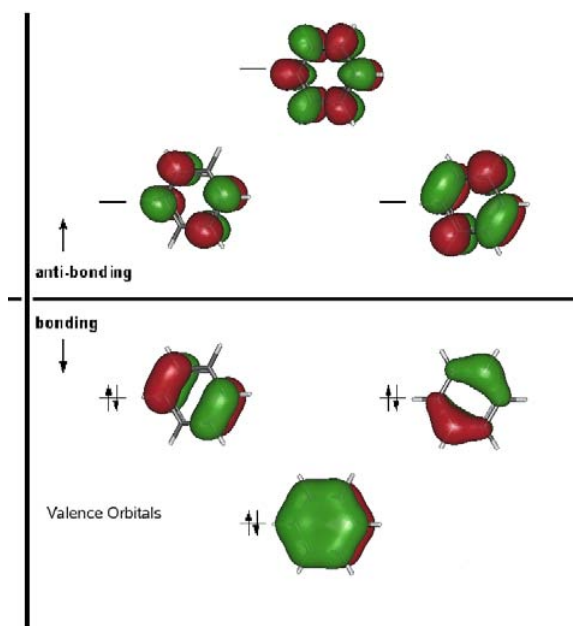


Fig. 4.1: The  $\pi$  valence orbitals in benzene. The lowest three are doubly occupied in the ground state determinant. The unoccupied  $\pi^*$  orbitals ( $e_{2u}$  and  $b_{1g}$ ) are occupied in the most important excited determinants and therefore are required to provide the electron correlation required to give a good energetic description of the excited states.

intersystem crossing (channel 2) to the low lying triplet states [98,99]. Photophysical data shows that the fluorescence from this state disappears when the molecule is excited  $3000\text{cm}^{-1}$  above the band origin [95]. The explanation of this decay has been a source of debate since it was first reported by Calloman *et al* [100], however it is now widely accepted that at this energy a CI leading to a dark state becomes available [88].

Photochemically, benzene undergoes significant rearrangement upon irradiation. Fulvene, benzvalene and dewar benzene (shown in figure 4.2) have all been detected, with yields depending on the initial wavelength of light used [92,93]. Excitation to  $\tilde{A}$  at 254nm gives quantum yields of 0.01:0.01:0.00 respectively, however excitation to  $\tilde{B}$  at 165nm results in 0.05:0.02:0.01. It has been demonstrated that the  $\tilde{X}/\tilde{A}$  CI plays an important role in this process leading directly to prefulvene, the precursor for the transformation [101]. However it is thought that excitation into these photochemical channels requires excitation of a very specific combination of normal modes.



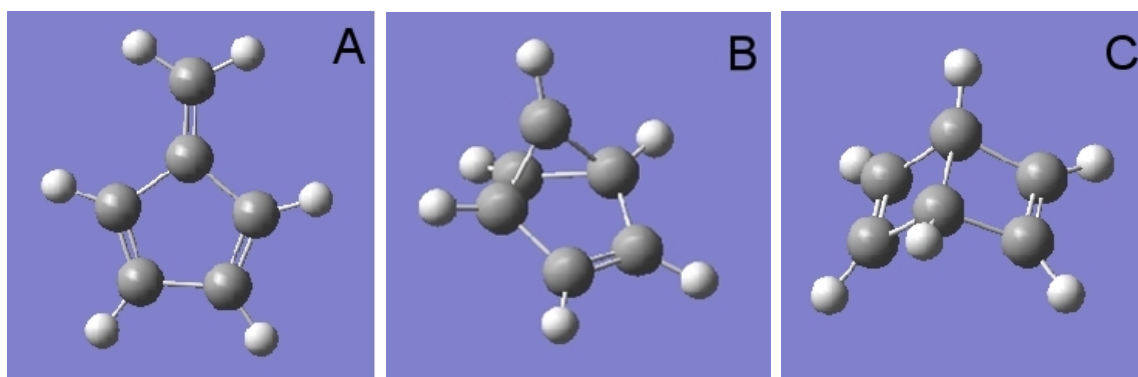


Fig. 4.2: Ground state minimum energy geometry structure of (a) fulvene (b) benzvalene and (c) dewar benzene.

This chapter is a development on a previous CASSCF study, enabling us to accurately describe the dynamics of benzene in the manifold of states involved [102]. In the following sections a diabatic potential operator matrix suitable for studying the early time dynamics of benzene after photoexcitation is described using parameters obtained by a fit of the adiabatic PES along the vibrational modes. Data points along the normal modes and diagonally along the important combination modes were obtained using CASPT2 calculations [103]. These calculations include the required dynamic correlation to accurately describe the higher lying electronic states. The operator obtained is the Vibronic Coupling Hamiltonian [104] which has proved successful in describing a wide range of molecular systems in which non-adiabatic effects are important [10, 49]. This is described in detail in section 2.4. The simplicity of this model allows a natural description of the photo-initiated dynamics in terms of excitation of normal modes and couplings between the diabatic electronic states. This method has also been used to describe the benzene cation [48, 50] and due to symmetry many of the results for benzene are identical with the cation. By utilising the powerful MCTDH wavepacket dynamics method [57, 105] we are then able to study the dynamics of photo-excited benzene using two calculated Hamiltonians and compare results to experimental data obtain by the Fielding group [19].

The benzene photochemical surfaces are epitomised by avoided crossings and CI, to enable us to give a clear description of these features we introduce the following nomenclature. The diabatic states are labelled with  $\tilde{X}$ ,  $\tilde{A}$ ,  $\tilde{B}$  etc, while the adiabatic states are labelled  $S_0$ ,  $S_1$ ,  $S_2$  etc. At the ground state equilibrium geometry (the FC point) the states are equivalent.

## 4.1 The Model Hamiltonian

Benzene contains 30 vibrational modes and in the energy range of interest 7 states. Quantum dynamics using a model containing all of them would be very computationally demanding. However using the linear coupling scheme (described in section 2.4) [102], many of the less important modes, i.e. with no first order coupling, can be ignored, as they make little difference to the dynamics.

The CAS(6,6)/6-31g\* frequencies, which define the normal mode coordinates and provide the zero-order harmonic diabatic surfaces, are listed in tables 4.1 and 4.2. They are in reasonable agreement with the experimental values, with the modes in the correct order. CASPT2 frequency calculations did not change the values significantly and therefore were not used so that easier comparisons with the CASSCF model of [102] were possible. The high energy modes, which are mostly unimportant in this work, have an error of  $\sim 0.035\text{eV}$  ( $280\text{cm}^{-1}$ ), the low frequency modes have an error  $\sim 0.01\text{eV}$  ( $90\text{cm}^{-1}$ ).

The modes of critical importance to the benzene model are: the low frequency ( $a_{1g}$ ) breathing mode, the lowest frequency JT active ( $e_{2g}$ ) mode, the lowest two frequency  $e_{1u}$  modes, the boat mode ( $e_{2u}$ ) and the chair ( $b_{2g}$ ) mode. The combination of the boat and chair modes results in the formation of prefulvene, the reaction intermediate for the formation of benzvalene and fulvene.

As stated above this is a development of previous electronic structure calculations performed at CASSCF level [102]. These were unable to accurately describe the  $B_{1u}$

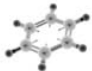

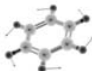
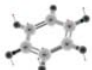
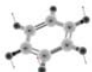
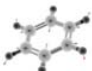
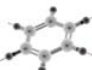
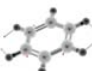


Mode	Symmetry	Vibration	Theory	Experimental [106]	Description
1	$1a_{1g}$		0.1292	0.1231	C-H Breathing
2	$2a_{1g}$		0.4198	0.3811	C-H Breathing
3	$1a_{2g}$		0.1861	0.1674	C-H Twist
4	$1b_{2g}$		0.0898	0.0877	Chair
5	$2b_{2g}$		0.1286	0.1227	Antisymmetric C-H Bend
6	$1e_{2g}$		0.0886	0.0754	Quinoid
7	$4e_{2g}$		0.4160	0.3790	C-H Breathing
8	$3e_{2g}$		0.2157	0.1985	Antisymmetric C-H Bend
9	$2e_{2g}$		0.1582	0.1460	Symmetric C-H Bend
10	$1e_{1g}$		0.1086	0.1050	Antisymmetric C-H Bend

Table 4.1: Mode symmetry and vibration energies (in eV) for the gerade normal modes of benzene, using Wilson numbering. Calculated using a CAS(6,6) active space and 6-31g\* basis set.



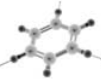
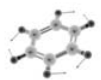
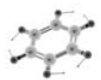
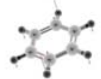
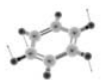
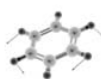
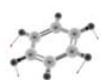
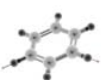
Mode	Symmetry	Vibration	Theory	Experimental [106]	Description
11	$1a_{2u}$		0.0811	0.0834	C-H Bend
12	$1b_{1u}$		0.1363	0.1252	Antisymmetric Twist
13	$2b_{1u}$		0.4148	0.3790	C-H Breathing
14	$2b_{2u}$		0.1662	0.1623	C-C Stretch
15	$1b_{2u}$		0.1470	0.1423	C-C Stretch
16	$1e_{2u}$		0.0535	0.0493	Boat
17	$2e_{2u}$		0.1231	0.1199	Out of Plane C-H Bend
18	$1e_{1u}$		0.1382	0.1287	Twist
19	$2e_{1u}$		0.2021	0.1840	C-H Antisymmetric Twist
20	$3e_{1u}$		0.4183	0.3799	C-H Breathing

Table 4.2: Mode symmetry and vibration energies (in eV) for the ungerade normal modes of benzene, using Wilson numbering. Calculated using a CAS(6,6) active space and 6-31g\* basis set.

State	SA-CAS(6,6)	CASPT2(6,6)	CASPT2(6,10)	Experimental [63]
$\tilde{A}^1 B_{2u}$	4.895	4.76	4.84	4.90
$\tilde{B}^1 B_{1u}$	8.166	6.55	6.45	6.20
$\tilde{C}^1 E_{1u}$	9.542	7.29	6.94	6.94
$\tilde{D}^1 E_{2g}$	8.110	7.81	7.81	7.8

Table 4.3: Vertical excitation energies (in eV) of six singlet excited states of benzene, calculated at equilibrium geometry. The SA-CAS(6,6) used a 6-31g\* basis and is averaged over all 6 states plus the ground state. The PT2(6,6) and PT2(6,10) uses a Molpro specific Roos(3s2p1d/2s) basis.

and  $E_{1u}$  states due to the lack of dynamic correlation, which is important for describing states with significant ionic character. This can be seen in Table 4.3, which lists the energies of each state at the ground state equilibrium geometry. The CASSCF states are not ordered correctly and the  $E_{2g}$  state is the lowest doubly degenerate state. This is likely to have a big effect on the coupling parameters obtained.

Throughout this work CASPT2 implemented in Molpro [107] was used. CASPT2 uses the CASSCF wavefunction as a zeroth order approximation, and adds a second order perturbation (see section 3.3). Developed by Roos *et al* [103], this method has been used on a large variety of chemical systems. For the cuts along the vibrational modes we used a CAS(6,6) active space in combination with a Molpro specific Roos(3s2p1d/2s) basis, which uses the atomic natural orbitals (ANO) basis truncated to 6-31g\* size. Following [63] a larger (6,10) active space, which includes diffuse Rydberg orbitals was tested. Despite being slightly more accurate at the equilibrium geometry, it proved difficult to converge calculations along symmetry breaking modes. The difference in the two calculations at ground state equilibrium geometry can again be seen in Table 4.3. The larger active space, which includes diffuse Rydberg orbitals, important in the excitation process, is very accurate. Despite being less accurate the smaller (6,6) space is able to describe the surfaces well and is preferred because of the computational expense and lack of stability of the larger active space.

The adiabatic PES are the eigenvalues of the diabatic Hamiltonian matrix (equation

2.33). A model Hamiltonian using a particular set of expansion coefficients can thus provide the adiabatic PES at a particular value of  $\mathbf{Q}$  by diagonalising the matrix. As a result the parameters can be obtained from a fit of the model to adiabatic PES obtained from quantum chemistry calculations.

The fit was performed using the VCHAM program. This program helps to automate the procedure and is distributed with the MCTDH quantum dynamics package [79]. It has been used previously to provide a model Hamiltonian for a number of systems [52, 108, 109].

The starting point is the ground state minimum energy  $D_{6h}$  structure,  $\mathbf{Q}_0$ . The coordinates for the Hamiltonian are obtained from the dimensionless normal modes at this point. The seven surfaces were calculated with a spacing of  $\Delta Q=1.0$  at 21 points along each normal mode (10 either side of  $\mathbf{Q}_0$ ). Fewer points were calculated along the breathing mode due to difficulties associated with the highly distorted structure. Combination modes were also calculated, the most important of these is the prefulvene mode ( $\nu_4+\nu_{16}$ ), however others containing intra-state coupling that contribute to IVR were also fitted. A database is prepared containing the vibrational and energetic information, and the parameters are obtained by a least squares fit using a simple conjugate gradient optimisation scheme with the mean-square difference between the *ab-initio* and model adiabatic energies at all points as a penalty function. Due to the dependencies between parameters of different order the fit is performed in stages, first optimising the linear parameters before including the higher order ones. The linear Hamiltonian has a total of 93 parameters that need to be evaluated. This demonstrates the power of symmetry. There are 796 linear parameters, but most are zero by symmetry.

The parameters obtained from the fitting are listed in tables 4.4, 4.5, 4.6, 4.7, 4.8, 4.9 and 4.10. Cuts through the PES along the important modes are shown in figures 4.3, 4.4, 4.5, 4.6, 4.7, 4.8 and 4.9. The quality of the fitted model is judged

by how closely the eigenvalues fit the *ab-initio* points. The root-mean square standard deviation (RMSD) between the model surfaces and *ab-initio* points is 0.154eV over 2546 datasets. An exponential weighting to the points ( $w_i = \exp -R(E_i - E_0)$ ), where  $R$  is an input parameters,  $E_i$  is the *ab-initio* energy and  $E_0$  is the energy of the relevant surface at  $Q_0$  can enhance the fit in the important low energy regions. When this weighting is used during the fit the weighted RMSD falls to 0.08eV, showing that most of the error is in the regions unvisited by the wavepacket.

### 4.1.1 First Order Parameters

Table 4.4 lists the on-diagonal linear coupling constants ( $\kappa_\alpha$ ). These values are non-zero along all totally symmetric modes. The importance of this parameter is related to  $\kappa_\alpha/\omega_\alpha$ , the distance the excited state minima is shifted from the ground state minimum in the harmonic approximation. The FC overlap and hence transition strengths have a direct dependence on this factor because when  $\kappa_\alpha/\omega_\alpha$  is larger the transition band in the spectra will be wider. The frequency of the second totally symmetric mode is 0.4198eV and therefore is less important than its lower energy counterpart whose excited state minima show significant displacement from the FC point.  $\kappa_\alpha$  values can also arise in doubly degenerate states along doubly degenerate modes. In benzene this can occur along the  $e_{2g,x}$  modes, as part of the JT interaction as shown in equation 2.41. Displacement due to this coupling is largest in  $\nu_8$ , but is still small in comparison to  $\nu_1$ .

The linear off-diagonal coupling parameters ( $\lambda$ ) are listed in table 4.5. Non-zero parameters can be found for pairs of states dependent on the symmetry involved [102]. The most significant coupling is between the  $\tilde{X}$ ,  $\tilde{A}$ ,  $\tilde{B}$  and  $\tilde{C}$  states. The coupling between  $\tilde{X}/\tilde{A}$  is along  $\nu_{14}$  and  $\nu_{15}$  and  $\tilde{X}/\tilde{C}$  is along  $\nu_{18}$  and  $\nu_{19}$ . There is also large coupling between  $\tilde{B}/\tilde{C}$  along  $\nu_8$ , however  $\tilde{B}$  and  $\nu_8$  play little role in the dynamics and therefore this can be considered unimportant.

Although at first appearance it seems that the coupling between  $\tilde{X}/\tilde{A}$  is the most

	$\tilde{A}$	$\tilde{B}$	$\tilde{C}$	$\tilde{C}$	$\tilde{D}$	$\tilde{D}$
Mode	$B_{2u}$	$B_{1u}$	$E_{1u, x}$	$E_{1u, y}$	$E_{2g, x}$	$E_{2g, y}$
$\nu_1$ ( $1a_{1g}$ )	0.173	0.244	0.388	0.388	0.093	0.093
$\nu_2$ ( $2a_{1g}$ )	0.125	0.015	0.106	0.106	0.094	0.094
$\nu_{6a}$ ( $1e_{2g, x}$ )	–	–	0.029	-0.029	0.024	-0.024
$\nu_{7a}$ ( $4e_{2g, x}$ )	–	–	–	–	–	–
$\nu_{8a}$ ( $3e_{2g, x}$ )	–	–	0.128	-0.128	0.103	-0.103
$\nu_{9a}$ ( $2e_{2g, x}$ )	–	–	0.056	-0.056	0.122	-0.122

Table 4.4: On-diagonal linear coupling constants,  $\kappa_\alpha$ , for the normal modes of benzene (in eV). Obtained by fitting a Vibronic Coupling Hamiltonian to the adiabatic potential energy surface at the CASPT2(6,6) level. There are no values for  $\nu_{7a}$  because they are so small they can be considered negligible.

significant to the dynamics at the  $S_1/S_0$  CI, it is actually the coupling between  $\tilde{X}/\tilde{C}$  which is most important when the two surfaces cross at the prefulvene CI. This is shown and discussed in more detail in section 4.4.2.

JT coupling in which a doubly degenerate state is split by coupling involving a doubly degenerate mode is present for both the  $\tilde{C}$  and  $\tilde{D}$  states. In both cases it is the  $y$  component of the  $e_{2g}$  mode responsible for splitting the degeneracy. The strength of the coupling is equal to the on-diagonal elements shown in Table 4.4. Between the  $E_{1u}$  state components this is largest along  $\nu_{7b}$ , and between the  $E_{2g}$  state components the largest is along  $\nu_{9b}$ .

Pseudo Jahn-Teller (PJT) interactions, in which a singly degenerate state couples to a doubly degenerate state along a doubly degenerate mode completes the set of linear inter-state interactions. The PJT couples the  $x$  component of each vibration to the  $x$  component of the electronic state and the  $y$  component of each vibration to the  $y$  component of the electronic state. This splits the degenerate state in a similar topological manner to that seen in the JT interaction. The PJT interaction is the most prominent coupling type in benzene. The most significant is between  $\tilde{X}/\tilde{C}$  which is very large and plays an important role in the dynamics at the  $S_1/S_0$  CI (discussed later). There is also extensive coupling between the  $\tilde{X}$  and  $\tilde{A}$  states to the doubly



	$\tilde{X}$	$\tilde{A}$	$\tilde{B}$	$\tilde{C}$	$\tilde{D}$
	A <sub>1g</sub>	B <sub>2u</sub>	B <sub>1u</sub>	E <sub>1u,x</sub>	E <sub>2g,x</sub>
$\tilde{A}B_{2u}$	$\lambda_{14} = 0.220$ $\lambda_{15} = 0.352$	–	–	–	–
$\tilde{B}B_{1u}$	$\lambda_{12} = 0.140$ $\lambda_{13} = 0.078$	$\lambda_3 = 0.020$ –	– –	– –	– –
$\tilde{C}E_{1u,x}$	$\lambda_{18a} = 0.210$ $\lambda_{19a} = 0.350$ $\lambda_{20b} = 0.060$ –	$\lambda_{6a} = 0.111$ $\lambda_{7a} = 0.129$ $\lambda_{9a} = 0.124$ –	$\lambda_{6a} = -0.033$ $\lambda_{7a} = -0.072$ $\lambda_{8a} = -0.241$ $\lambda_{9a} = -0.086$	– – – –	– – – –
$\tilde{C}E_{1u,y}$	$\lambda_{18b} = -0.210$ $\lambda_{19b} = -0.350$ $\lambda_{20a} = -0.060$ –	$\lambda_{6b} = -0.111$ $\lambda_{7b} = -0.129$ $\lambda_{9b} = -0.124$ –	$\lambda_{6b} = 0.033$ $\lambda_{7b} = 0.072$ $\lambda_{8b} = 0.241$ $\lambda_{9b} = 0.086$	$\lambda_{6b} = 0.030$ $\lambda_{7b} = 0.128$ $\lambda_{8b} = 0.056$ –	– – – –
$\tilde{D}E_{2g,x}$	$\lambda_{9a} = 0.047$ –	$\lambda_{18b} = 0.180$ $\lambda_{19b} = 0.120$	– –	– –	– –
$\tilde{D}E_{2g,y}$	$\lambda_{9b} = -0.047$ – –	$\lambda_{18a} = -0.180$ $\lambda_{19a} = -0.120$ –	– – –	– – –	$\lambda_{6b} = 0.025$ $\lambda_{8b} = 0.043$ $\lambda_{9b} = 0.122$

Table 4.5: Off-diagonal linear coupling constants,  $\lambda_\alpha$ , for the normal modes of benzene (in eV). Obtained by fitting a Vibronic Model Hamiltonian to the adiabatic potential energy surface at the CASPT2(6,6) level. The columns and rows are the different states, subscripts denote the normal modes providing the coupling. The E<sub>1u,y</sub> and E<sub>2g,y</sub> columns are not included as they symmetrically replicate the  $x$  component data.

degenerate states along the  $e_{2g}$  modes. The coupling between  $\tilde{A}$  and  $\tilde{C}$  is strongest along  $\nu_{7b}$ , there is also significant coupling along  $\nu_{6b}$  and  $\nu_{9b}$ . The PJT between  $\tilde{B}$  and  $\tilde{C}$  is very strong along  $\nu_{8b}$  while the other  $e_{2g}$  modes play little part. There is also PJT coupling between  $\tilde{A}/\tilde{D}$  however these do not play a significant role in the dynamics and are therefore not important.

In most cases the linear coupling forms the major component of non-adiabatic coupling within a model, and will alone describe most of the prominent features in the crossing region of the PES nearest the expansion (FC) point. This is also the case for benzene and it is clear that, mainly due to the  $e_{2g}$  modes, there is a multitude of possible pathways for the wavepacket to spread through. However to obtain a more accurate model, which includes finer details of the dynamics, higher order terms must be included.

### 4.1.2 Morse Parameters

The first term in Vibronic Coupling Hamiltonian, equation 2.33, is the zeroth order approximation for the PES. This is typically a harmonic oscillator term including the frequency of the mode. However in some cases the PES is too unsymmetric to use the harmonic approximation. In this case a Morse potential is implemented in the form described in equation 2.44.

The parameters obtained by fitting a Morse potential are shown in table 4.6. The  $\tilde{D}E_{2g}$  is not shown because this state does not play a key role in the dynamics. There are 3 modes which require the potential in this form:  $\nu_1$ ,  $\nu_{8a}$  and  $\nu_{9a}$ . The most important of these is the totally symmetric low frequency breathing mode ( $\nu_1$ ). The parameters shows that  $\tilde{A}$  is the shallowest (smallest  $D_0$ ) of the excited state surfaces along this mode. This is indicative of a state with little ionic character, meaning there is less repulsion upon compression. All 4 surfaces indicate a degree of shifting from the equilibrium geometry ( $X_0$ ) associated with the degree of double excitation in the determinant and therefore the occupation of the anti-bonding orbitals.

Mode	B <sub>2u</sub>			B <sub>1u</sub>			E <sub>1u</sub>			
	D <sub>0</sub>	$\alpha$	X <sub>0</sub>	D <sub>0</sub>	$\alpha$	X <sub>0</sub>	D <sub>0</sub>	$\alpha$	X <sub>0</sub>	E <sub>0</sub>
$\nu_1$	0.363	-0.062	-1.701	3.638	-0.0244	-1.835	3.638	-0.0236	-2.6259	-0.015
$\nu_{8a}$	3.638	0.033	0.000	3.638	0.033	0.000	3.638	0.033	0.000	0.000
$\nu_{9a}$	6.982	0.021	-0.074	21.68	0.0108	-0.058	290.0	0.003	-0.0599	0.000

Table 4.6: The parameters for the Morse potentials in atomic units (au) for the modes which exhibit a lot of antisymmetric behaviour. Obtained by fitting a Vibronic Coupling Hamiltonian to the adiabatic potential energy surface at the CASPT2(6,6) level.

### 4.1.3 Second Order Parameters

The frequencies of the excited state are changed from those of the ground state by the second order on-diagonal parameters,  $\gamma_{\alpha\alpha}$ . Due to the coordinate scaling used in this Hamiltonian, the frequency of a mode with potential:

$$V = \frac{1}{2}(\omega_\alpha + \gamma_{\alpha\alpha}^{(i)})Q_\alpha^2 \quad (4.2)$$

is  $\sqrt{\omega_\alpha^2 + \omega_\alpha \gamma_{\alpha\alpha}^{(i)}}$ . The parameters are shown in tables 4.7 and 4.8. A 5% change in the frequency is given by the ratio:

$$\left| \frac{\gamma_{\alpha\alpha}^{(i)}}{\omega_\alpha} \right| > 0.1 \quad (4.3)$$

and therefore only values greater than this are listed. In general the  $\gamma$  parameters are small, however noticeable effects can be seen along several modes, including  $\nu_4$  and  $\nu_{16}$ . The lowering of the frequency flattens the PES allowing the wavepacket to spread more easily [110].

As well as on-diagonal  $\gamma_{\alpha\alpha}$  parameters, the off-diagonal  $\gamma_{\alpha\beta}$  parameters which are responsible for IVR can be important (shown in table 4.8). These parameters tend to be small and generally do not have a large effect of the appearance of the absorption spectra, however they can play a critical role in the subtle dynamics of a model system.

The off-diagonal second-order coupling parameters ( $\mu$ ), listed in table 4.9, are responsible for inter-state coupling diagonally between the vibrational modes. They are typically quite small, however again they can be important to the dynamics of the model. Coupling elements for this model were considered for the first three excited states, as it is these that are most important in the dynamics following excitation into the  $B_{2u}$  state. In this model the  $\mu$  parameters are small and therefore will have an almost negligible effect on the dynamics of the overall system, this is a significant change from the CASSCF model in which they play an important role in an accurate description of the surfaces [102].

In cases when the PES are anharmonic but symmetric, fourth order terms are some-

	$\tilde{A}$	$\tilde{B}$	$\tilde{C}$	$\tilde{C}$	$\tilde{D}$	$\tilde{D}$
	B <sub>2u</sub>	B <sub>1u</sub>	E <sub>1u,x</sub>	E <sub>1u,y</sub>	E <sub>2g,x</sub>	E <sub>2g,y</sub>
$\nu_1$	-0.116	-0.006	0.025	0.025	-0.015	-0.015
$\nu_2$	0.028	0.012	0.024	0.024	-0.031	-0.031
$\nu_4$	-0.048	-0.033	-0.062	-0.062	-0.093	-0.093
$\nu_5$	-0.073	-0.041	-0.048	-0.048	-0.048	-0.048
$\nu_{6a}$	-0.018	-0.017	–	–	-0.034	-0.034
$\nu_{6b}$	-0.015	–	–	–	-0.015	-0.015
$\nu_{7a}$	–	–	0.012	0.012	0.012	0.012
$\nu_{7b}$	–	–	–	–	–	–
$\nu_{8a}$	0.01	–	-0.039	–	–	–
$\nu_{8b}$	–	–	–	–	–	–
$\nu_{9a}$	–	-0.025	–	-0.025	-0.048	–
$\nu_{9b}$	–	-0.021	-0.01	-0.01	–	–
$\nu_{10a}$	-0.051	-0.040	-0.074	-0.074	-0.113	-0.113
$\nu_{10b}$	-0.056	-0.040	-0.114	-0.114	-0.157	-0.157
$\nu_{11}$	-0.033	-0.024	-0.030	-0.030	-0.072	-0.072
$\nu_{13}$	–	–	–	–	-0.055	-0.055
$\nu_{16a}$	-0.039	-0.019	-0.091	-0.021	-0.026	-0.026
$\nu_{16b}$	-0.045	-0.063	-0.109	-0.023	-0.033	-0.033
$\nu_{17a}$	-0.079	-0.021	-0.090	-0.090	-0.118	-0.118
$\nu_{17b}$	-0.046	-0.011	-0.095	-0.095	-0.094	-0.094
$\nu_{18a}$	–	–	0.015	0.015	-0.016	-0.016
$\nu_{18b}$	–	–	0.015	0.015	-0.016	-0.016
$\nu_{19a}$	–	–	0.301	0.301	-0.04	-0.04
$\nu_{19b}$	–	–	0.034	0.034	-0.037	-0.037
$\nu_{20a}$	-0.030	–	0.05	0.05	-0.04	-0.04
$\nu_{20b}$	–	–	0.02	0.02	-0.02	-0.02

Table 4.7: On-diagonal second order coupling constants,  $\gamma_\alpha$  for the normal modes of benzene (in eV). Obtained by fitting a Vibronic Coupling Hamiltonian to the adiabatic potential energy surface at CASPT2(6,6) level.

	$\tilde{X}$	$\tilde{A}$	$\tilde{B}$	$\tilde{C}$	$\tilde{C}$	$\tilde{D}$	$\tilde{D}$
	$A_{1g}$	$B_{2u}$	$B_{1u}$	$E_{1u,x}$	$E_{1u,y}$	$E_{2g,x}$	$E_{2g,y}$
$\nu_{12-13}$	-0.0212	-0.0208	-0.0210	-0.0187	-0.0187	-0.0230	-0.0230
$\nu_{13-9a}$	–	–	–	0.009	0.0013	0.012	0.0113
$\nu_{6a-9a}$	0.0285	0.0246	0.0415	0.0422	0.0283	0.0151	0.0219
$\nu_{1-2}$	0.0271	0.0256	0.0228	0.0320	0.0191	0.0254	0.0254
$\nu_{1-6a}$	–	–	–	0.070	–	0.0122	–
$\nu_{1-16a}$	–	–	–	–	–	0.0122	–
$\nu_{1-16a}$	–	–	–	0.070	–	–	–
$\nu_{1-16b}$	–	–	–	0.070	–	–	–

Table 4.8: Off-diagonal intrastate second order coupling constants,  $\gamma_{\alpha\beta}$  for the normal modes of benzene (in eV). Obtained by fitting a Vibronic Coupling Hamiltonian to the adiabatic potential energy surface at CASPT2(6,6) level.

	$\tilde{X}$	$\tilde{A}$	$\tilde{B}$	$\tilde{C}$	$\tilde{C}$
	$A_{1g}$	$B_{2u}$	$B_{1u}$	$E_{1u,x}$	$E_{1u,y}$
$\tilde{A} B_{2u}$	$\nu_{1-14} = 0.00645$	–	–	$\nu_{6a-9a} = -0.00679$	$\nu_{6a-9b} = -0.00749$
$\tilde{B} B_{1u}$	$\nu_{1-12} = 0.01800$	–	–	$\nu_{6a-9a} = -0.01480$	–
	–	–	–	$\nu_{1-9a} = -0.00525$	–
	–	–	–	$\nu_{1-6a} = 0.01194$	–
$\tilde{C} E_{1u,x}$	–	–	–	–	$\nu_{12-13} = 0.0010$
	–	–	–	–	$\nu_{11-16a} = 0.0043$
$\tilde{C} E_{1u,y}$	–	–	–	–	–

Table 4.9: Off-diagonal inter state second-order coupling terms  $\mu_{\alpha\beta}$  (see equation 2.41) for the normal modes of benzene (in eV). Obtained by fitting a Vibronic Coupling Hamiltonian to the adiabatic potential energy surface at PT2(6,6) level. The  $\tilde{D}E_{2g}$  state is not included in this table because there were no significant parameters for this state required.

	$\tilde{X}$	$\tilde{A}$	$\tilde{B}$	$\tilde{C}$	$\tilde{C}$	$\tilde{D}$	$\tilde{D}$
	$A_{1g}$	$B_{2u}$	$B_{1u}$	$E_{1u,x}$	$E_{1u,y}$	$E_{2g,x}$	$E_{2g,y}$
$\nu_{10a}$	0.006	0.008	0.009	0.012	0.012	0.014	0.014
$\nu_{10b}$	0.011	0.014	0.013	0.026	0.026	0.030	0.030
$\nu_{16a}$	0.002	0.003	0.002	0.006	0.001	0.003	0.003
$\nu_{16b}$	0.002	0.003	0.005	0.010	0.010	0.003	0.003
$\nu_{17a}$	0.006	0.015	0.003	0.013	0.013	0.018	0.018
$\nu_{17b}$	0.003	0.005	–	0.011	0.011	0.011	0.011
$\nu_{20a}$	0.039	0.043	0.039	0.020	0.020	0.051	0.051
$\nu_{20b}$	0.048	0.049	0.049	0.047	0.047	0.051	0.051

Table 4.10: On-diagonal quartic coupling constants,  $\epsilon_\alpha$  (see equation 2.44) for the normal modes of benzene (in eV). Obtained by fitting a Vibronic Coupling Hamiltonian to the adiabatic potential energy surface at CASPT2(6,6) level.

times required to improve the fit, especially at points a long way from the equilibrium geometry. These were required for  $\nu_{10}$ ,  $\nu_{16}$ ,  $\nu_{17}$  and  $\nu_{20}$  and are listed in table 4.10.

## 4.2 Cuts Through The Potential Energy Surfaces

### 4.2.1 Along The Normal Modes

Figures 4.3, 4.4, 4.5, 4.6 and 4.7 show fitted cuts through the adiabatic PES for the most important modes in benzene. In the case of doubly degenerate modes only the  $x$  component is shown, because of the similarity between the two components. Figures 4.1 and 4.2 contain the most important modes which are involved in the prefulvenic reaction coordinate, groupings which follow are chosen by symmetry or characteristics, where possible.

Along  $\nu_1$  (figure 4.3(a)) the excited state minima are shifted from the ground state minima. This is most apparent in  $\tilde{C}$ , where occupation of the anti-bonding orbitals results in the weakening of the bonds. A variation in the frequency of electronic states is also most apparent in  $\tilde{C}$  which crosses both the  $\tilde{B}$   $B_{1u}$  and doubly degenerate  $\tilde{D}$   $E_{2g}$  at points along the coordinate. This behaviour is attributed to the significant ionic character of this state leading to increased repulsion on compression. The very

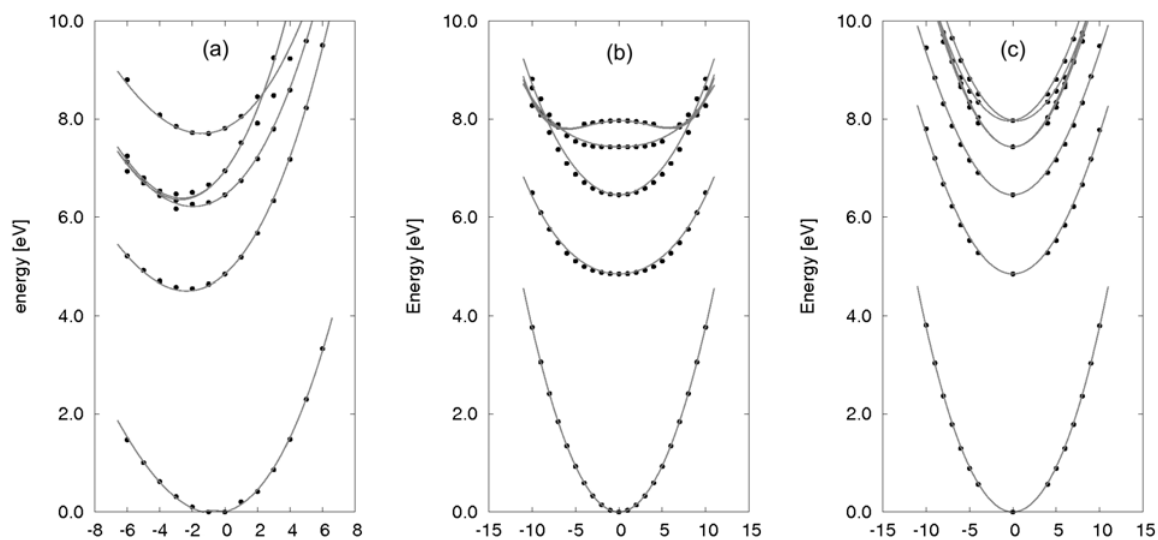


Fig. 4.3: Cuts through the adiabatic potential energy surfaces for benzene, including the ground states and 6 excited states. In order of energy at  $\mathbf{Q}=0$  these states are  $\tilde{X} A_{1g}$ ,  $\tilde{A} B_{2u}$ ,  $\tilde{B} B_{1u}$ ,  $\tilde{C} E_{1u}$ ,  $\tilde{D} E_{2g}$ . (a)  $\nu_1$  ( $1a_{1g}$ ), the breathing mode, (b)  $\nu_4$  ( $1b_{2g}$ ), the chair mode, (c)  $\nu_{6a}$  ( $1e_{2g}$ ), the quinoid mode

antisymmetric nature of this mode means a Morse potential was required for the fit (see section 4.1.2).

The chair mode,  $\nu_4$ , (figure 4.3(b)) has a significant change of frequency in the excited states. This is most significant in  $\tilde{A}$  and  $\tilde{D}$ , the latter is very flat and is indicative of states with less ionic character and more double excitations, which results in the molecule having more freedom to vibrate. The quinoid mode,  $\nu_6$ , (figure 4.3(c)) is the main JT active  $e_{2g}$  mode. Splitting due to linear coupling is seen in both  $\tilde{C}$  and  $\tilde{D}$ , it is however quite small.

The boat/twist,  $\nu_{16}$ , (figure 4.4(a)) is the lowest frequency mode. Being  $e_{2u}$  symmetry there is no linear coupling but strong second order coupling which results in  $2^{nd}$  order JT splitting for  $\tilde{C}$  and  $\tilde{D}$ . It is clearly a very strong effect in  $\tilde{C}$  leading to a deep double well along this mode and lowering the energy enough to bring  $\tilde{C}$  below  $\tilde{B}$  at large distortions along the mode.

Figures 4.4(b) and 4.4(c) show the  $e_{1g}$  mode,  $\nu_{10}$  and the  $a_{2u}$  mode,  $\nu_{11}$  respectively. Both have relatively flat PES, especially  $\nu_{11}$ . This is a similar behaviour as that seen



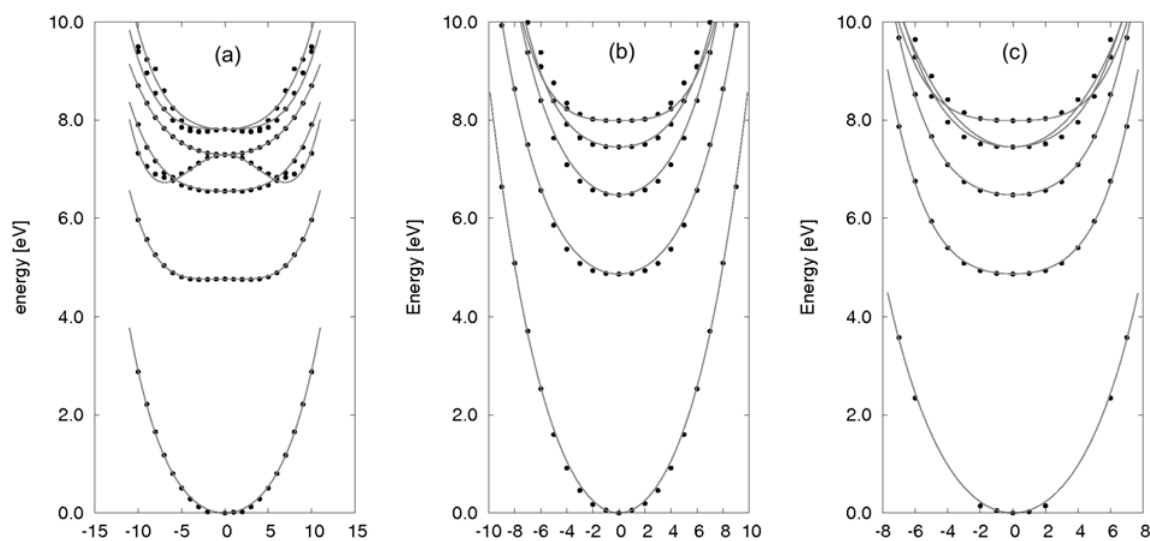


Fig. 4.4: Cuts through the adiabatic potential energy surfaces for benzene, including the ground states and 6 excited states. In order of energy at  $\mathbf{Q}=0$  these states are  $\tilde{X} A_{1g}$ ,  $\tilde{A} B_{2u}$ ,  $\tilde{B} B_{1u}$ ,  $\tilde{C} E_{1u}$ ,  $\tilde{D} E_{2g}$ . (a)  $\nu_{16a}$  ( $1e_{2u}$ ), the boat mode, (b)  $\nu_{10a}$  ( $1e_{1g}$ ) (c)  $\nu_{11}$  ( $1a_{2u}$ ).

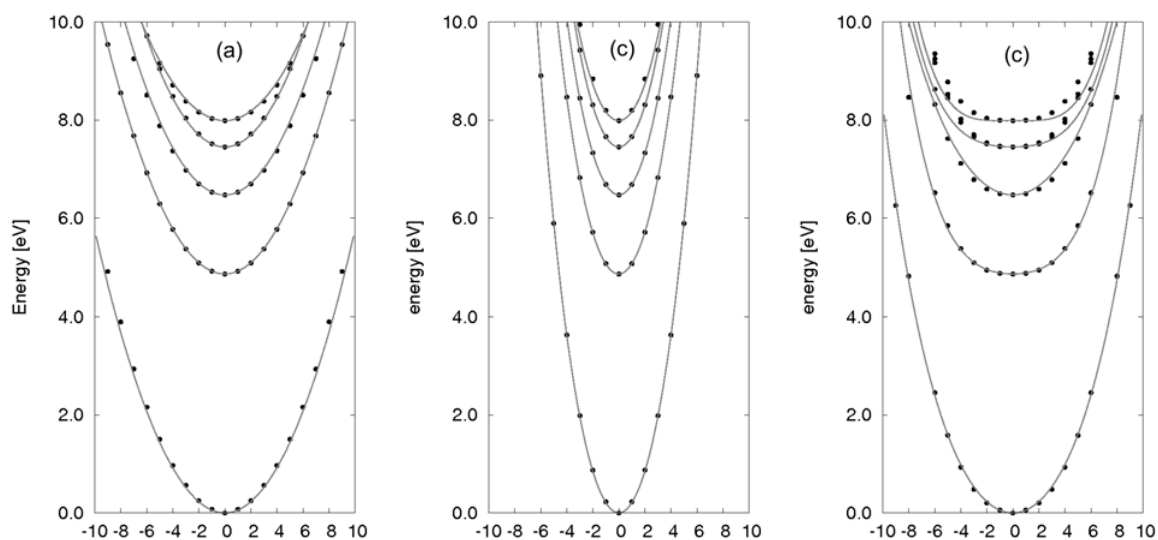


Fig. 4.5: Cuts through the adiabatic potential energy surfaces for benzene, including the ground states and 6 excited states. In order of energy at  $\mathbf{Q}=0$  these states are  $\tilde{X} A_{1g}$ ,  $\tilde{A} B_{2u}$ ,  $\tilde{B} B_{1u}$ ,  $\tilde{C} E_{1u}$ ,  $\tilde{D} E_{2g}$ . (a)  $\nu_{12}$  ( $1b_{1u}$ ) (b)  $\nu_{13}$  ( $2b_{1u}$ ) (c)  $\nu_{17a}$  ( $2e_{2u}$ ).

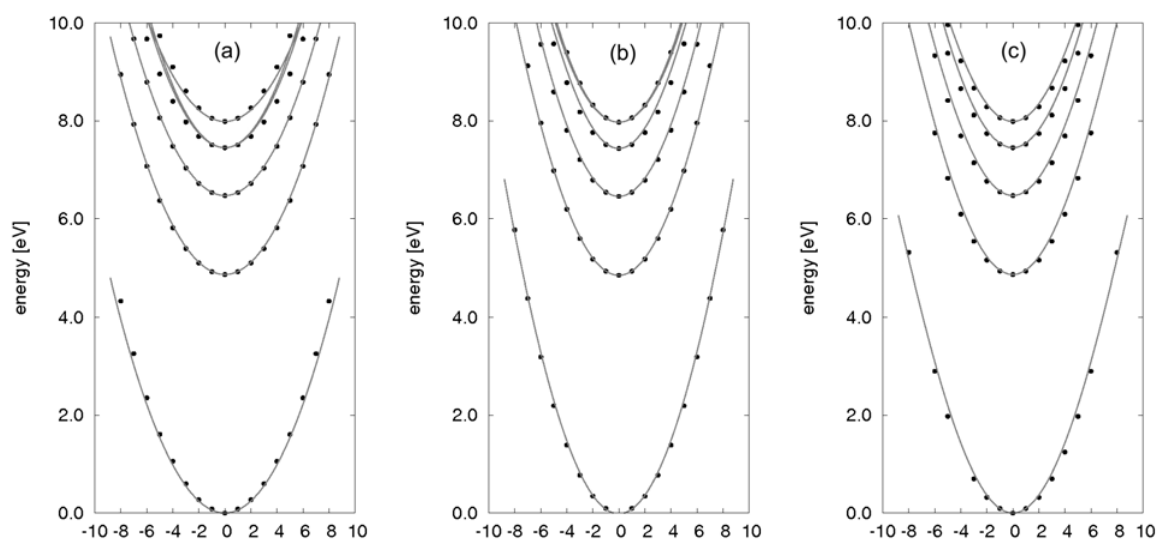


Fig. 4.6: Cuts through the adiabatic potential energy surfaces for benzene, including the ground states and 6 excited states. In order of energy at  $\mathbf{Q}=0$  these states are  $\tilde{X} A_{1g}$ ,  $\tilde{A} B_{2u}$ ,  $\tilde{B} B_{1u}$ ,  $\tilde{C} E_{1u}$ ,  $\tilde{D} E_{2g}$ . (a)  $\nu_{18a}$  ( $1e_{1u}$ ) (b)  $\nu_{19a}$  ( $2e_{1u}$ ) (c)  $\nu_{20a}$  ( $3e_{1u}$ ).

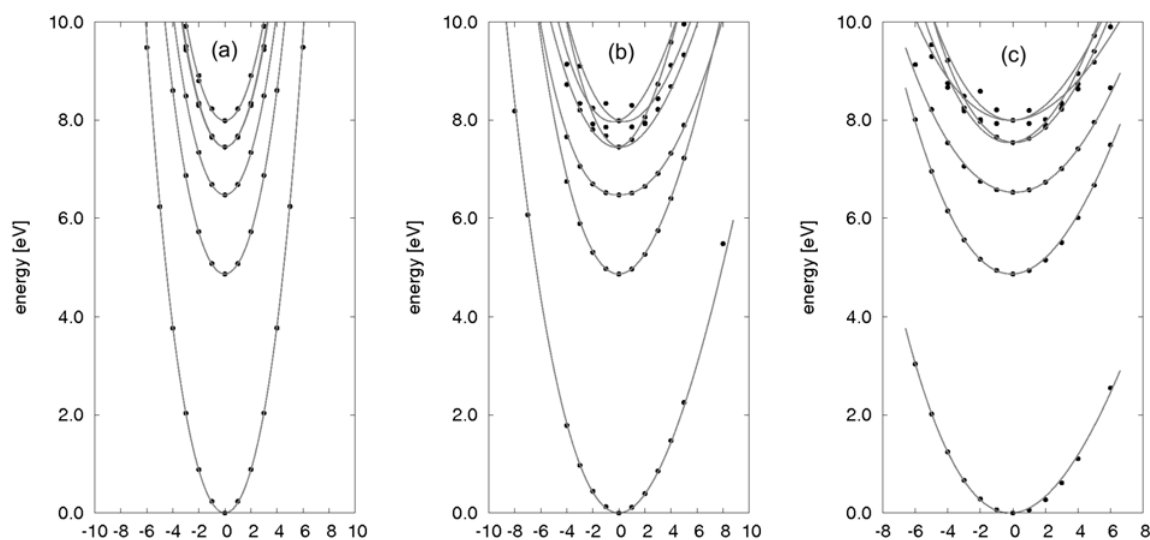


Fig. 4.7: Cuts through the adiabatic potential energy surfaces for benzene, including the ground states and 6 excited states. In order of energy at  $\mathbf{Q}=0$  these states are  $\tilde{X} A_{1g}$ ,  $\tilde{A} B_{2u}$ ,  $\tilde{B} B_{1u}$ ,  $\tilde{C} E_{1u}$ ,  $\tilde{D} E_{2g}$ . (a)  $\nu_{7a}$  ( $4e_{2g}$ ) (b)  $\nu_{8a}$  ( $3e_{2g}$ ) (c)  $\nu_{9a}$  ( $2e_{2g}$ ).

in the PES of the chair mode. Like the chair mode, the vibration is dominated by C-H bending and the flat shape of the surface can be attributed to the dominance of doubly excited determinants in the overall wavefunction.

Figures 4.5(a) and 4.5(b) shows the low and high frequency  $b_{1u}$  modes. These modes are responsible for the linear coupling between  $\tilde{X}$  and  $\tilde{B}$ . Figure 4.5(a) is the lower frequency mode, and one can see that motion along this mode is energetically more favourable than its higher frequency counterpart  $\nu_{13}$ , which has a very steep PES. Figure 4.5(c) shows the high frequency  $e_{2u}$  mode, which due to symmetry contains no linear coupling. There is no splitting between the degenerate states, but the each state has a slightly flat profile indicating the role of double excitations.

Figures 4.6(a), 4.6(b) and 4.6(c) shows the  $x$  component of the doubly degenerate  $e_{1u}$  modes. These modes are responsible for the coupling between  $\tilde{X}$  and  $\tilde{C}$ . This is critically important at the  $S_1/S_0$  CI. All three have very similar shaped surfaces, however it is possible to see that the lowest frequency mode has the most  $\tilde{X}/\tilde{C}$  coupling due to the flatter shape of the ground state.

Figures 4.7(a), 4.7(b) and 4.7(c) shows the  $x$  component of the doubly degenerate  $e_{2g}$  modes,  $\nu_7$ ,  $\nu_8$  and  $\nu_9$ .  $\nu_{7a}$  (figure 4.7(a)) is the highest frequency  $e_{2g}$  mode and hence the PES has a very steep gradient, there is also very little splitting due to JT coupling.  $\nu_{8a}$  and  $\nu_{9a}$  are both lower frequency and so that structure of the surface is easier to ascertain. In both cases there is significant splitting and the asymmetric behaviour, meaning that in both cases a Morse potential fit is required.

### 4.2.2 Combination Modes

As discussed in section 4.1.3 second order terms, and especially off-diagonal second order terms can be very important in the fine dynamic structure of the model. In order to obtain such parameters we are required to fit to *ab-initio* points calculated along combinations of normal modes. These combination modes can play a key role, and parameters obtained from them are essential for describing the ultrafast dynamics.

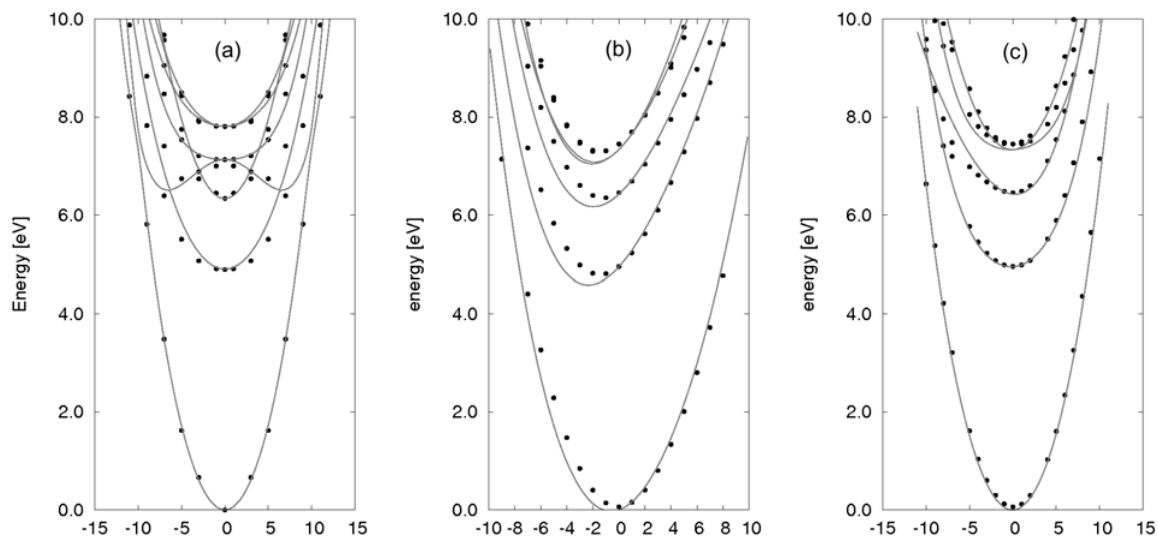


Fig. 4.8: Cuts through the adiabatic potential energy surfaces for benzene, including the ground states and 4 excited states. In order of energy at  $\mathbf{Q}=0$  these states are  $\tilde{X} A_{1g}$ ,  $\tilde{A} B_{2u}$ ,  $\tilde{B} B_{1u}$  and  $\tilde{C} E_{1u}$ . (a)  $\nu_{4+16a}$  (b)  $\nu_{1+16a}$  (c)  $\nu_{6a+16a}$ .

This is especially true for a highly symmetric molecule such as benzene.

Figures 4.8 and 4.9 show the PES of five such calculated combination modes. In each case only 4 excited states have been calculated because the higher order parameters needed to describe the dynamics were only required for the states most actively involved in the dynamics. This does not include  $\tilde{D} E_{2g}$  and therefore, to make the electronic structure calculations easier to converge, this state was removed from the calculations.

Figure 4.8(a) is the combination mode ( $\nu_{4+16}$ ) thought to be the photochemical pathway for the creation of prefulvene and the precursor for fulvene. Figure 4.8(a) shows the splitting of the  $\tilde{C}$  state in this mode and results in the  $x$  component crossing both the  $\tilde{A}$  and  $\tilde{B}$  state. This forms an avoided crossing between  $S_1/S_0$  at  $Q_4=Q_{16}=10$  from the FC point. This plot clearly shows that the  $S_1/S_0$  intersection will not be formed from crossing between  $\tilde{X}$  and  $\tilde{A}$ , instead from one component of the doubly degenerate  $\tilde{C}$  splitting and intersection  $\tilde{B}$  and  $\tilde{A}$  before reaching  $\tilde{X}$ .

Figures 4.8(b), 4.8(c), 4.9(a) and 4.9(b) show four other combination modes calculated. In each case it can be seen that there is significant asymmetric behaviour

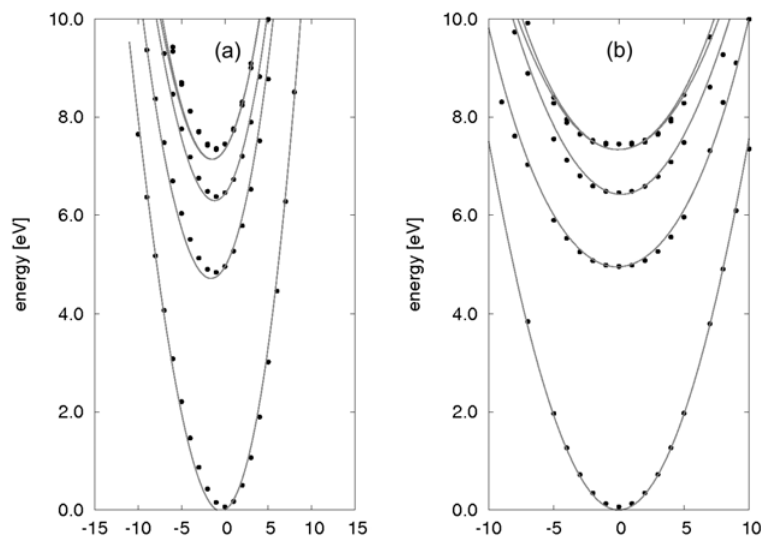


Fig. 4.9: Cuts through the adiabatic potential energy surfaces for benzene, including the ground states and 4 excited states. In order of energy at  $\mathbf{Q}=0$  these states are  $\tilde{X} A_{1g}$ ,  $\tilde{A} B_{2u}$ ,  $\tilde{B} B_{1u}$  and  $\tilde{C} E_{1u}$ . (a)  $\nu_{1+6a}$  (b)  $\nu_{4+6a}$

and therefore the  $\gamma$  parameters shown in table 4.8 and  $\mu$  parameters shown in 4.9 are required for a good fit. The fits in these plots, especially figures 4.8(b) and 4.8(c), although still close the *ab-initio* points are not as good as those shown along the normal modes. This is because they require higher than 3<sup>rd</sup> and 4<sup>th</sup> order terms to give an excellent fit. However to obtain these parameters is computationally expensive and since they are typically small and have little effect on the dynamics they have not been calculated in this study.

### 4.3 The Prefulvene Vector and $S_0/S_1$ Conical Intersection

The combination mode,  $\nu_{4+16}$ , shown in figure 4.8(a) is referred to above as the prefulvene mode because it leads to the prefulvene  $S_1/S_0$  CI, a precursor to the formation of fulvene and benzvalene. The adiabatic PES calculated shows that although the two surfaces ( $S_0$  and  $S_1$ ) become close, the crossing does not actually occur along this combination mode.

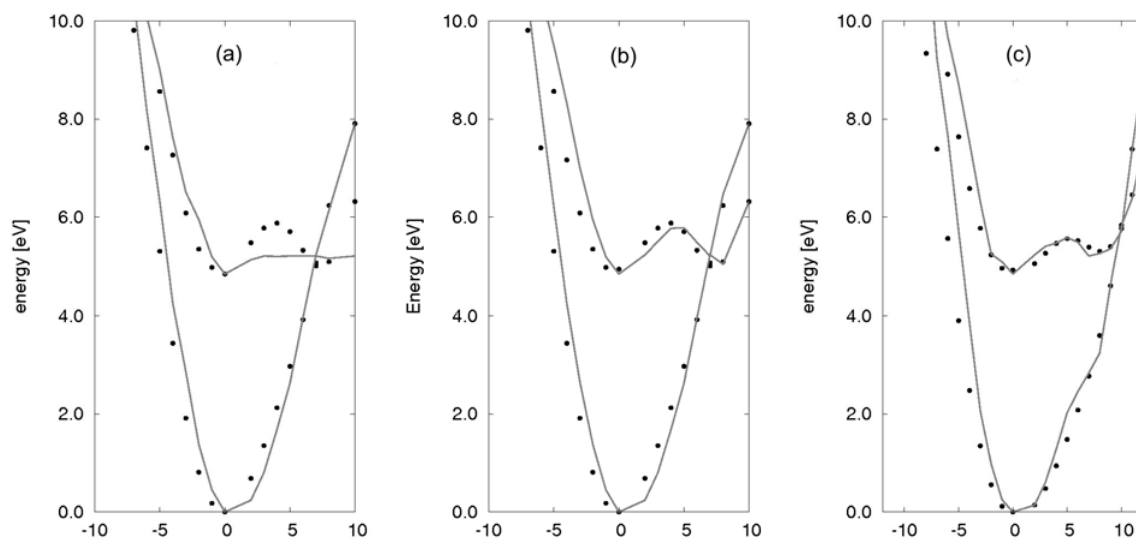


Fig. 4.10: Cuts along the vector for the prefulvene S<sub>1</sub>/S<sub>0</sub> minimum energy CI and the minimum barrier height leading to the S<sub>1</sub>/S<sub>0</sub> CI. (a) The prefulvene S<sub>1</sub>/S<sub>0</sub> minimum energy CI along  $Q_{CoIn}$ , using parameters up to second order. (b) Including the third order parameters. (c) Fit of the minimum barrier height along  $Q_{barrier}$  including third order parameters. The *ab-initio* points were calculated at PT2(6,6) level.

In order to locate the lowest point on the CI seam a CAS(6,6) CI minimisation was performed using Gaussian03 [111]. This point in the space of normal modes is termed  $Q_{CoIn}$ . The *ab-initio* points were then calculated using CASPT2(6,6) at equal steps along the vector from the FC point,  $Q_0$ , to  $Q_{CoIn}$ .

Figures 4.10(a) and 4.10(b) show the fitted *ab-initio* points along the reaction coordinate from the FC point to the minimum energy point on the S<sub>1</sub>/S<sub>0</sub> CI seam. Figure 4.10(a) shows the fit using parameters only up to 2<sup>nd</sup> order. Although this describes the intersection region relatively well, it does not give any barrier on the S<sub>1</sub> surface leading to the crossing. Lasorne *et al* [110] showed that 3<sup>rd</sup> order parameters can be important. These parameters take the form of the change in on-diagonal  $\gamma_{\alpha\alpha}$  parameters with respect to another mode. In this case the most important parameter is the change in the gradient of boat mode as a function of the breathing mode:  $W_{ii}^{(3)} = \ell_{(i)441} Q_4^2 Q_1$ .

In good agreement with data obtained by Lasorne *et al* [110], a value of -0.01eV is required to obtain the correct barrier along the prefulvene vector, this is shown in figure

4.10(b) which includes the third order parameters. However the barrier leading directly to the energy minima of the CI is approximately  $7000\text{cm}^{-1}$ , this is too high for the wavepacket to cross over. Figure 4.10(c) is a plot of the vector leading to the minimum barrier height, the most likely route of the wavepacket to the intersection region. The barrier height at the point is under  $4000\text{cm}^{-1}$  and is low enough for the wavepacket to cross to the intersection. Once these terms have been included the calculated RMSD for this cut is  $0.153\text{eV}$ .

The barrier seen along these vectors (figure 4.10) arises as a result of  $\tilde{C}E_{1u}$  state crossing  $\tilde{A}B_{2u}$ . This barrier can also be seen in figure 4.10(c), the prefulvene combination mode. The point in space of the minimum energy point on the  $S_1/S_0$  CI seam expressed as a function of the normal mode coordinates is:  $\nu_1=3.09$ ,  $\nu_2=2.14$ ,  $\nu_4=6.27$ ,  $\nu_5=1.21$ ,  $\nu_{6a}=-4.13$ ,  $\nu_{7a}=-1.38$ ,  $\nu_{9a}=2.52$ ,  $\nu_{10b}=-2.64$ ,  $\nu_{11}=2.36$ ,  $\nu_{12}=-3.28$ ,  $\nu_{13}=-2.10$ ,  $\nu_{16b}=8.15$ ,  $\nu_{18a}=3.45$ ,  $\nu_{20a}=-1.17$ . The actual intersection, although heavily dependent on the the two modes,  $\nu_4$  and  $\nu_{16b}$ , also relies on the totally symmetric mode, JT active modes  $\nu_6$  and  $\nu_9$ , the lowest frequency  $e_{1u}$  vibrational modes and both  $b_{1u}$  modes. The vector leading to the minimum barrier height is very similar to the minimum energy point on the  $S_1/S_0$  CI seam, with only slight differences in the magnitude of each mode. The most significant differences are as follows:  $\nu_1=1.62$ ,  $\nu_{6a}=-2.96$ ,  $\nu_4=5.14$ ,  $\nu_{16b}=7.20$ .

## 4.4 The Absorption Spectra

The quantum dynamics were performed with using the MCTDH quantum dynamics package [112]. This efficient algorithm which has been used on a wide variety of systems allows us to set up a 5 state and 9 mode model, a size which represents a significant challenge for many quantum dynamics methods [78]. Details of the calculations performed can be found in table 4.11.

The experimental spectra are shown in figure 4.11. Figures 4.12 and 4.13 show the calculated absorption spectra. Each of the spectra have been shifted to account for

Mode	$N_i, N_j$	$n_0, n_1, n_2, n_3, n_4$
$\nu_{16a}$ and $\nu_4$	60,60	5,6,4,5,5
$\nu_{6a,6b}$	30,30	5,6,4,5,5
$\nu_1$	60	5,6,4,5,5
$\nu_{14}$ $\nu_{15}$	30,30	5,6,4,5,5
$\nu_{9a}$	30	5,6,4,5,5
$\nu_{8a}$	30	5,6,4,5,5

Table 4.11: Computational details for the quantum dynamics simulations for the calculation of the absorption spectra.  $N_i, N_j$  are the no. of primitive Harmonic oscillator DVR basis functions used to describe each mode [78].  $n_i$  are the number of single-particle functions used for the wavepacket on each state. CPU time for the  $B_{2u}$  spectra was just over 2hrs, for the other two spectra ( $B_{1u}$  and  $E_{1u}$ ) the CPU was just under 30mins, as these calculations required fewer modes.

match the experimental spectra. The initial wavepacket for the  $E_{1u}$  spectra is prepared using a vertical excitation into  $\tilde{C}$ . For the  $B_{1u}$  and  $B_{2u}$  spectra, a dipole operator along the  $e_{2g}$  modes was used to excite the wavepacket into the appropriate state. For the  $B_{2u}$  spectra a damping time of 150fs was used, but for the  $B_{1u}$  and  $E_{1u}$  spectra a damping time of 20fs was used. In all three cases the calculations were propagated for 300fs.

The  ${}^1B_{2u} \leftarrow \tilde{X}$  spectra (figure 4.12(a)), which becomes an allowed transition by a first order Herzberg-Teller coupling along the lowest frequency  $e_{2g}$  mode shows excellent agreement with the experimentally obtained spectra. Since this is a forbidden transition the band origin (0-0) transition is not present, the apparent origin is actually the  $6_0^1$  transition, which involves the  $e_{2g}$  vibration to induce intensity. The breathing mode progression ( $6_0^1 1_0^n$ ), is well replicated in this model, in terms of both spacing and relative peak height. The most important hotbands have also been included in the calculation, these are the  $6_0^1 1_6^1$  and the  $6_1^2$  and have been weighted according to experimental spectra [91].

Figure 4.12(b) shows the calculated  $B_{1u}$  spectra, this, like the  $B_{2u}$  is a forbidden transition and is calculated using a first order Herzberg-Teller coupling along the lowest frequency  $e_{2g}$  mode  $\nu_6$ . The main progression in the spectra is a result of a progression with mode  $9_0^1$ . This band is fairly structureless and so the importance of other modes



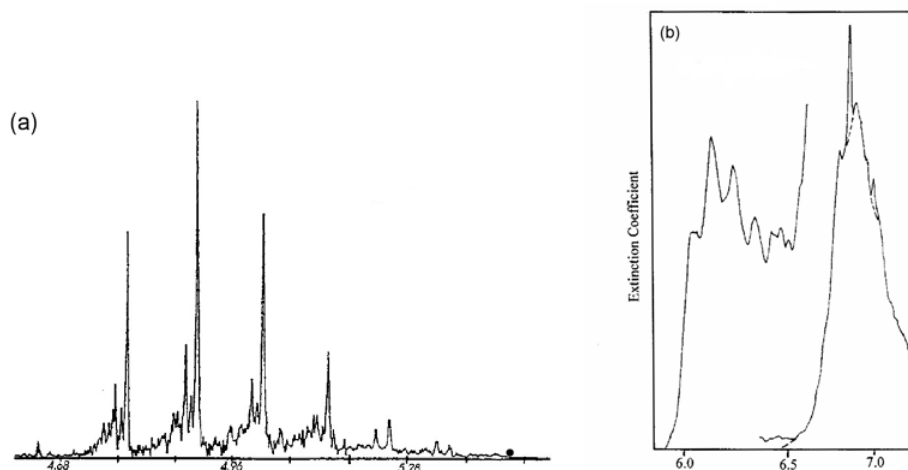


Fig. 4.11: The experimental spectra [90, 113]. (a) The  ${}^1B_{2u} \leftarrow \tilde{X}$  spectra. The four major peaks are a breathing mode progression coupled with  $6_0^1$  to make it allowed transition. One can also see  $6_0^1 6_1^1$  and  $6_1^2$  hotbands. (b) The  ${}^1E_{1u} \leftarrow \tilde{X}$  absorption spectra, with the  ${}^1B_{1u} \leftarrow \tilde{X}$  spectra inset. The  ${}^1E_{1u} \leftarrow \tilde{X}$  transition is an allowed transition and therefore produces a broad and structureless band.

are hidden by the weak and broad structure.

Figure 4.13 shows the  ${}^1E_{1u} \leftarrow \tilde{X}$  absorption spectra. There is again good agreement with experimental spectra. This allowed transition produces an broad, intense and structureless band. The tail structure (enlarged inset) is the  ${}^1B_{1u} \leftarrow \tilde{X}$  spectra arising from intensity borrowing of the allowed transition. This  $B_{1u}$  tail agrees well with the calculated spectra in figure 4.12(b), however it is a little too strong in comparison to the experimentally obtained  ${}^1E_{1u} \leftarrow \tilde{X}$  spectra suggesting the coupling between the two states is larger than actually exists.

## 4.5 Quantum Dynamics Calculations

### 4.5.1 Experimental Data

The dynamics of vibrationally and electronically excited benzene were studied experimentally using an ultrafast laser and the pump-probe scheme, pioneered by Zewail (see

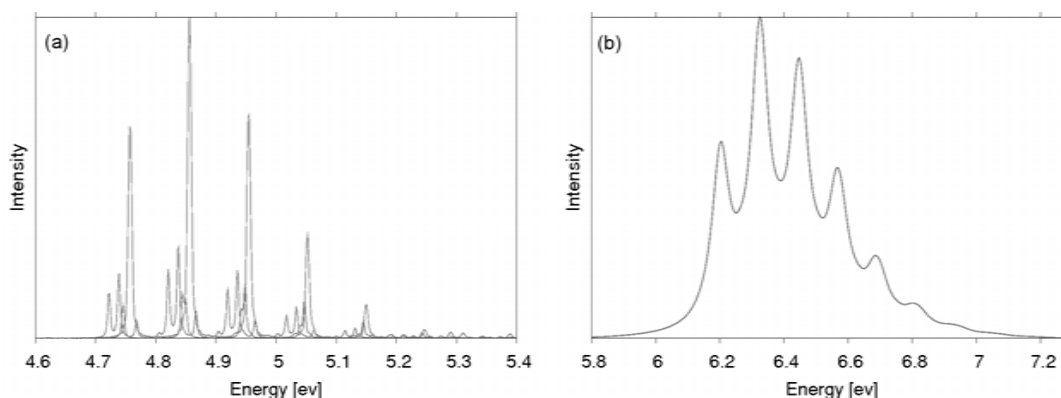


Fig. 4.12: (a) The  ${}^1B_{2u} \leftarrow \tilde{X}$  absorption spectra. This shows agreement with the experimental spectra. The spectra includes the main breathing mode progression and the  $6_0^1 16_1^1$  and  $6_1^2$  hotbands. (b) The  ${}^1B_{1u} \leftarrow \tilde{X}$  absorption spectra. Main progression in the spectra is a breathing mode progression with mode  $9_0^1$

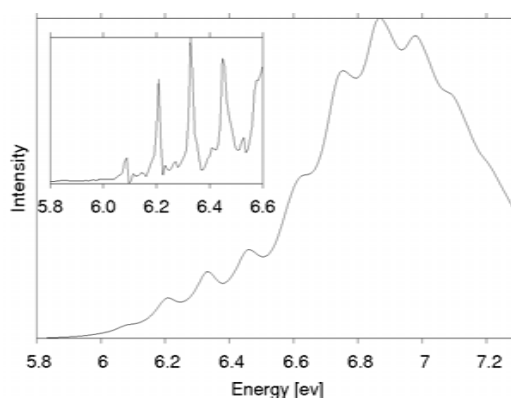


Fig. 4.13: The  ${}^1E_{1u} \leftarrow \tilde{X}$  absorption spectra. This allowed transition produces an broad, intense and structureless band. The tail structure (enlarged inset) is the  ${}^1B_{1u} \leftarrow \tilde{X}$  spectra arising from intensity borrowing of the allowed transition as a result of the vibronic coupling which exists between the two states.

introduction). The experimental apparatus consisted of a femtosecond laser system, molecular beam and velocity map imaging spectrometer. The commercial femtosecond laser system consisted of an ultrafast oscillator and amplifier producing a 1kHz train of 2.5mJ pulses of 35fs duration and a central wavelength of 795nm [19]. Results obtained by the Fielding group (University College London) are shown in figures 4.14, 4.15 and 4.16.

A pump pulse, centred at 243nm, excited the ground state wavepacket into  $S_1$  at  $3070\text{cm}^{-1}$ , just above the onset of the channel 3 region. The initial wavepacket on the ground state was prepared in two ways, (1) vibrationally excited ( $v=1$ ) along  $\nu_{16}$ , this is done by a thermal excitation. This from now on is termed the hot wavepacket. (2) Vibrational ground state of  $S_0$ , achieved by cooling using a supersonic molecular beam. From now on this is referred to as the cold wavepacket. Following the pump pulse, a probe pulse using wavelengths between 235-260nm was used to ionise the wavepacket, the photoelectrons emitted were then detected.

Figure 4.14a shows the intensity of the photoelectron yield as a function of the temporal delay in the probe pulse following excitation of the hot wavepacket into  $S_1$  and ionisation by probe pulses of 235nm (blue) and 254nm (red). Both decay curves show two distinct timescales, an initial fast decay which occurs for the first 500fs, this is followed by a slower decay. Figure 4.14b shows a plot of the ratio between the fast and slow decay as a function of the probe wavelength. A clear step is visible at 250nm, this is a clear indication of a photochemical channel that can only be ionised by a probe pulse of wavelength below 250nm. From these two plots we can conclude that following excitation of the hot wavepacket into  $S_1$  about 50% of the wavepacket propagates away from the FC point, approximately 30% through a photochemical channel which is not accessible to any probe wavelength and 20% which can be ionised by a probe wavelength under 250nm.

Further information can be obtained from the kinetic energies of the expelled photo-

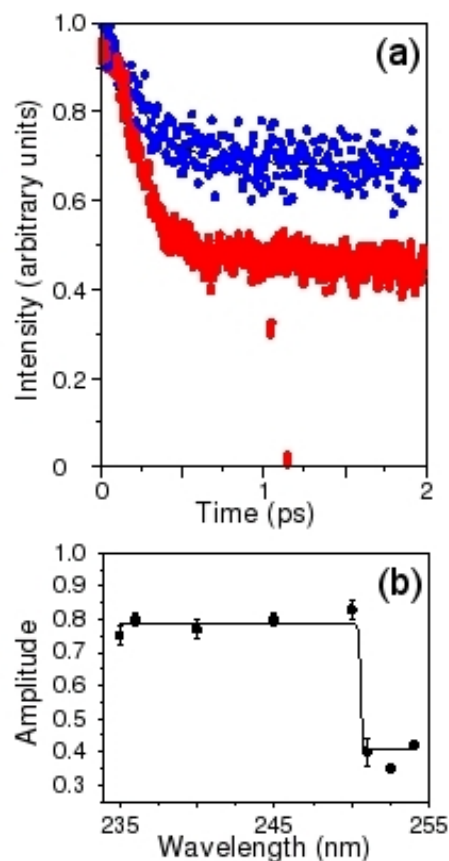


Fig. 4.14: (a) Experimental decay curves, detecting the photoelectron yield as a function of probe delay of hot wavepacket following excitation into  $S_1$ . The pump pulse was 243nm and the probe pulse 235nm (blue) and 254nm (red). (b) The ratio of the amplitude of the slow component to the amplitude of the fast component is plotted as a function of the probe wavelength. The step at 250nm is a signature of a new ionisation pathway opening. Figure reproduced with the permission of Prof. H. Fielding, UCL, London. [19].

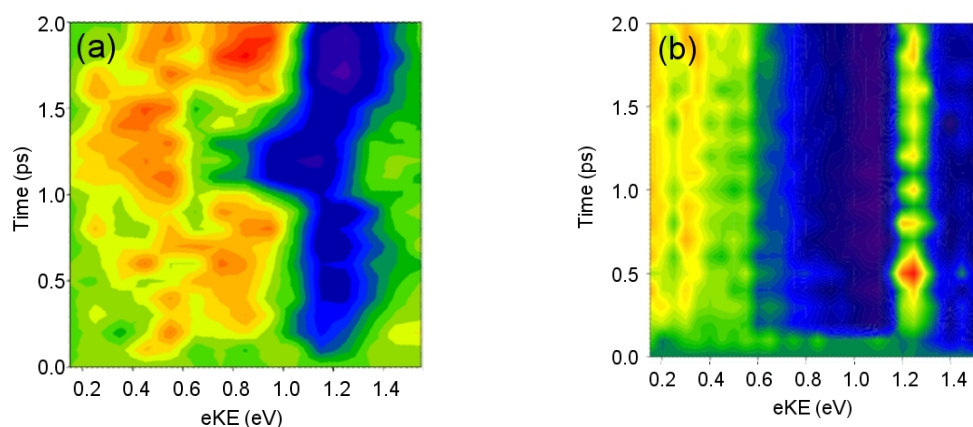


Fig. 4.15: Intensity of kinetic energies of the expelled photoelectrons as a function of pump-probe delay, the exponential decay has been removed. (a) Photoelectron kinetic energies following a Franck-Condon excitation of the hot wavepacket into  $S_1$  (b) Photoelectron kinetic energy following a Franck-Condon excitation of the cold wavepacket into  $S_1$ . Figure reproduced with the permission of Prof. H. Fielding, UCL, London. [19].

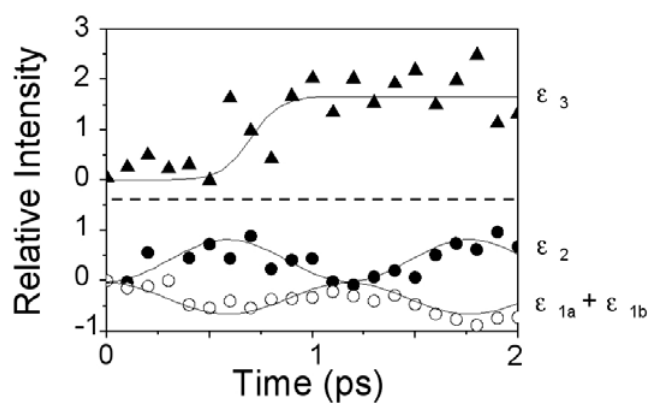


Fig. 4.16: Integrated intensities of photoelectrons as a function of pump-probe delay with the exponential decay removed. The open circles correspond to integration over the range  $\varepsilon_{1a}$  and  $\varepsilon_{1b}$ . The closed circles correspond to integration over the range  $\varepsilon_2$  and the filled triangles correspond to integration over the range  $\varepsilon_3$ .  $\varepsilon_{1a}=1.25-1.35\text{eV}$ ,  $\varepsilon_{1b}=1.13-1.23\text{eV}$ ,  $\varepsilon_2=0.75-0.95\text{eV}$  and  $\varepsilon_3=0.35-0.45\text{eV}$ . Figure reproduced with the permission of Prof. H. Fielding, UCL, London. [19].

Mode	$N_i, N_j$	$n_0, n_1, n_2, n_3, n_4$
$\nu_{16a}$ and $\nu_{9a}$	111,27	40,22,3,18,4
$\nu_{6a}$ and $\nu_4$	27,91	40,22,3,18,4
$\nu_1$ and $\nu_{6b}$	91,27	40,22,3,15,4
$\nu_{14}$ and $\nu_{15}$	21,21	40,22,3,13,3

Table 4.12: Computational details for the quantum dynamics simulations for the diabatic 5 state model.  $N_i, N_j$  are the number of primitive Harmonic oscillator DVR basis functions used to describe each mode [78].  $n_i$  are the number of single-particle functions used for the wavepacket on each state. This ensured convergence for 1000fs in the hot wavepacket case and for the full 2000fs in the cold wavepacket case. The CPU time was 780hrs.

electrons. Figure 4.15 shows the intensity of the kinetic energy for photoelectrons as a function of the pump-probe delay. When the hot wavepacket is excited to  $S_1$  (shown in figure 4.15a) the intensity of photoelectrons rapidly decays from the region around 1.2 eV, attributed to photoelectrons expelled from the FC region of  $S_1$ . It then oscillates between two energy regions at 0.4eV and 0.8eV. Figure 4.16 replots figure 4.15a including only the energy regions of interest. This figure shows a 1.2ps oscillation between  $\varepsilon_1$  (1.13-1.35eV) and  $\varepsilon_2$  (0.75-0.95eV). There is also another channel,  $\varepsilon_3$  (0.35-0.45eV) which is accessed when the population of  $\varepsilon_2$  is at the maximum amplitude.

Figure 4.15b shows when the cold wavepacket is excited into  $S_1$ . This shows no decay from the FC region, indicating the wavepacket does not have enough energy in the right modes to surmount the barrier which exists on the PES near to the FC point.

### 4.5.2 5 State Diabatic Model

Using the Vibronic Coupling Hamiltonian (calculated in section 4.1) we performed quantum dynamics simulations to replicate and explain the experimental data. All of the quantum dynamics calculations are performed using MCTDH (see section 3.5). The computational details for these simulations are shown in table 4.12.

The experimental pump-probe setup is able to follow the time dependence of the wavepacket by relating the photoelectron intensity to FC factors. This can be simulated theoretically by following the time evolution of the diabatic state populations of the

important electronic states.

The probe pulses, used experimentally, are able to ionise different portions of the wavepacket on the PES. The lower energy pulse of 254nm is only able to ionise wavepacket in the FC region of  $S_1$ , but the higher energy pulse (235nm) is able to ionise all of the wavepacket on the PES in the region of the interest which leads to the  $S_1/S_0$  CI. Therefore we can attribute the population of  $\tilde{A}$  as corresponding to photoelectron yield arising from the lower energy pulse and wavepacket population in states  $\tilde{A} + \tilde{C}$  corresponding to photoelectron intensity arising from the higher energy pulse. Due to energetic considerations it is not possible to ionise  $\tilde{X}$  at any probe wavelength used in the experimental study.

Figure 4.17 shows the diabatic state population of  $\tilde{A}$  (blue line) and  $\tilde{A} + \tilde{C}$  (red line) for the first 2000fs following a dipole excitation of the wavepacket into  $\tilde{A}$ , (a) represents the dynamics from the hot wavepacket and (b) the dynamics from the cold wavepacket.

When the hot wavepacket is propagated (shown in figure 4.17a) there is rapid decay from  $\tilde{A}$  within the first 50fs. This is because of the wavepacket crossing into  $\tilde{C}$  via the CI along  $\nu_4$  and  $\nu_{16a}$ . Between 50-100fs a decay in the  $\tilde{A} + \tilde{C}$  curve is observed as the wavepacket reaches the  $S_1/S_0$  CI and crosses into the ground state  $\tilde{X}$ . After 500fs 70% of the wavepacket is in  $\tilde{A} + \tilde{C}$ , of which 60% of this remains in  $\tilde{A}$ . The  $\tilde{A} + \tilde{C}$  population agrees exactly with the experimental decay curves, however the population of  $\tilde{A}$  found in the theoretical calculations is approximately 10% greater than indicated in the experimental data, suggesting that a photochemical channel which contains a significant portion of the wavepacket is missing in this simulation.

Figure 4.17b shows the diabatic state populations of the dynamics using the cold wavepacket. We do see some decay from the FC point into both  $\tilde{C}$  and  $\tilde{X}$ , but this is slower and significantly reduced from the hot wavepacket case. This is because the wavepacket is not excited along  $\nu_{16a}$  before excitation in  $S_1$  and therefore there is not

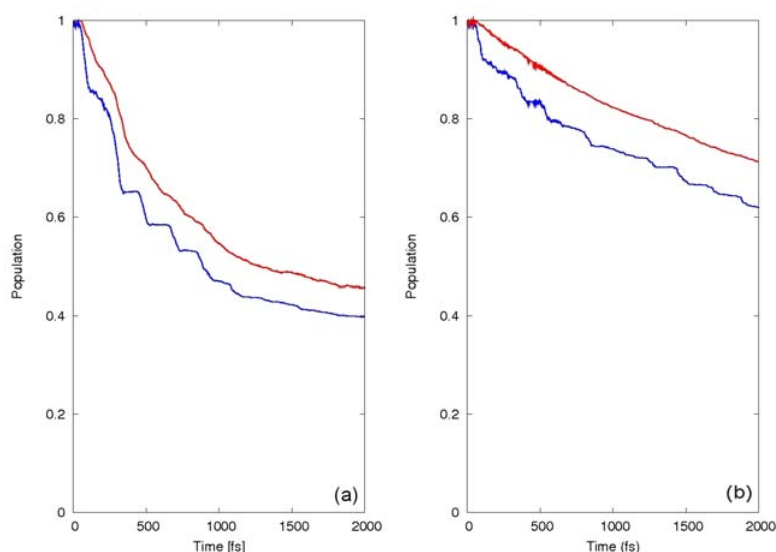


Fig. 4.17: (a) Diabatic state populations of  $\tilde{A}$  (blue) and  $\tilde{A}+\tilde{C}$  (red) following a excitation of the hot wavepacket into the Franck-Condon point on  $\tilde{A}$ . (b) Diabatic populations of  $\tilde{A}$  (red) and  $\tilde{A}+\tilde{C}$  (blue) following excitation of the cold packet into Franck-Condon point on  $\tilde{A}$ .

enough energy in the prefulvene mode to surmount the barrier on the PES leading to the  $S_1/S_0$  CI.

Comparison of the experimental results to the theoretical calculations reveal two differences. (1) Decay from  $\tilde{A}$  lasts longer then seen experimentally. In the hot wavepacket propagation the fast decay lasts for 1000fs, a lot longer then 500fs which is observed experimentally. (2) There is significant decay in the cold simulation, however in the experiment none is observed. Both of these can be explained by considering the reduced dimensionality of the model used. Due to the sheer size of the quantum basis required only 8 of the 30 modes of benzene are included in these calculations (table 4.12), therefore many of the modes which contribute second order on-diagonal coupling parameters (responsible for IVR) are left out. This means that the energy of the wavepacket is not distributed correctly throughout the model and energy remains concentrated in the modes included. These modes are all involved in the motion towards the  $S_1/S_0$  intersection and therefore it is unsurprising that decay is enhanced.



This also causes the decay in the cold wavepacket propagation. Instead of initial fast decay we find a constant slower decay. Following the dipole excitation into  $S_1$ , both  $\nu_1$  and  $\nu_{6a}$  contains a reasonable amount of vibrational energy, this would gradually dissipate throughout the rest of the 28 modes in the full model, however in the reduced space a larger amount will dissipate along  $\nu_{16a}$  and  $\nu_4$ , giving enough energy in these modes for slow decay to occur.

Further analysis of the dynamics can be obtained by plotting expectation values of the position and width of the wavepacket and the density of the wavepacket in normal mode space. Figures 4.18 and 4.19 show the expectation values and figures 4.20, 4.21, 4.22, 4.23, 4.24 and 4.25 show the densities of the wavepacket on states  $\tilde{X}$ ,  $\tilde{A}$  and  $\tilde{C}$  along modes  $\nu_1, \nu_4, \nu_{6a}$  and  $\nu_{16a}$ . These are only plotted for the hot wavepacket calculations. In the cold wavepacket calculation similar dynamics are obtained, but the amplitude of the oscillations are reduced, this is especially evident along the critical prefulvene combination mode and is why the decay is slower.

Figures 4.18c and e and 4.19c and e shows the importance of the motion along  $\nu_4$  and  $\nu_{16a}$  to the ultrafast dynamics. Initially small oscillations and the spreading of the wavepacket along both  $\nu_4$  and  $\nu_{16a}$  on  $\tilde{A}$  causes the wavepacket to reach the intersection with  $\tilde{C}$ .  $\tilde{C}$  has a steep gradient along these modes and crosses both  $\tilde{A}$  and  $\tilde{X}$ . This causes the wavepacket to follow the profile of the surface to large negative values along these modes towards the  $S_1/S_0$  CI. Upon inspection the width of the wavepacket on  $\tilde{A}$  along  $\nu_4$  and  $\nu_{16a}$  one can immediately see a 900fs oscillation. This is in good agreement with the experimental oscillation of 1.2ps. We therefore predict that the oscillation is the wavepacket either side of the barrier leading to the  $S_1/S_0$  CI. We see a reduced time period in this model because the coordinate spans two electronic states ( $\tilde{A}$  and  $\tilde{C}$ ). This is discussed further in section 4.5.3 when the reaction coordinate is treated as one adiabatic state.

The wavepacket on  $\tilde{A}$  along  $\nu_1$  (shown in figure 4.18d) shows large rapid oscillations

because the  $S_1$  minima along  $\nu_1$  is shifted, and therefore the wavepacket is not excited into the minima. Oscillations along  $\nu_1$  on  $\tilde{C}$  are much smaller. The motion along mode  $\nu_{6a}$  on  $\tilde{A}$  and  $\tilde{C}$  are small in both cases. Oscillation around the equilibrium position on these state occur on a faster timescale, but with much less motion.

The width of the wavepacket on each of the states of interest are shown in figure 4.19. Modes  $\nu_1$  and  $\nu_{6a}$  both show rapid and large oscillations on  $\tilde{A}$ , this is most evident in  $\nu_1$  whose width oscillates between 0.7-1.2au with a timescale period of approximately 25fs. The wavepacket is widest on  $\tilde{X}$  this is because the position of the  $S_1/S_0$  CI means that the wavepacket which crosses into the ground state is very vibrationally hot and will quickly spread around the surface. This is most evident along modes  $\nu_4$  and  $\nu_{16a}$  which are very wide, this is because these modes require the largest motion to reach the CI.

The wavepacket density plots are shown in figures 4.19-4.24. The density along  $\nu_4$  and  $\nu_{16a}$  exhibits the most significant motion. Figure 4.21 shows the wavepacket on  $\tilde{A}$ . It very quickly spreads along both coordinates, due to the flat profile of the PES on the diagonal. When the wavepacket oscillates to negative values along these two modes it reaches the intersection between  $\tilde{A}$  and  $\tilde{C}$ , resulting the transfer of population to  $\tilde{C}$ . This can be seen in the wavepacket on  $\tilde{C}$  in figure 4.22, density increases between 50-100fs, and propagates to large negative positions, around the intersection region. Upon reaching the intersection point, the density is able to cross onto  $\tilde{X}$  (shown in figure 4.20). Because of the location of the CI, the density crossing onto this state is very vibrationally hot and therefore the wavepacket spreads throughout these modes very quickly. This dispersed nature is why a large number of SPF are required on the ground state.

The density along  $\nu_1$  and  $\nu_{6a}$  shows a tight and well structured packet on all states. Oscillations due to the FC excitation are visible on  $\tilde{A}$  along  $\nu_1$ . On  $\tilde{X}$  the wavepacket is more spread out and the width increases throughout the propagation as the population

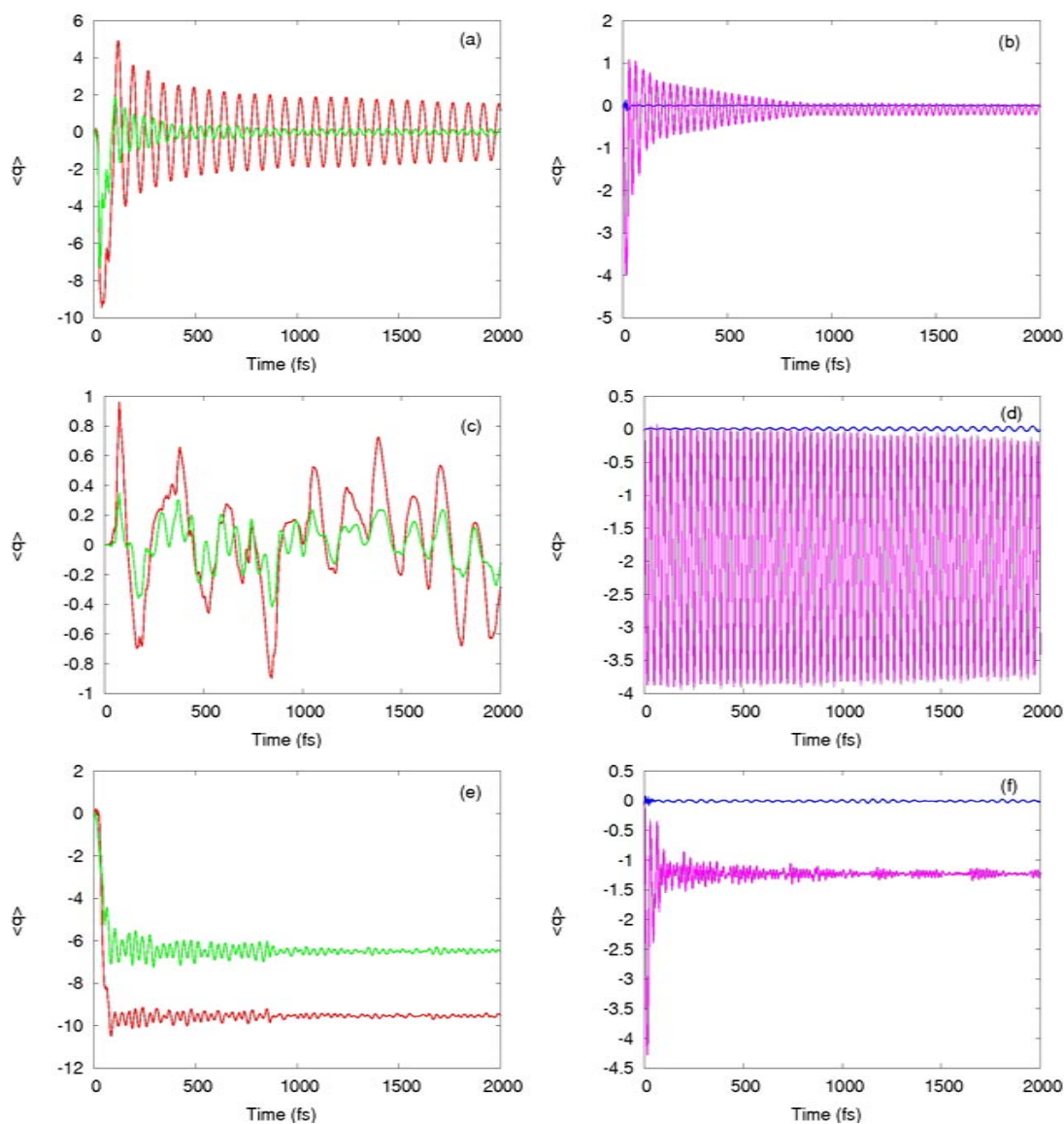


Fig. 4.18: Expectation values of the position of the hot wavepacket during propagation for the first 2000fs. (a)  $\langle q \rangle$  of  $\nu_4$  (green) and  $\nu_{16}$  (red) on  $S_0$ . (b)  $\langle q \rangle$  of  $\nu_1$  (purple) and  $\nu_6$  (blue) on  $S_0$ . (c)  $\langle q \rangle$  of  $\nu_4$  (green) and  $\nu_{16}$  (red) on  $S_1$ . (d)  $\langle q \rangle$  of  $\nu_1$  (purple) and  $\nu_6$  (blue) on  $S_1$ . (e)  $\langle q \rangle$  of  $\nu_4$  (green) and  $\nu_{16}$  (red) on  $S_3$ . (f)  $\langle q \rangle$  of  $\nu_1$  (purple) and  $\nu_6$  (blue) on  $S_3$ .

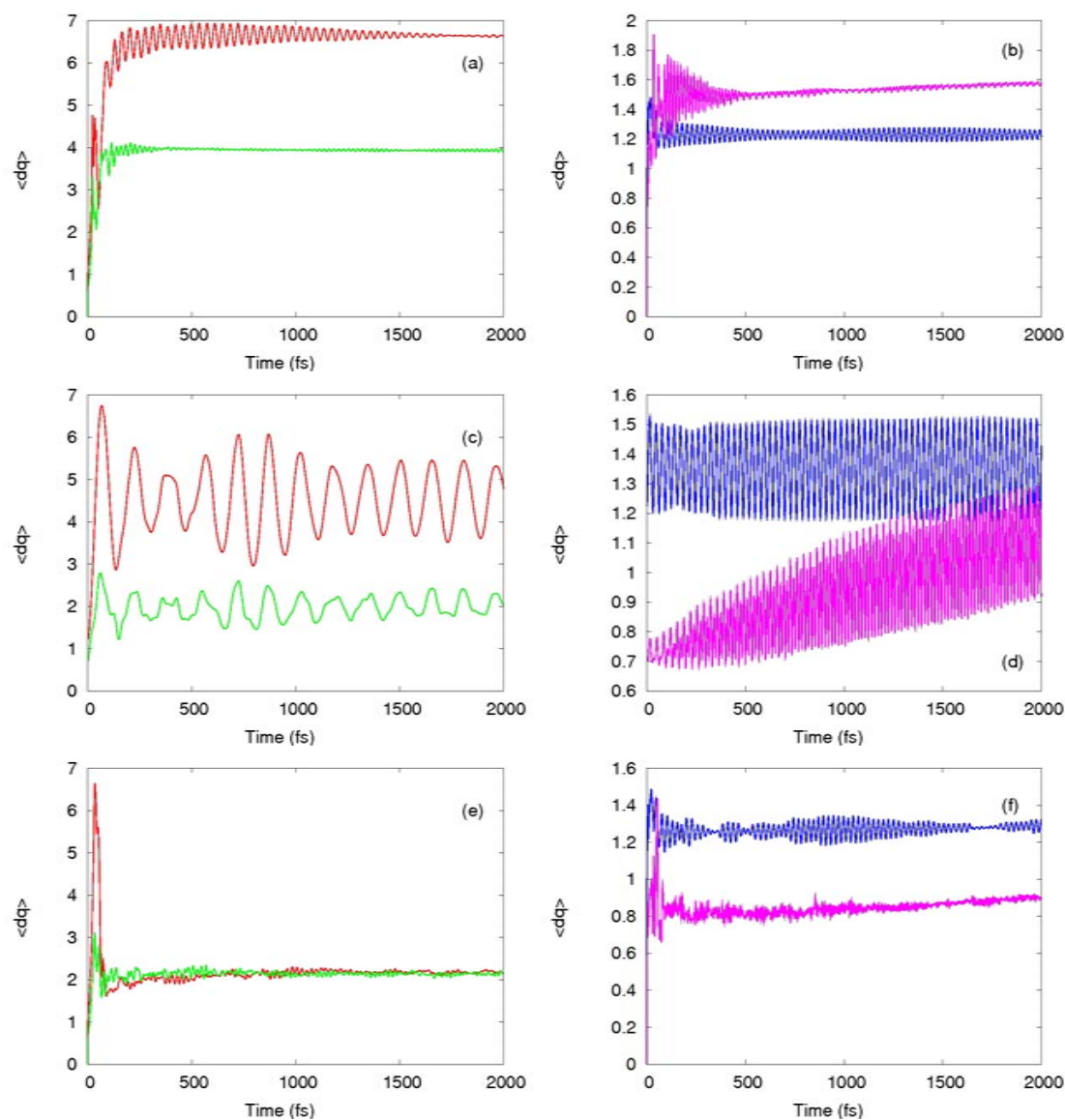


Fig. 4.19: Expectation values of the width of the hot wavepacket during propagation for the first 2000fs. (a)  $\langle dq \rangle$  of  $\nu_4$  (green) and  $\nu_{16}$  (red) on  $S_0$ . (b)  $\langle dq \rangle$  of  $\nu_1$  (purple) and  $\nu_6$  (blue) on  $S_0$ . (c)  $\langle dq \rangle$  of  $\nu_4$  (green) and  $\nu_{16}$  (red) on  $S_1$ . (d)  $\langle dq \rangle$  of  $\nu_1$  (purple) and  $\nu_6$  (blue) on  $S_1$ . (e)  $\langle dq \rangle$  of  $\nu_4$  (green) and  $\nu_{16}$  (red) on  $S_3$ . (f)  $\langle dq \rangle$  of  $\nu_1$  (purple) and  $\nu_6$  (blue) on  $S_3$ .

on this state increases. On  $\tilde{C}$  very little motion is observed.

### 4.5.3 2 State Adiabatic Model

The dynamics calculations performed using the 5 state Hamiltonian are able to accurately describe the early time dynamics in the excited states of benzene and especially to explain the importance of the  $\tilde{X}$ ,  $\tilde{A}$  and  $\tilde{C}$  interaction in the ultrafast dynamics. However such a calculation is very computationally expensive. Large displacements of the wavepacket along the normal modes means that each calculation requires a large number of DVR grid points and SPF to ensure convergence.

In order to make full convergence for 2000fs a more realistic objective a new Hamiltonian has been calculated in which the coordination space has been reduced to 2 electronic states and 6 vibrational DOF. This model uses most of the parameters from the large model, but some of the combination modes refitted with only two electronic states. In this model the barrier formed by the intersection between  $\tilde{A}$  and  $\tilde{C}$  in the previous model is now treated adiabatically, arising from third and fourth order intra-state couplings on  $S_1$ .

The vibrational modes included in this model are the boat and chair modes which are required to reach the  $S_1/S_0$  CI, the JT active mode ( $\nu_{6a}$ ), the breathing mode ( $\nu_1$ ) and  $\nu_{14,15}$  responsible for coupling between  $S_1/S_0$ . The computational details are shown in table 4.13. This ensures that  $\tilde{A}$  is converged for the full calculations. Due to the nature of the wavepacket on the  $\tilde{X}$  surface this state is only converged for the first 1000fs, however because the important dynamics occurs on  $\tilde{A}$  within the first 500fs this loss of convergence is not expected to be important.

As discussed in the previous section for the 5 state model, we perform two calculations (1) the hot wavepacket and (2) the cold wavepacket. Figure 4.26a shows the hot wavepacket dynamics and figure 4.26b shows the cold wavepacket dynamics. In both cases the green line represents the state population of  $\tilde{A}$  and the red line is  $\tilde{A}$  minus the population which has crossed the barrier on  $S_1$ , which in the 5 state model is the

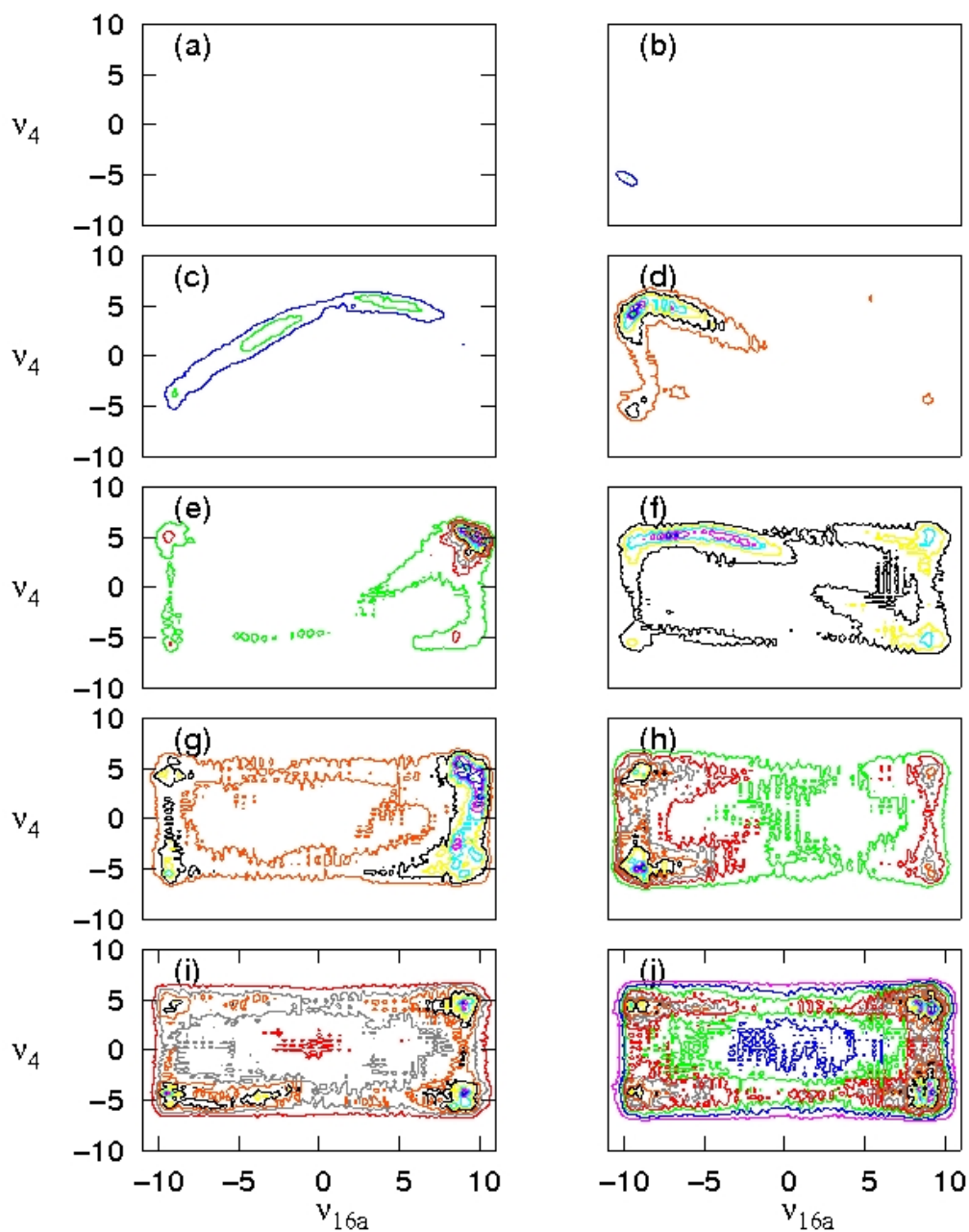


Fig. 4.20: The wavefunction density on  $\tilde{X}$  in benzene along  $\nu_4$  and  $\nu_{16a}$ . (a) 0fs (b) 50fs (c) 100fs (d) 150fs (e) 200fs (f) 250fs (g) 350fs (h) 450fs (i) 550fs (j) 1000fs.

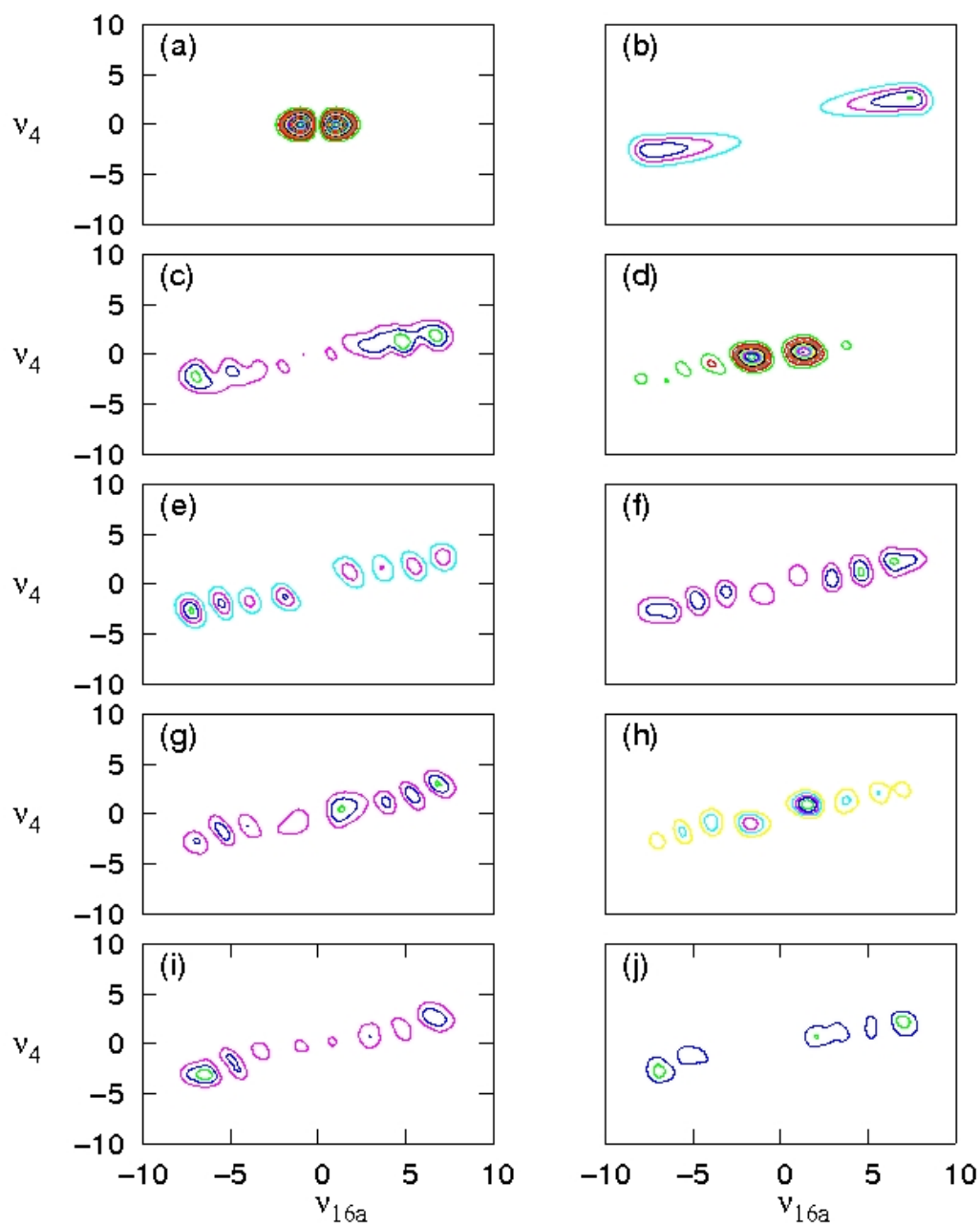


Fig. 4.21: The wavefunction density on  $\tilde{A}$  in benzene along  $\nu_4$  and  $\nu_{16a}$ . (a) 0fs (b) 50fs (c) 100fs (d) 150fs (e) 200fs (f) 250fs (g) 350fs (h) 450fs (i) 550fs (j) 1000fs.

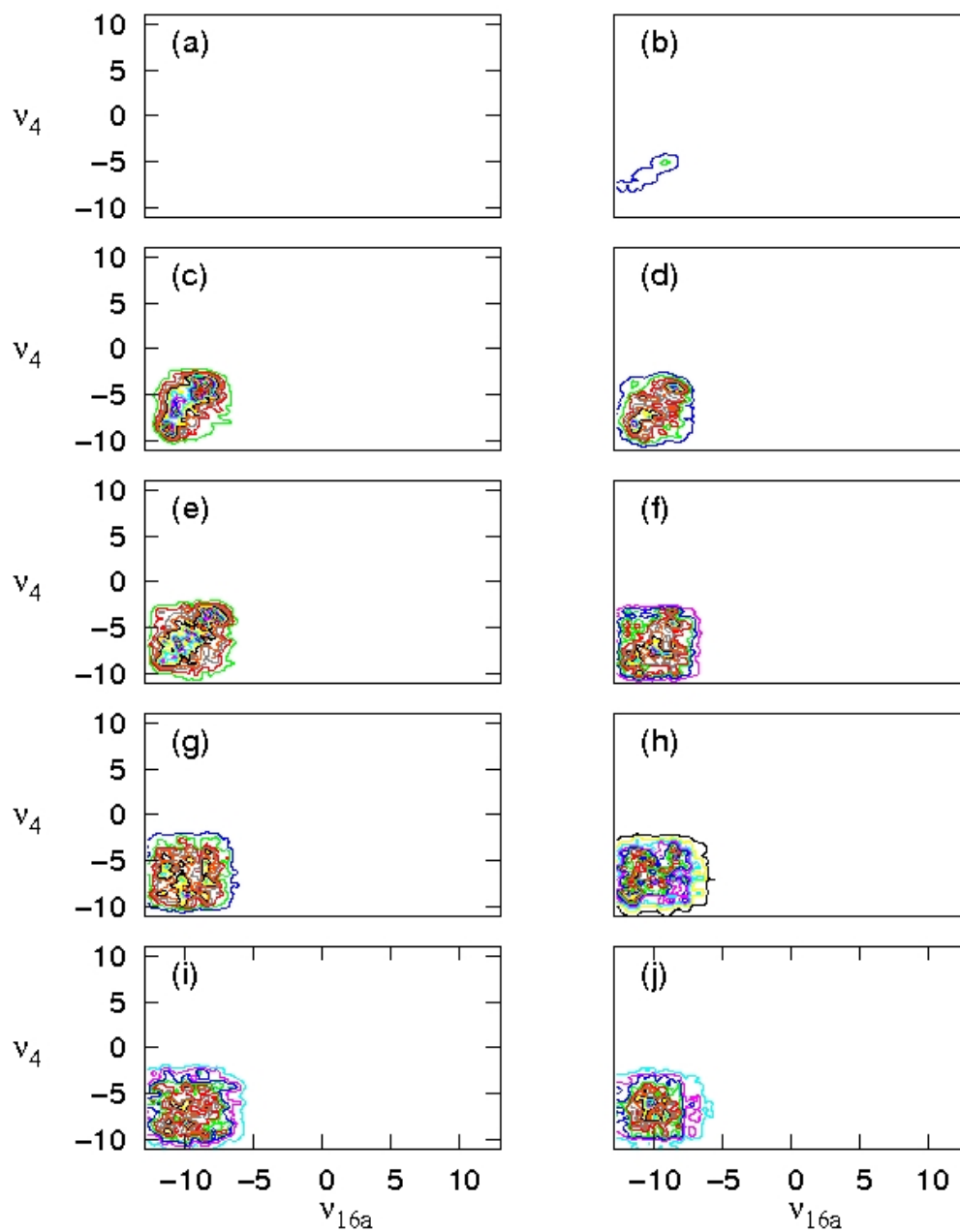


Fig. 4.22: The wavefunction density on  $\tilde{C}$  in benzene along  $\nu_4$  and  $\nu_{16a}$ . (a) 0fs (b) 50fs (c) 100fs (d) 150fs (e) 200fs (f) 250fs (g) 350fs (h) 450fs (i) 550fs (j) 1000fs.



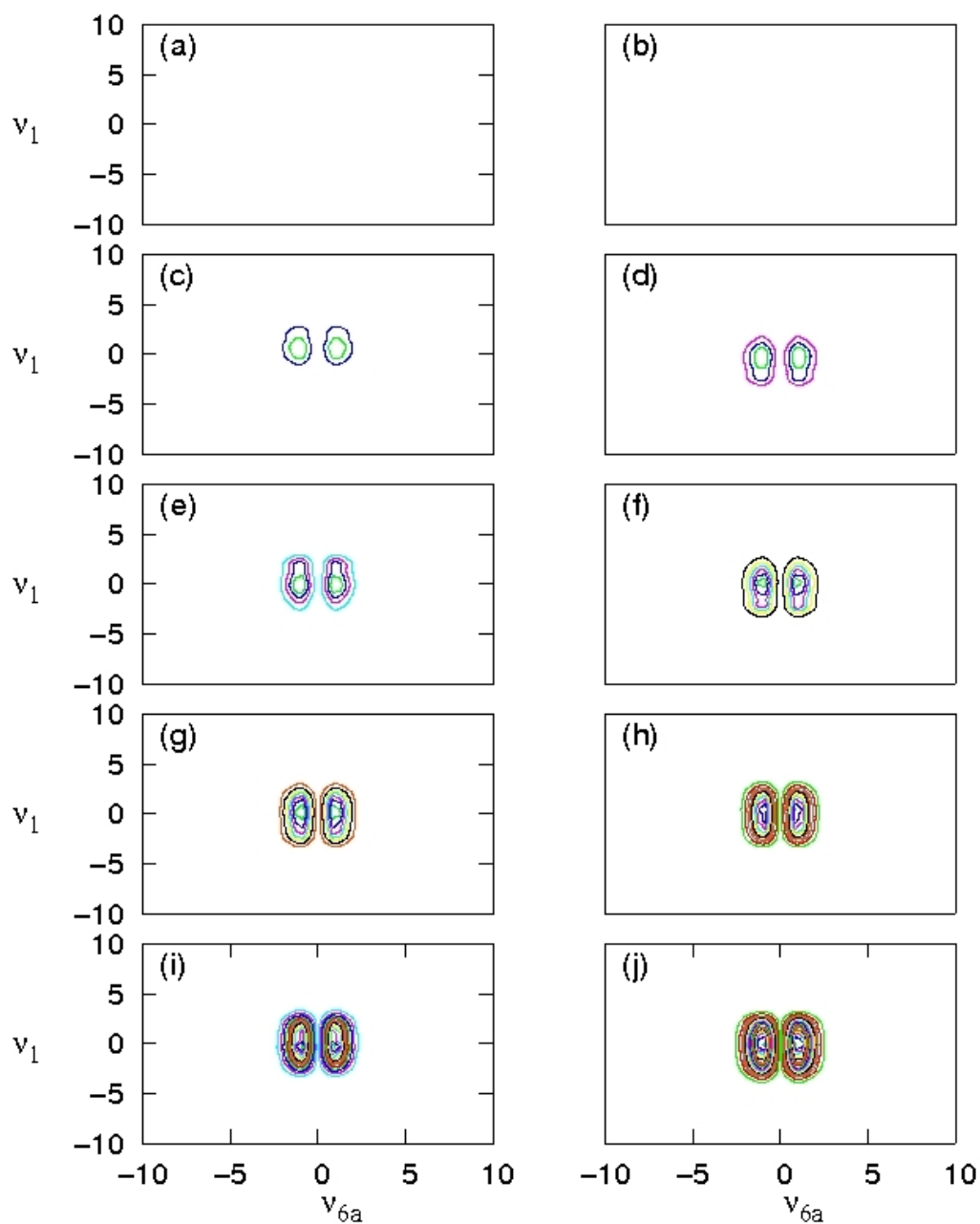


Fig. 4.23: The wavefunction density on  $\tilde{X}$  in benzene along  $\nu_1$  and  $\nu_{6a}$ . (a) 0fs (b) 50fs (c) 100fs (d) 150fs (e) 200fs (f) 250fs (g) 350fs (h) 450fs (i) 550fs (j) 1000fs.

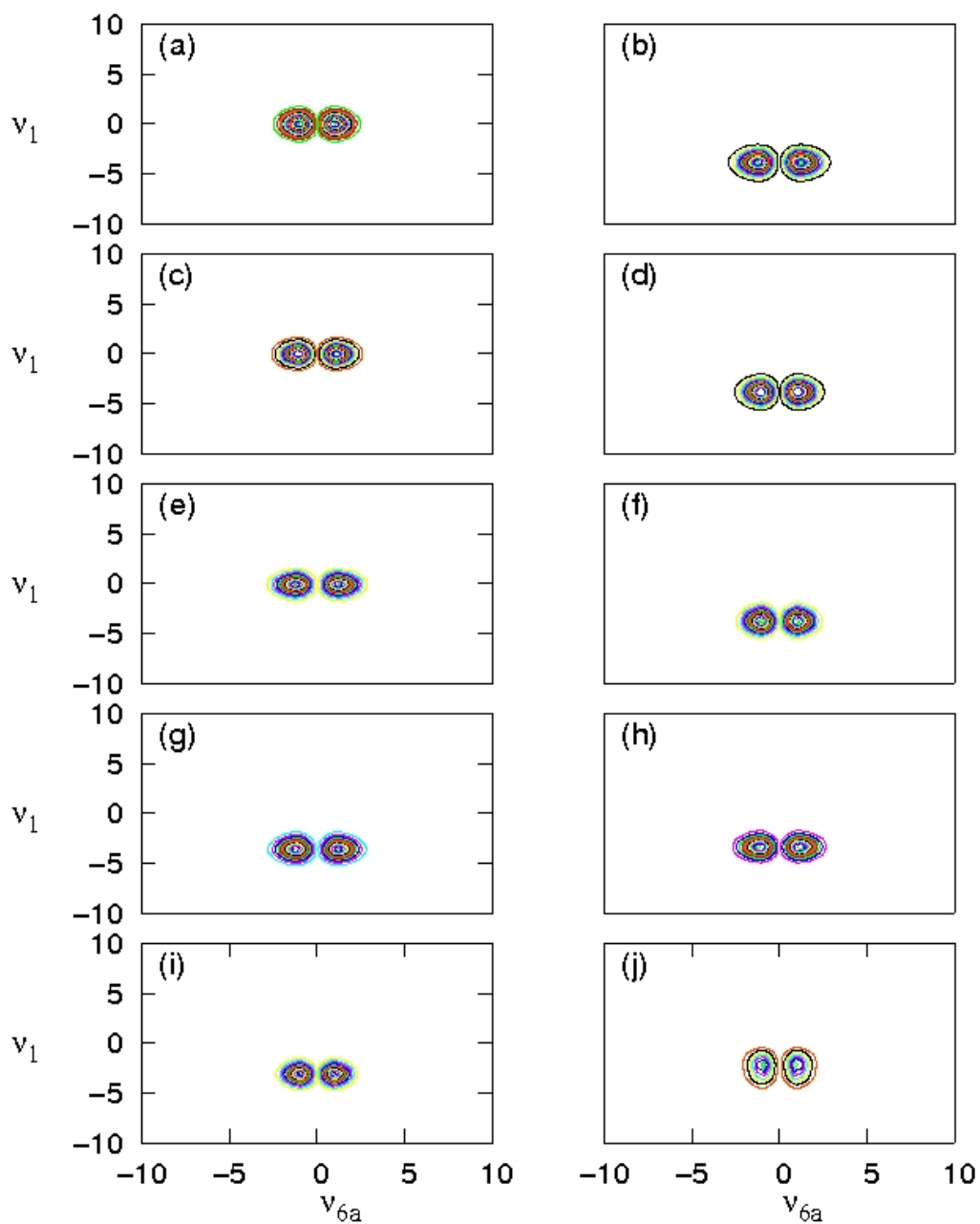


Fig. 4.24: The wavefunction density on  $\tilde{A}$  in benzene along  $\nu_1$  and  $\nu_{6a}$ . (a) 0fs (b) 50fs (c) 100fs (d) 150fs (e) 200fs (f) 250fs (g) 350fs (h) 450fs (i) 550fs (j) 1000fs.

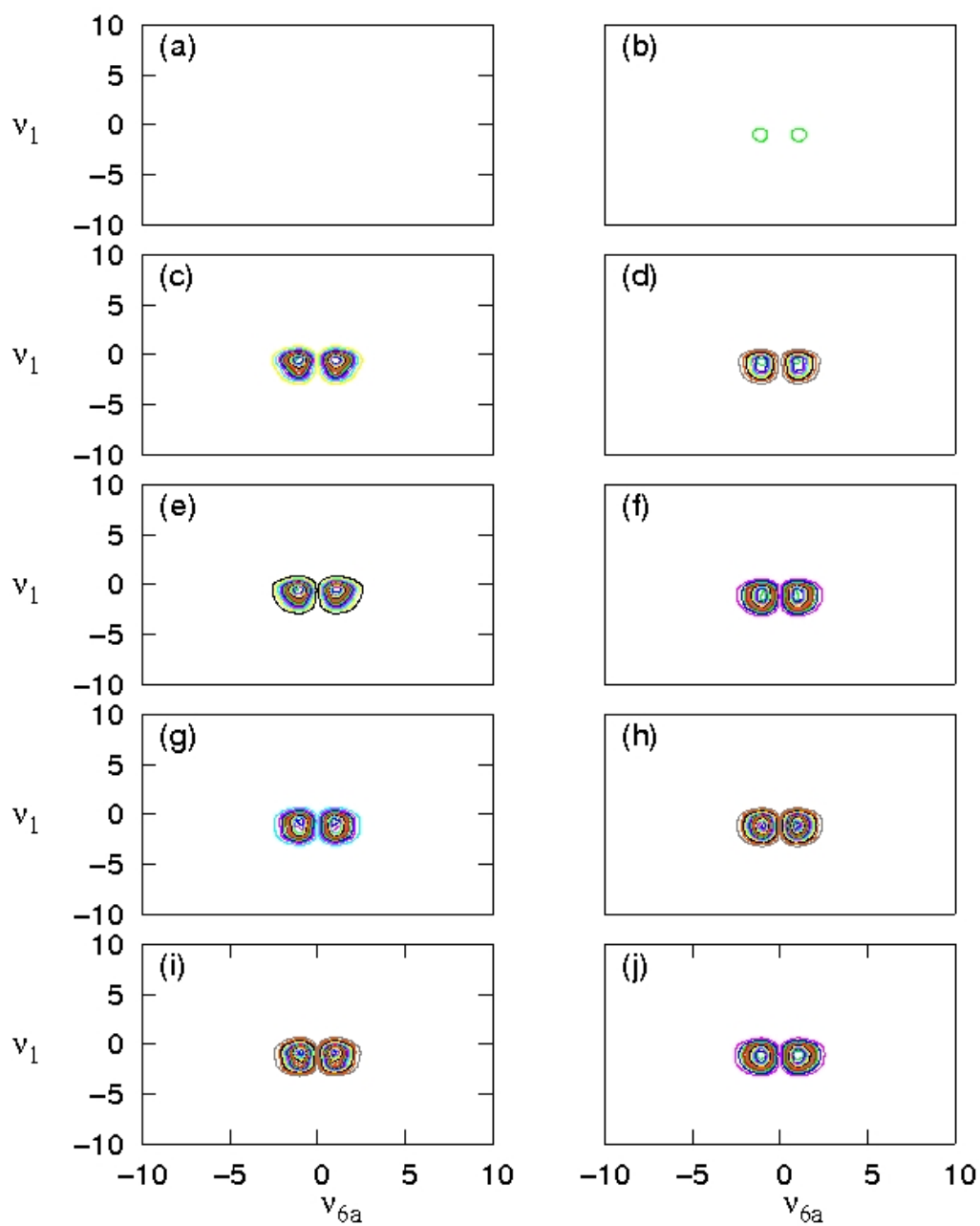


Fig. 4.25: The wavefunction density on  $\tilde{C}$  in benzene along  $\nu_1$  and  $\nu_{6a}$ . (a) 0fs (b) 50fs (c) 100fs (d) 150fs (e) 200fs (f) 250fs (g) 350fs (h) 450fs (i) 550fs (j) 1000fs.

Mode	$N_i$	$n_0, n_1$
$\nu_{16a}$	121	40,22
$\nu_4$	111	40,22
$\nu_{6a}$	27	40,22
$\nu_1$	60	40,22
$\nu_{14}$	91	40,22
$\nu_{15}$	15	40,22

Table 4.13: Computational details for the quantum dynamics simulations using the 2 state model Hamiltonian.  $N_i$  is the no. of primitive Harmonic oscillator DVR basis functions used to describe each mode [78].  $n_i$  are the number of single-particle functions used for the wavepacket on each state. This ensured full convergence on  $S_1$  for 2000fs and on  $S_0$  for 1000fs. The CPU time was 380hrs.

equivalent of populating  $\tilde{C}$ . This population is calculated as the expectation value of a step function operator defined at the peak barrier height in normal mode space.

The state populations for the hot wavepacket propagation (shown in figure 4.26a) shows the two decay timescales seen in the experimental data. In this model, unlike the 5 state model, this lasts for only 500fs, in excellent agreement with the experiment results. The slow decay is larger then seen in the experiments, but this is due to the reduced dimensionality of the model. After 500fs 75% of the wavepacket remains in  $S_1$ , while 65% of this remains in the FC region of  $\tilde{A}$  and has not crossed the barrier leading to the intersection. This is approximately 5% more then seen in the 5 state model. This represents good agreement with both the previous model and experimental data.

Figure 4.26b shows the state populations from the cold wavepacket propagation following a dipole excitation in  $\tilde{A}$ . One can immediately see there is about a 10% decay from  $\tilde{A}$  into  $\tilde{X}$ . This is significantly less then the 5 state model, and is therefore in better agreement with the experimental data.

Figure 4.27 shows the expectations value,  $\langle q \rangle$ , for the four most important normals modes ( $\nu_1$ ,  $\nu_4$ ,  $\nu_6$  and  $\nu_{16a}$ ) on  $\tilde{X}$  and  $\tilde{A}$  states. Figure 4.27c and d shows the  $\langle q \rangle$  on  $\tilde{A}$ . Along  $\nu_{16a}$  and  $\nu_4$  (figure 4.27c) it is immediately apparent there are two distinct oscillatory timescales, one faster relating to the vibrational period of the mode and a slower superimposed period with a wavelength of 1.2ps, like that seen in the experi-

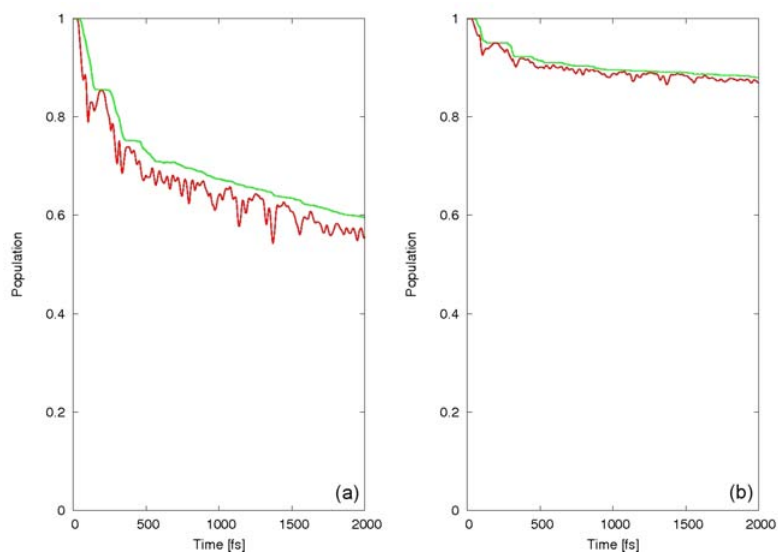


Fig. 4.26: (a) Diabatic state population of  $\tilde{A}$  (green) and  $\tilde{A}$  minus population on the CI side of the barrier (red) for the two state model Hamiltonian following excitation of the hot wavepacket into  $\tilde{A}$ . (b) Diabatic state population of  $\tilde{A}$  (green) and  $\tilde{A}$  minus population on the CI side of the barrier (red) following excitation of the cold wavepacket into  $\tilde{A}$ .

mental data. This oscillation is the wavepacket moving either side of the barrier on the  $S_1$ . By comparing this with the width of the wavepacket along the same modes (figure 4.28) it is clear that this 1.2ps oscillation is out of phase between the position and width. As the wavepacket oscillates along these modes its becomes spreads along the whole mode, increasing the width, but reducing the overall size of oscillations. As part of the wavepacket decays to the lower state, the density is no longer spread along the entire mode and therefore the wavepacket can begin to oscillate again, the reduction in the overall density on  $S_1$  means that the size of the oscillations are reduced.

For  $\langle q \rangle$  on the ground state we see a initial large displacement from equilibrium as the wavepacket comes through the CI onto the  $S_0$  surface, following this the wavepacket oscillates, around the equilibrium position. As the dynamics proceeds we see the energy in modes  $\nu_4$  and  $\nu_{16}$  spread to the breathing mode, this is due to coupling parameters on the ground state between these modes. The width of the wavepacket on  $S_0$  is a lot larger than seen on  $S_1$ . This is because, as discussed in the previous model the wavepacket on  $S_0$  is very vibrationally hot due to the position of the CI.

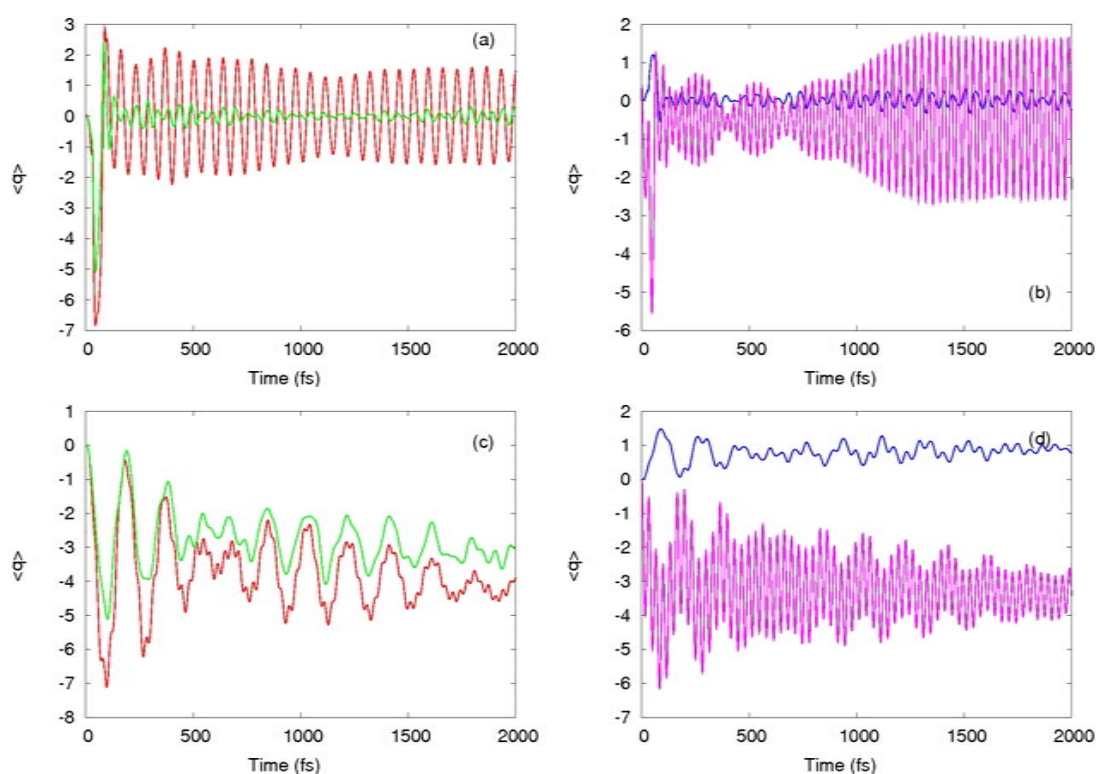


Fig. 4.27: Expectation values of the position of the hot wavepacket during propagations for first 2000fs. (a)  $\langle q \rangle$  of  $\nu_4$  (green) and  $\nu_{16}$  (red) on  $S_0$ . (b)  $\langle q \rangle$  of  $\nu_1$  (purple) and  $\nu_6$  (blue) on  $S_0$ . (c)  $\langle q \rangle$  of  $\nu_4$  (green) and  $\nu_{16}$  (red) on  $S_1$ . (d)  $\langle q \rangle$  of  $\nu_1$  (purple) and  $\nu_6$  (blue) on  $S_1$ .

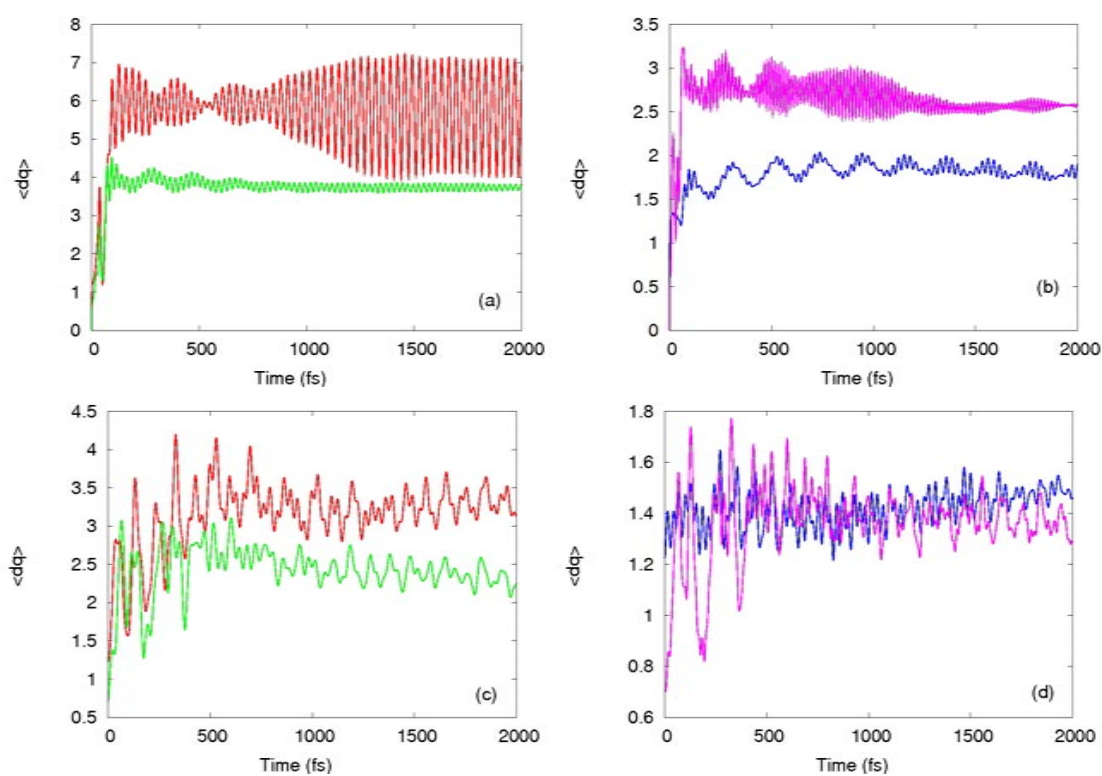


Fig. 4.28: Expectation values of the width of the hot wavepacket during propagations for first 2000fs. (a)  $\langle q \rangle$  of  $\nu_4$  (green) and  $\nu_{16}$  (red) on  $S_0$ . (b)  $\langle q \rangle$  of  $\nu_1$  (purple) and  $\nu_6$  (blue) on  $S_0$ . (c)  $\langle q \rangle$  of  $\nu_4$  (green) and  $\nu_{16}$  (red) on  $S_1$ . (d)  $\langle q \rangle$  of  $\nu_1$  (purple) and  $\nu_6$  (blue) on  $S_1$ .

Figures 4.29, 4.30, 4.31 and 4.32 show the motion of the wavepacket on both electronic states for the most important four DOF;  $\nu_{16a}$ ,  $\nu_{6a}$ ,  $\nu_4$  and  $\nu_1$ . Figures 4.29 and 4.30 confirms the observation that the wavepacket on  $S_0$  is very vibrationally hot, this results in the wavepacket very quickly spreading out on the  $S_0$  surface making the calculations much harder to converge. This is highlighted especially well in figure 4.29 in which the motion along  $\nu_4$  and  $\nu_{16a}$  is very rapid.

Figures 4.31 and 4.32 show the wavepacket motion on  $S_1$ . Figure 4.32 shows a simple oscillatory behaviour, of which neither modes  $\nu_1$  or  $\nu_{6a}$  show a huge amount of movement. Figure 4.31 shows the motion between  $\nu_{16a}$  and  $\nu_4$ . The oscillatory behaviour seen in the expectation value is seen again as the wavepacket oscillates along each coordinate. The flat nature of the surface along these modes allows the wavepacket to spread along the entire coordinate, this motion is the main vibration which leads to the CI.

## 4.6 Conclusion

The topology of the PES plays a crucial role in the dynamical behaviour of a system. This is particularly true if non-adiabatic effects are present when the highly coupled system that results can be sensitive to the accuracy of the PES obtained. As discussed the CASSCF method is unable to perform the dynamic correlation required to account for the double excitations associated with the  $\tilde{B}$  and  $\tilde{C}$  states in benzene. As a result the  $E_{2g}$  state lies below the  $E_{1u}$  state in the CASSCF model and is wrongly preferentially coupled to the  $B_{2u}$  state making the coupling between the  $E_{1u}$  and  $B_{2u}$  states small. The CASPT2 calculations corrects the order of the states, enabling a more accurate description of the inter-state coupling. This description has a significant effect on the dynamics and the accuracy of the model.

Benzene represents an ambitious target for full quantum dynamics calculations with seven coupled states and 30 vibrational modes, but the automatic fitting procedure



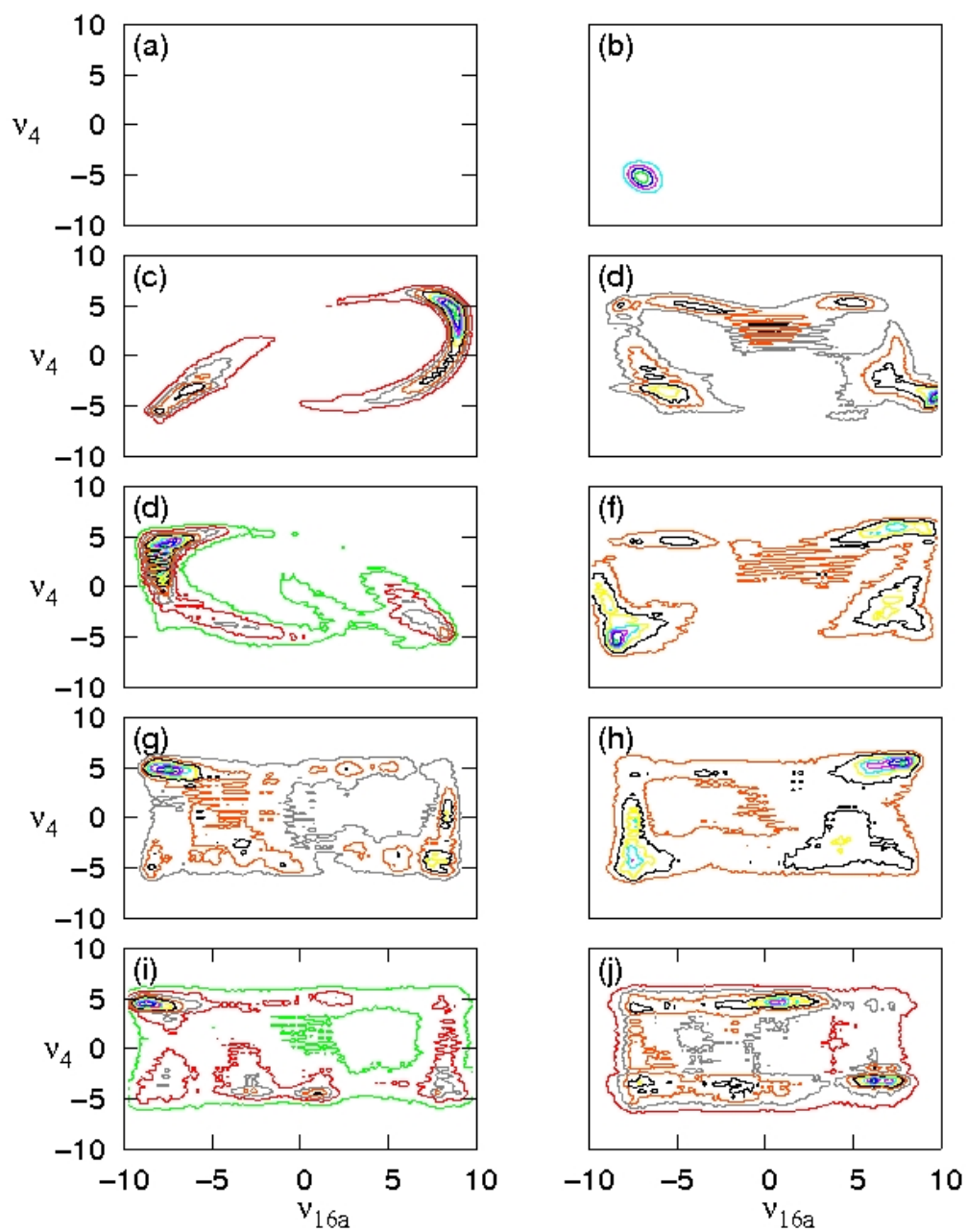


Fig. 4.29: The wavefunction density on  $S_0$  in benzene along  $\nu_4$  and  $\nu_{16a}$ . (a) 0fs (b) 50fs (c) 100fs (d) 150fs (e) 200fs (f) 250fs (g) 350fs (h) 450fs (i) 550fs (j) 1000fs.

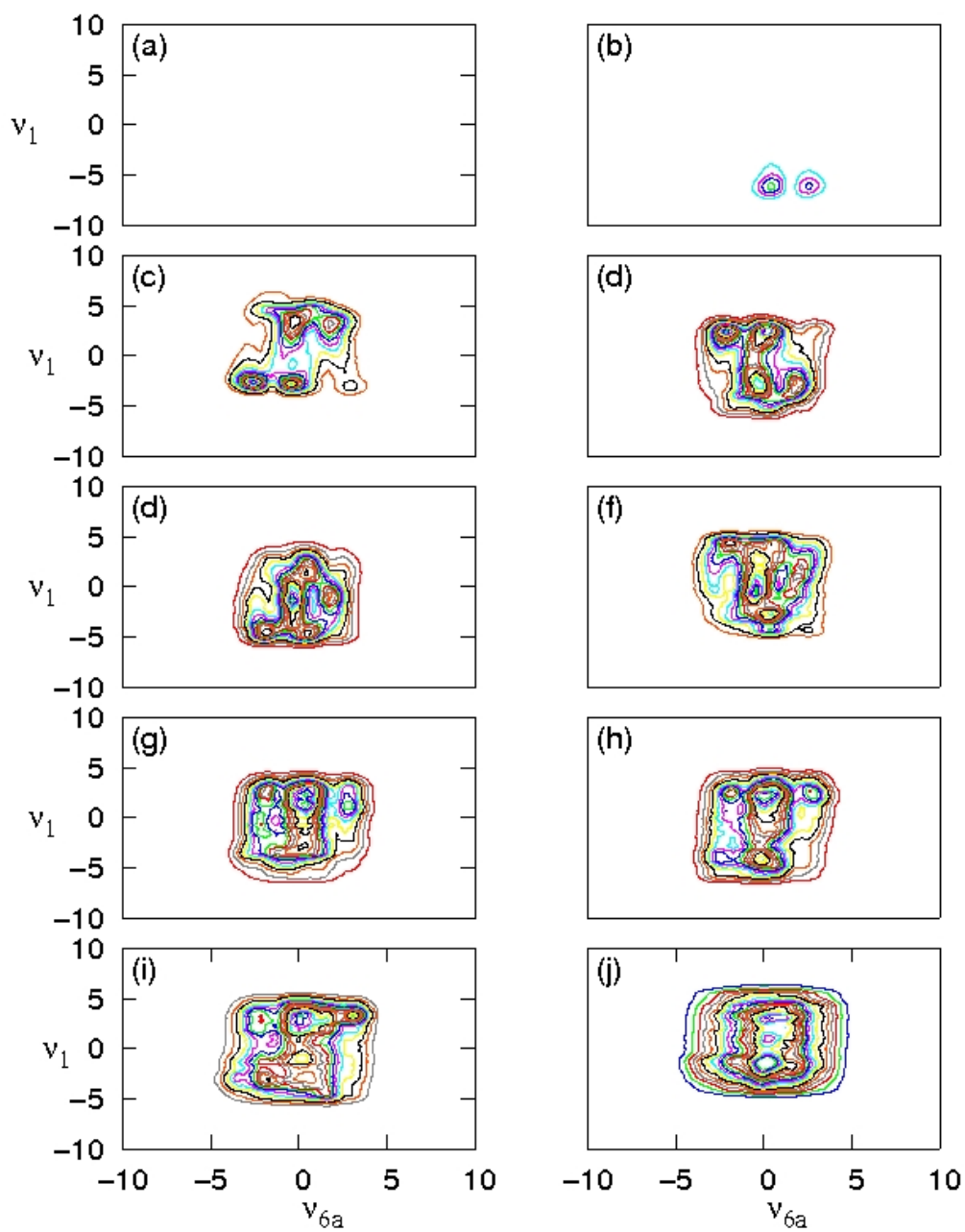


Fig. 4.30: The wavefunction density on  $S_0$  in benzene along  $\nu_1$  and  $\nu_{6a}$ . (a) 0fs (b) 50fs (c) 100fs (d) 150fs (e) 200fs (f) 250fs (g) 350fs (h) 450fs (i) 550fs (j) 1000fs.

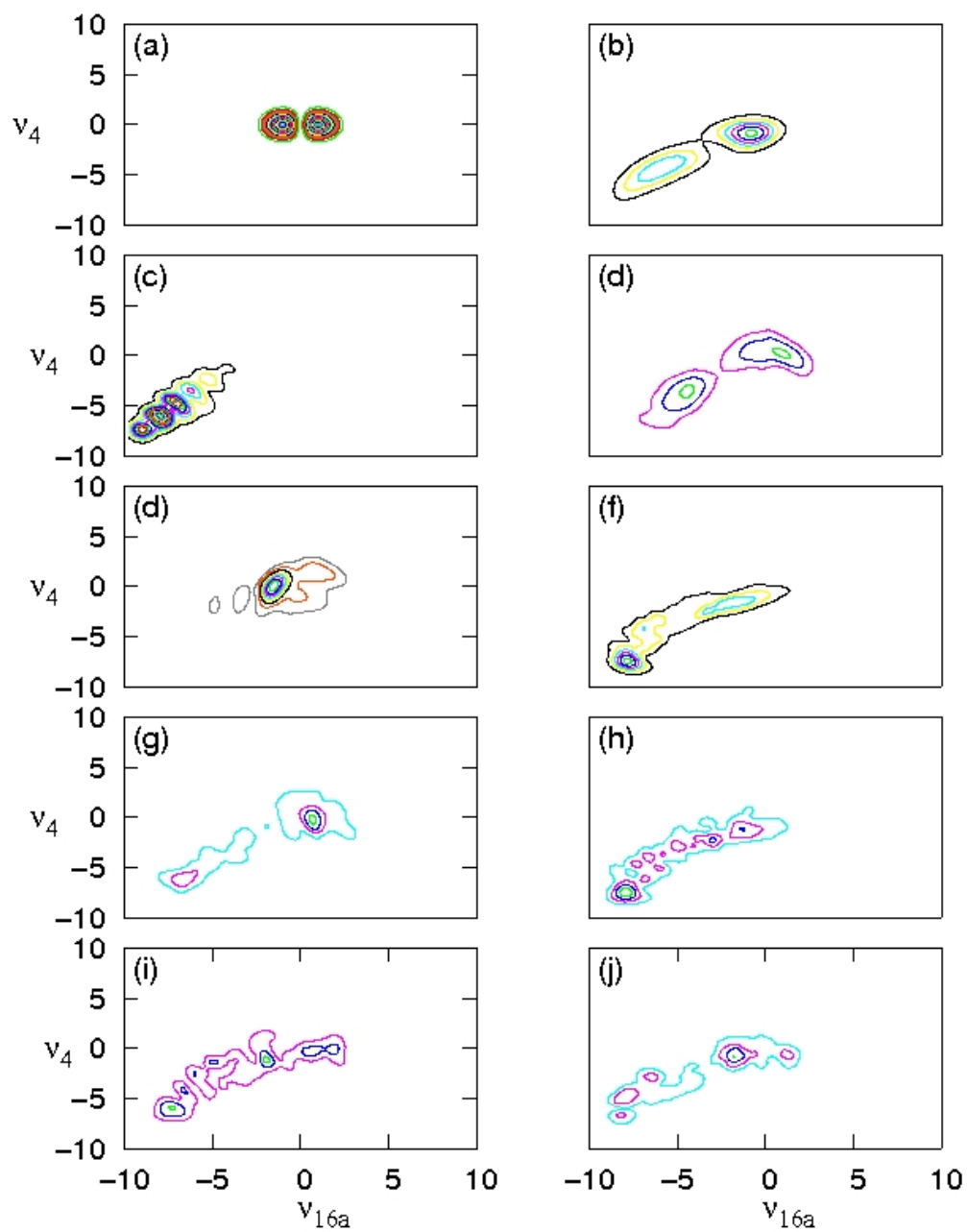


Fig. 4.31: The wavefunction density on  $S_1$  in benzene along  $\nu_4$  and  $\nu_{16a}$ . (a) 0fs (b) 50fs (c) 100fs (d) 150fs (e) 200fs (f) 250fs (g) 350fs (h) 450fs (i) 550fs (j) 1000fs.

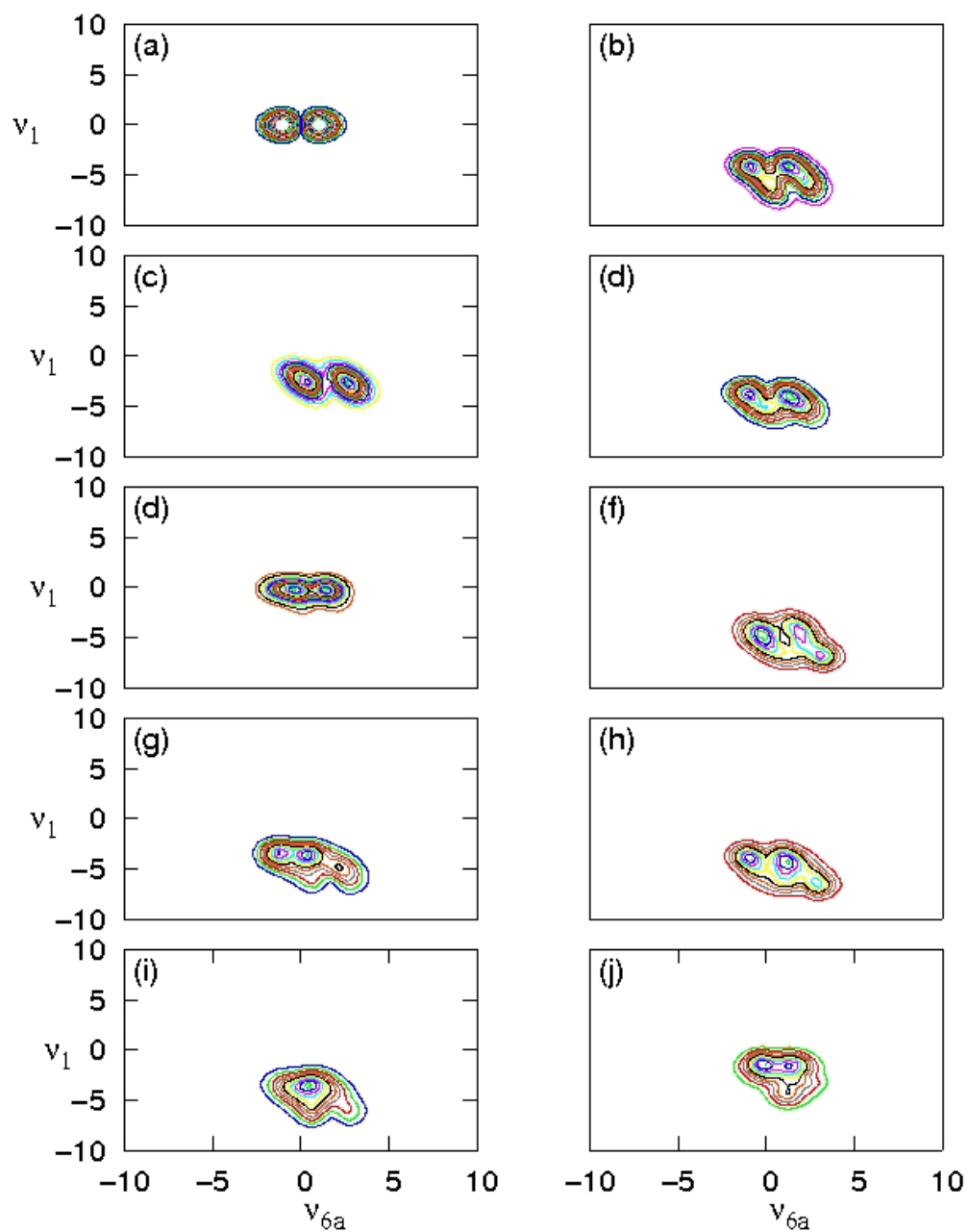


Fig. 4.32: The wavefunction density on  $S_1$  in benzene along  $\nu_1$  and  $\nu_{6a}$ . (a) 0fs (b) 50fs (c) 100fs (d) 150fs (e) 200fs (f) 250fs (g) 350fs (h) 450fs (i) 550fs (j) 1000fs.

used here is able to provide the necessary parameters. Due to the linear optimisation used there is unfortunately no guarantee that the parameters obtained are the best, and it is possible that a different set of parameters would obtain a similar fit. The procedure used takes an initial guess and first optimises the linear parameters before adding higher order terms. Despite this and the simplicity of the model, the surfaces obtained fit very well to those obtained from the quantum chemistry calculations.

Vibronic coupling can be conveniently characterised according to the symmetry of the the states and modes involved. In benzene there is both JT and PJT coupling present. Both arise as a result of  $e_{2g}$  vibrations coupling the states. We find that  $\nu_8$  and  $\nu_9$  are the most important for JT couplings, and modes  $\nu_7$  and  $\nu_8$  are the most important for PJT interactions. There are also significant first order couplings between the singly degenerate states, which contribute to an overall highly coupled multi-channel model, allowing the wavepacket, in various quantities, to spread throughout the whole system after an initial excitation. This model, as shown, is accurate enough to enable good reproduction of the lowest three absorption bands, thus describes the region around the FC point well. After adding some third order terms to the model, it is also able to reproduce the adiabatic surfaces leading to the  $S_1/S_0$  CI.

Using the full 5 state and reduced space 2 state Hamiltonian we were able to perform quantum dynamics simulations for the first 2000fs following excitation into  $S_1$ . In both cases it was shown that when vibrationally hot, there is significant decay away from the FC point towards and through the  $S_1/S_0$  CI. In the case of the 5 state model the barrier was created from a diabatic crossing between the  $\tilde{A}$  and  $\tilde{C}$  and therefore in order to reach the intersection the wavepacket initially populates  $\tilde{C}$ . In the two state model the barrier is treated adiabatically, arising from intra-state coupling parameters.

The results obtained show good agreement with the experimental data. There is an initial fast decay, followed by a slower one. In both calculations the fast decay continues for longer than seen experimentally, but this is attributed to the reduced

dimensionality. The calculations allow us to conclude that much of the decay in the channel 3 region of benzene occurs through the  $S_1/S_0$  CI. We are also able to attribute the 1.2ps oscillations seen experimentally to oscillations along the reaction coordinate. However the singlet model is unable to fully assign the step in the ion yield arising from altering the energy of the probe pulse. Part of this step arises from wavepacket population in  $\tilde{C}$ , which cannot be ionised at longer wavelengths of the probe pulse. Despite this, 10% of the decay from the FC region is not shown in this singlet model, indicating that we are still missing a photochemical channel.

# Chapter 5

## Spin Orbit Coupling

### 5.1 Introduction

The factors effecting ultrafast internal conversion (IC) in small hydrocarbon molecules has been widely discussed in regards to photochemical behaviour [10, 11, 114, 115]. The importance of such topological features as CI in singlet transitions is well documented [116–121]. In comparison the behaviour and importance of intersystem crossing (ISC) in the same time regime is relatively unknown [122–126].

The involvement of triplet states in the ultrafast dynamics of hydrocarbons is often dismissed due to the strength of the coupling that exists between the two manifolds. However the lowest triplet states tend to lie in close proximity to the lowest singlet excited states and it has been shown that in some cases the lowest triplet state intersects the  $S_0$  at the same point as  $S_1$ , forming a triple intersection point [123]. This behaviour gives rise to a high density of states, and increases the probability of ISC, even when the coupling is relatively small.

The strength of SOC is strongly dependent on (a) nuclear charge, (b) the availability of transitions between orthogonal orbitals and (c) spatial proximity of the two orbitals. Singlet-triplet transitions are governed by El-Sayed’s rule [122], which states:

$$f[S(n, \pi^*) \leftrightarrow T(\pi, \pi^*)] \text{ and } f[S(\pi, \pi^*) \leftrightarrow T(n, \pi^*)] \quad (5.1a)$$

are much greater than transitions arising from:

$$f[S(\pi, \pi^*) \leftrightarrow T(\pi, \pi^*)] \text{ and } f[S(n, \pi^*) \leftrightarrow T(n, \pi^*)] \quad (5.1b)$$

Equations 5.1a and 5.1b express that transitions between a singlet and a triplet state will be more efficient when the associated change in spin angular momentum is accompanied by a change in orbital angular momentum. A spin flip that occurs via a  $n \leftrightarrow \pi^*$  transition may be considered as an orbital angular momentum change associated with a transition from a p orbital in the plane to one which is perpendicular. This orbital angular momentum change can couple to the spin momentum change associated with a  $\alpha\beta \rightarrow \alpha\alpha$  spin flip [1], therefore conserving the total angular momentum. This is highlighted in figure 5.1. In figure 5.1(a) the HOMO-LUMO transition from  $S_0$  to  $T_1$  is a  $\pi \rightarrow \pi^*$  transition, this does not involve an angular momentum change and is therefore forbidden. However in the figure 5.1(b), the transition from  $S_0$  to  $T_3$  (involving LUMO+1) requires a one-centre jump in p-orbitals and therefore a change in orbital angular momentum is coupled with the same change in spin angular momentum, making this an allowed transition [1].

Aromatic hydrocarbons, such as benzene, have very small SOC at the equilibrium geometry because they are unable to invoke  $n \rightarrow \pi^*$  transitions. The closest analogous transition is  $\sigma \rightarrow \pi^*$  or  $\pi \rightarrow \sigma^*$ . However in planar geometry the  $\pi, \pi^*$  states and  $\sigma, \sigma^*$  states do not mix and therefore there is no mechanism for coupling. Out of plane vibrations, such as C-H bends (shown in figure 5.2), break the symmetry and allow mixing between  $\sigma$  and  $\pi$  states. This symmetry breaking operation transforms the originally symmetric p-orbital into an  $sp^n$  orbital providing a weak mechanism for SOC.

Symmetry considerations play a key role in all electronic transitions, as described in section 2.4. For coupling between the two different spin states the product of the state symmetries must be a subset of a rotational symmetry from the symmetry group



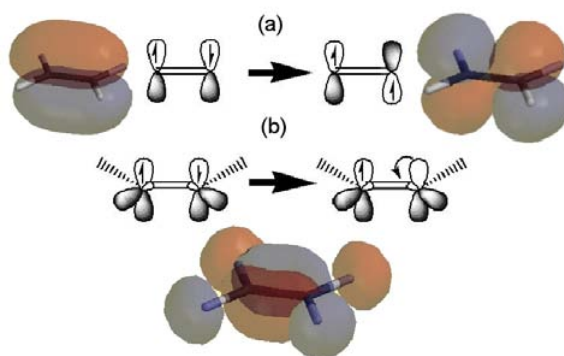


Fig. 5.1: (a) The HOMO and LUMO orbitals of ethylene and the spin flip involved in a  $\pi\pi^*$  transition from  $S_0$  to  $T_1$ . There is no possible change in angular momentum and hence the spin-flip is forbidden. (b) The electron one-centre jump involved in  $S_0$  to  $T_3$  transition (HOMO and LUMO+1). The change in angular momentum involved in a jump from a  $p_z$  to  $p_y$  is match exactly by the change in angular momentum associated with a spin-flip, conserving angular momentum and making this an allowed transition.

of the molecule [127].

$$\Gamma_i \otimes \Gamma_j \otimes \Gamma_\alpha \supset R_x, R_y \text{ or } R_z \quad (5.2)$$

where  $\Gamma_i$  and  $\Gamma_j$  are the two coupled states and  $\Gamma_\alpha$  is the coordinate. The rotational symmetries in  $D_{2h}$  are  $B_{3g}$  ( $R_x$ ),  $B_{2g}$  ( $R_y$ ) and  $B_{1g}$  ( $R_z$ ) and therefore SOC may exist at equilibrium between  $S_1$  ( $2^1A_g$ ) and  $T_1$  ( $3^1B_{1g}$ );  $A_g \otimes B_{1g} = B_{1g}$  ( $R_z$ ). Higher order coupling symmetry considerations follow the same analysis used for the Vibronic Coupling Hamiltonian (in section 2.4), in which the symmetry of the vibration is also included in the sum. An example is between  $1^1B_{1g}$  and  $1^3B_{1g}$  along a  $b_{1g}$  mode;  $B_{1g} \otimes B_{1g} \otimes b_{1g} = B_{1g}$  ( $R_z$ ). First and higher order vibronic couplings are critical in accurately describing the PES and hence dynamics in singlet models, especially in the non-adiabatic regime. By contrast the effects of vibrations on SOC couplings are often not considered in such detail and only a few literature examples exist, these include studies on naphthalene and anthracene by Lawetz *et al* and benzene by Fujimura *et al* [124,125]. These higher

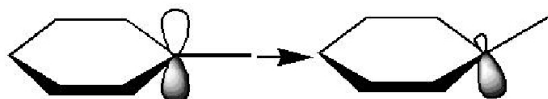


Fig. 5.2: The pure p orbital is able to mix when an out of plane C-H bend occurs. This create an  $sp^n$  orbital and the mixing between  $\sigma$  and  $\pi$  states provides a mechanism for spin orbit coupling.

order terms are likely to be important when considering the interactions between the singlet and triplet manifold.

This chapter has been motivated by work presented in the previous chapter involving the channel 3 region of benzene. As discussed in chapter 4 excitation into the high vibrational states of  $S_1$  results in a sudden loss of fluorescence. Radiationless transitions in the singlet manifold account for a lot of this behaviour but experimental results have indicated that a small portion of the wavepacket is crossing onto the triplet states in the ultrafast timescale, through the  $S_1/S_0/T_1$  CI. Recent publications have also postulated that the SOC increases at CI [123]. Therefore the high density of states and larger coupling at the CI would result in a mechanism for ultrafast ISC.

In this chapter we calculate the SOC for cyclobutadiene and benzene. Cyclobutadiene represents an excellent starting point because there are many similarities between the two system, but being a smaller molecule is easier to characterise with a range of active spaces and basis sets. Performing these calculations along all the normal modes and the vector in normal mode space between the FC point and the  $S_1/S_0/T_1$  CI we hope to characterise the behaviour of SOC in these simple hydrocarbons and discuss the possibility of its importance in ultrafast dynamics.

## 5.2 Methodology and Computation

Geometry optimisations of the  $S_0$  equilibrium geometry and  $S_1/S_0$  CI were determined using Gaussian03 [111] and Molpro [107]. They were performed at CASSCF level with a 6-31g\* basis. Results obtained gave good agreement between each other and previously obtained results [128–130].

*Ab-initio* points and SOC energies calculated using Molpro were initially performed with a variety of basis sets and active spaces, the most appropriate was selected for the normal mode cuts based upon accuracy and computational expense. Molpro uses a full two electron Breit-Pauli Hamiltonian for SOC calculations (this is discussed in chapter 2). The internal configurations are treated exactly, while contributions from the external configurations are treated using a one electron mean field approach. This method has proved successful in a variety of systems and the error caused by this approximation is usually smaller than  $1\text{cm}^{-1}$  [68].

The geometries along the normal mode coordinates were obtained using the VCHAM program distributed with the MCTDH package [112]. Coordinates are generated from dimensionless (mass-frequency scaled) normal modes along each vibration, in the same manner as chapter 4. The cuts along the vector leading to  $S_1/S_0/T_1$  CI were calculated by using the intersection geometry as the mid-point of the plot and taking a number of equal predefined steps to the equilibrium geometry and in the opposite direction away from the intersection.

## 5.3 Results

### 5.3.1 Cyclo-Butadiene

Cyclobutadiene,  $C_4H_4$ , is a simple hydrocarbon, whose stable structure has  $D_{2h}$  symmetry. Upon inspection one might expect a  $D_{4h}$  geometry but due to vibronic coupling between the ground ( $\tilde{X}^1B_{1g}$ ) and first excited state ( $\tilde{A}^1A_{1g}$ ) which makes the square planar  $D_{4h}$  geometry unstable. Extensive theoretical studies [129, 131–134] have suc-

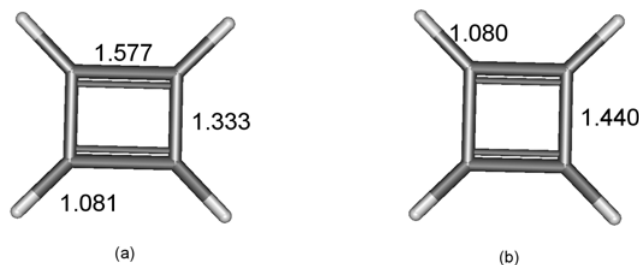


Fig. 5.3: Optimised structures of cyclobutadiene using a CAS(4,4)/6-31g\* basis. (a)  $D_{2h}$  rectangular form (b)  $D_{4h}$  square planar form. Bond lengths are in Å.

cessfully characterised the vibronic coupling which breaks the  $D_{4h}$  symmetry. The difference between the bond lengths of the two structures is shown in figure 5.3.

Various studies also exist characterising the triplet surfaces [134, 135] and isomerisation barrier between each rectangular form [131], however there remains little work on the nature of SOC [127]. In this section we characterise the vibrational effects on the SOC, using the  $D_{2h}$  minimum energy geometry as equilibrium.

Cyclobutadiene contains 18 vibrational normal modes (14 of which are shown in table 5.1). These are calculated at MP2 level with a 6-31g\* basis. The low frequency modes, which are most important in these calculations have an error of  $\sim 0.006\text{eV}$  ( $50\text{cm}^{-1}$ ). The higher frequency modes have an error of  $\sim 0.02\text{eV}$  ( $150\text{cm}^{-1}$ ), but these play little part in SOC.

Table 5.2 shows the ground and excited state energies and SOC between  $S_2/T_1$  in cyclobutadiene at equilibrium geometry. Two active spaces and three basis sets are used. The (4,4) active space incorporates the valence  $\pi$  orbitals and the (8,8) active space also includes the most important  $\sigma$  and  $\sigma^*$  orbitals. The electronic structure calculations (shown in table 5.2) use CASSCF except where labelled Multireference configuration interaction (MRCI). The MRCI calculations use the Roos basis set.

In rectangular ( $D_{2h}$ ) form the occupied  $\pi$  valence orbitals have  $b_{1u}$  and  $b_{2g}$  sym-


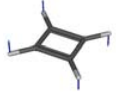

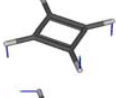
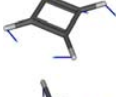

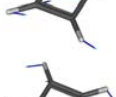

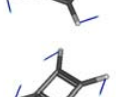
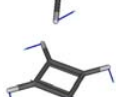


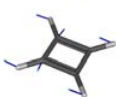
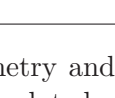
Mode	Symmetry	Vibration	Theory	Expt [129]	Description
1	1a <sub>u</sub>		0.059	-	Anti-Symmetric C-H Bending
2	1b <sub>2g</sub>		0.060	0.066	Anti-Symmetric C-H Bending
3	1b <sub>3u</sub>		0.069	0.070	Symmetric C-H Bending
4	2a <sub>u</sub>		0.088	-	Anti-Symmetric C-H Bend
5	1b <sub>2u</sub>		0.093	0.089	In plane C-H bend
6	1b <sub>1g</sub>		0.096	-	Anti-Symmetric C-H Bend
7	1b <sub>3g</sub>		0.106	0.090	C-H Breathing
8	1a <sub>g</sub>		0.123	0.123	In plane C-H bend
9	1b <sub>1u</sub>		0.134	0.127	In plane C-H bend
10	2a <sub>g</sub>		0.142	0.131	In plane C-H bend
11	2b <sub>3g</sub>		0.140	-	In plane C-H bend
12	2b <sub>2u</sub>		0.160	0.154	In plane C-H bend
13	3a <sub>g</sub>		0.198	0.208	Ring Distortion
14	2b <sub>1u</sub>		0.200	0.189	Anti-Symmetric Ring Distortion

Table 5.1: Mode symmetry and vibration energies (in eV) for the lowest 14 normal modes of cyclobutadiene. Calculated using MP2 and 6-31g\* basis set. The last 4 high frequency vibrational modes not included because they play no role in this study but can be found in [129].

metry, the  $\pi^*$  orbitals have  $b_{3g}$  and  $a_u$  symmetry [136]. The excited determinants in the  $\pi$  space are responsible for the singlet and triplet states that we consider. The  $\sigma$  orbitals, included in the larger active space do not contribute much to the accuracy of the vertical excitation energies. The excited state energies (table 5.2) obtained shows good agreement with previously calculated values [137]. The first singlet excited state ( $1^1B_{1g}$ ) and lowest triplet state ( $1^3B_{1g}$ ) is poorly described using the smaller basis set, but using a the large basis gives energies close to the experimental values even using CASSCF with the smaller active space. The second excited state ( $2^1A_g$ ) is poorly described when the smaller active space is used, this is unsurprising because analysis of the orbitals shows that the wavefunction for this state contains significant doubly excited determinants.

At equilibrium SOC exists between the  $S_2$  ( $2^1A_g$ ) and  $T_1$  ( $3^3B_{1g}$ ) in the  $z$  (out of the plane) direction. It is very small, as one would expect for an aromatic type system. This is because hydrocarbons, like cyclobutadiene are unable to invoke the  $n \rightarrow \pi^*$  transitions responsible for strong SOC. The closest analogous transition is  $\sigma \rightarrow \pi^*$  or  $\pi \rightarrow \sigma^*$ . In planar geometry the  $\pi, \pi^*$  states and  $\sigma, \sigma^*$  states do not mix and therefore there is no mechanism for coupling.

The size of SOC increases when the basis set and active space are enlarged, although the increase is only from  $\sim 0.04\text{cm}^{-1}$  to  $\sim 0.08\text{cm}^{-1}$  in the former case and  $\sim 0.08\text{cm}^{-1}$  to  $\sim 0.1\text{cm}^{-1}$  in the latter case. This suggests that the  $\sigma$  and  $\sigma^*$  orbitals (included in the (8,8) active space) are not important for obtaining accurate values for SOC. However as mentioned the  $\sigma$  and  $\pi$  orbitals do not mix at planer geometry and therefore their inclusion will have little effect. Distortions from the equilibrium geometry along out of plane modes will invoke  $\sigma/\pi$  mixing and therefore the larger (8,8) active space is likely to make a big difference to the SOC energies. For the rest of the calculations MRCI with the (8,8) active space with a Roos basis set is used.

Figure 5.4 shows the change in SOC along the normals modes which exhibit signifi-

	(4,4)			(8,8)			Ref [137]		
	sto-3g	6-31g*	Roos	MRCI	sto-3g	6-31g*	Roos	MRCI	
$1^1A_g$	0	0	0	0	0	0	0	0	
$1^1B_{1g}$	5.88	3.93	3.16	3.10	5.11	3.91	3.30	3.23	
$2^1A_g$	6.61	5.28	5.03	4.68	6.15	4.13	4.16	4.10	
$1^3B_{1g}$	1.95	1.66	1.61	1.36	1.93	1.38	1.28	1.20	
SOC $2^1A_g/{}^3B_{1g}$	0.013	0.045	0.081	0.080	0.000	0.071	0.107	0.103	

Table 5.2: Vertical excitation energies (in eV) and spin orbit coupling (in  $\text{cm}^{-1}$ ) of 3 singlet and 1 triplet states of cyclobutadiene, calculated at  $D_{2h}$  equilibrium geometry. Two active spaces and 3 basis sets are used. The Roos basis is a Roos(3s2p1d/2s) basis which uses an ANO basis truncated to 6-31g\* size. CASSCF is used except in the final columns for each active space which uses MRCI with a Roos basis.

cant vibrational effects, these are  $\nu_1$ ,  $\nu_2$ ,  $\nu_3$  and  $\nu_4$ . The vibrational SOC terms are most evident, as predicted, in normal modes which contain out of plane C-H bends. The largest effect is observed along  $\nu_3$  (seen in figure 5.4c); the SOC between  $2^1A_{1g}/^3B_{1g}$  and  $1^1A_{1g}/^3B_{1g}$  rises to  $5\text{cm}^{-1}$  and  $4\text{cm}^{-1}$  respectively. At this point the hydrogen atom is bent  $63^\circ$  out of the plane of the molecule and the C-H bond length has extended to  $1.67\text{\AA}$ . The SOC gradient is largest in this mode because all of the C-H bonds bend out of the plane in the same direction, causing the most mixing between  $\pi$  and  $\sigma$  orbitals. The extent of the mixing is illustrated in figure 5.5. At the equilibrium position (shown in figure 5.5a) the unperturbed valence  $\pi$  orbitals show no s type character and are therefore symmetric through the plane of the molecule. However following a displacement along  $\nu_3$  so that the hydrogen atom is bent  $63^\circ$  out of plane, (figure 5.5b), it can be clearly seen that the  $\pi$  orbitals have mixed with  $\sigma$  orbitals giving slight  $sp^n$  character to the  $\pi$  orbitals.

Figure 5.4a shows the effect of  $\nu_1$  on SOC. In this mode there is still a C-H bending motion, however the most dominant motion in this mode is an out of plane C-C torsion. This torsion reduces the extent of the mixing between  $\pi$  and  $\sigma$  orbitals and therefore the gradient of SOC is reduced significantly.

Figures 5.4b and 5.4d show an increase in the SOC between  $2^1A_{1g}/^3B_{1g}$  and  $1^1A_{1g}/^3B_{1g}$  along modes  $\nu_2$  and  $\nu_4$  respectively. Both modes contain two up and two down C-H bends. The SOC gradient along  $\nu_4$  is a lot greater than  $\nu_2$  because it is a higher frequency mode and therefore the out of plane motion of the hydrogen is greater. For  $\nu_2$  the C-H bending angle is  $64^\circ$  at 10units from equilibrium, but for  $\nu_4$  the C-H bending angle is  $68^\circ$  at 10units. The coupling between  $1^1A_{1g}/^3B_{1g}$  in both modes shows an increase before decaying. This occurs due to vibronic mixing between the  $1^1A_g$  and  $1^1B_{1g}$  electronic states. This effectively changes the symmetry, making SOC forbidden at large distortions.



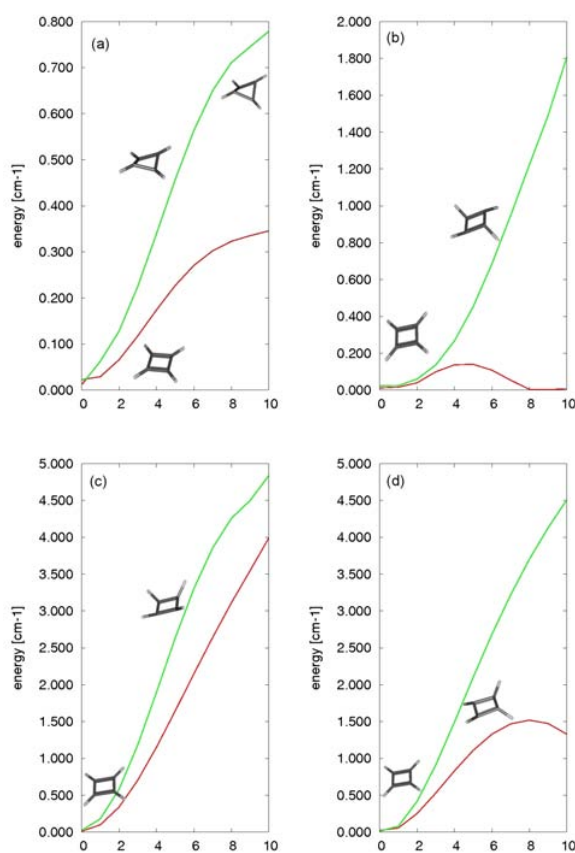


Fig. 5.4: Changes in spin orbit coupling values along selected normal modes of cyclobutadiene: (a)  $\nu_1$  ( $1a_u$ ) (b)  $\nu_2$  ( $1b_{2g}$ ) (c)  $\nu_3$  ( $1b_{3u}$ ) (d)  $\nu_4$  ( $2a_u$ ). In all cases the green line is spin orbit coupling between  $2^1A_{1g}/3^3B_{1g}$ . The red curve is spin orbit coupling between  $1^1A_{1g}/3^3B_{1g}$ .

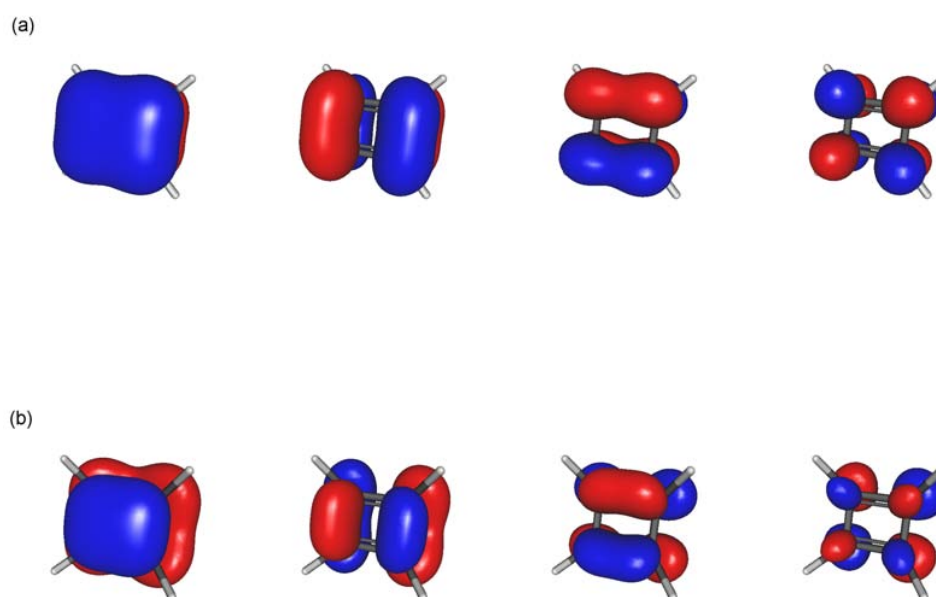


Fig. 5.5: The  $\pi$  valence orbitals of cyclobutadiene. (a) Equilibrium geometry (b) Distorted along  $\nu_3$ , an out of the plane C-H bend. At this point the hydrogen atom is bent  $63^\circ$  out of plane of the molecule. The orbitals show  $sp^n$  character responsible for a mechanism for spin orbit coupling.

### 5.3.2 Benzene

In chapter 4 we presented work on the singlet manifold of benzene. This described the competing pathways in the photochemistry of benzene following excitation into the higher vibrational states of  $S_1$  [19, 138]. Much of the behaviour can be described within the singlet manifold, but some questions still remain. Early research considered the involvement of triplet states in the dynamics [139], however this idea was gradually dropped due to the small size of the SOC. Recent experimental studies have indicated that although dominated by the ultrafast  $S_1/S_0$  transition through the prefulvenoid CI, ISC may play a small role [19]. Another recently published paper has stated that SOC increases at a CI [123], and therefore this could provide a mechanism for ultrafast ISC to occur.

Table 5.3 shows the vertical excitation energies calculated at equilibrium geometry using a variety of basis sets and active spaces. The (6,6) active space (as described and used in chapter 4) contains the  $\pi$  valence orbitals, the (10,10) active space also includes the most important  $\sigma$  and  $\sigma^*$  orbitals. The electronic structure calculations in table 5.3 uses CASSCF except where labelled as MRCI. The MRCI calculation uses the Roos basis. As expected there is a steady improvement in the energy with the size of basis and active space (this is discussed in more detail in chapter 4).

At the equilibrium geometry benzene has symmetry allowed SOC between  $1^1B_{2u}/1^3B_{1u}$ . Like cyclobutadiene the SOC is very small due to its aromatic nature. There is a steady increase in the size of SOC when the basis set and active space sizes are increased, but the values remain small even in the largest calculations. As expected, from cyclobutadiene calculations, the inclusion of the  $\sigma$  orbitals has little effect at equilibrium, due to their inability to mix. However the larger active space does have an effect at large distortions from equilibrium geometry. The effect is less than found in cyclobutadiene and is limited to modes which strongly promote SOC, however in such cases the (10,10) active space increased the SOC at large distortions by  $\sim 10\%$  compared to the (6,6)

	(6,6)				(10,10)				Ref [63]
	sto-3g	6-31g*	Roos	MRCI	sto-3g	6-31g*	Roos	MRCI	
$1^1A_g$	0	0	0	0	0	0	0	0	0
$1^1B_{2u}$	6.96	4.90	4.87	5.00	6.90	4.99	4.94	4.92	4.90
$1^1B_{1u}$	10.08	8.11	8.01	6.30	9.60	7.97	7.95	6.29	6.20
$1^1E_{1u}$	11.68	9.54	9.40	7.20	11.56	9.15	8.78	7.07	6.94
$1^3B_{1u}$	4.35	4.02	3.96	3.95	4.31	3.99	3.95	3.92	3.94
$1^3E_{1u}$	5.90	5.04	4.81	4.74	5.89	4.99	4.78	4.75	4.76
SOC $1^1B_{2u}/^3B_{1u}$	0.0135	0.070	0.080	0.090	0.038	0.1041	0.113	0.118	0.33 [140]

Table 5.3: Vertical excitation for benzene singlet and triplet excited states (in eV) and spin orbit coupling calculations (in  $\text{cm}^{-1}$ ) at  $D_{6h}$  equilibrium geometry.

active space.

Calculations for SOC using Gaussian [111] yielded a SOC between  $1^1B_{2u}/1^3B_{1u}$  at equilibrium geometry of  $1.5\text{cm}^{-1}$ . The Gaussian method only contains one electron terms, this result highlights the importance of two electron terms in the SOC Hamiltonian. Analysis of the one and two electron terms using GAMESS [141] showed that for benzene ( $S_1/T_1$ ) the one electron term is  $\sim 1.5\text{cm}^{-1}$  but the two electron term is  $\sim -1.5\text{cm}^{-1}$ , therefore combined creates the almost zero SOC at equilibrium. By ignoring the two electron terms one obtains a seriously wrong description of SOC in benzene.

Throughout the rest of this chapter the (6,6) active space and Roos(3s2p1s/2d) basis was used for benzene calculations. This was selected to provide a continuity with *ab-initio* calculations performed in chapter 4 and because this gave the most reliable convergence at distorted geometries. The (10,10) active space was shown to produce slightly larger SOC values along some modes, but convergence was difficult along the symmetry breaking modes. The normal modes can be found in table 4.1.

Figure 5.6 shows the change in SOC along the normal modes which exhibit significant vibronic effects, these are  $\nu_4$ ,  $\nu_5$ ,  $\nu_{10}$ ,  $\nu_{11}$ ,  $\nu_{16}$  and  $\nu_{17}$ . Figure 5.6a shows the SOC along the chair ( $\nu_4$ ) mode, this mode is important because it is this mode in combination with  $\nu_{16}$  that is the important motion towards the prefulvenoid  $S_1/S_0$  CI. Displacement along this mode induces a small increase in SOC to  $0.5\text{cm}^{-1}$  at 10units. At first glance the motion of the mode is a carbon out of plane ring motion. However upon close inspection the hydrogens oscillate with a slightly greater amplitude, creating a slight C-H bend and mechanism for SOC. Symmetry considerations mean that the vibrationally induced SOC terms along this mode must be second order, because first order vibrational terms are forbidden by symmetry.

Figures 5.6b,c and d show the modes with the greatest SOC change. Unsurprisingly these are the modes which are dominated by out of plane C-H bends. Like cyclobutadiene it is  $\nu_{11}$ , a symmetric C-H bending mode which has the largest SOC, just over

$4\text{cm}^{-1}$  when the hydrogen atom is  $71^\circ$  out of the plane of the molecule. Along  $\nu_{10}$  (figure 5.6c), a higher frequency symmetry pair of the chair mode, this graph not only shows greater SOC which is a factor of 4 higher than  $\nu_4$ . The symmetry of this mode means that SOC is also between the  $S_1$  and  $T_2$  states, however this is a lot smaller than the  $S_1/T_1$  coupling.

Figures 5.6c,e and f are normal modes which induce coupling between  $S_1$  and the doubly degenerate  $T_2$ . The green line is coupling to the  $x$  component and the blue line is to the  $y$  component. This coupling is likely to be very important in dynamics calculations because  $T_2$  is degenerate with  $S_1$  at equilibrium, and this degeneracy is maintained along the vector leading to the  $S_1/S_0$  CI, providing a possible mechanism for ISC. One can see that it is  $\nu_{17}$  which results in the largest coupling between  $S_1$  and both components of the  $T_2$  state. The coupling strength reaches just under  $1.0\text{cm}^{-1}$  for the  $x$  component and just over  $0.5\text{cm}^{-1}$  for the  $y$  component at 10units from equilibrium. The boat mode ( $\nu_{16}$ ) in combination with the chair mode ( $\nu_4$ ) plays a critical role in the dynamics. This mode has the same symmetry as  $\nu_{17}$  and so the behaviour is similar, albeit slightly smaller. The SOC is always below  $0.5\text{cm}^{-1}$ .

### 5.3.3 Spin Orbit Coupling at the Intersection

A recent study by Cogan *et al* [123] has shown that SOC increases dramatically at a CI, for benzene a value of  $6.23\text{cm}^{-1}$  was been recorded between  $S_1/T_1$  at the CI. This study used a (8,7)CAS/DZV within the GAMESS package [141]. GAMESS, like Molpro, includes the two electrons terms in a rigorous description of the Breit-Pauli Hamiltonian.

This reported result is very important because a larger SOC at a CI in conjunction with the density of states which arises from the  $S_1$  and  $T_1$  states crossing the  $S_0$  at the same point could provide a mechanism for ultrafast ISC. However the study by Cogan *et al* has two main disadvantages, firstly it uses an unusual CAS space, which we found no justification for, secondly the SOC calculations were point calculations

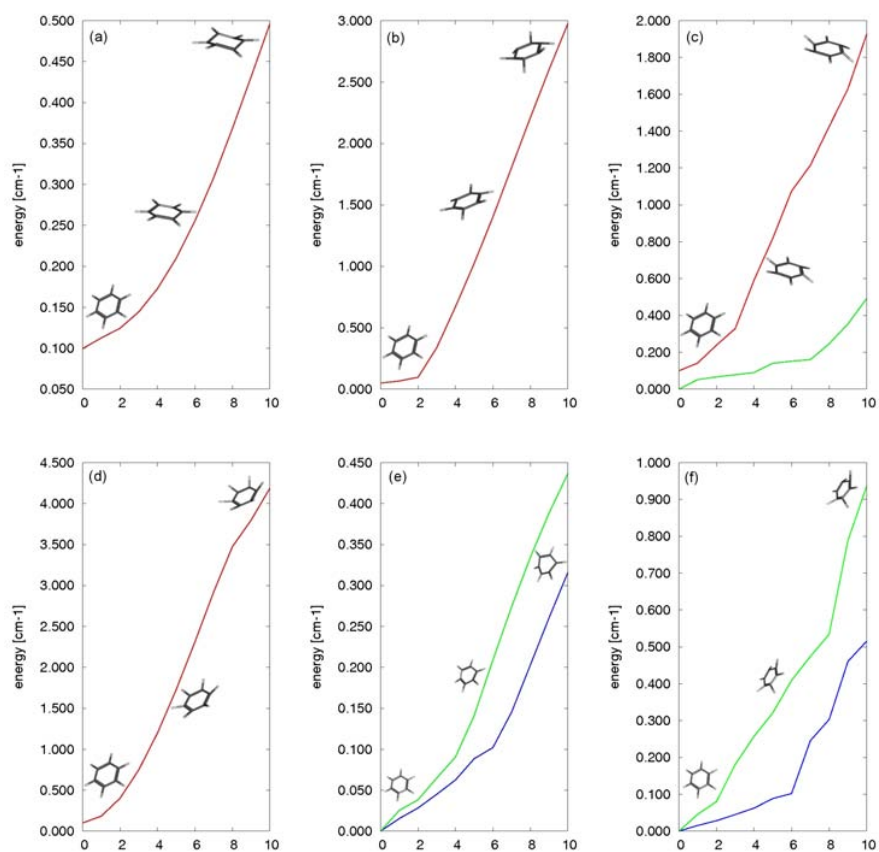


Fig. 5.6: Changes in spin orbit coupling values along the important vibrational modes of benzene: (a)  $\nu_4$  ( $1b_{2g}$ ), (b)  $\nu_5$  ( $2b_{2g}$ ), (c)  $\nu_{10}$  ( $1e_{1g}$ ), (d)  $\nu_{11}$  ( $1a_{2u}$ ), (e)  $\nu_{16}$  ( $1e_{2u}$ ), (f)  $\nu_{17}$  ( $2e_{2u}$ )

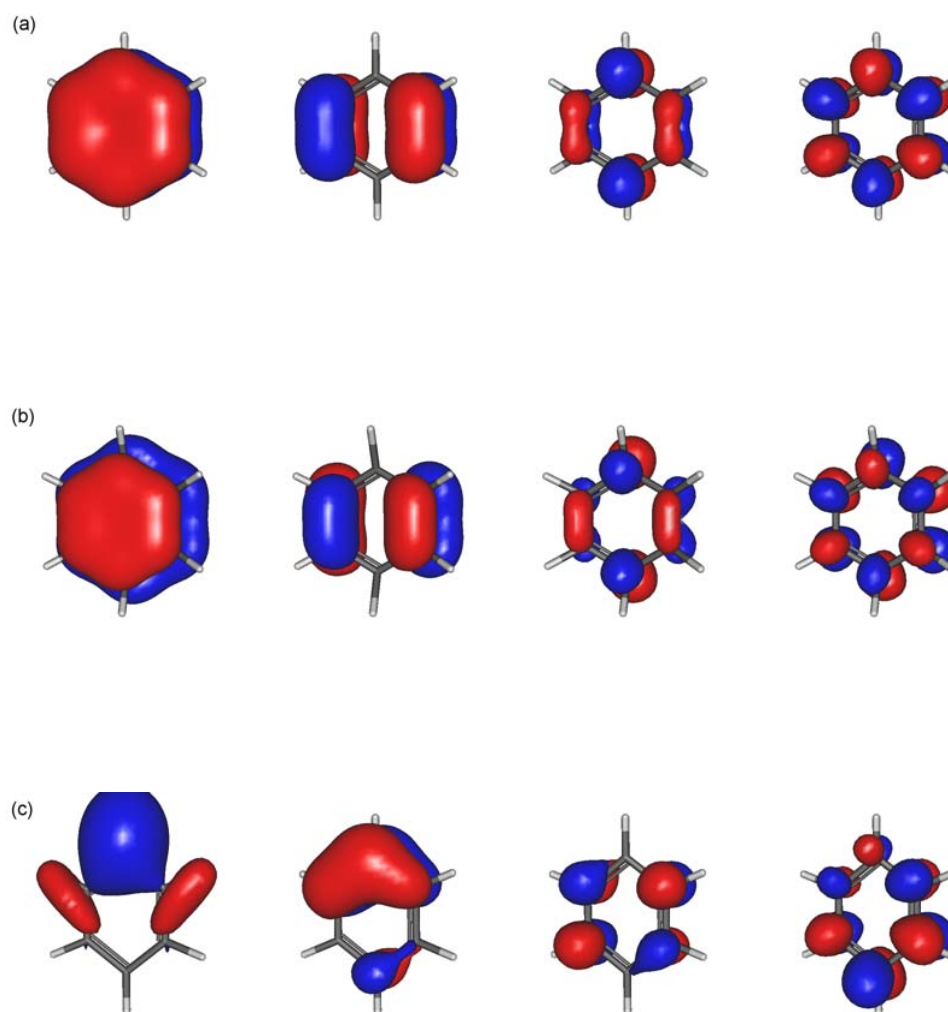


Fig. 5.7: The  $\pi$  valence orbitals (without the degenerate pairs) of benzene. (a) Equilibrium geometry (b) Distorted along  $\nu_5$ , an out of the plane C-H bend. The orbitals clearly show  $sp^n$  character responsible for a mechanism for spin orbit coupling. (c) Distorted along the Jahn-Teller mode  $\nu_6$ . Although the orbitals are distorted there is no out of plane C-H motion and no  $sp^n$  character. Therefore despite being a very important coupling mode in both the triplet and singlet manifold it is not responsible for linking the two.



which were only calculated at the intersection, this gave no insight into changes along the coordinate from the FC point.

Figures 5.8a and b show the PES for the states of interest along the vector from equilibrium to the intersection for both cyclobutadiene and benzene respectively. Figures 5.8c and d show the change in the SOC along this vector for cyclobutadiene and benzene respectively.

Figure 5.8c shows that in cyclobutadiene the SOC between  $2^1A_{1g}/1^3B_{1g}$  and  $1^1A_{1g}/^3B_{1g}$  gradually increases along the vector. We find that there is no dramatic increase at the intersection point. The increase observed is similar to that seen along the normal modes and this is because it is the combination of normal modes leading to the intersection, which involves  $\nu_1, \nu_3$  and  $\nu_4$ , which is the important factor in how the SOC will change. At the intersection the SOC between  $2^1A_{1g}/1^3B_{1g}=2.0\text{cm}^{-1}$  and between  $1^1A_{1g}/1^3B_{1g}=0.75\text{cm}^{-1}$ . This is attributed to the out of plane motion of the hydrogens and at this point the hydrogens are  $52^\circ$  out of the plane of the molecule. This can be seen in the orbital plots shown in figure 5.9a, although the orbitals are distorted due to other the modes involved in reaching the CI, there is clearly some  $sp^n$  character, as shown in figure 5.5.

Figure 5.8d shows the SOC along the vector leading to the  $S_1/S_0$  CI in benzene. This also shows a gradual increase in the SOC between  $1^1B_{2u}/1^3B_{1u}$ . However in this case it is not as large as seen in some of the normal modes especially those with out of plane C-H bends. This is because the normal mode combination required to reach the CI is dominated by  $\nu_4$  and  $\nu_{16}$ , and modes such as  $\nu_5$  and  $\nu_{11}$  which result in strong SOC are not as important. This is demonstrated in figure 5.9b, in which although distorted there is very little  $sp^n$  mixing, limiting the strength of SOC. A value of  $1.5\text{cm}^{-1}$  is found at the CI, we also recalculated this single point using a (10,10) active space to clarify the effect of the  $\sigma$  orbitals. In this calculation the SOC only increases to  $1.8\text{cm}^{-1}$  which is not surprising because  $\sigma/\pi$  mixing due to out of plane motions are

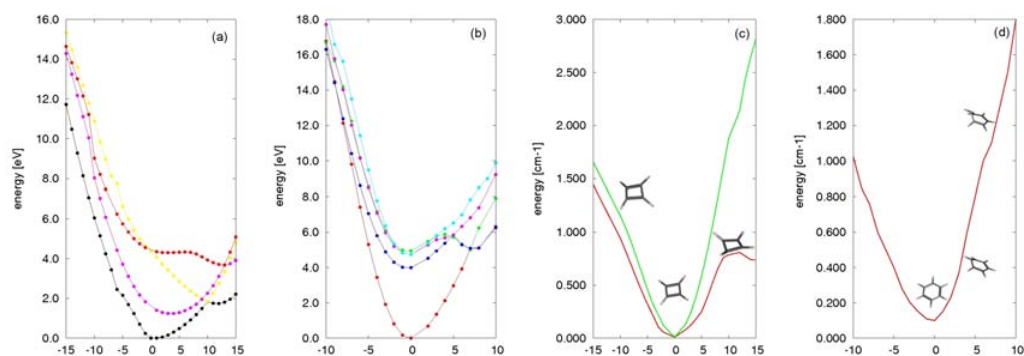


Fig. 5.8: The potential energy surface cuts along the vector from the Franck-Condon point to the  $S_1/S_0$  conical intersection and corresponding spin orbit coupling values. (a) Cyclobutadiene: States at  $\mathbf{Q}_0$  are ordered  $S_0$ ,  $T_1$ ,  $S_1$  and  $T_2$  at equilibrium. (b) Benzene: States at  $\mathbf{Q}_0$  are ordered  $S_0$ ,  $T_1$ ,  $T_2$ ,  $x$ ,  $T_2$ ,  $y$  and  $S_2$  at equilibrium. (c) Spin orbit coupling between  $2^1A_{1g}/1^3B_{1g}$  (green) and  $1^1A_{1g}/1^3B_{1g}$  (red) towards the  $S_1/S_0$  conical intersection for cyclobutadiene. (d) Spin orbit coupling between  $1^1B_{2u}/1^3B_{1u}$  towards the  $S_1/S_0$  conical intersection for benzene

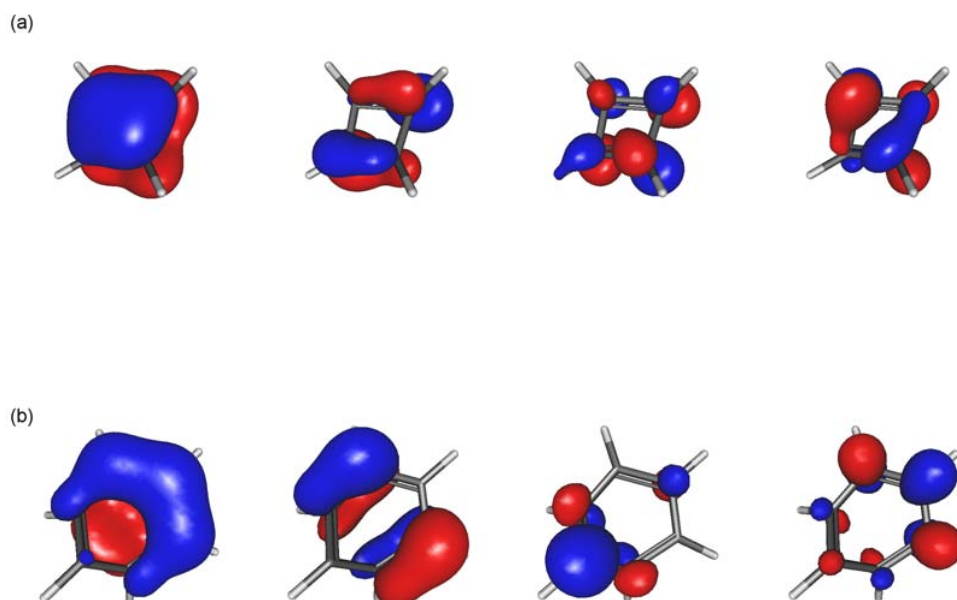


Fig. 5.9: The  $\pi$  valence orbitals (without the degenerate pairs) at the conical intersection of (a) cyclobutadiene and (b) benzene

not huge at the CI point in this case. Both of these values are significantly lower than that reported by Cogan *et al*, which seems unreasonably high.

Calculations of the SOC along the benzene CI vector show that there is not huge SOC coupling, however the density of vibronic states and highly symmetrical nature means that there is a large number of small couplings present along this vector. Although not shown in figure 5.8d, many of the singlet and triplet states couple along this vector with a strength of  $\sim 0.4\text{cm}^{-1}$ .

## 5.4 Conclusion

The triplet states are often neglected from ultrafast dynamics calculations in hydrocarbons due to the size of the coupling. Despite being small, especially at equilibrium, this chapter has indicated that higher order vibrational terms can induce a degree of coupling that could be important especially in regions around the  $S_1/S_0$  CI where the density of states is high and there are numerous possible channels for decay.

In cyclobutadiene, the low frequency out of plane C-H bends provide a mechanism for SOC to occur. This results in SOC energies two orders of magnitude greater than seen at equilibrium. Such observations are explained by plots of the distorted orbitals which are able to show the mixing of the  $\sigma$  and  $\pi$  states. The SOC also increases along the vector towards the CI, this is because the combination of normal modes required to reach the CI includes modes which strongly promote SOC, this again is confirmed by the distortions seen in the molecular orbitals.

A similar behaviour of SOC is seen in benzene. Modes which have some degree of C-H bending contribute the most to SOC. The combination of normal modes required to reach the  $S_1/S_0$  CI in benzene is dominated by modes which contribute smaller second order effects to the mechanism for SOC. As a result the gradient along this vector is not as great as seen in cyclobutadiene. Our calculations disagree with previous, less detailed calculations performed by Cogan *et al* which suggested SOC increased

dramatically at the CI to a value of  $6.23\text{cm}^{-1}$ . This value is unrealistic considering the type of distortions along the this vector.

From this study we can conclude that SOC is a well defined and smooth function, whose behaviour can be easily described with the considerations of orbital interactions, proximity and mixing of electronic states. Despite having small SOC at equilibrium, we have shown that vibrational effects in these two simple cyclic hydrocarbons can induce significant SOC. This is likely to be especially important when the density of states is high and degeneracy occurs.

In the next chapter we investigate the ultrafast dynamics of benzene, as before, but including the triplet manifold and see as a result that the triplet manifold, especially under the conditions described above should not be discarded. This is especially important when considering the detail that can be achieved from spectroscopic data using modern ultrafast laser techniques.

## Chapter 6

# Ultrafast Intersystem Crossing Dynamics in Benzene

ISC which occurs due to SOC between the singlet and triplet states creates a reservoir of energy within the triplet manifold. This energy is ultimately responsible for phosphorescence [142,143] and in some cases the formation of photoproducts [144]. Examples of ISC are ubiquitous throughout chemistry and recent work has implicated an important involvement within the photochemistry of DNA and the protection against UV radiation [145,146].

It is well known that timescales for ISC are typically much slower than the corresponding singlet transitions. However examples of ultrafast ISC do exist, but tend to be limited to molecular systems which contain heavier atoms such as nitropolycyclic aromatic hydrocarbons [147] and metal complexes [148].

Figure 4.14a in chapter 4 shows experimental data of the decay in the photoelectron yield as a function of the probe pulse delay (time) following excitation into the higher vibrational states of  $S_1$ . Using the singlet Hamiltonian calculated in chapter 4 we have used quantum dynamics simulations to describe many of the features seen experimentally. However these models were unable to account for some of the decay especially when using the shorter probe wavelengths. In this regime a portion of the wavepacket unaccounted for during the singlet calculations decays from the FC region. This has been attributed to ultrafast ISC which occurs along the reaction coordinate

State	SA-CAS(6,6)	CASPT2(6,6)	CASPT2(6,10)	Experimental [63]
$\tilde{A}^3 B_{1u}$	3.98	3.96	3.95	3.94
$\tilde{B}^3 E_{1u}$	5.06	4.85	4.74	4.76
$\tilde{C}^3 B_{2u}$	7.53	5.79	5.56	5.60

Table 6.1: Vertical excitation energies (in eV) of lowest three triplet states of benzene relative to the benzene singlet ground state, calculated at equilibrium geometry. The SA-CAS(6,6) used a 6-31g\* basis and are averaged over three states. The PT2(6,6) and PT2(6,10) uses a Molpro specific Roos(3s2p1d/2s) basis.

towards the  $S_1/S_0$  CI [19].

In this chapter we further develop the singlet model Hamiltonian presented in the chapter 4. Diabatic PES and couplings for the triplet states are calculated and fitted to obtain parameters for the model Hamiltonian along the important modes. We use the same method described for the benzene singlet model in chapter 4. The singlet and triplet manifolds are then coupled using SOC values obtained from the investigation described in chapter 5. We then perform a detailed analysis of the ISC dynamics and compare to the experimental data.

## 6.1 The Model Hamiltonian

The model used to study ultrafast ISC in benzene is a development of the 2 state model presented in chapter 4. The new model includes eight normal modes DOF (shown in table 6.9), two singlet states,  $S_0$  ( $A_{1g}$ ) and  $S_1$  ( $B_{2u}$ ) and 2 triplet states,  $T_1$  ( $B_{1u}$ ) and the  $x$  component of the doubly degenerate  $T_2$  ( $E_{1u}$ ) state. The parameters for the triplet states have been obtained by performing a fit to *ab-initio* points, as described for the singlet states in chapter 4.

The vertical excitation energies for the triplet states are shown in table 6.1. Values obtained for both  ${}^3B_{1u}$  and  ${}^3E_{1u}$  are close to experimental values, even at CASSCF level. This shows that these states are dominated by singly excited determinants. The  ${}^3B_{2u}$  state is poorly described at CASSCF level, but is much improved by the addition of dynamic correlation with CASPT2. Following calculation of the PES along the normal

Mode	T <sub>1</sub> <sup>3</sup> B <sub>1u</sub>	T <sub>2</sub> <sup>3</sup> E <sub>1u,x</sub>	T <sub>2</sub> <sup>3</sup> E <sub>1u,y</sub>
$\nu_1$ (1a <sub>1g</sub> )	0.280	0.347	0.347
$\nu_{6a}$ (1e <sub>2g</sub> , x)	–	0.014	-0.014
$\nu_{9a}$ (1e <sub>2g</sub> , x)	–	0.080	-0.080

Table 6.2: On-diagonal linear coupling constants,  $\kappa_\alpha$  (in eV), for the important normal modes of benzene in the triplet manifold. Obtained by fitting a Vibronic Coupling Hamiltonian to the adiabatic potential energy surfaces at the CASPT2(6,6) level.

modes it was decided that  $\tilde{C}^3B_{2u}$  plays no significant role in the dynamics in the triplet manifold and therefore was ignored for the rest of the calculations. All of the *ab-initio* points along the normal modes were calculated using PT2(6,6)/Roos(3s2p1d/2s) basis to keep continuity with the singlet calculations.

The PES along the normal modes in the triplet manifold closely mirror the behaviour seen in the singlet manifold and parameters up to 4<sup>th</sup> order are required to produce an accurate fit. Symmetry considerations and the reduced dimensionality means that many of the possible parameters do not need to be evaluated, greatly reducing the computational effort.

### 6.1.1 First Order Parameters

Tables 6.2 and 6.3 show the on- and off-diagonal first order parameters. The on-diagonal,  $\kappa$ , parameters, as discussed in chapter 4 define the distance the excited state minima is shifted from the ground state minimum. The off-diagonal,  $\lambda$ , are responsible for coupling between electronic states. Comparison between the  $\kappa$  parameters in the triplet and singlet manifold shows that the displacement of <sup>3</sup>B<sub>1u</sub> and <sup>3</sup>E<sub>1u</sub> along  $\nu_1$  corresponds very closely to that seen in <sup>1</sup>B<sub>1u</sub> and <sup>1</sup>E<sub>1u</sub> respectively, indicating the similarity between states of the same symmetry despite differing multiplicities.

Table 6.3 shows the off-diagonal inter-state coupling. Similar to the on-diagonal parameters, these parameters show the same effects as seen in the singlet manifold. There is significant PJT coupling between <sup>3</sup>B<sub>1u</sub> and <sup>3</sup>E<sub>1u</sub> along  $\nu_{6a}$ ,  $\nu_{8a}$  and  $\nu_{9a}$ . JT coupling is present along  $\nu_6$  and  $\nu_9$ , but is small.

	$T_1 \ ^3B_{1u}$	$T_2 \ ^3E_{1u,x}$
$T_1 \ ^3B_{1u}$	–	–
$T_2 \ ^3E_{1u,x}$	$\lambda_{6a} = 0.013$	–
	$\lambda_{8a} = 0.143$	–
	$\lambda_{9a} = 0.157$	–
$T_2 \ ^3E_{1u,y}$	$\lambda_{6b} = -0.013$	$\lambda_{6b} = 0.014$
	$\lambda_{8b} = -0.143$	$\lambda_{9b} = 0.08$
	$\lambda_{9b} = -0.157$	–

Table 6.3: Off-diagonal linear coupling constants,  $\lambda_\alpha$  (in eV), for the important normal modes of benzene in the triplet manifold. Obtained by fitting a Vibronic Coupling Hamiltonian to the adiabatic potential energy surfaces at the CASPT2(6,6) level. The columns and rows are the different states, subscripts denote the normal modes providing the coupling. The  $E_{1u,y}$  column is not included as it would symmetrically replicate the  $x$  component data.

### 6.1.2 Second Order Parameters

Tables 6.4 and 6.5 show the on- and off- diagonal second order coupling constants. Comparison between the triplet and singlet parameters for the on-diagonal elements shows that they follow the same trends, albeit with a smaller magnitude. The largest parameters are found for  $\nu_4$  and  $\nu_{16}$ , showing that the potential along these modes, like in the singlet manifold are very flat.

Table 6.5 shows the off-diagonal elements which is responsible for coupling between vibrational degrees of freedom and phenomena such as IVR. The parameters are generally very small, but show a slight coupling between all the important vibrational degrees of freedom. These parameters are generally between 2-4 times smaller than found in the singlet manifold and thus are not expected to have a huge effect of the nature of the dynamics

Some of the surfaces are anharmonic, therefore third and fourth order terms are required to improve the fit, especially at points a long way from the equilibrium geometry and along diagonal cuts between normal modes. Table 6.6 shows the quartic fourth order parameters required for the triplet states. These parameters show that in general the triplet states are much more harmonic because these parameters are typically an order of magnitude smaller than their singlet counterparts.



	$T_1 \ ^3B_{1u}$	$T_2 \ ^3E_{1u,x}$	$T_2 \ ^3E_{1u,y}$
$\nu_1$	0.032	-0.011	-0.011
$\nu_4$	-0.072	-0.071	-0.071
$\nu_{6a}$	-0.014	-0.010	-0.009
$\nu_{6b}$	-0.016	-0.004	-0.011
$\nu_{14}$	0.046	0.075	0.075
$\nu_{15}$	0.004	0.005	0.005
$\nu_{16a}$	-0.028	-0.076	-0.018
$\nu_{16b}$	-0.025	-0.066	-0.017

Table 6.4: On-diagonal second order coupling constants (in eV),  $\gamma_\alpha$ , for the important normal modes of benzene in the triplet manifold. Obtained by fitting a Vibronic Coupling Hamiltonian to the adiabatic potential energy surfaces at CASPT2(6,6) level.

	$T_1 \ ^3B_{1u}$	$T_2 \ ^3E_{1u,x}$	$T_2 \ ^3E_{1u,y}$
$\nu_{1-4}$	–	-0.005	–
$\nu_{1-16a}$	0.009	-0.018	-0.010
$\nu_{1-16b}$	–	-0.019	-0.010
$\nu_{4-16a}$	–	-0.009	–
$\nu_{16a-16b}$	-0.011	-0.013	-0.009
$\nu_{6a-16b}$	–	0.014	–
$\nu_{4-16b}$	–	-0.006	–

Table 6.5: Off-diagonal intrastate second order coupling constants (in eV),  $\gamma_{\alpha\beta}$  for the important normal modes of benzene in the triplet manifold. Obtained by fitting a Vibronic Coupling Hamiltonian to the adiabatic potential energy surfaces at CASPT2(6,6) level.

	$T_1 \ ^3B_{1u}$	$T_2 \ ^3E_{1u, x}$	$T_2 \ ^3E_{1u, y}$
$\nu_4$	0.003	0.004	0.004
$\nu_{6a}$	-0.001	–	–
$\nu_{6b}$	-0.002	–	–
$\nu_{14}$	0.016	0.005	0.006
$\nu_{15}$	0.006	0.006	0.007
$\nu_{16a}$	0.003	0.003	0.003
$\nu_{16b}$	0.004	0.003	0.003

Table 6.6: On-diagonal quartic coupling constants,  $\epsilon_\alpha$  (in eV) for the normal modes of benzene. Obtained by fitting a vibronic Hamiltonian to the adiabatic potential energy surfaces at CASPT2(6,6) level.

In order to accurately describe the profile of triplet states, particularly  $T_{2,x}$  along the vector leading to the  $S_1/S_0$  CI we are required to include off-diagonal third order terms ( $\iota$ ), as discussed in section 4.3. In this model we include two important  $\iota$  terms on  $T_{2,x}$ :  $\iota_{1-4}^{(i)} = 0.0150\text{eV}$  and  $\iota_{1-16a}^{(i)} = 0.0142\text{eV}$ .

### 6.1.3 Cuts Through The Potential Energy Surfaces

Figures 6.1 and 6.2 show fitted cuts through the triplet PES for the most important modes in benzene. In the case of doubly degenerate modes only the  $x$  component is shown, because of the similarity between the two components.

Both of the minima of the triplet states along  $\nu_1$  are shifted from the singlet ground state equilibrium, and like the singlet excited states this is due to the significant role that excited determinants plays in these states.  $\nu_4$  the chair mode is a particularly flat mode, in which degeneracy of  $T_2$  is not broken at any point.

Along  $\nu_{6a}$  there is splitting of  $T_2$ , this is a combination of JT and PJT coupling, however as shown in the parameters section both of these are quite small. Splitting is also seen along the very flat  $\nu_{16a}$ , this is due to a second order JT splitting, first order couplings along this mode are zero by symmetry. Along the higher frequency  $e_{2g}$  modes,  $\nu_{8a}$  and  $\nu_{9a}$  we see significant splitting of the two components of the  $T_2$  state. This is due to strong PJT coupling along these modes.

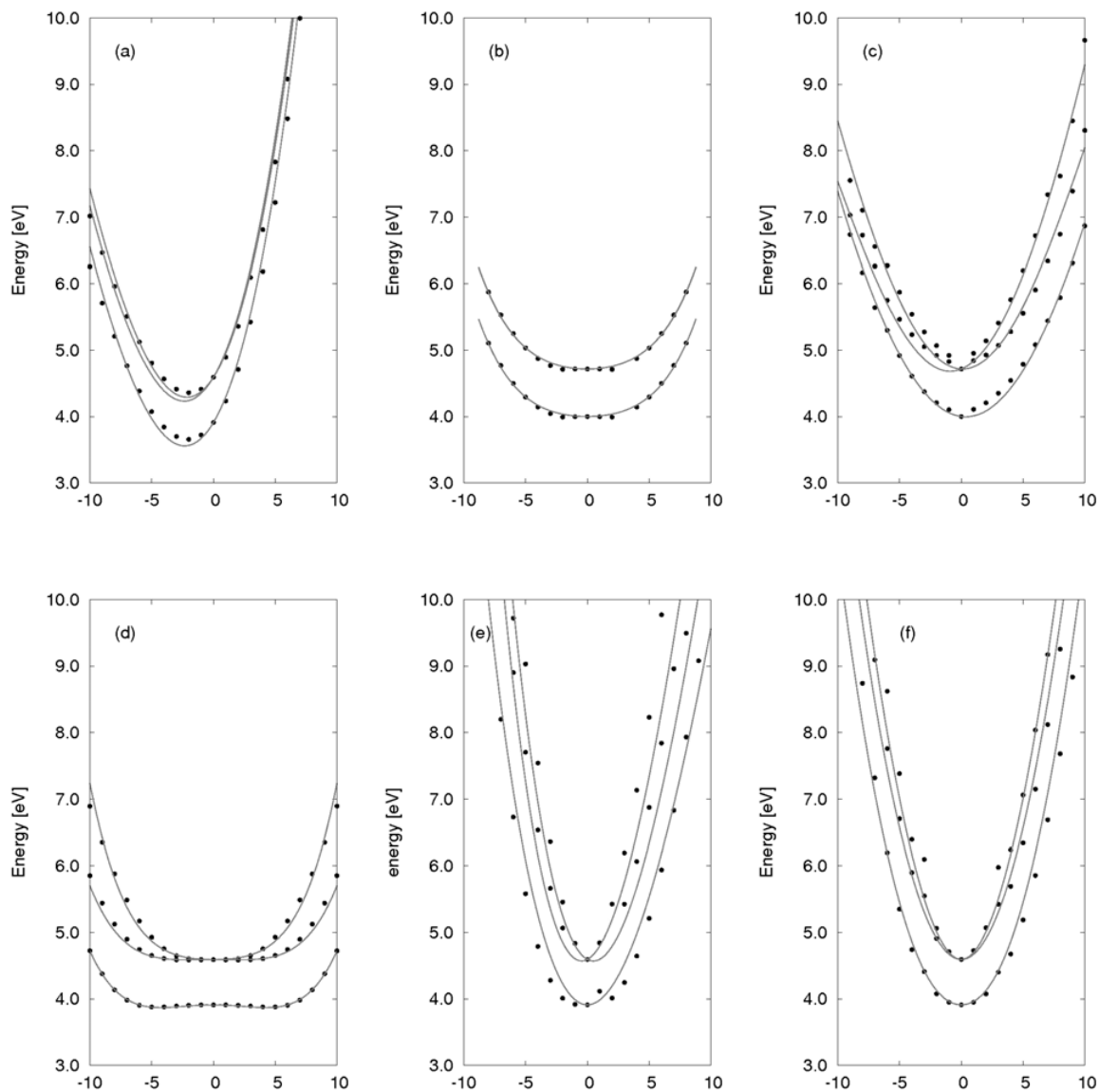


Fig. 6.1: Cuts along the normal modes for the triplet potential energy surfaces in benzene. In order of energy at  $\mathbf{Q}=0$  these states are  $T_1$  ( $B_{1u}$ ) and  $T_2$  ( $E_{1u}$ ). (a)  $\nu_1$  ( $1a_{1g}$ ), the breathing mode, (b)  $\nu_4$  ( $1b_{2g}$ ), the chair mode, (c)  $\nu_{6a}$  ( $1e_{2g}$ ), the quinoid mode (d)  $\nu_{16a}$  ( $1e_{2u}$ ), the boat mode, (e)  $\nu_{8a}$  ( $3e_{1g}$ ) (f)  $\nu_{9a}$  ( $2e_{1g}$ )

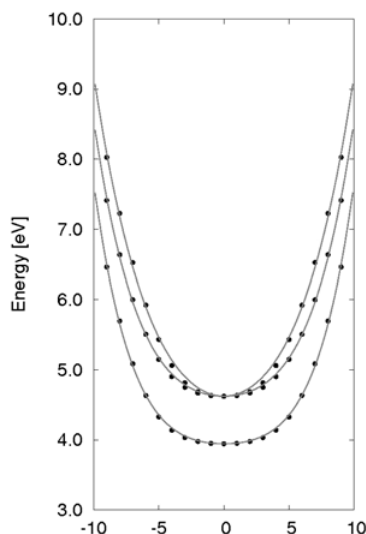


Fig. 6.2: Cut along the prefulvene combination mode ( $\nu_4 + \nu_{16a}$ ) for the triplet potential energy surfaces in benzene. In order of energy at  $\mathbf{Q}=0$  these states are  $T_1$  ( $B_{1u}$ ) and  $T_2$  ( $E_{1u}$ ).

Figure 6.2 shows the cut along the prefulvene combination mode ( $\nu_{4-16a}$ ). This shows the flat nature of the triplet states along this mode and splitting of the  $T_2$  degeneracy due to second order JT coupling.

### 6.1.4 Spin Orbit Coupling Parameters

The nature and effect of vibrations on SOC in benzene was discussed in detail in chapter 5. There is symmetry allowed SOC at equilibrium between  $S_1/T_1 \sim 0.11\text{cm}^{-1}$ . Higher order terms, included by calculating the gradient of the SOC along each normal mode and the important combination modes, are shown in the tables 6.7 and 6.8. It is noted that in the final model some of the couplings used are greater than presented in tables 6.7 and 6.8, but are within  $1\text{cm}^{-1}$ .

Tables 6.7 and 6.8 shows the first and second order spin orbit coupling terms which are included into the Hamiltonian in the same manner as the parameters for the singlet

Mode	S <sub>1</sub> /T <sub>1</sub> (cm <sup>-1</sup> )	S <sub>1</sub> /T <sub>2,x</sub> (cm <sup>-1</sup> )	S <sub>1</sub> /T <sub>2,y</sub> (cm <sup>-1</sup> )
$\nu_1$	0.01 ( <i>z</i> )	0	0
$\nu_2$	0.02 ( <i>z</i> )	0	0
$\nu_{6a}$	0	0.04 ( <i>x,y</i> )	0
$\nu_{6b}$	0	0	0.04 ( <i>x,y</i> )
$\nu_{7a}$	0	0.09 ( <i>x,y</i> )	0
$\nu_{7a}$	0	0	0.09 ( <i>x,y</i> )
$\nu_{8a}$	0	0.07 ( <i>x,y</i> )	0
$\nu_{8a}$	0	0	0.07 ( <i>x,y</i> )
$\nu_{9a}$	0	0.05 ( <i>x,y</i> )	0
$\nu_{9a}$	0	0	0.05 ( <i>x,y</i> )
$\nu_{10a}$	0.08 ( <i>z</i> )	0.16 ( <i>x,y</i> )	0
$\nu_{10b}$	0.08 ( <i>z</i> )	0	0.17 ( <i>x,y</i> )

Table 6.7: First order vibrational spin orbit coupling terms. Calculations performed with (6,6) active space and Molpro specific Roos(3s2p1d/2s) basis.

and triplet surfaces. i.e

$$W_{st}^{(1)} = \sum_{\alpha} \kappa_{\alpha}^{(st)} Q_{\alpha} \quad (6.1)$$

$$W_{st}^{(2)} = \frac{1}{2} \sum_{\alpha,\beta} \gamma_{\alpha,\beta}^{(st)} Q_{\alpha} Q_{\beta} \quad (6.2)$$

Where  $\kappa_{\alpha}^{(st)}$  and  $\gamma_{\alpha,\beta}^{(st)}$  are the first and second order parameters for the Hamiltonian (see also section 2.4).

One can see that the most significant vibrational first order term are between S<sub>1</sub>/T<sub>2</sub>, this is most evident along  $\nu_{10a}$  and  $\nu_{10b}$ , however there is also significant coupling along  $\nu_{6a}$  and  $\nu_{7a}$ . Second order coupling is most significant along  $\nu_{11}$ , an out of plane hydrogen bending mode, importantly there is significant coupling along  $\nu_4$ ,  $\nu_5$ ,  $\nu_{16}$  and  $\nu_{4+6}$  whose motion has been shown to be critical to the dynamics of benzene.

### 6.1.5 Effective Couplings

Quantum dynamics simulations are extremely computational expensive, this expense increases exponentially with the number of electronic states and DOF included in the calculation. This is be a huge problem in systems which contain significant vibronic coupling because there are many states that play a role. However the highly symmetric

Mode(s)	$S_1/T_1$ (cm <sup>-1</sup> )	$S_1/T_{2,x}$ (cm <sup>-1</sup> )	$S_1/T_{2,y}$ (cm <sup>-1</sup> )
$\nu_4$	0.05 ( $x,y$ )	0	0
$\nu_5$	0.35 ( $x,y$ )	0	0
$\nu_{11}$	0.11 ( $z$ )	0.41 ( $x,y$ )	0.41 ( $x,y$ )
$\nu_{16a}$	0.04 ( $z$ )	0.06 ( $x,y$ )	0
$\nu_{16b}$	0.04 ( $z$ )	0	0.06 ( $x,y$ )
$\nu_{17a}$	0.06 ( $z$ )	0.11 ( $x,y$ )	0
$\nu_{17b}$	0.06 ( $z$ )	0	0.11 ( $x,y$ )
$\nu_4 + \nu_{6a}$	0.04 ( $x,y$ )	0.10 ( $x,y,z$ )	0
$\nu_4 + \nu_{6b}$	0.04 ( $x,y$ )	0	0.10 ( $x,y,z$ )
$\nu_{6a} + \nu_{10a}$	0.11 ( $x,y$ )	0.16 ( $x,y$ )	0
$\nu_{6a} + \nu_{10b}$	0.11 ( $x,y$ )	0	0.16 ( $x,y$ )
$\nu_{6b} + \nu_{10a}$	0.11 ( $x,y$ )	0.16 ( $x,y$ )	0
$\nu_{6b} + \nu_{10b}$	0.11 ( $x,y$ )	0	0.16 ( $x,y$ )
$\nu_{11} + \nu_{16a}$	0	0.18 ( $z$ )	0
$\nu_{11} + \nu_{16b}$	0	0	0.18 ( $z$ )
$\nu_{16a} + \nu_{16b}$	0.03 ( $z$ )	0.10 ( $x,y$ )	0.05 ( $x,y$ )
$\nu_{16a} + \nu_{17a}$	0.09 ( $z$ )	0.12 ( $z$ )	0
$\nu_{16a} + \nu_{17b}$	0.09 ( $z$ )	0	0.12 ( $z$ )
$\nu_{16b} + \nu_{17a}$	0.09 ( $z$ )	0	0.12 ( $z$ )
$\nu_{16b} + \nu_{17b}$	0.09 ( $z$ )	0.12 ( $z$ )	0

Table 6.8: Second order vibrational spin orbit coupling terms. Values above the middle double line are on-diagonal terms and below are off-diagonal. Calculations performed with (6,6) active space and Molpro specific Roos(3s2p1d/2s) basis.

nature of couplings such as JT and PJT make it possible to ignore one half of doubly degenerate modes and states and form an effective coupling. This has been previously considered by Domcke *et al* [149]. The resulting Hamiltonian is referred to as a cluster Hamiltonian.

If we consider a 3x3 case, a singlet state coupled to the  $x$  and  $y$  component of a doubly degenerate triplet state we write:

$$W_{11} = \langle {}^1\phi | H_{el} | {}^1\phi \rangle \quad (6.3a)$$

$$W_{22} = \langle {}^3\phi_x | H_{el} | {}^3\phi_x \rangle \quad (6.3b)$$

$$W_{33} = \langle {}^3\phi_y | H_{el} | {}^3\phi_y \rangle \quad (6.3c)$$

$$W_{12} = \langle {}^1\phi | H_{so} | {}^3\phi_x \rangle \quad (6.3d)$$

$$W_{13} = \langle {}^1\phi | H_{so} | {}^3\phi_y \rangle \quad (6.3e)$$

where  $|{}^1\phi\rangle$ ,  $|{}^3\phi_x\rangle$  and  $|{}^3\phi_y\rangle$  are eigenfunctions of  $H_{el}$  and  $H_{so}$  is the spin orbit Hamiltonian. The secular determinant can be written:

$$W = \begin{vmatrix} W_{11} - V & W_{12} & W_{13} \\ W_{21} & W_{22} - V & W_{23} \\ W_{31} & W_{32} & W_{33} - V \end{vmatrix} = 0 \quad (6.4)$$

We are only considering the coupling between the singlet and triplet manifold, and therefore ignore coupling between the triplet states, therefore  $W_{23}$  and  $W_{32} = 0$ . Expanding the secular determinant we write:

$$(W_{11} - V) \begin{vmatrix} W_{22} - V & 0 \\ 0 & W_{33} - V \end{vmatrix} - W_{12} \begin{vmatrix} W_{21} & 0 \\ W_{31} & W_{33} - V \end{vmatrix} + W_{13} \begin{vmatrix} W_{21} & W_{22} - V \\ W_{31} & 0 \end{vmatrix} = 0 \quad (6.5a)$$

$$\begin{aligned} -V^3 + W_{22}V^2 + W_{33}V^2 + W_{11}V^2 - W_{11}W_{22}V - W_{11}W_{33}V - W_{22}W_{33}V + W_{12}^2V \\ - W_{13}^2V + W_{11}W_{22}W_{33} + W_{12}^2W_{33} + W_{13}^2W_{22} = 0 \end{aligned} \quad (6.5b)$$

By removing the orthogonal terms the equation reduces to:

$$-V^3 + W_{22}V^2 + W_{33}V^2 + W_{11}V^2 + W_{12}^2V + W_{13}^2V = 0 \quad (6.6)$$

Because the coupling between the singlet state and each component of the triplet is the same, hence  $W_{12}=W_{13}$ , we can rewrite the above equation as:

$$-V^3 + W_{11}V^2 + W_{22}V^2 + W_{33}V^2 + 2W_{13}^2V = 0 \quad (6.7)$$

This can be factorised:

$$-V(V^2 - (W_{11} + W_{22} + W_{33})V - 2W_{13}^2) = 0 \quad (6.8)$$

By solving the quadratic we can write:

$$V = \frac{W_{11} + W_{22} + W_{33}}{2} \pm \frac{1}{2} \sqrt{(W_{11} + W_{22} + W_{33})^2 + 4 \times 2W_{13}^2} \quad (6.9)$$

By comparing this to the 2\*2 diabatic coupling matrix, equation 2.20, instantly we can see that by considering the  $W_{12}=W_{13}$ , we obtain a prefactor to the coupling term of  $\sqrt{2}$ . Therefore to treat a doubly degenerate states which are both coupled to the same singly degenerate state with the same magnitude, the state can be treated as one state providing the coupling size is multiplied by  $\sqrt{2}$ .

## 6.2 The Dynamics

The dynamics calculation includes both singlet state, the  $T_1$  state and the  $x$  component of the doubly degenerate  $T_2$  state, taking into account the effective coupling discussed above. The normal modes included are the same used in the singlet model, but  $\nu_{8a}$  and  $\nu_{9a}$  are also included due to the strong PJT effect in the triplet manifold along these modes. The dynamics were performed using the details shown in table 6.9. This basis guaranteed convergence for 1000fs on all states and for the full 2000fs for  $S_1$ ,  $T_1$ ,  $T_2$ . The highly vibrationally excited nature of the  $S_0$  state made convergence for 2000fs unrealistic.

Figure 6.3a shows the relative diabatic state populations of  $\tilde{A}$  ( $S_1$  in the FC region before the barrier) and  $S_1$ +triplet population. These have been plotted to replicate the experimental data presented in 4.14b. The dynamics show, like the singlet model



Mode	$N_i$	$n_0, n_1, n_2, n_3, n_4$
$\nu_{16b}$	121	40,22,8,8
$\nu_4$	111	40,22,8,8
$\nu_{6a}$	27	40,22,8,8
$\nu_{8a}$	27	10,10,4,4
$\nu_{9a}$	27	10,10,4,4
$\nu_1$	60	40,22,8,8
$\nu_{14}$	91	40,22,8,8
$\nu_{15}$	15	40,22,8,8

Table 6.9: Computational details for the quantum dynamics simulations using the Intersystem crossing model Hamiltonian.  $N_i$  is the number of primitive Harmonic oscillator DVR basis functions used to describe each mode [78].  $n_i$  are the number of single-particle functions used for the wavepacket on each state. The modes are combined to produce 4 2D singlet particle functions, to reduce the computational expense. The CPU was 620 hours

two distinct decay timescales, a faster timescale for the first 500fs followed by a slower decay. After 500fs the population of  $\tilde{A}$ , corresponding to the ionisation using the weaker probe pulse, is 51% and the population  $S_1$ +triplet state population, corresponding to the ionisation using the stronger probe pulse, is 68%. These values agree very closely with those found from experimental data (shown in 4.14b).

After 500fs a slower decay occurs, this decay is larger than found experimentally, this highlights the inaccuracies created by using the reduced dimensionality model, discussed with respect to the two state singlet model in chapter 4. The reduced dimensionality means that the barrier which exists near to the FC point on  $S_1$  along the prefulvene reaction coordinate is not described as well as would be in full space and hence after 500fs small amounts of the wavepacket is still able to surmount the barrier and propagate along the prefulvene coordinate, decay through the  $S_1/S_0$  CI and also to populate the triplet states.

Figure 6.3b shows the diabatic state populations of each triplet state. The total population of the triplet states (blue line) shows that the population increases throughout. The population of the triplet states occurs with the same two timescale increase as seen in the decay through the  $S_1/S_0$  CI. The initial population is of the  $T_{2,x}$  state,

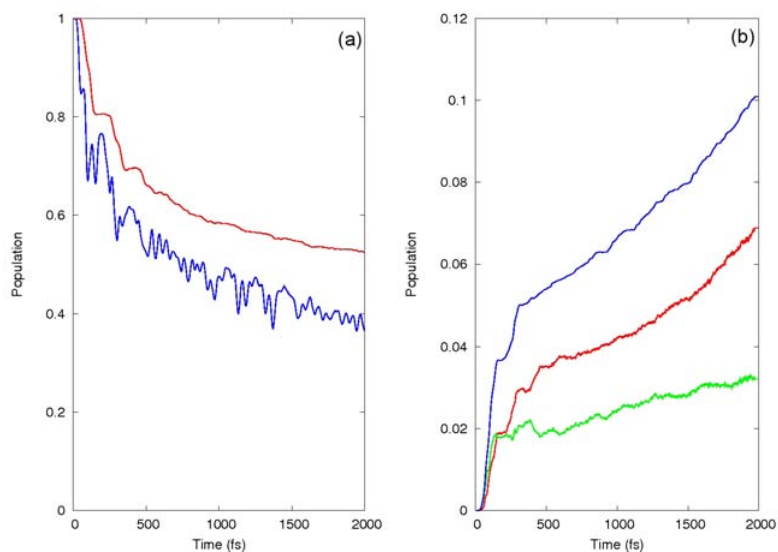


Fig. 6.3: (a) Diabatic state populations of benzene during the first 2000fs following excitation of the hot wavepacket into  $S_1$ . The blue line is the population of  $S_1$  minus the population which is over the barrier to the  $S_1/S_0$  population. This corresponds to the photoelectron data using the 254nm probe wavelength. The red line is the population of  $S_1$  plus the triplet populations corresponding the photoelectron data using the 235nm probe wavelength. (b) Diabatic state populations of the benzene triplet states during the first 2000fs following excitation of the hot wavepacket into  $S_1$ .  $T_1$  (red),  $T_{2,x}$  (green) and the sum of all of the triplets (blue).

however due to the strong vibronic coupling which exists between  $T_{2,x}$  and  $T_1$  along  $\nu_{8a}$  and  $\nu_{9a}$  population of  $T_1$  occurs very rapidly and contains the greatest population after 250fs. After 500fs the population of the total population of the triplet states is 6%, this is significant considering the size of the SOC.

The population of the triplet state occurs along the prefulvene coordinate due to degeneracy between  $S_1$  and  $T_{2,x}$  along with reaction vector. We see an increase in the population of  $T_1$  around 1500fs. Although this is not a fast decay, it is larger than expected and is because the reduced dimensionality means more wavepacket is able to cross the barrier on  $\tilde{A}$ , however after 1500fs of the propagation the wavepacket does not have enough energy to reach the  $S_1/S_0$  CI, but can still reach the  $S_1/T_1$  CI which is along the same coordinate, but closer to the FC point.

The position and width of the wavepacket in the triplet states are shown in figures

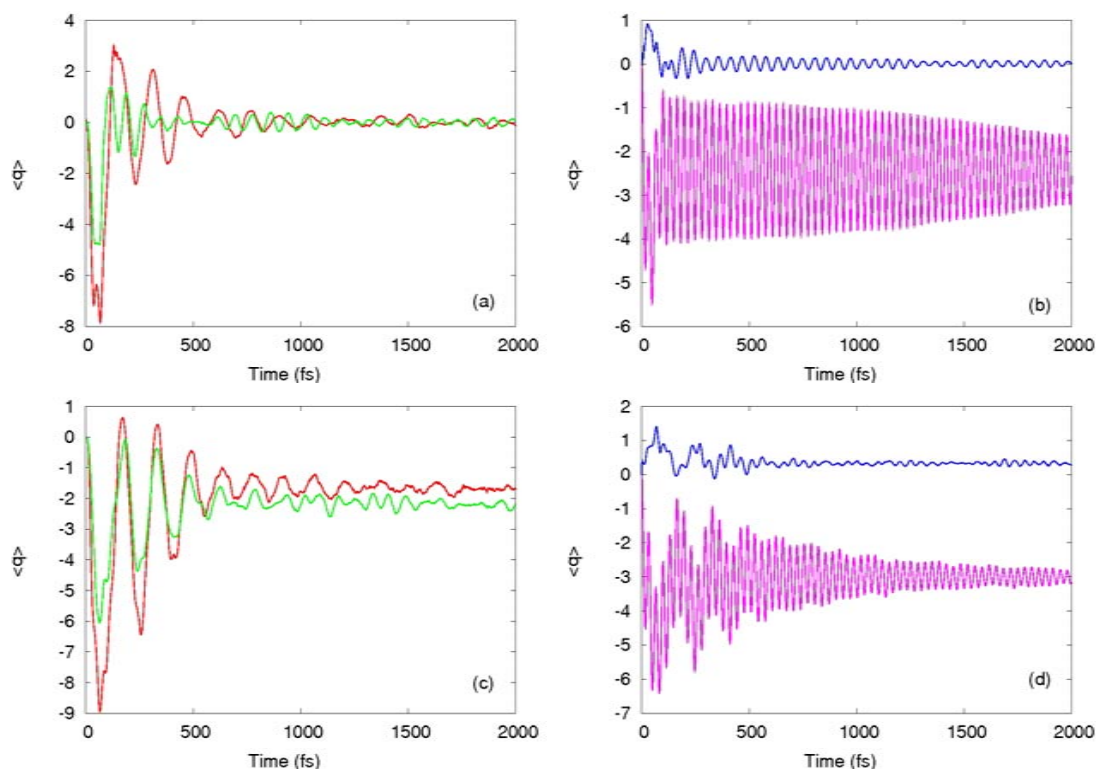


Fig. 6.4: Expectation values of the position of the hot wavepacket in the triplet states during propagations for first 2000fs. (a)  $\langle q \rangle$  of  $\nu_4$  (green) and  $\nu_{16}$  (red) on  $T_1$ . (b)  $\langle q \rangle$  of  $\nu_1$  (purple) and  $\nu_6$  (blue) on  $T_1$ . (c)  $\langle q \rangle$  of  $\nu_4$  (green) and  $\nu_{16}$  (red) on  $T_{2,x}$ . (d)  $\langle q \rangle$  of  $\nu_1$  (purple) and  $\nu_6$  (blue) on  $T_{2,x}$ .

6.4 and 6.5. Upon inspection of the figure 6.4a,b and c,d we see that population of the  $T_1$  and  $T_{2,x}$  state initially occurs at their respective intersections with  $S_1$  along the prefulvene reaction coordinate. Following population, the wavepacket oscillates along the reaction coordinate, this is most evident in  $T_{2,x}$  state. In both cases the oscillations reduce after 500fs, as the wavepacket begins to relax into the equilibrium position. The width of the wavepacket (shown in figure 6.5) is similar on both triplet states. This is because the location of the intersection for both states means that any population will be very vibrationally hot and therefore the wavepacket will spread over a large part of the coordinate space.

The motion of the wavepacket along modes  $\nu_1$ ,  $\nu_4$ ,  $\nu_{6a}$  and  $\nu_{16a}$  for each of the triplet states is shown in figures 6.6, 6.7, 6.8, 6.9. We see that most of the wavepacket

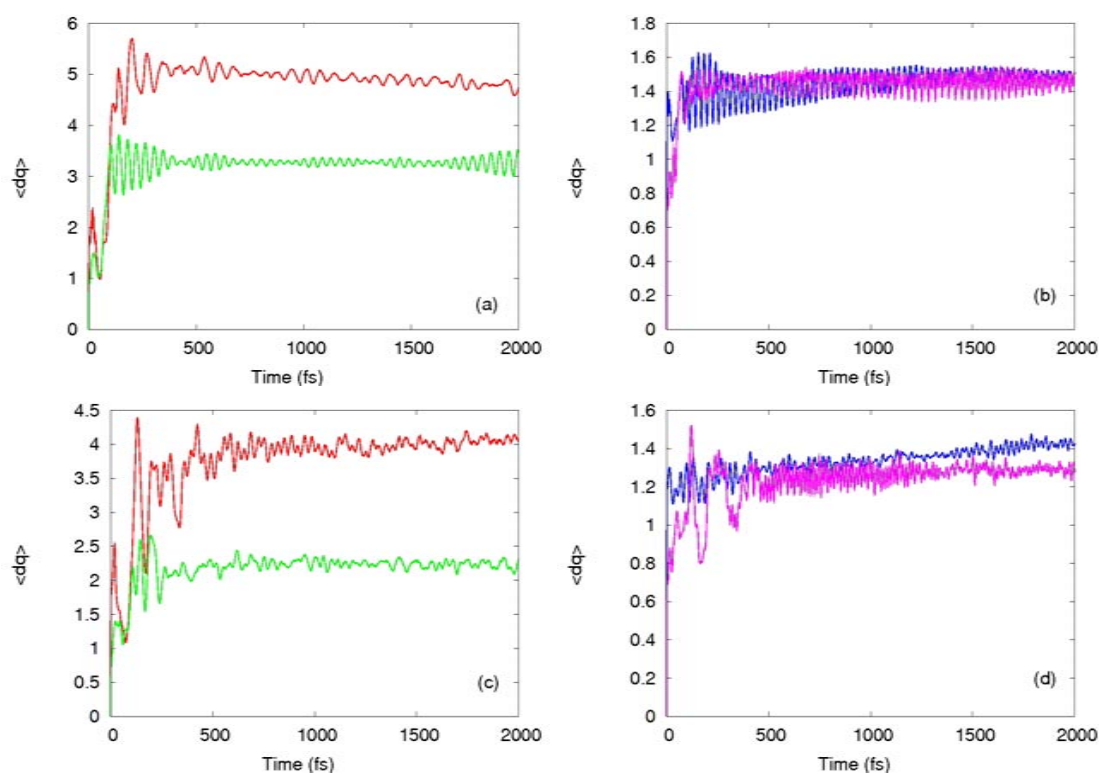


Fig. 6.5: Expectation values of the width of the hot wavepacket in the triplet states during propagations for first 2000fs. (a)  $\langle q \rangle$  of  $\nu_4$  (green) and  $\nu_{16}$  (red) on  $T_1$ . (b)  $\langle q \rangle$  of  $\nu_1$  (purple) and  $\nu_6$  (blue) on  $T_1$ . (c)  $\langle q \rangle$  of  $\nu_4$  (green) and  $\nu_{16}$  (red) on  $T_{2,x}$ . (d)  $\langle q \rangle$  of  $\nu_1$  (purple) and  $\nu_6$  (blue) on  $T_{2,x}$ .

in the triplet manifold populates the  $T_1$ , as discussed this is due to the strong vibronic coupling between the  $T_1$  and  $T_{2,x}$  states.

Figures 6.6 and 6.7 show the wavepacket on  $T_1$ . These show that the initial population on the  $T_1$  state is slow and it is not until 200fs that there is significant population. It is clear from the plots that the wavepacket in this state is very vibrationally hot, this is most evident in figure 6.6j which has a similar structure to the vibrationally hot wavepacket in  $S_0$  shown in figure 4.29.

The wavepacket motion on  $T_{2,x}$  (shown in figures 6.8 and 6.9), are unsurprisingly very similar to those seen on  $S_1$  (figures 4.31 and 4.32). Population of this state initially occurs around the region close to the  $S_1/S_0$  CI. Further population also occurs along the whole coordinate leading to the CI as the wavepacket oscillates along this entire mode and  $S_1$  and  $T_{2,x}$  are degenerate at all points.

## 6.3 Conclusion

ISC crossing and the triplet states are known to play an important role in dynamics. Their involvement depends entirely on the strength of SOC which exists, for this reason the triplet states in molecules such as benzene are often ignored because the absence of heavy atoms means that SOC is typically small.

In this chapter we have presented a model containing 4 electronic states and 8 nuclear DOF. This model is a development of the 2 state singlet model presented in chapter 4. The triplet states ( $T_1$  and  $T_2$ ) which play a significant role in the dynamics are included by using parameters obtained from the fit to *ab-initio* data. SOC coupling parameters included are obtained from the study of the nature of SOC in simple hydrocarbons presented in chapter 5

Dynamics results obtained in this chapter support the experimental observations that, following excitation in the higher vibrational states of benzene ultrafast ISC is witnessed along side the IC which occurs at the  $S_1/S_0$  CI. During the first 500fs between

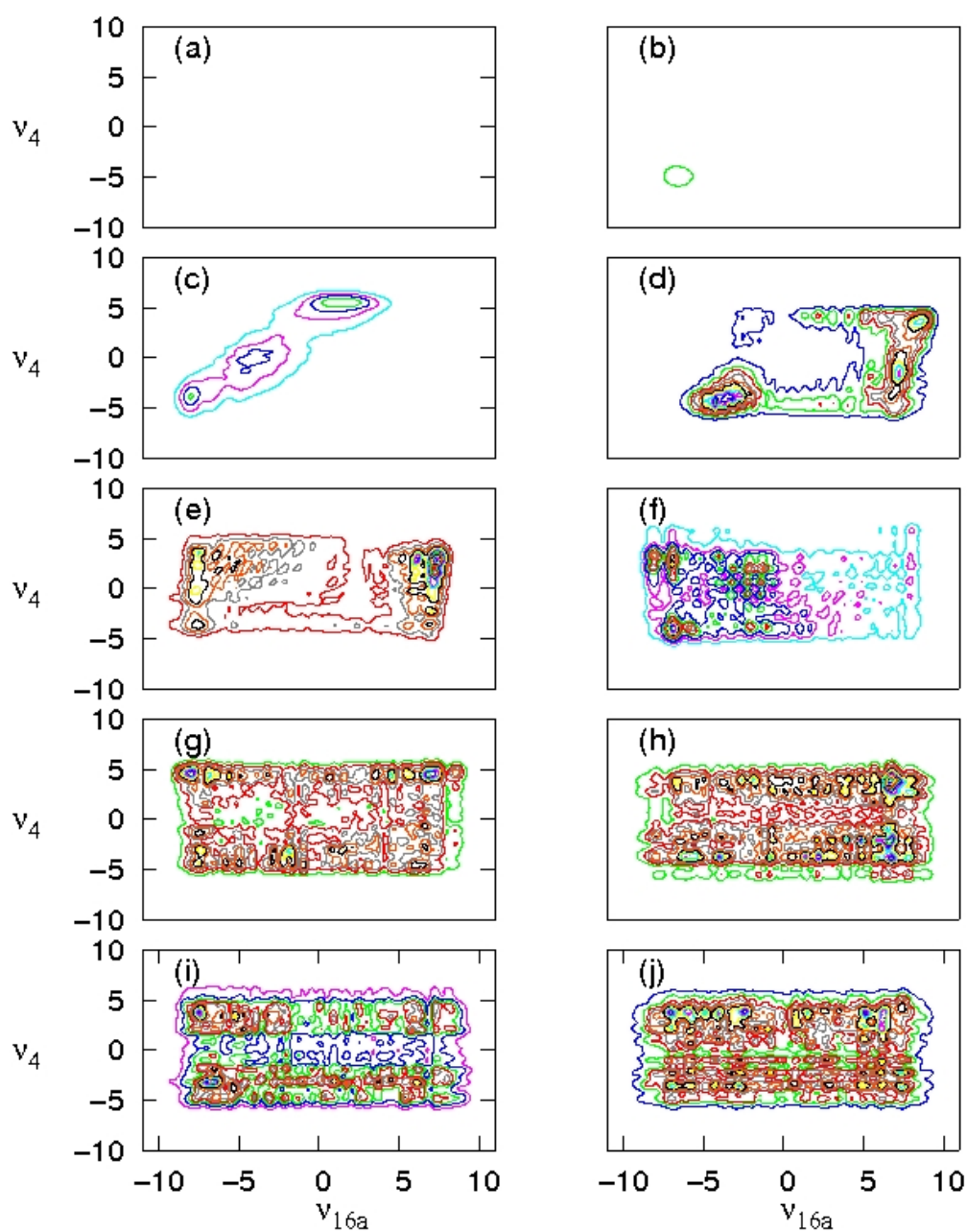


Fig. 6.6: The wavefunction density on  $T_1$  in benzene along  $\nu_4$  and  $\nu_{16a}$ . (a) 0fs (b) 50fs (c) 100fs (d) 150fs (e) 200fs (f) 250fs (g) 350fs (h) 450fs (i) 550fs (j) 1000fs.

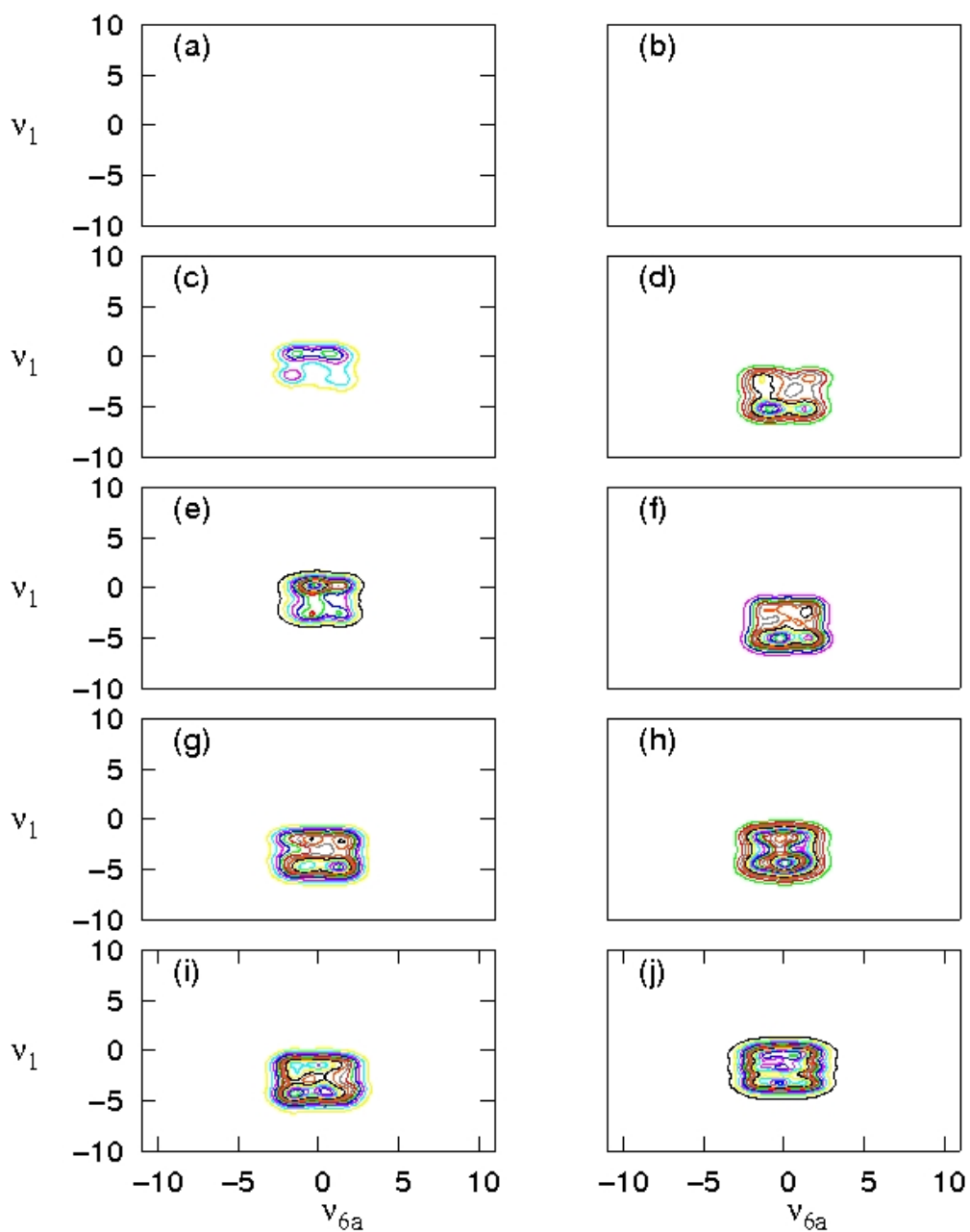


Fig. 6.7: The wavefunction density on T<sub>1</sub> in benzene along  $\nu_1$  and  $\nu_{6a}$ . (a) 0fs (b) 50fs (c) 100fs (d) 150fs (e) 200fs (f) 250fs (g) 350fs (h) 450fs (i) 550fs (j) 1000fs.

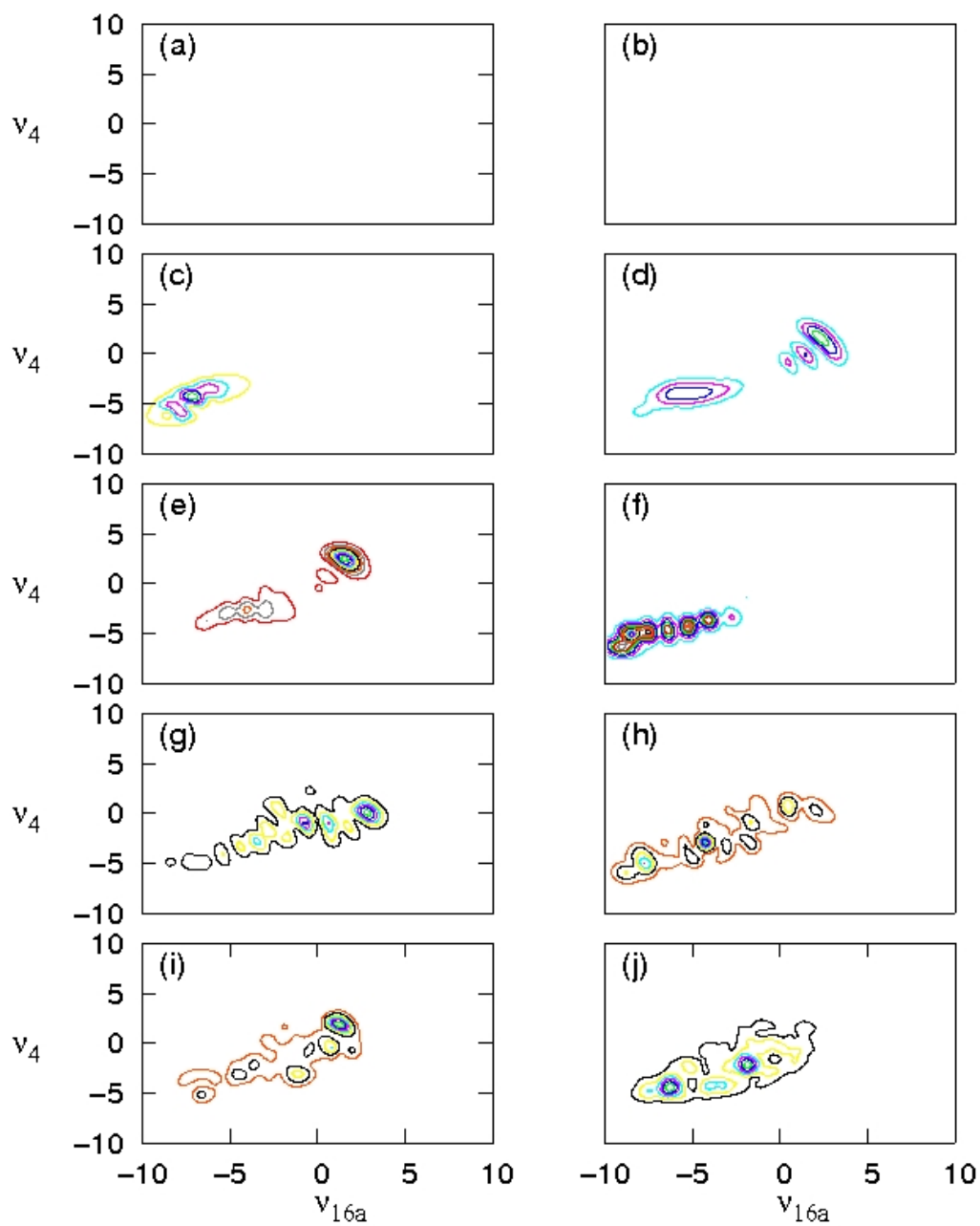


Fig. 6.8: The wavefunction density on  $T_{2,x}$  in benzene along  $\nu_4$  and  $\nu_{16a}$ . (a) 0fs (b) 50fs (c) 100fs (d) 150fs (e) 200fs (f) 250fs (g) 350fs (h) 450fs (i) 550fs (j) 1000fs.



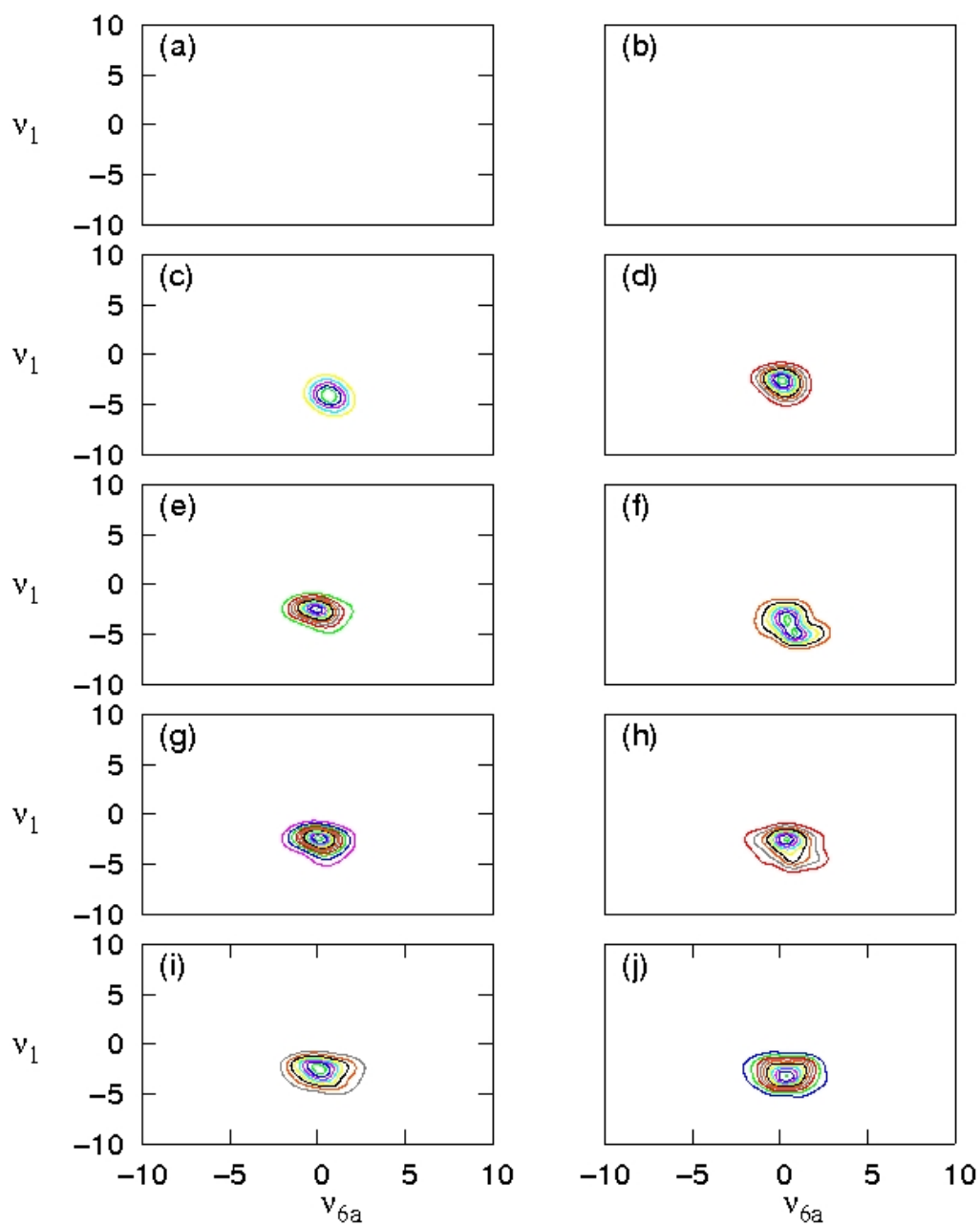


Fig. 6.9: The wavefunction density on  $T_{2,x}$  in benzene along  $\nu_1$  and  $\nu_{6a}$ . (a) 0fs (b) 50fs (c) 100fs (d) 150fs (e) 200fs (f) 250fs (g) 350fs (h) 450fs (i) 550fs (j) 1000fs.

5-10% of the wavepacket crosses into the triplet states giving excellent agreement with experimental data.

These dynamics results allow us to describe the step in the experimental decay curves shown in figure 4.14 and 4.16. When the lower frequency probe (red line) pulse is used, it is only possible to ionise wavepacket in the FC region of  $S_1$ , both theory and experiment show that approximately 50% of the wavepacket decays from this region. Using the higher frequency probe pulse (shown in the slower decaying (blue) line in figure 4.14) it is possible to ionise wavepacket which exists on all of the  $S_1$  surface and triplet states. Experimental and theoretical data indicates that approximately 30% of the wavepacket decay from this region, into  $S_0$ .

These dynamics show the first example of ultrafast intersystem crossing in a simple hydrocarbon. The triplet states in such systems are generally ignored, however the combination of vibronic effects and degeneracy between  $S_1$  and  $T_{2,x}$  along the reaction coordinate provide conditions for ultrafast intersystem crossing to occur.

# Chapter 7

## Coherent Control

Since the advent of femtosecond lasers and the pioneering work of Ahmed Zewail [15, 16, 18, 19] it has been possible to not only witness chemical reactions in real time, but to control them [150]. Lasers, which operate on timescales that are an order of magnitude faster than IVR, in conjunction with pulse shapers utilise the advantages of the wave properties of light to control chemical reactions. This has become a very exciting and active area of research in recent years with a wide range of both experimental and theoretical studies [24, 29, 35, 150–155].

The first control strategies were a simple resonant force approach. A pulse was tuned to the frequency of a selected bond, a second pulse was then used to increase the energy in the excited bond until it broke. Despite promising results with deuterated water [156] these approaches ultimately failed in larger systems due to IVR [20–22]. Since then there has been a wide variety of control strategies developed, the most well known of which are the Brumer-Shapiro (BS) method [24] and the Tannor-Rice-Kosloff (TRK) method [25, 26]. The former showed that by altering the relative phase between two pulses which couple an initial state to a final state allows control of the outcome in the final state. The TRK method uses a more time dependent picture. By timing an ultrashort pulse correctly it was shown to be possible to drive the wavepacket into a desired product channel. The use of the excited state to access the desired minima on the ground state led to this method being referred to as the pump-dump

---

approach. Both of these techniques proved successful for a variety of chemical systems, but more importantly exhibited the strong time and frequency dependence required for controlling chemical reactions.

One of the most commonly used techniques in coherent control is OCT. First proposed by Judson and Rabitz [31, 157], this technique uses a variational principle and iterative process of forward and backward propagations to construct a field which guides the wavefunction optimally towards a predefined target wavefunction. This method has been shown to be extremely successful in numerous theoretical calculations [32, 33]. The nature of the forward and backwards optimisations shows many similarities with the experimental learning algorithm approach commonly used. Despite the successes of the OCT method, there exists two main drawbacks. The nature of the iterative process means that this method can be extremely computational expensive, hence limiting the size of the systems possible to study. Also optimisation of a field using a “global view” can make the pulses very complex and therefore hard to relate to the atomic/molecular dynamics.

LCT first appeared in the formulation of OCT [31, 157], introduced by Kosloff [34, 35]. This method moves away from the picture of a global target, instead the concept used is that the control field is calculated as a function of the instantaneous dynamics of the system at each time step. By defining some operator, such as electronic state population, vibrational state population or nuclear motion, the field is calculated to ensure an increase or decrease in its expectation value. A rigorous explanation is presented in section 2.5.

In this chapter we present preliminary results using operators to control electronic transfer after implementing the local control method in the Heidelberg MCTDH package. We show results of calculations controlling the dynamics in model systems for neutral and cationic cyclobutadiene, pyrazine and ammonia, giving a detailed analysis of the field and resulting dynamics. Comparisons with optimal control calculations are

provided where appropriate. Each of these models contain strong non-adiabatic effects such as vibronic coupling and CI. Control of these multidimensional models therefore represents a challenge for any proposed method.

## 7.1 Methodology and Computation

The dynamics were performed with the Heidelberg MCTDH quantum dynamics package. This efficient algorithm has been used to perform molecular dynamics calculations on a large range of multidimensional system, performing particularly well on larger systems which are typically beyond most other methods [57–59]. The details of each calculation can be found in tables in each section. The Hamiltonian in each calculation has been previously published, the references are included. The FT are performed with the Xmgr semistatic program this can be found at the web page address given in reference [158].

## 7.2 Results

### 7.2.1 Neutral cyclobutadiene

Cyclobutadiene,  $C_4H_4$ , is a simple cyclic hydrocarbon which is a prime example of the importance vibronic coupling can play in the structure and stability of a molecular system. Upon inspection one might expect a square planar  $D_{4h}$  geometry, however this is unstable according to the Hückel  $4n+2$  rule and the geometry is in fact  $D_{2h}$ . This reduction in symmetry is caused by vibronic coupling which exists between the ground state ( $\tilde{X}^1B_{1g}$ ) and first excited state ( $\tilde{A}^1A_{1g}$ ) at  $D_{4h}$  symmetry [129].

The Vibronic Coupling Hamiltonian was calculated in the same manner as the benzene Hamiltonian in chapter 4. Using the  $D_{4h}$  minimum energy as the expansion point *ab-initio* calculations were performed along the normal modes using CASSCF with a (4,4)/6-31g\* basis. First order on-diagonal coupling parameters are present along the breathing ( $\nu_1$ ) mode, causing the displacement of the excited state minima

Mode	$N_i, N_j$	$n_0, n_1, n_2$		
		No control	Maximise $S_1$	Maximise $S_3$
$\nu_4, \nu_6$	51,19	4,4,4	14,14,8	9,14,9
$\nu_1, \nu_5$	11,13	4,4,4	14,14,8	9,14,9
$\nu_7, \nu_2$	21,13	4,4,4	14,14,8	9,14,9
CPU Time	$\lambda=0.01$	1min 53secs	1hrs 37mins	1hrs 36mins
	$\lambda=0.25$	–	1hrs 32mins	33mins 3secs

Table 7.1: Computational details of the quantum dynamics simulations for the control of cyclobutadiene.  $N_i$  is the no. of primitive Harmonic oscillator DVR basis functions used to describe each mode [78].  $n_i$  are the number of singlet particle functions used for the wavepacket on each state.  $\lambda$  denotes the strength parameter of the pulse. Note that some of the variation in the CPU is because of different  $T_{final}$ .

from the ground state minima (figure 7.1a). There is also significant first order off-diagonal coupling between  $S_0/S_1$  along  $\nu_4$ . This is responsible for the lowering of symmetry and double minima along this mode (figure 7.1b). Coupling between  $S_1/S_2$  exists along  $\nu_6$  (figure 7.1c). Second order coupling parameters are present along  $\nu_5$ . Further details and discussion of the model can be found in [129].

Details of the MCTDH calculations are shown in table 7.1, convergence is ensured for the full propagation. Each calculation contains 3 electronic states which play an important role in the dynamics and 6 vibrational DOF which contain significant coupling parameters and the higher frequency  $a_g$  mode and  $b_{2g}$  mode. In the control calculations from  $S_1$  to  $S_0$  the transition dipole is consider linear along  $\nu_4$ . For the transfer from  $S_1$  to  $S_2$  the transition dipole is consider linear along  $\nu_6$ .

Figure 7.3 shows the diabatic state populations of the three lowest singlet states in neutral cyclobutadiene (with no external field) following a vertical excitation into  $S_1$ . There are small oscillations in the populations between all the states due to vibronic coupling, however there is no significant electronic transfer and wavepacket is stable in the  $S_1$  minima.

Figures 7.4a and 7.5a show the diabatic state populations when the calculated external field (figures 7.4b and 7.5b), is applied to control the transfer of electronic

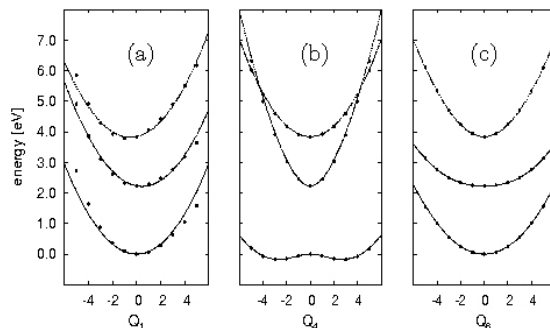


Fig. 7.1: “Cuts through potential energy surface for the lowest 3 singlet states  $\tilde{X}^1B_{1g}$ ,  $\tilde{A}^1A_g$ , and  $\tilde{B}^1B_{2g}$  of neutral cyclobutadiene along the  $D_{4h}$  normal vibrational modes (a)  $\nu_1(1a_g)$ , (b)  $\nu_4(2b_{1g})$  and (c)  $\nu_6(1b_{2g})$ . Points are energies calculated using SA-CAS(4,4)/6-31G\*, lines are from the Vibronic Coupling Hamiltonian.” Figure used with permission of Dr G. Worth, taken from [129].

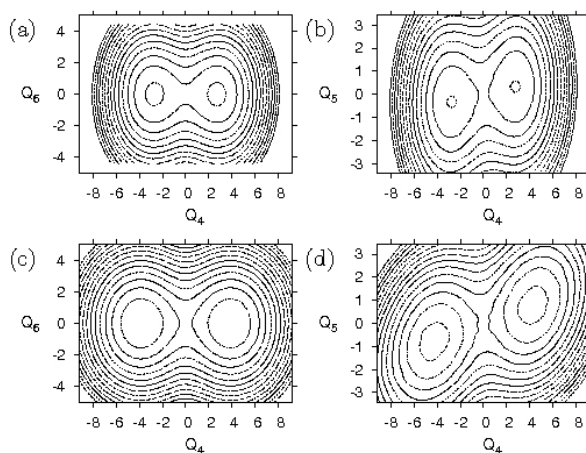


Fig. 7.2: “Contour plots of the potential energy surface for the lowest adiabatic singlet state,  $\tilde{X}^1B_{1g}$ , of neutral cyclobutadiene in the space of (b), (d) the  $b_{1g}$  modes,  $\nu_4$  and  $\nu_5$ , and (a), (c) the strongest vibronically coupled modes,  $\nu_4$  and  $\nu_6$ . Surfaces are from the vibronic coupling model Hamiltonian fitted to SA-CAS(4,4)/6-31G\* data: (a) and (b) include only linear coupling, (c) and (d) including second-order terms.” Figure used with permission of Dr G. Worth, taken from [129]

population from  $S_1$  to  $S_0$ . In figure 7.4 the strength parameter ( $\lambda$ ) for the pulse is 0.25 and in figure 7.5  $\lambda$  is 0.01. These figures highlight the importance of  $\lambda$  to the success of the control calculations. When  $\lambda=0.25$  60% of the wavepacket is transferred from  $S_1$  to  $S_0$ , this is approximately 10% less than when  $\lambda=0.01$  (for equal real time). Also the control shown in figure 7.4a, using a larger  $\lambda$ , is more chaotic. Following the initial population of  $S_0$ , at just below 20fs, we observe oscillatory population transfer between  $S_1$  and  $S_0$ . There is no consistent increase in the  $S_0$  population. However when  $\lambda=0.01$  (shown in figure 7.5a) the control is more stable. Following the initial population of  $S_0$ , at 40fs, oscillations between  $S_1$  and  $S_0$ , due to vibronic coupling, are observed but there is always a steady increase in  $S_0$  population.

The difference in the dynamics of the control is highlighted in the two calculated pulses. When  $\lambda=0.25$  the calculated pulse is very unphysical and contains a large range of frequencies (shown in the FT in figure 7.6a). The frequencies are difficult to attribute to the nuclear dynamics. However when  $\lambda=0.01$  a much simpler attenuating pulse is produced. This contains a narrow range of frequencies (figure 7.6b) which can be easily assigned to parameters of the model system, in this case to the energy gap between the two electronic states.

The difference between the dynamics using the different  $\lambda$  values is also shown in the wavepacket density plots in figure 7.7. When  $\lambda=0.25$  (figure 7.7b) the stronger pulse, means that the wavepacket, upon transfer to the ground state, has more energy and is more dispersed along the normal modes. In this case the density is dispersed along  $\nu_1$  and  $\nu_4$  and the largest density is around the CI between the two states. This causes the constant oscillations in the populations and the very complicated and unphysical pulse. When  $\lambda=0.01$  (figure 7.7a) the largest density of the wavepacket is at the  $S_0$  minima. Therefore the crossing at the CI is greatly reduced making the control easier.

Figures 7.8a and 7.9a shows the diabatic state population when the calculated field (figures 7.8b and 7.9b) is applied to control the transfer of population from  $S_1$  to  $S_2$



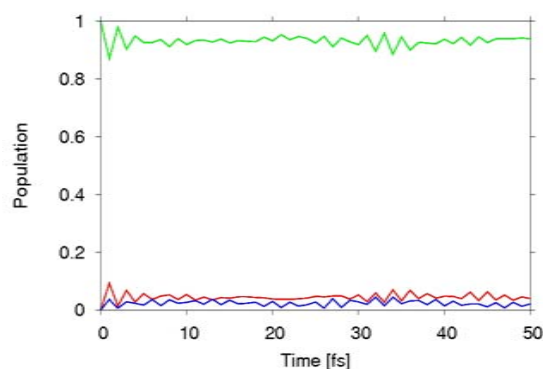


Fig. 7.3: The diabatic state populations for 50fs of the lowest three singlet states,  $\tilde{X}^1B_{1g}$  (red),  $\tilde{A}^1A_g$  (green), and  $\tilde{B}^1B_{2g}$  (blue) in neutral cyclobutadiene, without an external field following a vertical excitation into  $\tilde{A}$ .

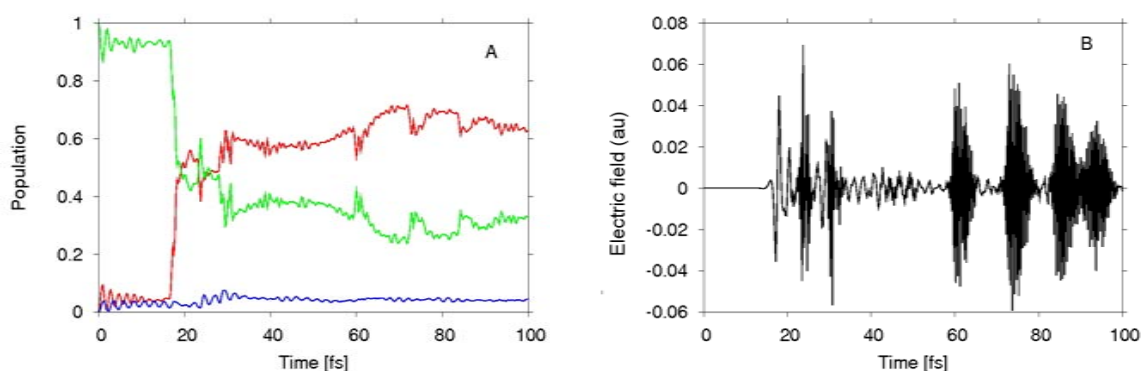


Fig. 7.4: (a) The diabatic state populations of of the lowest three singlet states,  $\tilde{X}^1B_{1g}$  (red),  $\tilde{A}^1A_g$  (green), and  $\tilde{B}^1B_{2g}$  (blue) in neutral cyclobutadiene for 100fs of controlled dynamics to populate  $S_0$ ,  $\lambda=0.25$ . (b) Electric field calculated by the local control algorithm.

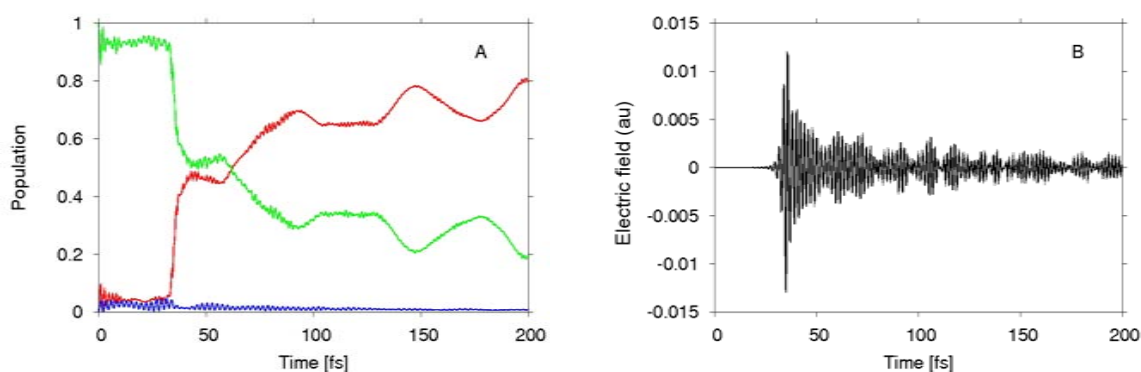


Fig. 7.5: (a) The diabatic state populations of of the lowest three singlet states,  $\tilde{X}^1B_{1g}$  (red),  $\tilde{A}^1A_g$  (green), and  $\tilde{B}^1B_{2g}$  (blue) in neutral cyclobutadiene for 200fs of the controlled dynamics to populate  $S_0$ ,  $\lambda=0.01$ . (b) Electric field calculated by the local control algorithm.

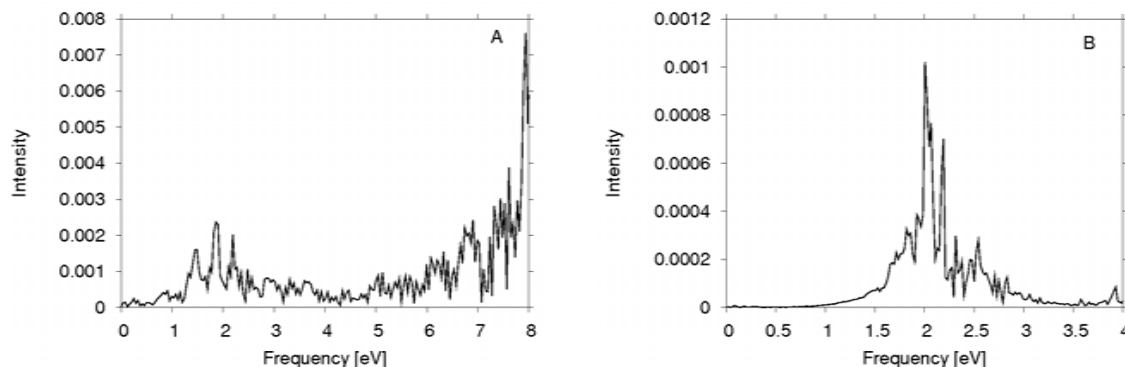


Fig. 7.6: Fourier transform of the pulse calculated to control the dynamics of population transfer between  $S_1$  and  $S_0$  of neutral cyclobutadiene: (a)  $\lambda=0.25$  (b)  $\lambda=0.01$ .

(following a vertical excitation from  $S_0$ ). Like the previous example, this demonstrates the importance of the  $\lambda$  parameter to the control calculations. Figure 7.8 shows the control performed when  $\lambda$  is 0.25. Initially there is some control with population of  $S_2$  reaching 50% after only 20fs. However after 40fs the state populations become very chaotic and uncontrolled with rapid oscillations between the two states. This behaviour is also shown in the very unphysical behaviour of the pulse. The FT of the calculated pulse (figure 7.10a) shows a large range of frequencies with no obvious physical relation to the chemical system.

Figure 7.9 shows the control dynamics performed when  $\lambda=0.01$ . We observe a very simple control, with 95% of the wavepacket successfully transferred into  $S_2$  within 100fs. There are minor oscillations between the populations of  $S_1$  and  $S_2$  this is due to the large vibronic coupling between the two states. However this stops once the full transfer has occurred, showing that the wavepacket is stable in  $S_2$  despite the vibronic coupling. A FT (figure 7.10b) of the pulse shows a single frequency field which corresponds to the energy gap between the two states.

The difference in the dynamics using the different strength factors ( $\lambda$ ) is highlighted in figure 7.11. Figure 7.11a shows the wavepacket on  $S_2$  along  $\nu_5$  and  $\nu_6$  after 65fs when  $\lambda=0.01$ . It is a very well structured wavepacket which following excitation into the potential minima shows very little motion along either mode, making the population of  $S_2$

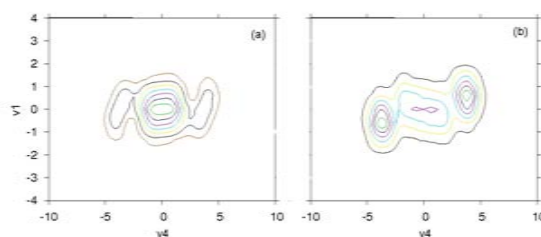


Fig. 7.7: Snapshot of wavepacket on  $S_0$  for neutral cyclobutadiene during the control of  $S_1$  and  $S_0$  population after 100fs: (a)  $\lambda=0.01$  (b)  $\lambda=0.25$

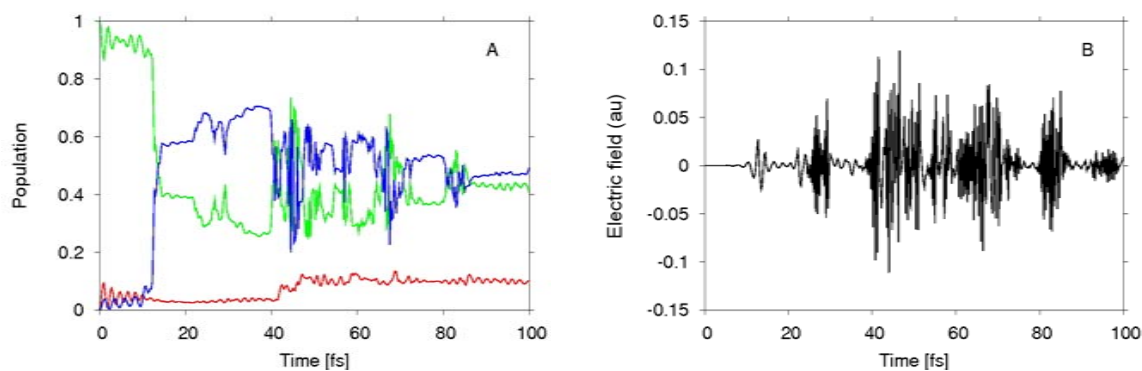


Fig. 7.8: (a) The diabatic state populations of the lowest three singlet states,  $\tilde{X}^1B_{1g}$  (red),  $\tilde{A}^1A_g$  (green), and  $\tilde{B}^1B_{2g}$  (blue) in neutral cyclobutadiene over 100fs for the control of population to  $S_2$ ,  $\lambda=0.25$ . (b) Electric field calculated by the local control algorithm.

very stable. However 7.11b shows the same wavepacket when  $\lambda=0.25$ , the extra energy clearly excites the wavepacket into  $S_2$  with more energy and therefore large oscillations are seen along both modes, this causes the wavepacket to reach and repeatedly cross the intersection between  $S_1/S_2$  and make the population unstable.

### 7.2.2 Cyclobutadiene Radical Cation

The model Hamiltonian for the cyclobutadiene radical cation is obtained in the same manner as the neutral species and is explained in [129]. This surface is dominated by a JT interaction which lifts the degeneracy of the  ${}^2E_{2g}$  state along  $b_{1g}$  and  $b_{2g}$  modes. PJT interactions are also present [159], but these are weak in comparison to the JT interaction and are ignored in this model. The model contains one doubly degenerate

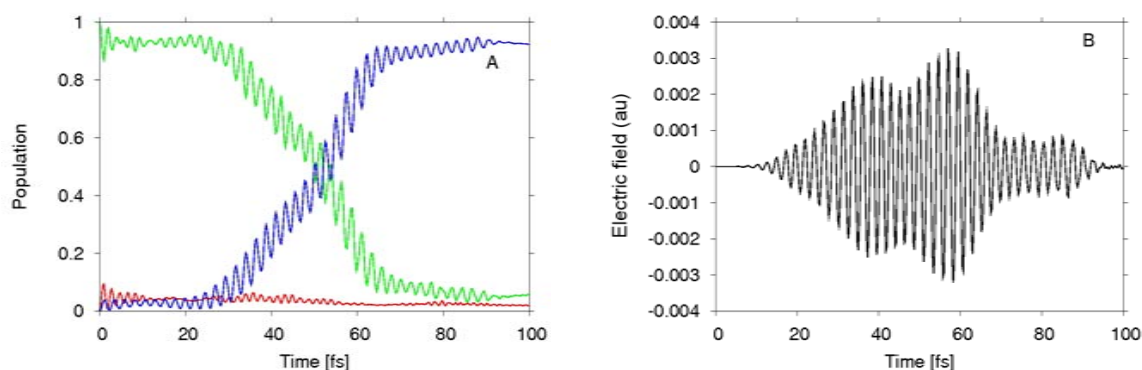


Fig. 7.9: (a) The diabatic state populations of the lowest three singlet states,  $\tilde{X}^1B_{1g}$  (red),  $\tilde{A}^1A_g$  (green), and  $\tilde{B}^1B_{2g}$  (blue) in neutral cyclobutadiene over 100fs for the controlled population of  $S_2$ ,  $\lambda=0.01$ . (b) Electric field calculated by the local control algorithm.

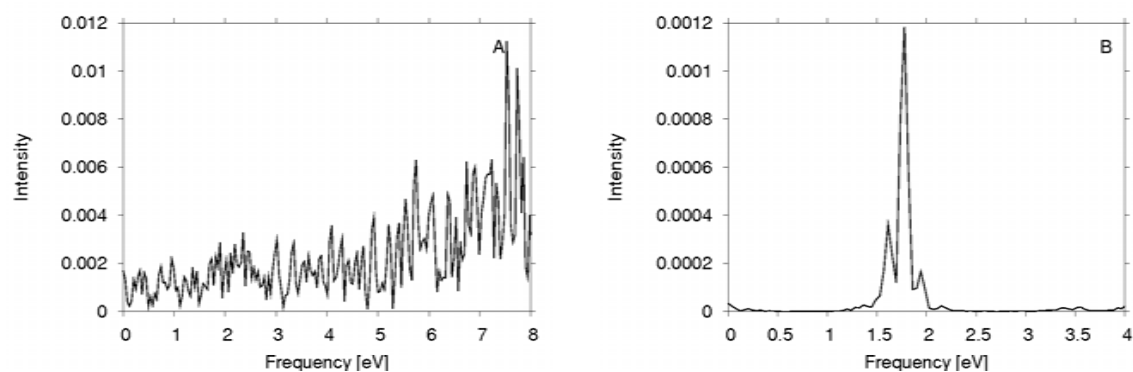


Fig. 7.10: Fourier transform of calculated pulse for the control of populations from  $S_1$  to  $S_2$  of neutral cyclobutadiene using (a)  $\lambda=0.25$  (b)  $\lambda=0.01$

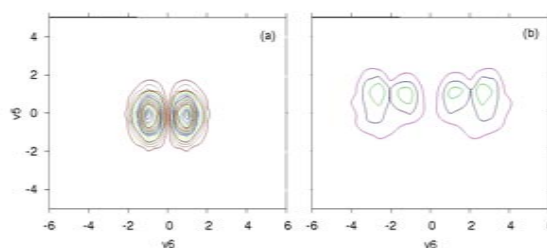


Fig. 7.11: Snapshot of the wavepacket on  $S_2$  of neutral cyclobutadiene after 65fs for control of  $S_1$  and  $S_2$  population: (a)  $\lambda=0.01$  (b)  $\lambda=0.25$

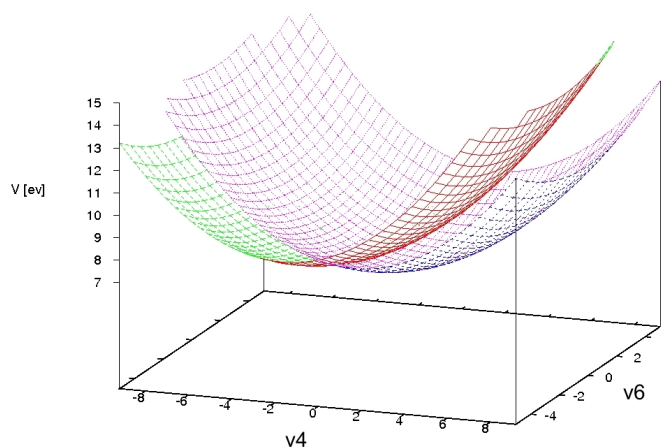


Fig. 7.12: The diabatic PES of the  ${}^2E_{2g}$  state along  $\nu_4$  ( $b_{1g}$ ) and  $\nu_6$  ( $b_{2g}$ ) modes of the radical cationic cyclobutadiene. The two minima represent the rectangular structures, while the transition state is the square planar geometry.

electronic state and two vibrational degrees of freedom,  $\nu_4$  and  $\nu_6$ . The PES is shown in figure 7.12 and the details of the calculations are shown in table 7.2. The control objective for this model is to transfer the wavepacket between minima in the  ${}^2E_{2g}$  state formed by JT coupling, this corresponds to electronic transfer between the  $x$  and  $y$  components of the split degenerate state. Throughout these calculations we consider the transition dipole moment as linear along  $\nu_6$ .

Figure 7.13 shows the diabatic state populations for the first 8ps without pertur-

Mode	$N_i, N_j$	$n_0, n_1$	
		No control	Control
$\nu_4$	51	8,8	8,8
$\nu_6$	19	8,8	8,8
CPU Time	$\lambda=0.002$	22mins 49secs	23mins 25secs

Table 7.2: Computational details for the quantum dynamics simulations for control of the radical cation of cyclobutadiene for 8ps.  $N_i$  is the no. of primitive Harmonic oscillator DVR basis functions used to describe each mode [78].  $n_i$  are the number of SPF used for the wavepacket on each state.

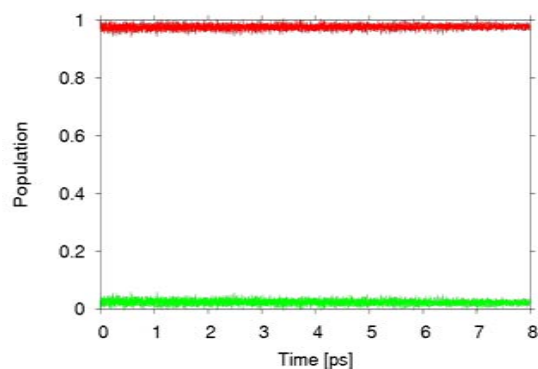


Fig. 7.13: The diabatic state populations of the lowest doubly degenerate  ${}^2E_{2g}$  state,  ${}^2E_{2g,x}$  (red) and  ${}^2E_{2g,y}$  (green) of radical cation cyclobutadiene for 8ps.

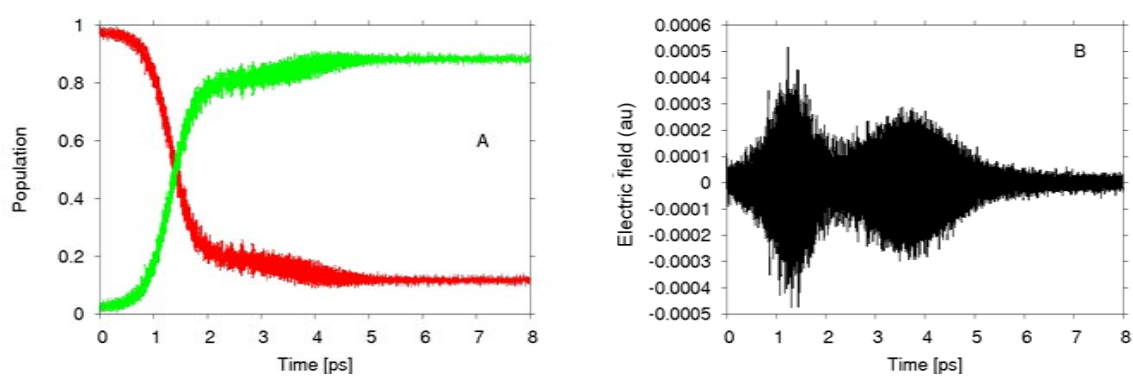


Fig. 7.14: (a) The diabatic state populations of the lowest doubly degenerate  ${}^2E_{2g}$  state,  ${}^2E_{2g,x}$  (red) and  ${}^2E_{2g,y}$  (green) of radical cation cyclobutadiene for 8ps using the control field (b).

bation from an external field. This shows that the wavepacket cannot overcome the barrier between the two minima and therefore the wavepacket stays in its initial state. Figure 7.14 shows the diabatic state populations and calculated pulse when using the local control algorithm. The pulse excites 90% of the wavepacket onto the  $D_{0,y}$  surface. The gradient along  $\nu_4$  on the  $D_{0,y}$  surface causes the wavepacket to propagate down the steepest gradient to the  $D_{0,y}$  minima.

In order to establish more detailed analysis of the dynamical information of the control scenario we plot the position and width of the wavepacket on each state as a function of time, these are shown in figure 7.16. We also plot the wavepacket density on each state, this is shown in figure 7.15.

From inspection of the wavepacket plots in figure 7.15 we see that the wavefunction on the initial state,  $D_{0,x}$ , oscillates slightly along  $\nu_4$  and  $\nu_6$ , however most density remains around the equilibrium position between 0 and -2units. After 1000fs only a small amount of density populates  $D_{0,y}$ , this is because the overlap between ground and excited state wavefunctions is small up to this point, making the pulse weak. After 1800fs the density on  $D_{0,y}$  has increased dramatically, following the energy profile of the pulse. The wavefunction on  $D_{0,y}$  is bifurcated due to the dipole interaction. We also see that the wavepacket is split into 5 distinct packets along  $\nu_4$ , relating to each excitation from the pulse. After 4000fs one can see that the wavepacket is beginning to cool into the minima on  $D_{0,y}$  and the width is greatly reduced. After 4700fs the wavefunction on  $D_{0,y}$  is almost exclusively relaxed at the minima,  $Q_4=0.5\text{au}$ .

Such observations are supported by inspection of the  $\langle q_4 \rangle$  and  $\langle dq_4 \rangle$  (shown in figure 7.16). Between 1-3ps there is continuous excitation to  $D_{0,y}$ . The gradient of the PES causes the wavepacket to spread along this mode, this is reflected in the size of  $\langle dq_4 \rangle$  on  $D_{0,y}$ . At longer timescales the size of  $\langle dq_4 \rangle$  falls because the wavepacket is cooled into the  $D_{0,y}$  minima.

The  $\langle q_4 \rangle$  and  $\langle dq_4 \rangle$  on  $D_{0,x}$  shows the wavepacket increasing in width, as more energy

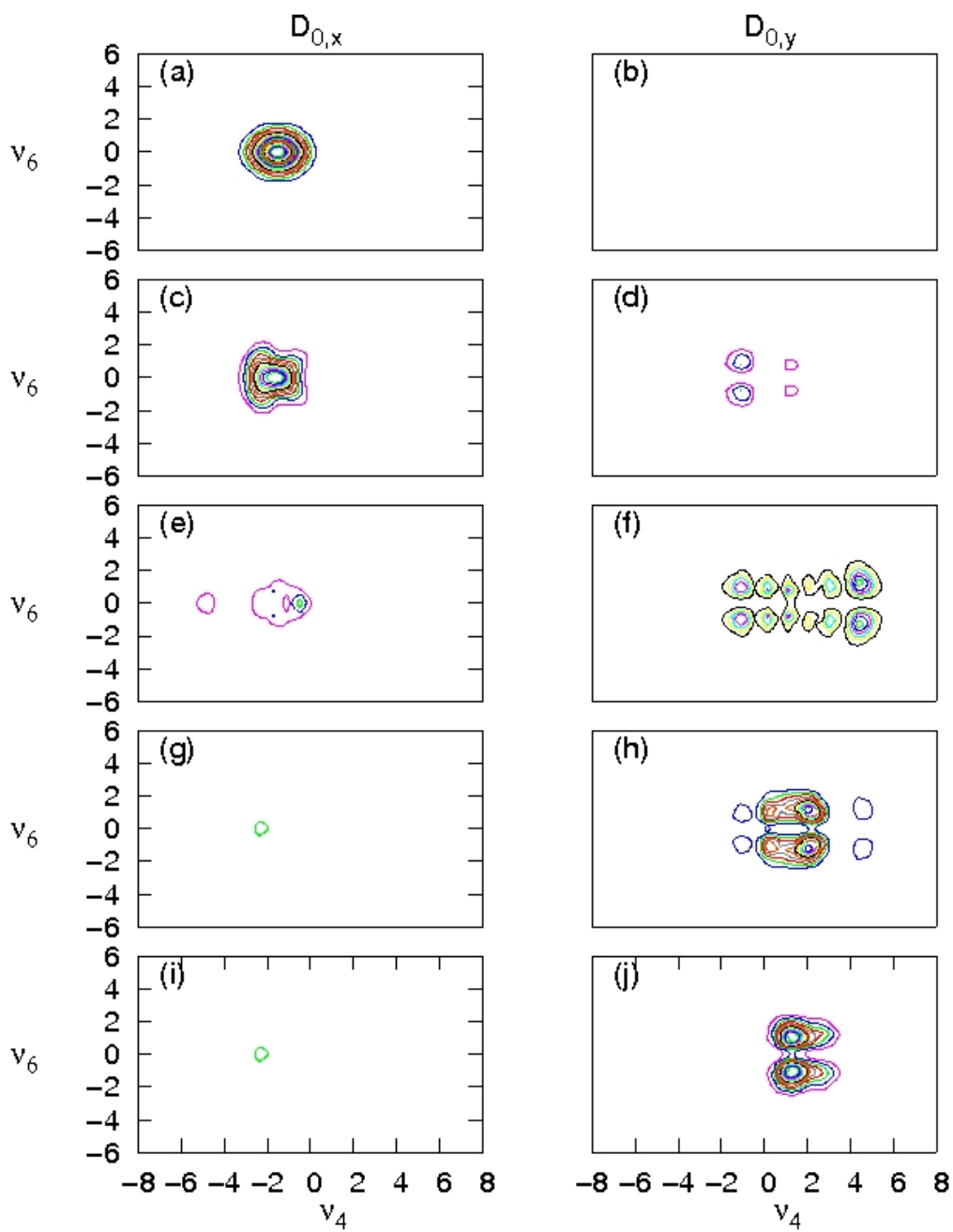


Fig. 7.15: The wavefunction density on  $D_{0,x}$  and  $D_{0,y}$  in the radical cation cyclobutadiene along  $\nu_4$  and  $\nu_6$  (a)/(b) 0fs, (c)/(d) 1000fs (e)/(f) 1800fs (g)/(h) 4000fs and (i)/(j) 4700fs.



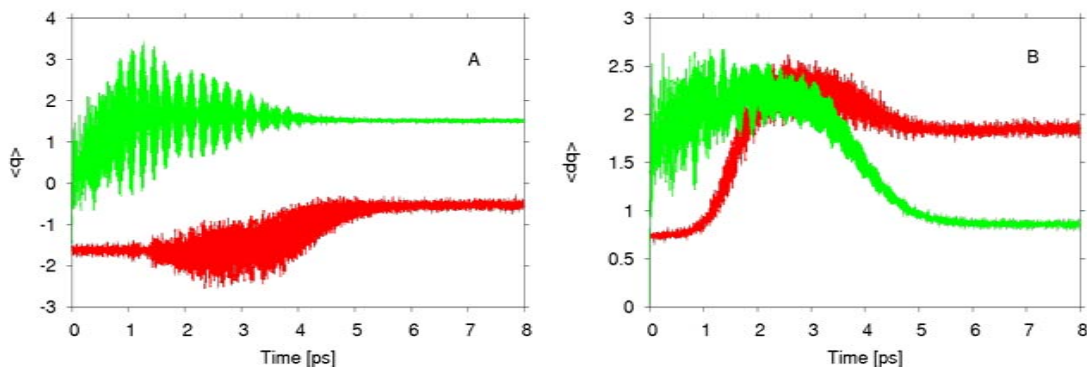


Fig. 7.16: (a)  $\langle q_4 \rangle$  for  $D_{0,x}$  and  $D_{0,y}$ . (b)  $\langle dq_4 \rangle$  for  $D_{0,x}$  and  $D_{0,y}$ . In both cases red represents  $D_{0,x}$  and green represents  $D_{0,y}$ .

is added to the system from the pulse. At  $-0.5\text{au}$  along  $\nu_4$  the overlap between the lower and upper states ensures efficient population transfer. The fraction that remains on  $D_{0,x}$  following the control settles at the  $D_{0,x}$  minima at  $Q_4 = -0.5\text{au}$ .

### Filtering the pulse

A FT of the pulse (shown in figure 7.17a) can reveal more information about the dynamics of the system and mechanism for control. In the calculated pulse 4 frequencies dominate these are at  $0.54\text{eV}$ ,  $0.64\text{eV}$ ,  $0.85\text{eV}$  and  $0.95\text{eV}$  and there is also a large number of low intensity frequencies. The strongest two frequencies ( $0.54$  and  $0.85$ ) are separated by  $0.31\text{eV}$ , this corresponds to the sum of the vibrational frequencies of the normal modes,  $\nu_4$  and  $\nu_6$ . The gap between the major peak and its pair (i.e.  $0.54$  and  $0.64$ ) corresponds to the off-diagonal coupling element between the two states along  $\nu_6$ . This does not apply for  $\nu_4$  because all coupling elements are zero by symmetry. The FT also shows a low intensity peak at around  $0.25\text{eV}$ , this peak matches the energy gap between vibrational states and is therefore likely to be responsible for the cooling of the wavepacket on the  $D_{0,y}$  surface following excitation.

The calculated pulse for the control of the radical cation of cyclobutadiene contains a lot of low intensity frequencies, this makes it more difficult to reproduce experimentally and give an accurate assignment of the role of each frequency. It is therefore desirable

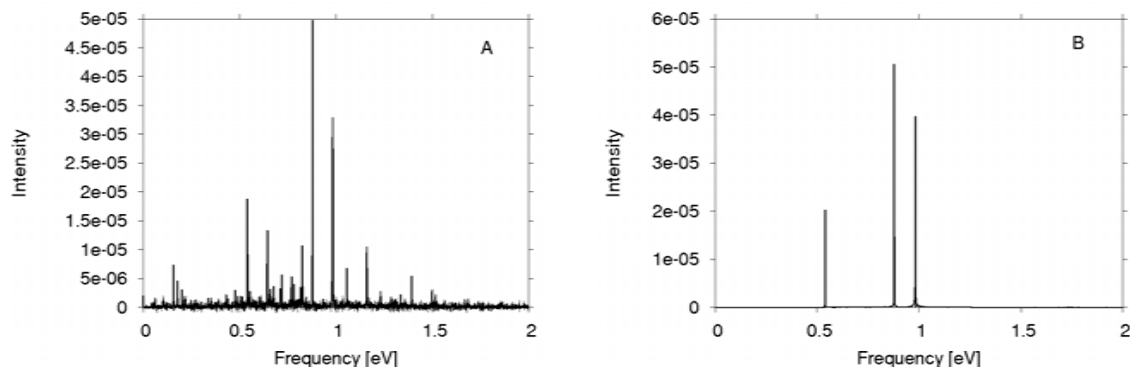


Fig. 7.17: Fourier transform of the calculated pulses for the radical cation cyclobutadiene. (a) Unfiltered (b) Filtered.

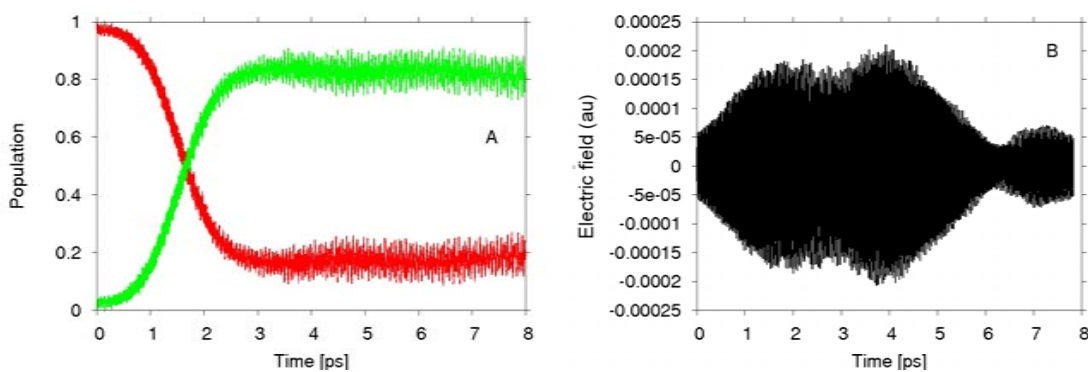


Fig. 7.18: Controlled dynamics performed with the filtered field. (a) Controlled diabatic state populations,  ${}^2E_{2g,x}$  (red) and  ${}^2E_{2g,y}$  (green). (b) Filtered control pulse. This pulse contains only the four main frequencies highlighted from the first control.

to filter the control pulse. This will help assign the role of each frequency and will become increasingly important as the pulses become more complex in larger systems.

To filter the frequencies a discrete FT is performed, producing a spectra of intensity vs index. Any peaks below a preset threshold are removed from the spectra and the inverse transform is calculated to return the new filtered pulse. In this test case frequencies with an intensity lower than 0.000015 were removed.

Figure 7.18 shows the control using the filtered pulse and figure 7.17b shows the FT of the filtered field. The diabatic state populations show that 85% of the wavepacket is excited in this control, 5% less than the unfiltered pulse. This is still a very effective control especially considering the number of frequencies in the field has been reduced

to three. At later timescales in the control using the filtered pulse, the diabatic state populations (figure 7.18a) show rapid oscillations between the two states, suggesting the wavepacket still contains a lot of energy and is able to surmount the barrier between the two minima. This supports the observation that the frequency at 0.25eV is cooling the wavepacket, because upon its removal this is no longer the case.

### 7.2.3 Pyrazine

Pyrazine,  $C_4H_4N_2$ , has been extensively studied in both experiment and theory [104, 115, 160, 161], including a 24 dimensional model performed using MCTDH, [84] (and references therein). The model used in this study has three electronic states and three nuclear DOF. The PES along the two DOF showing the CI between  $S_1/S_2$  is shown in figure 7.19. There is first order on-diagonal coupling along  $\nu_1$ ,  $\nu_{6a}$  and  $\nu_{9a}$  and off diagonal coupling between  $S_1/S_2$  along  $\nu_{10a}$ . This model has been used in an OCT study [157], therefore we can draw direct comparisons in the performance of the two methods. We will perform three control calculations, two controlling the population of  $S_2$  with and without the vibronic coupling which exists between  $S_1$  and  $S_2$  and one control using the vibronic coupling between  $S_1$  and  $S_2$  to efficiently populate  $S_1$ . In all control cases we consider the transition dipole moment as linear along  $\nu_{10a}$ .

#### Maximising $S_2$ : No $S_1/S_2$ coupling

The objective of this first control is to selectively populate  $S_2$  in the absence of the non-adiabatic coupling between  $S_1$  and  $S_2$ . Figure 7.20 shows the diabatic state populations and calculated field for the first 500fs of propagation. The pulse successfully manages to transfer 90% of the wavepacket to  $S_2$  in a step wise manner, this performance is equal to the OCT calculation. The OCT calculation achieves the target state population in a much faster real time of 100fs.

Figure 7.22 plots the wavefunction on each electronic state during the control process. After 30fs there is significant population of the excited  $S_2$  state and the wavefunc-

Mode	$N_i, N_j$	$n_0, n_1, n_2$			Maximise $S_1$
		No control	Maximise $S_2$ (NIC)	Maximise $S_2$	
$\nu_{10a}$	22	8,7,8	8,7,8	8,7,8	8,7,8
$\nu_{6a}$	32	8,7,8	8,7,8	8,7,8	8,7,8
$\nu_1$	21	8,7,8	8,7,8	8,7,8	8,7,8
CPU Time (LCT)	$\lambda=0.05$	7mins 53secs	10mins 35mins	12mins 30secs	8mins 26secs

Table 7.3: Computational details for the quantum dynamics simulations for pyrazine.  $N_i$  is the no. of primitive Harmonic oscillator DVR basis functions used to describe each mode [78].  $n_i$  are the number of single-particle functions used for the wavepacket on each state. NIC stands for No internal conversion.

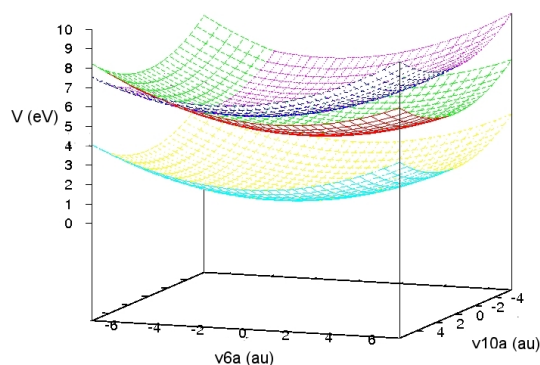


Fig. 7.19: The diabatic potential energy surface for pyrazine along  $\nu_{6a}$  and  $\nu_{10a}$  showing the conical intersection which is located close to the Franck-Condon point on  $S_2$ .

tion is slightly bifurcated due to the dipole excitation. The most significant motion on the excited state is along  $\nu_{6a}$ , this is due to the slope of the PES. This motion leads to the CI between  $S_1/S_2$ , however in this case no crossing occurs because the coupling is ignored.

The wavepacket plots shows that the oscillation period of the wavepacket in this state is approximately 60fs, this is also shown in the time between first two major pulses in the calculated field. This is unsurprising as a pulse will only be large when overlap between the wavefunctions the initial and target state is good. This can only been seen in the pulse in early timescales, because as the propagation time continues the wavepacket becomes more spread allowing more smaller overlap to occur at smaller time intervals.

The FT of the pulse (figure 7.21) shows a broad peak around 4-5eV, this is equivalent to the energy gap between the two states, showing that the control mechanism is a simple excitation process. There is a small amount of structure which is a vibrational progression of  $\nu_{10a}$ .

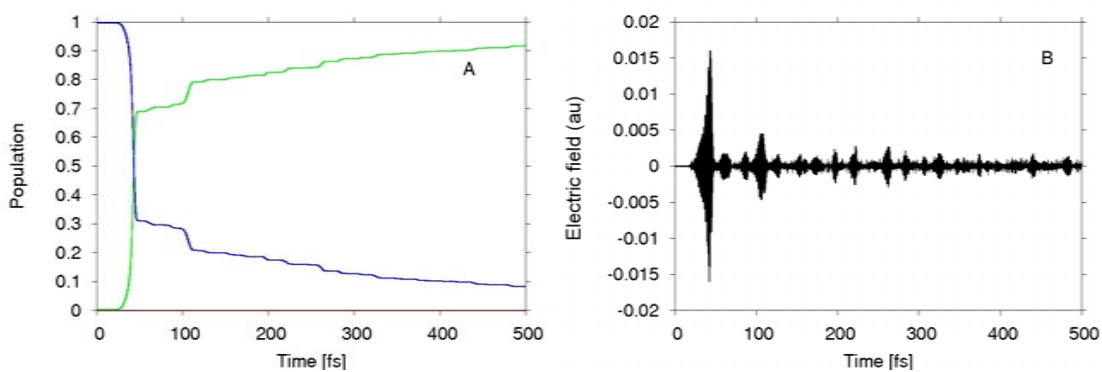


Fig. 7.20: (a) The diabatic state populations of pyrazine over 500fs under the influence of the field shown in (b). In this control the coupling between  $S_1$  and  $S_2$  has been ignored.  $S_0$  (blue) and  $S_2$  (green)

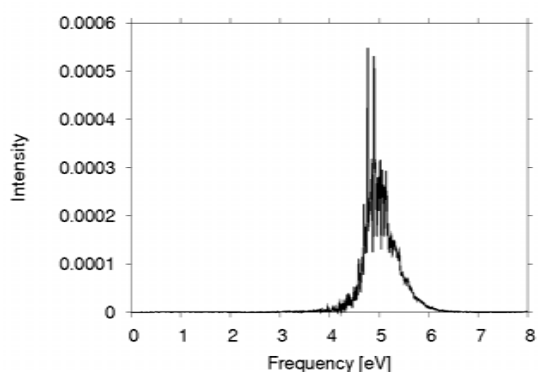


Fig. 7.21: Fourier transform of the electric field for pyrazine control, selectively populating  $S_2$  in the absence of vibronic coupling between  $S_1$ - $S_2$ .

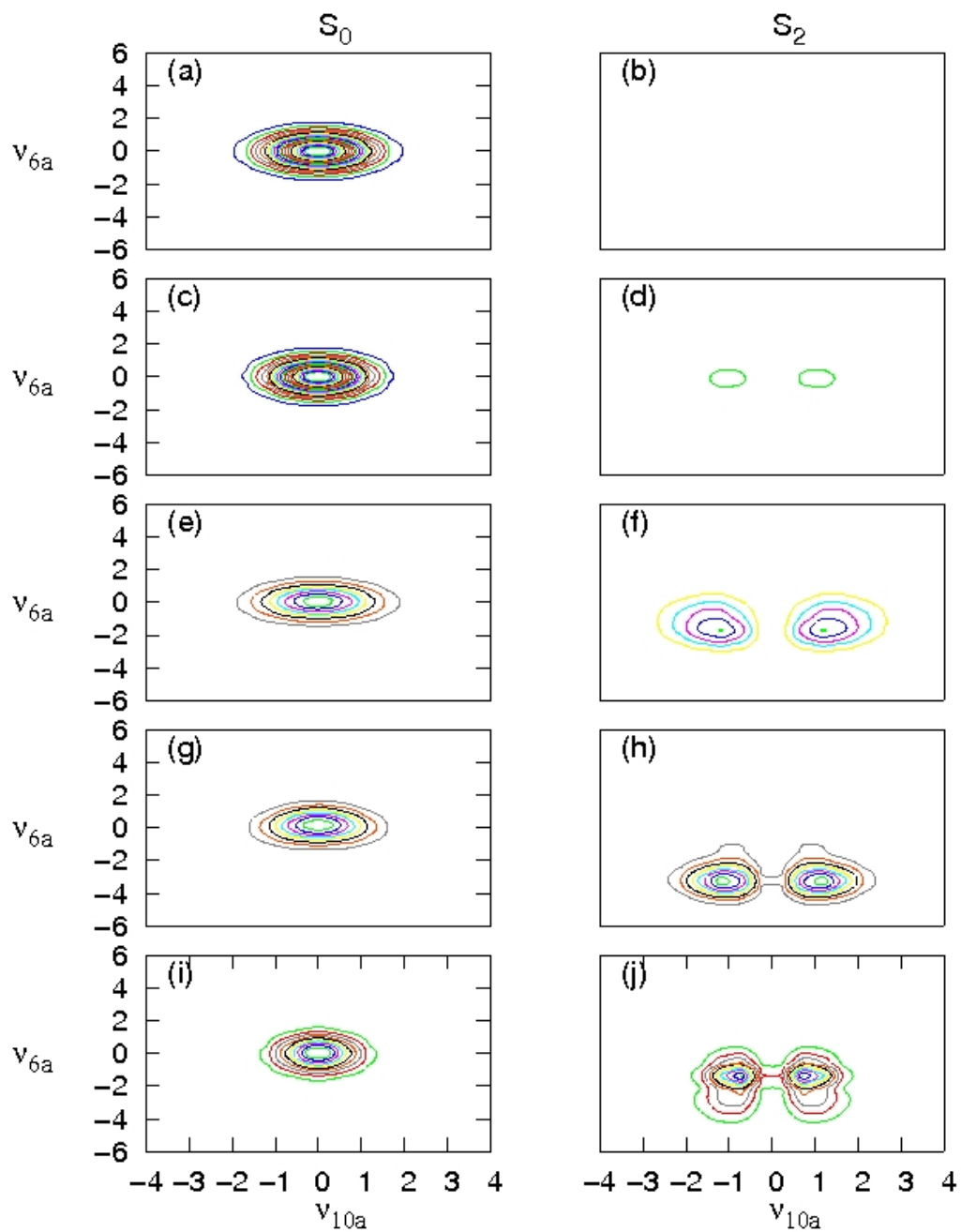


Fig. 7.22: The wavefunction density on  $S_0$  and  $S_2$  in pyrazine along  $\nu_{6a}$  and  $\nu_{10a}$  (a)/(b) 0fs, (c)/(d) 30fs (e)/(f) 45fs (g)/(h) 60fs and (i)/(j) 75fs.

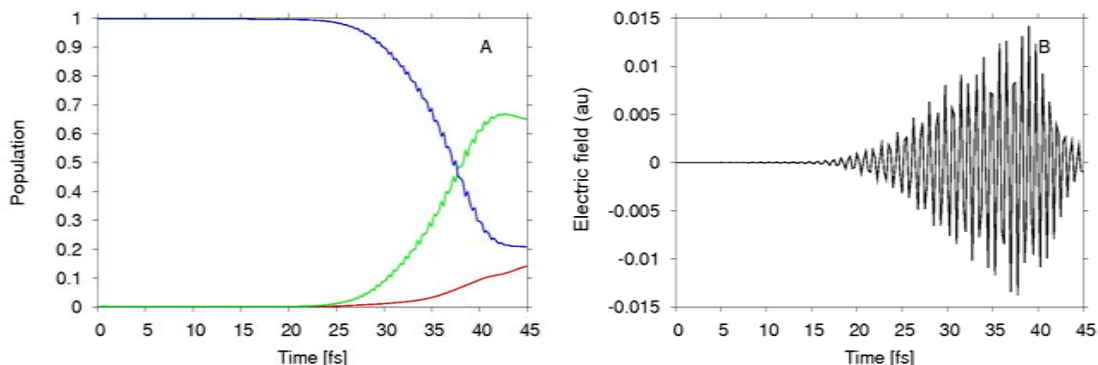


Fig. 7.23: Control to maximise the  $S_2$  population (a) The diabatic state populations of pyrazine over 45fs under the influence shown of the field shown in (b). The coupling between  $S_1$  and  $S_2$  is included.  $S_0$  (blue),  $S_1$  (red) and  $S_2$  (green).

### Maximising $S_2$ and $S_1$ : Including internal conversion

In the last section we considered only the  $S_0$  and  $S_2$  states by ignoring the vibronic coupling which exists between  $S_1$  and  $S_2$ . In this section we include the vibronic coupling, this significantly complicates the control. Figure 7.19 shows that there is a CI between  $S_1$  and  $S_2$  very close to the FC point therefore IC will occur on an ultrafast timescale.

In the first instance we perform the same control as before, attempting to achieve maximum population of  $S_2$ , but including vibronic coupling between  $S_1$  and  $S_2$ . Figure 7.23 shows the diabatic state population and the field for the first 45fs. In this control scenario the pulse is able to transfer 75% of the wavepacket to  $S_2$ , with just over 10% of this crossing through the CI to  $S_1$ . This population is unstable due to the IC and continued propagation would result in increased decay to  $S_1$ . This result was also reported using the OCT approach [157] and encouragingly both results show excellent agreement on real time scales.

In the second instance we use the IC to create a pulse which will efficiently transfer population to  $S_1$ . The oscillator strength of the  $S_0$ - $S_2$  transition is much greater than that of the  $S_0$ - $S_1$  transition, so excitation to  $S_2$  will be more efficient. Utilising the IC



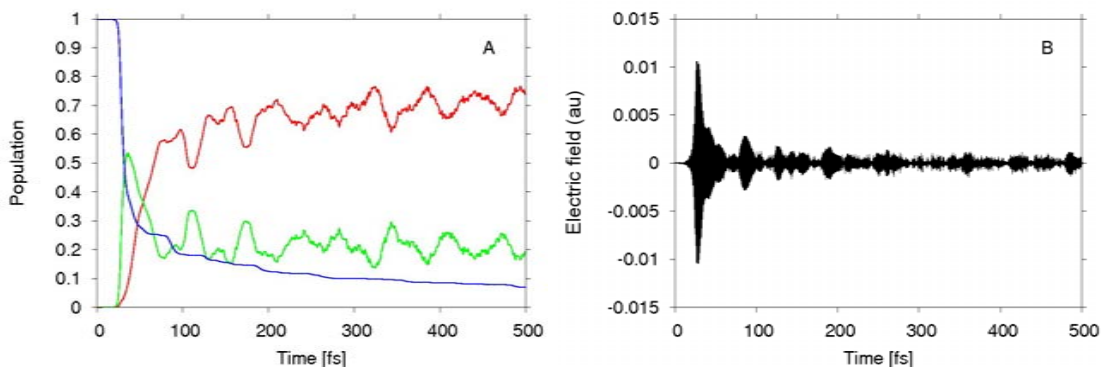


Fig. 7.24: Control to maximise the  $S_1$  population (a) The diabatic state populations of pyrazine over 200fs under the influence shown of the field shown in (b). The coupling between  $S_1$  and  $S_2$  is included.  $S_0$  (blue),  $S_1$  (red) and  $S_2$  (green).

will allow efficient mechanism for the population of  $S_1$ .

Figure 7.24 shows the diabatic state population and the field over the first 500fs. Following the initial excitation into  $S_2$  there is rapid decay into  $S_1$ . The population of  $S_1$  is already 75% within the first 150fs and reaches 80% by 500fs. This population continues to rise in a step wise manner, due to the kicking nature of the pulse, which arises due to overlap considerations.

Following excitation into  $S_2$  population in this state decays rapidly into  $S_1$ . Oscillations between  $S_1$  and  $S_2$  are seen throughout the control because the wavepacket passing through the CI is very vibrationally hot and has enough momentum to cross back onto the upper surface. This reduces at longer timescales.

This result gives a similar population agreement with that obtained in the equivalent OCT study [157]. Due to the global view of the OCT control the pulse calculated cools the wavepacket when crossing to  $S_1$  and the oscillations between  $S_1$  and  $S_2$  are not seen.

#### 7.2.4 Ammonia

The photodissociation of ammonia has been studied extensively both theoretically and experimentally [162–165]. The theoretical work has led to the PES being well charac-

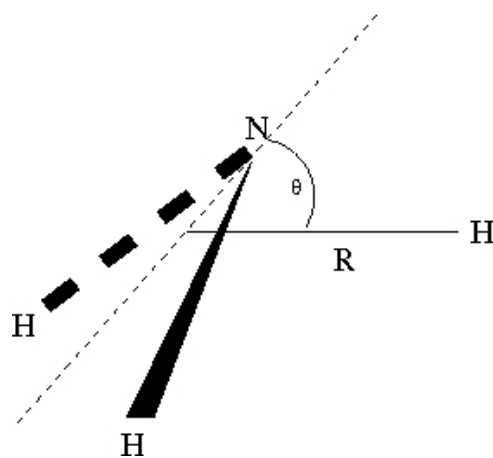


Fig. 7.25: 2D  $\text{NH}_3$  model with DOF  $R$  and  $\theta$  defining the umbrella mode by the motion of one proton relative to a fixed  $\text{NH}_2$  group [169].

terised, diabatic PES with coupling have been calculated by Truhlar *et al* [166, 167]. These surfaces show that the ground state has a double minimum along the inversion mode, with each minima corresponding to a pyramidal,  $C_{3v}$ , structure. The first singlet excited state has a single minimum at the  $D_{3h}$  planar geometry where a CI exists between the 2 states. These features can be seen in figure 7.26.

The shape of the PES means that upon excitation into  $S_1$ , there are two possible routes to dissociation: non-adiabatically via the CI in to the ground electronic state to form  $\text{NH}_2(\tilde{X}^2B_1) + \text{H}$ , and adiabatically on the first excited state to form  $\text{NH}_2(\tilde{A}^2A_1) + \text{H}$ .

The competition between these two routes has been studied by by Crim *et al* [168]. Using velocity map imaging (VMI) the paths to dissociation were studied for different vibrations in the excited state. It was found that molecules with an excited symmetric N-H stretch ( $\nu_1$ ) dissociated to produce ground state  $\text{NH}_2$  and that the antisymmetric N-H stretch ( $\nu_3$ ) resulted in production of  $\text{NH}_2$  in the excited  $\tilde{A}^2A_1$  state. They concluded that the antisymmetric stretching mode caused the photodissociation to avoid the CI.

We use a 2D model which provides a description, using Jacobi coordinates (figure

Mode	$N_i, N_j$	$n_0, n_1$		
		No control	Control 1	Control 2
$\nu_\theta$	61	1,1	1,1	1,1
$\nu_{rd}$	61	1,1	1,1	1,1
CPU Time	$\lambda=1.0$	10mins 30sec	40mins 5secs	36mins 10secs

Table 7.4: Computational details of the quantum dynamics simulations for ammonia.  $N_i$  is the no. of primitive Harmonic oscillator DVR basis functions used to describe each mode [78].  $n_i$  are the number of SPF used for the wavepacket on each state.

7.25), of the umbrella mode of  $\text{NH}_3$  with the motion of just one proton relative to the fixed  $\text{NH}_2$  group. For more extensive on reading this model see [169]. We aim to control the dissociation dynamics following excitation into  $S_1$ . This is complicated due to the strong coupling and presence of CI close to the FC point. The computational details can be found in table 7.4. In order to stop grid edge effects occurring a complex absorbing potential (CAP) [170] was placed on the dissociative channel at 8.0 au. The dipole surfaces were calculated using MRCI and are shown in figure 7.27.

### Control

Figure 7.28 shows the diabatic state populations for the two electronic states of ammonia in the first 50fs following vertical excitation into  $S_1$  from one of the  $S_0$  minima. This shows in that in this model the favoured dissociative channel is the diabatic channel leaving  $\text{NH}_2$  in its ground state. However, most of the wavepacket has still not dissociated on this timescale, this can be seen in the wavepacket density plots in figure 7.31. The density plots shows the wavepacket oscillates back and forth along  $\theta$ , each time it passes the CI, at the centre of the surface, some of the wavepacket proceeds along the dissociative mode.

Figure 7.29a shows the diabatic state populations of the two states of ammonia under control of an external pulse (figure 7.29b), in the first 50fs following excitation to  $S_1$ . The effect of the field is large and immediately obvious. One can observe that the

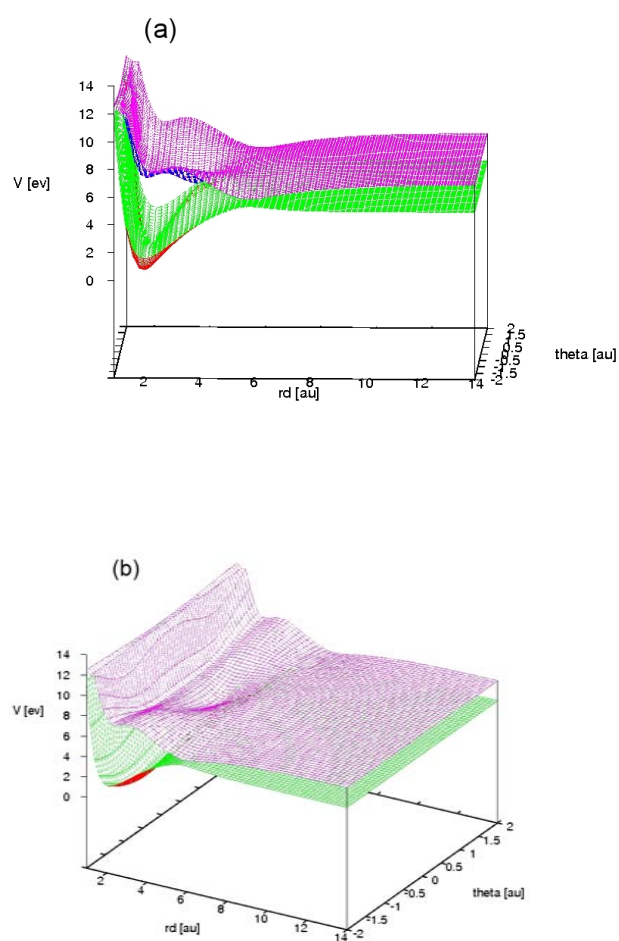


Fig. 7.26: Lowest two excited states ( $\tilde{X}^1A'$  and  $\tilde{A}^1A''$ ) of ammonia. The two coordinates are expressed in terms of the dissociating H atom where  $R$  is the distance between H and the centre of mass of the  $\text{NH}_2$ , and  $\theta$  is the angle that  $R$  makes with the plane of the  $\text{NH}_2$ .

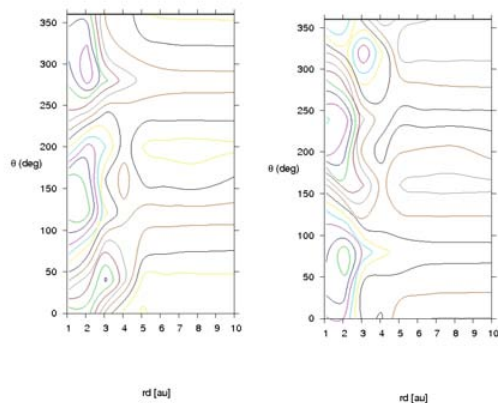


Fig. 7.27: Calculated transition dipole surfaces between  $\tilde{X}^1A'$  and  $\tilde{A}^1A''$  for ammonia (a)  $x$  component (b)  $z$  component. Calculated at MRCI level.

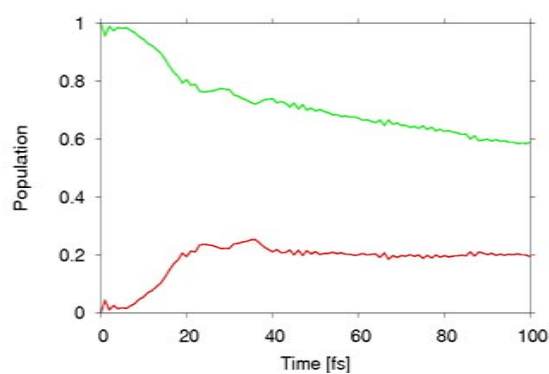


Fig. 7.28: The diabatic state populations for the lowest singlet state ( $\tilde{X}^1A'$  and  $\tilde{A}^1A''$ ) of ammonia in an unperturbed system.  $\tilde{X}^1A'$  (green) and  $\tilde{A}^1A''$  (red).

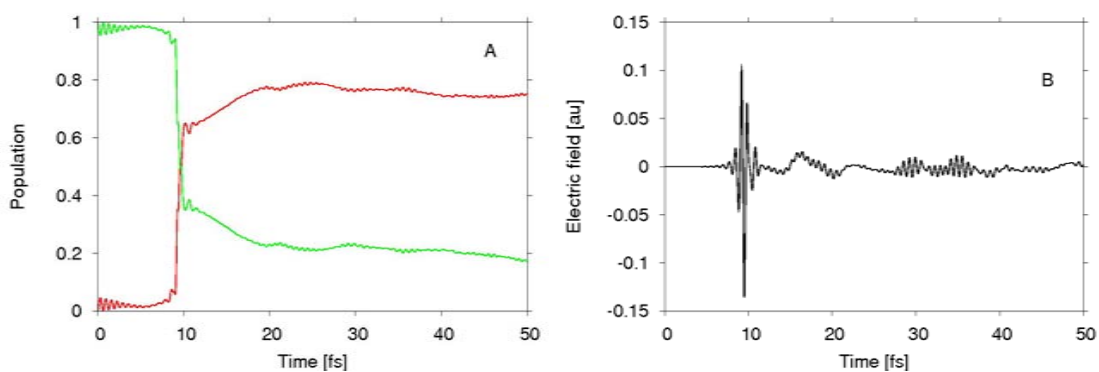


Fig. 7.29: (a) The diabatic state populations for the lowest singlet state ( $\tilde{X}^1A'$  and  $\tilde{A}^1A''$ ) of ammonia under the influence shown of the field shown in (b).  $\tilde{X}^1A'$  (green) and  $\tilde{A}^1A''$  (red).

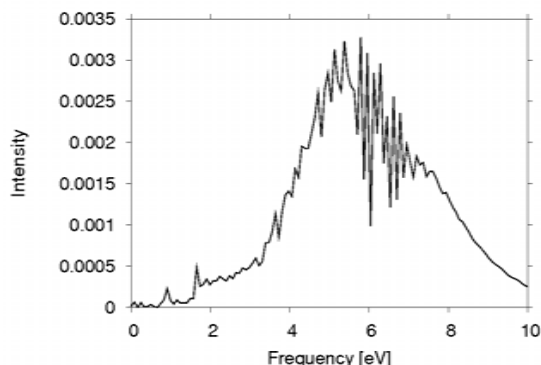


Fig. 7.30: Fourier transform of the control pulse obtained from the local control calculation of ammonia.

field selectively populates the  $S_0$  state with 80% compared to 20% on the uncontrolled dynamics.

The wavepacket plots for the controlled dynamics are shown in figure 7.32. We see that instead of the wavepacket propagating along the dissociative channel, the pulse pushes the wavepacket back to the ground state minima at positive value of  $\theta$ . This is because as the wavepacket moves across the  $\theta$  coordinate on the excited state a large overlap with the ground state is created around the intersection due to the strong vibronic coupling and therefore a pulse is created and transfers the wavepacket onto  $S_0$ . The FT of the pulse (figure 7.30) shows frequencies centred at 6eV. This is equal to the energy gap between the two states at the point the wavepacket is dumped back to the ground state.

## 7.3 Conclusion

LCT uses the instantaneous dynamics of the system at each time step to calculate a pulse which ensures the desired change in the expectation value of an operator. This approach which is focused upon a particular element of the system provides an alternative to the global optimisation used in OCT. During this chapter we have presented the initial results obtained following the implementation of the LCT-MCTDH. Despite there being a wide range of operators appropriate for control in this chapter we have

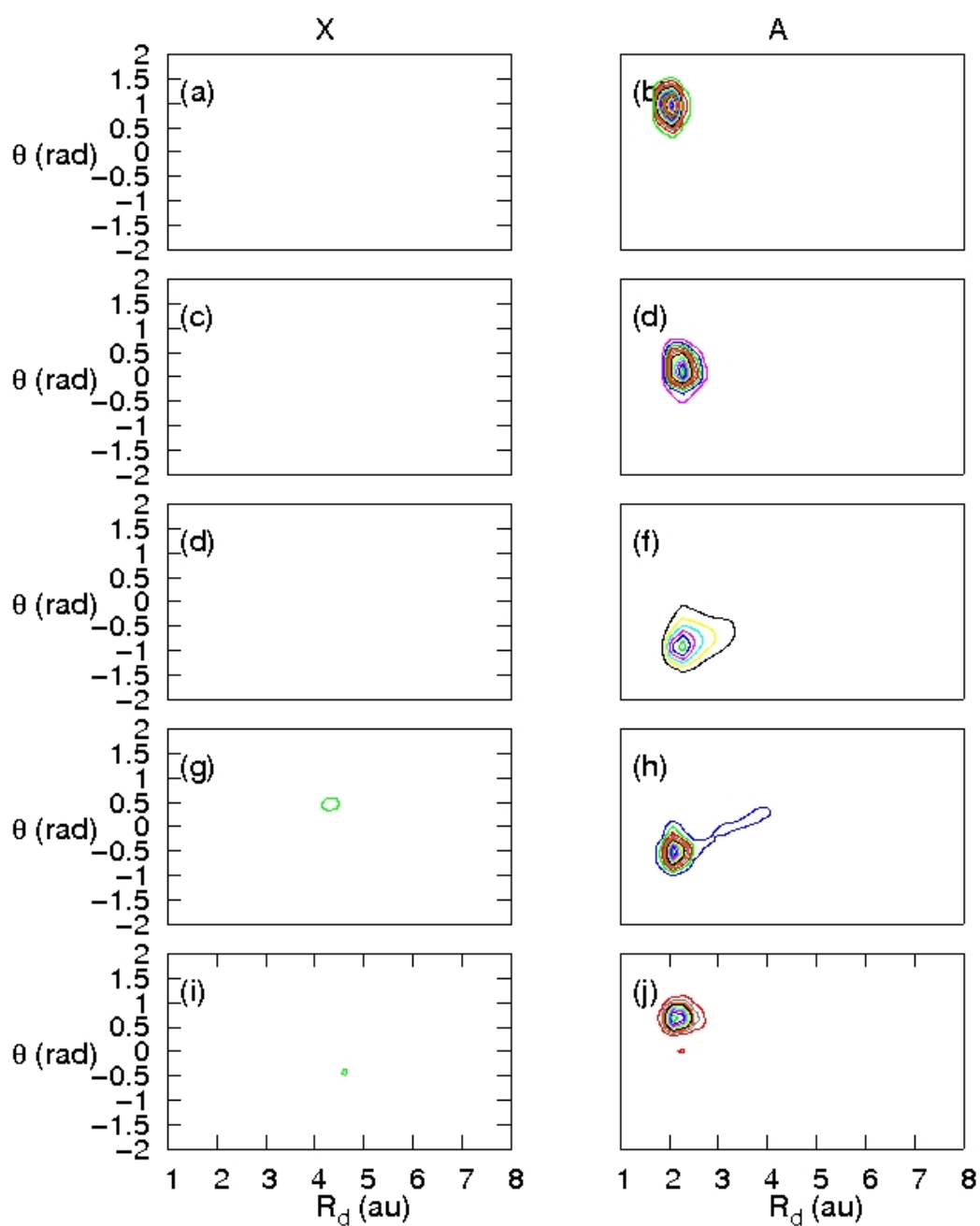


Fig. 7.31: Wavefunction density plots for  $S_0$  and  $S_1$  for ammonia with no pulse applied along  $r_d$  and  $\theta$ . (a)/(b) 0fs, (c)/(d) 5fs (e)/(f) 10fs (g)/(h) 20fs and (i)/(j) 30fs.

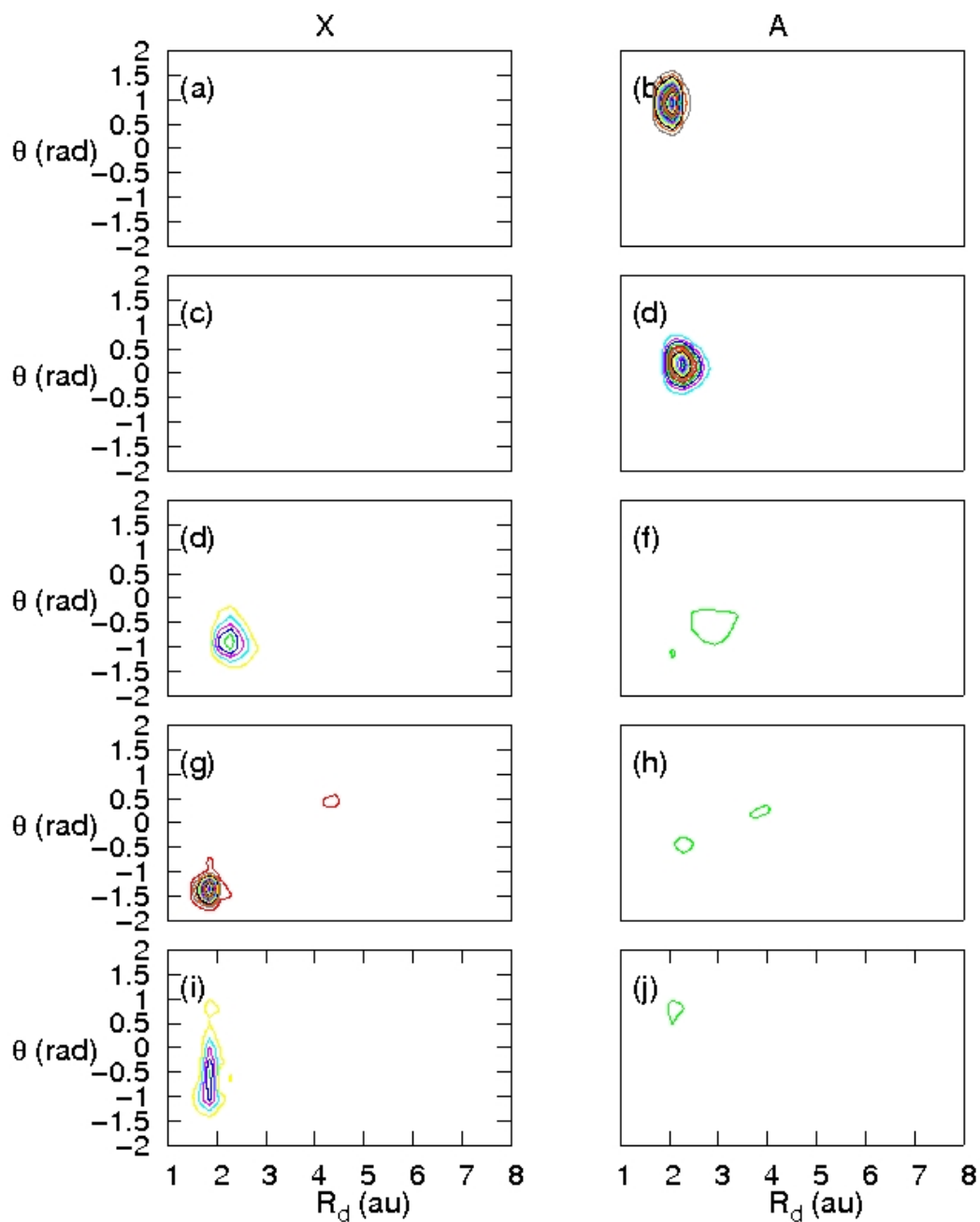


Fig. 7.32: Wavefunction density plots for  $S_0$  and  $S_1$  for ammonia with pulse applied along  $r_d$  and  $\theta$ . (a)/(b) 0fs, (c)/(d) 5fs (e)/(f) 10fs (g)/(h) 20fs and (i)/(j) 30fs.



focused on control of electronic state population.

The control of neutral cyclobutadiene using a 6 dimensional, 3 electronic state model shows the importance of the  $\lambda$  parameter to the LCT method. Both control of the population to  $S_0$  and  $S_2$  show very encouraging control, especially considering the vibronic coupling involved which significantly complicates the Hamiltonian. However when  $\lambda$  is too large the control fails, too much energy creates a very vibrationally excited wavepacket on the target state enabling it to cross to the CI that exist between the surfaces destroying the control.

The second example of control was demonstrated on a 2 dimensional model of the radical cation of cyclobutadiene. By controlling the population transfer between the two components of the doubly degenerate  $D_0$  we are able to switch between the two  $D_{2h}$  minima which exist in the molecule due to JT coupling. Results demonstrated that the algorithm is able to create a field which was able to transfer 90% of the wavepacket from one minima to the other.

A FT of the control field resolved the frequencies that were responsible for the control. This revealed a range of frequencies which could easily be related to the properties of the model, such as vibrational frequency and inter-state vibronic coupling. However even in a relatively simple control objective the pulse utilised a wide range of frequencies which would make it more difficult to reproduce experimentally. By filtering some of the frequencies in the frequency spectra of the pulse and performing an inverse FT we show that by limiting the number of frequencies we are able provide a simpler pulse but also a more detailed understanding of how the pulse controls the dynamics. By filtering the pulse obtained from the initial control we are able to assign the important frequencies and demonstrate that even when all other frequencies are removed this control is still effective, transferring 85% of the wavepacket from one minima to the other.

The pyrazine model presented in this chapter has been previously used in a study of

---

OCT-MCTDH, this makes it the perfect test system to compare the two methods. We presented results controlling the population of  $S_2$  in the absence of vibronic coupling and controlling the population of  $S_1$  and  $S_2$  with the vibronic coupling included.

The control of the  $S_2$  population in the absence of vibronic coupling is able to excited 90% of the wavepacket into  $S_2$ . This performance is equivalent to the OCT methods, but occurs on a much slower real time period, taking 500fs to reach this as opposed to 100fs seen in OCT. The optimisation of  $S_2$  with the presence of vibronic coupling between  $S_1/S_2$  is very difficult, because a CI which exists not far from the FC point on  $S_2$  and therefore any excitation is followed by rapid internal conversion. Despite being unstable a population of 70% on  $S_2$  is reached after 45fs. This is in excellent agreement with OCT in both population and the field produced.

Because the oscillator strength for the  $S_0$ - $S_2$  transition is an order of magnitude greater than the  $S_0$ - $S_1$  transition, controlling the  $S_1$  population is most efficient by taking advantage of the fast IC. Using this method we manage to transfer 80% of the wavepacket to  $S_1$ . This, as before, occurs on a slower real time period than the OCT. In this control we see oscillations between  $S_1$  and  $S_2$ . Because the wavepacket on  $S_1$  is so vibrationally hot it has the energy to cross back to  $S_2$ , this is not seen in OCT [157].

The final control presented was to control the excitation and dissociative branching ratio in ammonia. The PES has been extensively studied and show two possible channels, a diabatic dissociation and a adiabatic channel. Unsurprisingly the diabatic channel is strongly favoured due to the profile of the PES. Both of the calculations presented showed a degree of control, however neither achieved the explicit prestated aim. This is because vibronic coupling around the FC point complicates the control and therefore more sophisticated implementation of the LCT method are required for a successful outcome of this control objective.

Throughout this chapter we have presented CPU times for the LCT calculations. One can see that they are typically not much slower than propagation without the

pulse. This is extremely encouraging for the prospect of moving onto larger systems.

These results, although in relatively simple systems shows incredible promise for the method for moving to more complex and larger systems. It is able to perform well in comparison to OCT in these cases, but with significantly less computational expense. The natural progression for this approach is to implement this into MCTDH with a wider range of possible operators, enabling a more flexible control on any given system.

# Chapter 8

## Conclusion

Early time ultrafast dynamics play a critical role in the outcome of chemical reactions. The motion of the wavepacket within the first few hundred femtoseconds will often define the overall outcome of the reaction, this is especially true in photochemical reactions. In such reactions the involvement of excited states results in the breakdown of the BOA and significantly complicates the Hamiltonian of the system. Coupling between nuclear and electronic motion can cause such topological features as CI, which provide an ultrafast radiationless transition between electronic states. Observing and understanding such features and their effect on the dynamics is critical to our understanding of many fundamental processes.

In this thesis we have presented a variety of methods required to study and control the ultrafast dynamics of photochemical processes. Electronic structure methods enabled us to obtain an accurate description of a PES and the MCTDH quantum dynamics method is able to perform dynamics on molecular systems containing a large number of nuclear and electronic DOF.

Benzene on inspection appears to be a highly symmetrical and relatively simple molecule. However it is its highly symmetrical nature which results in a multitude of possible photochemical pathways, making an accurate description very complicated. This is highlighted by the channel 3 problem. When a wavepacket is excited to  $3000\text{cm}^{-1}$  above the FC point in  $S_1$  fluorescence disappears due to the opening of

a radiationless pathway.

We have presented a Vibronic Coupling Hamiltonian suitable for studying the ultrafast dynamics of electronically and vibrationally excited benzene. The Vibronic Coupling Hamiltonian was calculated by performing a fit to *ab-initio* points calculated at various geometries on the PES. This Hamiltonian had been previously calculated using CASSCF, however this method does not include dynamic correlation critical for describing excited states with double excitations. We used CASPT2 with a (6,6) active space and Roos(3s2p1d/2s) basis set.

Cuts along the normal modes, important combination modes and the vector in normal mode space which leads to the S<sub>1</sub>/S<sub>0</sub> CI were all calculated and fitted to obtain the parameters for the description of the Hamiltonian. In order to properly describe the PES we were required to fit up to 4<sup>th</sup> order, this is especially important for the region around the CI.

The accuracy of the Hamiltonian was tested by calculating the absorption spectra,  ${}^1B_{2u} \leftarrow \tilde{X}$ ,  ${}^1B_{1u} \leftarrow \tilde{X}$  and  ${}^1E_{1u} \leftarrow \tilde{X}$ . In each case the calculated spectra reproduced the main features seen in the experimental spectra, indicating the accuracy and success of the calculated Hamiltonian. The  ${}^1B_{2u} \leftarrow \tilde{X}$  is dominated by a breathing mode progression, like the  ${}^1B_{1u} \leftarrow \tilde{X}$  spectra. It also contains two hotbands, one from the JT active,  $\nu_6$ , and other from the boat mode,  $\nu_{16}$ . The  ${}^1E_{1u} \leftarrow \tilde{X}$  is a symmetry allowed transition and therefore the spectra is a broad and structureless band, containing the tail structure which is the  ${}^1B_{1u} \leftarrow \tilde{X}$  spectra, arising from intensity borrowing due to coupling between the two states.

Using the Heidelberg MCTDH package we obtained dynamics simulations using the full 5 state Hamiltonian and a reduced space 2 state Hamiltonian. The parameters required for the 2 state Hamiltonian were fitted in the same manner as the larger 5 state model and was used to reduce the size of the calculations making it easier to converge. In this smaller model the barrier leading to the S<sub>1</sub>/S<sub>0</sub> CI is treated adiabatically instead

---

of a diabatic barrier which is formed by  $\tilde{C}$  crossing  $\tilde{A}$ .

Both models show good agreement with each other and experimental results. We performed two calculations, (a) cold wavepacket and (b) hot wavepacket (see chapter 4 for description). The cold wavepacket shows reduced decay from the FC region, because there is not enough energy in the right modes. The hot wavepacket dynamics shows rapid decay from the FC point occurring on two timescales as the wavepacket has enough energy in the right modes to surmount the barrier near the FC point.

The two state model also shows the wavepacket oscillating either side of the barrier on  $S_1$  which leads to the intersection, this oscillation has a timescale of 1.2ps giving excellent agreement with the experimental results. Despite accounting for much of the dynamics in the excited state of  $S_1$ , the singlet manifold does not account for all of the decay from the FC region in  $S_1$ .

Triplet states are often ignored, especially in hydrocarbons because the SOC is considered to small. However vibrational effects can be critical. First and second order effects, in which the symmetry of the vibrational mode can enhance or destroy the strength of the coupling, can play an important role. This, in conjunction with the degeneracy, found between the lowest singlet and triplet states at the  $S_1/S_0$  CI, could provide the required conditions for the triplet states play an important role in the dynamics, even if coupling is small.

In chapter 5 a detailed study into the nature of SOC in simple hydrocarbons was presented. Comprehensive studies of the vibrational effects of SOC are presented for cyclobutadiene and benzene by calculating the SOC along the normal modes and the vector in normal mode space leading to the  $S_1/S_0$  CI.

At equilibrium the SOC in both cases is very small because there is no mixing between the  $\sigma$  and  $\pi$  orbitals, which provides the mechanism for SOC. In cyclobutadiene SOC is enhanced by the low frequency modes which are out of plane C-H bends. The C-H bends allows mixing between the  $\sigma$  and  $\pi$  orbitals creating an  $sp^n$  type orbital

---

and a mechanism for SOC. This results in SOC energies which are as large as  $4.5\text{cm}^{-1}$  when the hydrogen is  $\sim 65^\circ$  out of the plane of the molecule.

In benzene first order vibrational effects are, like cyclobutadiene, dominated by out of plane C-H bends, which results in SOC coupling energies between  $3.5\text{-}4.5\text{cm}^{-1}$ . There are smaller second order effects which occur along the boat and chair modes, which play a critical role in the dynamics around the  $S_1/S_0$  CI. These modes not only increase the SOC between  $S_1/T_1$ , which is symmetry allowed at equilibrium, but also induced SOC between  $S_1$  and the doubly degenerate  $T_2$ .

The SOC along the vector in normal mode space leading to the  $S_1/S_0$  CI increases in both cyclobutadiene and benzene. This is dependent on the combination of modes required to reach the CI. In the case of cyclobutadiene the required modes include a larger dependence on out of plane C-H and therefore there is a large increase in SOC towards the intersection. However in the case of benzene although we still see an increase in SOC it is not as great as cyclobutadiene because there is less out of plane C-H bending motion.

In chapter 6 the 2 state model described in chapter 4 is developed to include a triplet manifold, using the spin orbit coupling values calculated in chapter 5. The parameters for the Hamiltonian in the triplet manifold were acquired using the same fitting procedure for the singlet states. The dynamics were performed using 4 state (2 singlet and 2 triplets) and 6 normal modes.

Comparing these dynamics to the experimentally obtained data shows excellent agreement. In both cases the fast decay is apparent for the first 500fs. After 500fs there is 55% of the wavepacket in the FC region of  $S_1$ , and 70% of the wavepacket in the  $S_1$  and triplet states, this is almost identical to the experimental results. Unlike the experiments after 500fs the wavepacket continues to decay out of  $S_1$ . This can be attributed to the reduced dimensionality of the model.

The dynamics obtained give a clear support to the ultrafast intersystem crossing

which has been observed experimentally in benzene. Despite the small coupling which exists between the singlet and triplet manifolds 5-10% of the wavepacket is still able to cross in the first 500fs. This is clear example of ultrafast intersystem crossing and the first example of it occurring in simple hydrocarbons.

Chapter 7 looks at controlling dynamics and shows the results obtained following the implementation of the LCT algorithm within the Heidelberg MCTDH package. In this chapter we present the control of the electronic state populations for neutral and radical cationic cyclobutadiene, pyrazine and ammonia.

The control of neutral cyclobutadiene using a 6 dimensional, 3 electronic state model shows the importance of the  $\lambda$  parameter to the LCT method. Both control of the population to  $S_0$  and  $S_2$  show very encouraging control, especially considering the vibronic coupling involved which significantly complicates the Hamiltonian. However when  $\lambda$  is too large the control fails, too much energy creates a very vibrationally excited wavepacket on the target state enabling it to cross to the CI that exist between the surfaces destroying the control.

Using a radical cationic cyclobutadiene model we controlled the wavepacket motion between the two  $D_{2h}$  minima. By using a projector onto the excited state a pulse was calculated which selectively transferred 90% from one minima to the other. FT of the calculated pulse shows the range of frequencies required, these could all be related to the parameters of the system, such as the vibrational frequencies and interstate vibronic coupling.

We also present a further analysis of the cyclobutadiene by filtering the some of the frequencies. Despite removing all except 3 of the major frequencies from the calculated pulse the new pulse is still able to transfer 85% of the wavepacket from one minima to the other. This is encouraging, especially considering that larger systems are likely to produce more complex pulses and therefore filtering will play a more important role in simplifying pulses to be reproduced experimentally and reveal the dynamics of the



control.

Using a model system for pyrazine we present results controlling the population of  $S_2$  in the absence of vibronic coupling and controlling the population of  $S_1$  and  $S_2$  with the vibronic coupling included. This has been previously used in a study of OCT-MCTDH, this makes it the perfect test system to compare the two methods. In all three control scenarios the LCT method was able to perform as well as OCT methods, achieving similar amounts of control.

The LCT method took longer in real time to match the OCT results, however from the propagation times displayed one can see that the LCT calculations did not use much more CPU time than the propagations without the field. This result is very encouraging as it shows that LCT is ideal for larger systems.

The final control presented aims to alter the dissociative branching ratio in ammonia. The PES has been extensively studied and shows two possible channels, a diabatic dissociation and an adiabatic channel. Unsurprisingly the diabatic channel is strongly favoured due to the profile of the PES. Our results show that by applying the LCT algorithm a pulse is produced which is able to stop much of the dissociation down the diabatic channel. The wavepacket is successfully transferred onto  $S_0$ , part of which dissociates and the rest returning to the equilibrium geometry.

The work presented in this thesis provides a detailed insight into elements of photo-dynamics and coherent control. The calculation of the benzene Hamiltonian is shown to be accurate from the calculation of absorption spectra and replication of experimental results. It represents the limit for such methods, calculating the full PES for larger systems becomes very difficult due to the sheer size of the coordinate space involved. As computational advancements and methods enable the possibility of larger and larger calculations, methods such as direct dynamics, in which the potential energy surface is calculated “on-the-fly” as and when it is required will become increasingly important.

The calculations performed on ultrafast intersystem crossing in benzene reveal that

the triplet states can play a role in early time dynamics even when coupling is small. Further work should be focused upon studying more systems which are likely to contain similar characteristics to benzene and are likely to also contain ultrafast intersystem crossing.

LCT-MCTDH results are encouraging, but should be viewed as a stepping stone to more complex systems. We have only presented results obtained by controlling the electronic state population and therefore by increasing the range of possible operators will provide a greater flexibility and success in control.

# Bibliography

- [1] Turro, N. J. *Modern Molecular Photochemistry*. University Science Books, 1991.
- [2] Hahn, S. & Stock, G. *Quantum-mechanical modelling of the femtosecond isomerization in rhodopsin*. *J. Phys. Chem. B*, 2000. **104**, 1146–1149.
- [3] Birge, R. R. *Nature of the primary photochemical events in Rhodopsin and Bacteriorhodopsin*. *Biochimica et Biophysica acta*, 1990. **1016**, 293–327.
- [4] Schoenlein, R., Peteanu, L., Mathies, R., & Shank, C. *The 1st step in vision - Femtosecond isomerization of Rhodopsin*. *Science*, 1991. **254** (5030), 412–415.
- [5] Klessinger, M. & Michl, J. *Excited states and photochemistry of organic molecules*. VCH, New York, 1994.
- [6] Michl, J. & Bonacic-Koutecky, V. *Electronic aspects of organic photochemistry*. Wiley, New York, 1990.
- [7] Robb, M. A., Bernardi, F., & Olivucci, M. *Conical intersections as a mechanistic feature of organic photochemistry*. *Pure and Appl. Chem.*, 1995. **67**, 783–789.
- [8] Born, M. & Oppenheimer, R. *Quantum theory of molecules*. *Ann. Phys.*, 1927. **84**, 457–484.
- [9] von Neumann, J. & Wigner, E. P. *On behaviour of eigenvalues in adiabatic processes*. *Physik Z*, 1929. **30**, 467.

- 
- [10] Worth, G. A. & Cederbaum, L. S. *Beyond Born-Oppenheimer: Conical intersections and their impact on molecular dynamics.* Ann. Rev. Phys. Chem., 2004. **55**, 127–158.
- [11] Mahapatra, S., Cederbaum, L. S., & Köppel, H. *Theoretical investigation of Jahn-Teller and pseudo-Jahn-Teller coupling effects on the photoelectron spectrum of allene.* J. Chem. Phys., 1999. **111**, 10,452–10,463.
- [12] Demtröder, W. *Laser Spectroscopy.* Springer, New York, 2001.
- [13] Dantus, M., Rosker, M., & Zewail, A. *Real-time femtosecond probing of transition states in chemical reactions.* J. Chem. Phys., 1987. **87** (4), 2395–2397.
- [14] Zewail, A. H. *Femtochemistry - Ultrafast Dynamics of the Chemical Bond.* World Scientific, Singapore, 1994.
- [15] Dantus, M., Rosker, M. J., & Zewail, A. H. *Femtosecond real-time probing of reactions: The dissociation of ICN.* J. Chem. Phys., 1999. **89**, 6128.
- [16] Zewail, A. *Femtochemistry: Atomic-scale dynamics of the chemical bond.* J. Chem. Phys., 2000. **104**, 5660.
- [17] Engel, V., Metiu, H., Almeida, R., Marcus, R., & Zewail, A. *Molecular-state evolution after excitation with an ultra-short laser-pulse: A quantum analysis of NaI and NaBr dissociation.* Chem. Phys. Lett., 1988. **152** (1), 1–7.
- [18] Engel, V., Metiu, H., Almeida, R., Marcus, R. A., & Zewail, A. H. *Molecular state evolution after excitation with an ultra-short laser pulse- A Quantum analysis of NAI and NABr dissociation.* Chem. Phys. Lett., 1988. **152**, 1–7.
- [19] Parker, D. N. S., Minns, R. S., Penfold, T. J., Worth, G. A., & Fielding, H. H. *Ultrafast dynamics of the S-1 excited state of benzene.* Chem. Phys. Lett., 2009. **469**, 43–49.

- 
- [20] Crim, F. F. *Selective excitation studies of unimolecular reaction dynamics*. Annual Rev. Phys. Chem., 1984. **35**, 657–691.
- [21] Ticich, T. M., Likar, M. D., Butler, L. J., & Crim, F. F. *Vibrationally mediated photodissociation of hydrogen-peroxide*. J. Chem. Phys., 1987. **87**, 5820–5829.
- [22] Crim, F. F. *State selective and bond selective unimolecular reactions*. Science, 1990. **249**, 1387–1392.
- [23] Bartels, R. A., editor. *Coherent control of atoms and molecules*. PhD Thesis, University of Michigan, 2002.
- [24] Shapiro, M. & Brumer, P. *Laser control of product quantum state populations in unimolecular reaction*. J. Phys. Chem., 1986. **84**, 4103.
- [25] Tannor, D. J., Kosloff, R., & Rice, S. A. *Coherent pulse sequence induced control selectivity of reactions : exact quantum mechanical calculations*. J. Chem. Phys., 1985. **85**, 5805.
- [26] Tannor, D. J. & Rice, S. A. *Control of selectivity of chemical reaction via control of wavepacket evolution*. J. Chem. Phys., 1985. **83**, 5013.
- [27] Mitric, R., Hartmann, M., Pittner, J., & Bonacic-Koutecky, V. *New strategy for optimal control of femtosecond pump-dump processes*. J. Phys. A, 2002. **106** (44), 10,477–10,481.
- [28] Balint-Kurti, G., G, Zou, S., & Brown, A. *Optimal control theory for manipulating molecular processes*. Advances in chemical physics, 2008. **138**, 43–94.
- [29] Gordon, R. J. & Rice, S. A. *Active control of the dynamics of atoms and molecules*. Annu. Rev. Phys. Chem., 1997. **48**, 601.
- [30] de Vivie-Riedle, R., Kurtz, L., & Hofmann, A. *Coherent control for photochemical reactions*. Pure Appl Chem, 2001. **73**, 525–528.

- 
- [31] Judson, R. S. & Rabitz, H. *Teaching Lasers to control molecules*. Phys. Rev. Lett., 1992. **68**, 1500.
- [32] Assion, A., Baumert, T., Bergt, M., Brixner, T., Kiefer, B., Seyfield, V., Strehle, M., & Gerber, G. *Control of chemical reactions by feedback optimised pulse-shaped femtosecond laser pulses*. Science, 1998. **282**, 919.
- [33] Nuernberger, P., Vogt, G., Brixner, T., & Gerber, G. *Femtosecond quantum control of molecular dynamics in the condensed phase*. Physical chemistry chemical physics, 2007. **9**, 2470–2497.
- [34] Tannor, D. J., Kosloff, R., & Bartana, V. *Laser cooling of internal degrees of freedom of molecules by dynamically trapped states*. Faraday Discussions, 1990. **113**, 365–383.
- [35] Engel, V., Meier, C., & Tannor, D. J. *Local control theory: Recent applications to energy and partical transfer processes in molecules*. Adv. Chem. Phys., 2009. **141**, 29.
- [36] Schödinger, E. *An undulatory theory of the mechanics of atoms and molecules*. Phys. Rev., 1926. **28**, 1049–1070.
- [37] Tannor, D. *Introduction to quantum mechanics: A time dependent perspective*. University Science Books, 2007.
- [38] Ratner, M. A. & Schatz, G. C. *Introduction to quantum mechanics in Chemistry*. Prentice Hall, 2001.
- [39] Atkins, P. W. *Molecular Quantum Mechanics 4nd edition*. OUP, Oxford, U.K., 2005.
- [40] Jahn, H. A. & Teller, E. *Stability of polyatomic molecules in degenerate electronic states. I. Orbital degeneracy*. Proc. R. Soc. A, 1937. **161**, 220–235.

- 
- [41] Jahn, H. A. *Stability of polyatomic molecules in degenerate electronic states II - Spin degeneracy*. Proc. R. Soc. A, 1938. **164**, 117.
- [42] Renner, R. Z. Phys., 1934. **92**, 172–193.
- [43] Van Vleck, J. H. *The Jahn-Teller effect and crystalline stark splitting for clusters of the form XY<sub>6</sub>*. J. Chem. Phys., 1939. **7**, 61.
- [44] Bersuker, I. B. *Retarded Motion in transition metal complexes*. Opt. Spektrosk, 1961. **11**, 319.
- [45] Woywod, C., Stengle, M., Domcke, W., Flöthmann, H., & Schinke, R. *Photodissociation of ozone in the chappuis band I. Electronic structure calculations*. J. Chem. Phys., 1997. **107**, 7282–7294.
- [46] Köppel, H., Domcke, W., & Cederbaum, L. S. *Multimode molecular dynamics beyond the Born Oppenheimer approximation*. adv Chem Phys, 84. **57**, 59.
- [47] Cederbaum, L. S., Köppel, H., & Domcke, W. *Multimode vibronic coupling effects in molecules*. Int. J. Quant. Chem., 1981. **15**, 251–267.
- [48] Köppel, H., Döscher, Bâldea, I., Meyer, H.-D., & Szalay, P. *Multistate vibronic interactions in the benzene radical cation. II. Quantum dynamical simulations*. J. Chem. Phys., 2002. **117**, 2657–2671.
- [49] Worth, G., Meyer, H.-D., & Cederbaum, L. *Multidimensional dynamics involving a conical intersection: Wavepacket calculations using the MCTDH method*. World Scientific, Singapore, 2004 pages 583–617.
- [50] Doscher, M., Köppel, H., & Szalay, P. G. *Multistate vibronic interactions in benzene radical cation: Electronic structure calculations*. J. Chem. Phys., 2002. **117**, 2645–2656.

- 
- [51] Eisfeld, W. & Viel, A. *Higher order  $(A \oplus E) \otimes E$  pseudo-Jahn-Teller coupling*. J. Chem. Phys., 2004. **122**, 4603–4613.
- [52] Markmann, A., Worth, G. A., & Cederbaum, L. S. *Allene and pentatetraene cations as models for intramolecular charge transfer: Vibronic coupling Hamiltonian and conical intersections*. J. Chem. Phys., 2005. **122**, 144,320–15.
- [53] Hill, W. & Lee, C. *Light-Matter Interaction*. Wiley, Weinham, 2007.
- [54] Marquetand, P., Gräfe, S., Scheidel, D., & Engel, V. *Local control of the quantum dynamics in multiple potential wells*. J. Chem. Phys., 2006. **124**.
- [55] Gräfe, S., Meier, C., & Engel, V. *Instantaneous dynamics and quantum control fields: Principle and numerical applications*. J. Chem. Phys., 2005. **122**.
- [56] Jensen, F. *Introduction to computational chemistry*. Wiley, 2002.
- [57] Beck, M. H., Jäckle, A., Worth, G. A., & Meyer, H.-D. *The multiconfiguration time-dependent Hartree method: A highly efficient algorithm for propagating wavepackets*. Phys. Rep., 2000. **324**, 1–105.
- [58] Light, J. C., Hamilton, I. P., & Lill, J. V. *Generalized discrete variable approximation in quantum mechanics*. J. Chem. Phys., 1985. **82**, 1400–1409.
- [59] Meyer, H.-D. & Worth, G. A. *Quantum molecular dynamics: propagating wavepackets and density operators using the multiconfiguration time-dependent Hartree method*. Theor. Chem. Acc., 2003. **109**, 251–267. Feature article.
- [60] Roothan, C. C. J. *New developments in molecular orbital theory*. Rev. Mod. Phys., 1951. **23**, 69–89.
- [61] Roos, B. O. & Taylor, P. R. *A complete active space scf method (CASSCF) using a density matrix formulated super-CI approach*. Chemical Physics, 1980. **48**, 151–173.



- 
- [62] Findlay, J., Malmqvist, P., Roos, B. O., & Serrano-Andres, L. *The multi-state CASPT2 method*. Chem. Phys. Lett., 1998. **288**, 299–306.
- [63] Lorentzon, J., Malmqvist, P., Fülischer, M., & Roos, B. O. *A CASPT2 study of the valence and lowest Rydberg electronic states of benzene and phenol*. Theor. Chim. Acta, 1995. **91**, 91.
- [64] Szabo, A. & Ostlund, N. S. *Modern Quantum Chemistry: Introduction to advanced electronic structure theory*. MacMillan, New York, 1982.
- [65] Roos, B. O. & Andersson, K. *Multiconfigurational perturbation-theory with level shift: The Cr<sub>2</sub> potential revisited*. Chem. Phys. Lett., 1995. **245**, 215–223.
- [66] Andersson, K., Malmqvist, P. A., & Roos, B. O. *2nd-Order perturbation theory with a complete active space self-consistent field reference function*. J. Chem. Phys., 1992. **96**, 1218.
- [67] Andersson, K. & Roos, B. O. *Multiconfiguration second-order perturbation theory*. In Yarkony, D., editor, *Modern Electronic structure theory*. World Scientific, Singapore, 1995 pages 55–109.
- [68] Berning, A., Schweizer, M., Werner, H.-J., Knowles, P., & Palmieri, P. *Spin orbit matrix elements for internally contracted multireference configuration interaction wavefunctions*. Mol. Phys., 2000. **98**, 1823–1833.
- [69] Fedorov, D. G. & Gordon, M. S. *A study of the relative importance of one and two-electron contributions to spin-orbital coupling*. J. Chem. Phys., 1999. **112**, 5611.
- [70] Alder, B. & Wainwright, T. *Phase transition for a hard sphere system*. J. Chem. Phys., 1957. **27** (5), 1208–1209.

- 
- [71] Alder, B. & Wainwright, T. *Studies in molecular dynamics .1. General Method.* J. Chem. Phys., 1959. **31** (2), 459–466.
- [72] Rahman, A. *Correlations in motion of atoms in liquid argon.* Physical review A- General Physics, 1964. **136** (2A), A405–&.
- [73] Heller, E. J. *Time-dependent approach to semiclassical dynamics.* J. Chem. Phys., 1975. **62**, 1544.
- [74] McCullough, E. A. & Wyatt, R. E. *Quantum dynamics of the collinear (H,H<sub>2</sub>) reaction.* J. Chem. Phys., 1969. **51**, 1253.
- [75] McCullough, E. A. & Wyatt, R. E. *Dynamics of the collinear (H,H<sub>2</sub>) reaction. I. Probability density and flux.* J. Chem. Phys., 1971. **54**, 3578.
- [76] Kosloff, D. & Kosloff, R. *A Fourier-method solution for the time-dependent Schrödinger equation as a tool in molecular dynamics..* J. Comp. Phys., 1983. **52**, 35.
- [77] Light, J. C. *Discrete Variable Representations in Quantum Dynamics.* In Broeckhove, J. & Lathouwers, L., editors, *Time-Dependent Quantum Molecular Dynamics.* Plenum, New York, 1992 pages 185–199.
- [78] Meyer, H.-D., Gatti, F., & Worth, G. A., editors. *Multidimensional Quantum Dynamics: MCTDH Theory and Applications..* Wiley, London, 2009.
- [79] Worth, G. A., Beck, M. H., Jäckle, A., & Meyer, H.-D. *The Heidelberg MCTDH Package: A set of programs for multi-dimensional quantum dynamics. User's Guide, Version 8*, 2000  
(The User's Guide can be downloaded from the URL: <http://www.pci.uni-heidelberg.de/tc/usr/mctdh/>).
-

- 
- [80] Light, J. C. & Carrington Jr., T. *Discrete variable representations and their utilization*. Adv. Chem. Phys., 2000. **114**, 263–310.
- [81] Harris, D. O., Engerholm, G. G., & Gwinn, G. W. *Calculation of matrix elements for one-dimensional quantum-mechanical problems and the application to anharmonic oscillators*. J. Chem. Phys., 1965. **43**, 1515.
- [82] Dickinson, A. S. & Certain, P. R. *Calculation of matrix elements for one-dimensional quantum-mechanical problems*. J. Chem. Phys., 1968. **49**, 4209.
- [83] Meyer, H.-D., Worth, G. A., & Fang, J.-Y. *Comment on “Generalization of the multiconfigurational time-dependent Hartree method to nonadiabatic systems”* [*J. Chem. Phys.* 105, 9191 (1996)]. J. Chem. Phys., 1998. **109**, 349.
- [84] Raab, A., Worth, G., Meyer, H.-D., & Cederbaum, L. S. *Molecular dynamics of pyrazine after excitation to the  $S_2$  electronic state using a realistic 24-mode model Hamiltonian*. J. Chem. Phys., 1999. **110**, 936–946.
- [85] Worth, G. A. *Accurate wave packet propagation for large molecular systems: The multi-configuration time-dependent Hartree (MCTDH) method with selected configurations*. J. Chem. Phys., 2000. **112**, 8322–8329.
- [86] Cohen, L. *Time frequency distributions: A review*. Proc. Inst. Elect. Electron. Engrs., 1989. **77**, 941–981.
- [87] Toniolo, A., Thompson, A. L., & Martínez, T. *Excited state direct dynamics of Benzene with parametrized multi-reference semiempirical configuration interaction methods*. Chem. Phys., 2004. **304**, 133–145.
- [88] Palmer, I. J., Ragazos, I. N., Bernardi, F., Olivucci, M., & Robb, M. A. *An MC-SCF study of the  $S_1$  and  $S_2$  photochemical reactions of benzene*. J. Am. Chem. Soc., 1993. **115**, 672–682.

- 
- [89] Roos, B. O., Andersson, K., & Fülischer, M. P. *Towards and accurate molecular orbital theory for excited states: the benzene molecule*. Chem. Phys. Lett., 1992. **192**, 5–13.
- [90] Bernhardsson, A., Forsberg, N., Malmqvist, P.-Å., & Roos, B. O. *A theoretical study of the  $^1B_{2u}$  and  $^1B_{1u}$  vibronic bands in Benzene*. J. Chem. Phys., 2000. **112**, 2798–2809.
- [91] Christiansen, O., Stanton, J. F., & Gauss, J. *A coupled cluster study of the  $1^1A_{1g}$  and  $1^1B_{2u}$  states of Benzene*. J. Chem. Phys., 1998. **108**, 3987–4001.
- [92] Scott, L. T. & Jones Jr., M. *Rearrangements and interconversions of compounds of the formula  $(CH)_n$* . Chem. Rev., 1972. **72**, 181–202.
- [93] Bryce-Smith, D. & Gilbert, A. *The organic photochemistry of Benzene-I*. Tetrahedron, 1972. **32**, 1309–1326.
- [94] Philis, J., Bolovinos, A., Andritsopoulos, G., Pantos, E., & Tsekeris, P. *A comparison of the absorption spectra of the fluorobenzenes and benzene in the region 4.5 - 9.5 eV*. J. Phys. B, 1981. **14**, 3621–3635.
- [95] Parmenter, C. S. *Radiative and Nonradiative Processes in Benzene*. Adv. Chem. Phys., 1972. **22**, 365–421.
- [96] Clara, M., Hellerer, T., & Neusser, H. J. *Fast decay of high vibronic  $S_1$  states in gas-phase benzene*. Appl. Phys. B, 2000. **71**, 431.
- [97] Lassetre, E. N., Skerbele, A., Dillon, M. A., & Ross, K. J. *High-resolution study of electron-impact spectra at kinetic energies between 33 and 100 ev and scattering angles to 16 degrees*. J. Chem. Phys., 1968. **48**, 5066–5096.
- [98] Spears, K. G. & Rice, S. A. *Study of Lifetimes of Individual Vibronic states of the Isolated Benzene molecule*. J. Chem. Phys., 1971. **55**, 5561.

- 
- [99] Stephenson, T. & Rice, S. *Relaxation dynamics of photoexcited benzene rare-gas vanderwaals*. J. Chem. Phys., 1984. **81** (3), 1083–1101.
- [100] Callomon, J. H., Dunn, T. M., & Mills, I. M. *Application of the time-dependent Hartree grid method to inelastic molecular scattering problems..* Chem. Phys. Lett., 1990. **165**, 443.
- [101] Radloff, W., Freudenberg, T., Ritze, H.-H., Stert, V., Weyers, K., & Noack, F. *Femtosecond dynamics of benzene (NH<sub>3</sub>)(N) complexes in highly excited states*. Chem. Phys. Lett., 1995. **245**, 400–406.
- [102] Worth, G. A. *A Model Hamiltonian to simulate complex photochemistry of Benzene*. J. Photochem and Photobiology, 2007. **190**, 190–199.
- [103] Roos, B., Linse, P., Siebahn, P., & Blomberg, M. *A simple method for the evaluation of the 2nd order perturbation energy from external double-excitations with a CASSCF reference*. Chemical Physics, 1982. **66**, 197.
- [104] Köppel, H., Domcke, W., & Cederbaum, L. S. *Multimode molecular Dynamics beyond the Born-Oppenheimer approximation*. Adv. Chem. Phys., 1984. **57**, 59–246.
- [105] Meyer, H.-D., Manthe, U., & Cederbaum, L. S. *The Multi-Configurational Time-Dependent Hartree Approach*. Chem. Phys. Lett., 1990. **165**, 73–78.
- [106] Goodman, L., Ozkabak, A. G., & Thakur, A. N. *A Benchmark Vibrational Potential Surface: Ground-State Benzene*. J. Phys. Chem., 1991. **95**, 9044–9058.
- [107] Werner, H.-J., Knowles, P. J., Lindh, R., Manby, F. R., Schütz, M., Celani, P., Korona, T., Mitrushenkov, A., Rauhut, G., Adler, T. B., Amos, R. D., Bernhardsson, A., Berning, A., Cooper, D. L., Deegan, M. J. O., Dobbyn, A. J., Eckert, F., Goll, E., Hampel, C., Hetzer, G., Hrenar, T., Knizia, G., Köppl, C.,

- Liu, Y., Lloyd, A. W., Mata, R. A., May, A. J., McNicholas, S. J., Meyer, W., Mura, M. E., Nicklass, A., Palmieri, P., Pflüger, K., Pitzer, R., Reiher, M., Schumann, U., Stoll, H., Stone, A. J., Tarroni, R., Thorsteinsson, T., Wang, M., & Wolf, A. *MOLPRO, version 2008.1, a package of ab initio programs*.
- [108] Cattarius, C., Worth, G. A., Meyer, H.-D., & Cederbaum, L. S. *All mode dynamics at the conical intersection of an octa-atomic molecules: MCTDH investigation on the butatriene cation*. J. Chem. Phys., 2001. **115**, 2088–2100.
- [109] Worth, G. A., Welch, G., & Paterson, M. J. *Wavepacket dynamics study of  $\text{Cr}(\text{CO})_5$  after formation by photodissociation: relaxation through an  $(E \oplus A) \otimes E$  Jahn-Teller conical intersection..* Mol. Phys., 2006. **104**, 1095–1105.
- [110] Lasorne, B., Sicilia, F., Bearpark, M., Robb, M., Worth, G., & Blancafort, L. *Automatic generation of active coordinates for quantum dynamics calculations: Applications to the dynamics of benzene photochemistry*. J. Chem. Phys., 2008. **128**.
- [111] Frisch, M. J., Trucks, G. W., Schlegel, H. B., Scuseria, G. E., Robb, M. A., Cheeseman, J. R., Montgomery, J. A., Jr., Vreven, T., Kudin, K. N., Burant, J. C., Millam, J. M., Iyengar, S. S., Tomasi, J., Barone, V., Mennucci, B., Cossi, M., Scalmani, G., Rega, N., Petersson, G. A., Nakatsuji, H., Hada, M., Ehara, M., Toyota, K., Fukuda, R., Hasegawa, J., Ishida, M., Nakajima, T., Honda, Y., Kitao, O., Nakai, H., Klene, M., Li, X., Knox, J. E., Hratchian, H. P., Cross, J. B., Bakken, V., Adamo, C., Jaramillo, J., Gomperts, R., Stratmann, R. E., Yazyev, O., Austin, A. J., Cammi, R., Pomelli, C., Ochterski, J. W., Ayala, P. Y., Morokuma, K., Voth, G. A., Salvador, P., Dannenberg, J. J., Zakrzewski, V. G., Dapprich, S., Daniels, A. D., Strain, M. C., Farkas, O., Malick, D. K., Rabuck, A. D., Raghavachari, K., Foresman, J. B., Ortiz, J. V., Cui, Q., Baboul, A. G., Clifford, S., Cioslowski, J., Stefanov, B. B., Liu, G., Liashenko, A., Piskorz, P.,

- Komaromi, I., Martin, R. L., Fox, D. J., Keith, T., Al-Laham, M. A., Peng, C. Y., Nanayakkara, A., Challacombe, M., Gill, P. M. W., Johnson, B., Chen, W., Wong, M. W., Gonzalez, C., & Pople, J. A. *Gaussian 03, Revision C.02*. Gaussian, Inc., Pittsburgh PA, 2003.
- [112] Worth, G. A., Beck, M. H., Jäckle, A., & Meyer, H.-D. *The MCTDH Package, Version 8.3*, See <http://www.pci.uni-heidelberg.de/tc/usr/mctdh/>, 2003.
- [113] Pantos, E., Philis, J., J., & Bolovinos, A. *Extinction coefficient of benzene vapor in region 4.6 to 36eV*. J. Mol. Spec., 1978. **72** (1), 36–43.
- [114] Mahapatra, S., Worth, G. A., Meyer, H.-D., Cederbaum, L. S., & Köppel, H. *The  $\tilde{A}^2E/\tilde{B}^2B_2$  photoelectron bands of allene beyond the linear coupling scheme: An ab initio dynamical study including all fifteen vibrational modes..* J. Phys. Chem. A, 2001. **105**, 5567–5576.
- [115] Yamazaki, I., Murao, T., Yamanaka, T., & Yoshihara, K. *Intramolecular electronic relaxation and photoisomerisation processes in the isolated Azabenzene molecules Pyridine, Pyrazine and Pyrimidine*. Faraday Discuss. Chem. Soc., 1983. **75**, 395.
- [116] Bernardi, F., Olivucci, M., & Robb, M. A. *Potential energy surface crossings in organic photochemistry*. Chem. Soc. Rev., 1996. **25**, 321–328.
- [117] Bearpark, M. J., Robb, M. A., & Schlegel, H. B. *A direct method for the location of the lowest energy point on a potential surface crossing*. Chem. Phys. Lett., 1994. **223** (3), 269–274.
- [118] Yarkony, D. *Current issues in nonadiabatic chemistry*. J. Phys. Chem., 1996. **100** (48), 18,612–18,628.
- [119] Köppel, H. *Diabatic representation: practical aspects: methods for the construction of diabatic representations*. In Domcke, W., Yarkony, D. R., & Köppel, H.,

- editors, *Conical intersections: Electronic structure, dynamics and spectroscopy*. World Scientific, Singapore, 2004 .
- [120] Yarkony, D. R. *Conical intersections: diabolical and often misunderstood*. *Acc. Chem. Res.*, 1998. **31**, 511–518.
- [121] Domcke, W., Yarkony, D. R., & Köppel, H., editors. *Conical intersections: Electronic structure, dynamics and spectroscopy*. World Scientific, Singapore, 2004.
- [122] El-Sayed, M. A. *Spin-orbit coupling and radiationless processes in nitrogen heterocyclics*. *J. Chem. Phys.*, 1963. **38**, 2834–2838.
- [123] Cogan, S., Haas, Y., & Zilberg, S. *Intersystem crossing at singlet conical intersections*. *Journal of photochemistry and photobiology A*, 2007. **190**, 200–2006.
- [124] Fujimura, Y., Shimakura, N., & Nakajima, T. *Mechanisms of intersystem crossing in aromatic hydrocarbons*. *J. Chem. Phys.*, 1977. **66**, 3530–3537.
- [125] Lawetz, V., Orlandi, G., & Siebrand, W. *Theory of intersystem crossing in aromatic hydrocarbons*. *J. Chem. Phys.*, 1972. **56**, 4058–4072.
- [126] Danovich, D., Marian, C. M., Neuheuser, T., Peyerimhoff, S. D., & Shalik, S. *Spin-orbit coupling patterns induced by twist and pyramidalization modes in CH: A quantitative study and a qualitative analysis*. *J. Phys. Chem.*, 1988. **102**, 5923–5936.
- [127] Shiota, Y., Kondo, M., & Yoshizawa, K. *Role of molecular distortions in the spin-orbit coupling between the singlet and triplet states of the 4 pi electron systems C<sub>4</sub>H<sub>4</sub>, C<sub>5</sub>H<sub>5</sub><sup>+</sup>, and C<sub>3</sub>H<sub>3</sub><sup>-</sup>*. *J. Chem. Phys.*, 2001. **115** (20), 9243–9254.
- [128] Wiberg, K. B., Hadad, C. M., Forsman, J. B., & Chupka, W. A. *Electronically excited states of ethylene*. *J. Chem. Phys.*, 1992. **96** (26), 10,756–10,768.



- 
- [129] Saddique, S. & Worth, G. *Applying the vibronic coupling model Hamiltonian to the photoelectron spectrum of cyclobutadiene*. Chem. Phys., 2006. **329**, 99–108.
- [130] Lorentzon, J., Malmqvist, P.-Å., Fülischer, & Roos, B. *A CASPT2 study of the valence and lowest Rydberg electronic states of Benzene and Phenol*. Theor. Chim. Acta., 1994. **91**, 91–108.
- [131] Eckert-Maksic, M., Vazdar, M., Barbatti, M., Lischka, H., & Maksic, Z. B. *Automerization reaction of cyclobutadiene and its barrier height: An ab initio benchmark multireference average-quadratic coupled cluster study*. J. Chem. Phys., 2006. **125** (6).
- [132] Bally, T. & Masamune, S. *Cyclobutadiene*. Tetrahedron, 1980. **36** (3), 343–370.
- [133] Buenker, R. & Peyerimh, S. *Ab-initio study on stability and geometry of cyclobutadiene*. J. Chem. Phys., 1968. **48** (1), 354–&.
- [134] Borden, W., Davidson, E., & Hart, P. *Potential surfaces for lowest singlet and triplet states of cyclobutadiene*. J. Am. Chem. Soc., 1978. **100** (2), 388–392.
- [135] Jafri, J. & Newton, M. *Potential energy surfaces of cyclobutadiene- Ab-initio SCF and CI calculations for low-lying singlet and triplet states..* J. Am. Chem. Soc., 1978. **100** (16), 5012–5017.
- [136] Haddon, R. C. & Williams, G. R. J. *Molecular orbital study of the electronic structure and spectrum of rectangular ( $D_{2h}$ ) cyclobutadiene*. J. Am. Chem. Soc., 1975. **22**, 6582.
- [137] Karadakov, P. B. *Ground- and excited-state aromaticity and antiaromaticity in benzene and cyclobutadiene*. J. Phys. A, 2008. **112** (31), 7303–7309.
- [138] Penfold, T. J. & Worth, G. A. *A model Hamiltonian to simulate the complex photochemistry of benzene II*. J. Chem. Phys., 2009. **131**.

- 
- [139] Henry, B. R. & Siebrand, W. *Spin-orbital coupling in Aromatic hydrocarbons-Analysis of nonradiative transitions between singlet and triplet states in benzene and naphthalene*. J. Chem. Phys., 1971. **54** (3), 1072-&.
- [140] Hamerka, H. F. & Oosterhoff, L. J. *The probabilities of triplet-singlet transitions in aromatic hydrocarbons and ketones*. Mol. Phys., 1958. **1** (4), 358-371.
- [141] Gordon, M. & Schmidt, M. *Theory and Applications of Computational Chemistry: the first forty years*. Elsevier, Amsterdam, 2005.
- [142] Lewis, G., Lipkin, D., & Magel, T. *The light absorption and fluorescence of triarylmethyl free radicals*. J. Am. Chem. Soc., 1944. **66**, 1579-1583.
- [143] Lewis, G. & Kasha, M. *Phosphorescence and the triplet state*. J. Am. Chem. Soc., 1944. **66**, 2100-2116.
- [144] Klessinger, M. *Theoretical models for the selectivity of organic singlet and triplet photoreactions*. Pure and applied chemistry, 1997. **69** (4), 773-778.
- [145] Merchan, M., Serrano-Andres, L., Robb, M., & Blancafort, L. *Triplet-state formation along the ultrafast decay of excited singlet cytosine*. J. Am. Chem. Soc., 2005. **127** (6), 1820-1825.
- [146] Gut, I., Wood, P., & Redmond, R. *Interaction of triplet photosensitizers with nucleotides and DNA in aqueous solution at room temperature*. J. Am. Chem. Soc., 1996. **118** (10), 2366-2373.
- [147] Morales-Cueto, R., Esquivelzeta-Rabell, M., Saucedo-Zugazagoitia, J., & Peon, J. *Singlet excited-state dynamics of nitropolycyclic aromatic hydrocarbons: Direct measurements by femtosecond fluorescence up-conversion*. Journal of physical chemistry A, 2007. **111** (4), 552-557.

- 
- [148] Damrauer, N. & McCusker, J. *Ultrafast dynamics in the metal-to-ligand charge transfer excited-state evolution of  $[Ru(4,4'$ -diphenyl-2,2'-bipyridine)(3)](2+)*. Journal Chem. Phys. A, 1999. **103** (42), 8440–8446.
- [149] Cederbaum, L., Haller, E., & Domcke, W. *Effective singlet-mode Hamiltonian for the calculation of multimode Jahn-Teller band shapes*. Solid state communications, 1980. **35** (11), 879–881.
- [150] Warren, R., W. S. Rabitz & Dahleh, M. *Coherent control of quantum dynamics: The dream is alive*. Science, 1993. **259**, 1581.
- [151] Zare, R. *Laser control of chemical reactions*. Science, 1998. **279**, 1875.
- [152] Rice, S. *Molecular dynamics - Optical control of reactions*. Nature, 2000. **403**, 496.
- [153] Rice, S. *Interfering for the good of a chemical reaction*. Nature, 2001. **496**, 422.
- [154] Shnitman, A., Sofer, I., Golub, I., Yogev, A., Shapiro, M., Chen, Z., & Brumer, P. *Experimental observation for laser control: Electronic branching in photodissociation of  $Na_2$* . Chem. Phys. Lett., 1997. **101**, 285.
- [155] Brumer, P. & Shapiro, M. *Molecules in Laser Fields*. Marcel Dekker, 1994.
- [156] Henriksen, N. & Amstrup, B. *Coherent control of HOD photodissociation dynamics in the 1st absorption band*. Chem. Phys. Lett., 1993. **213** (1-2), 65–70.
- [157] Wang, L., Meyer, H., & May, V. *Femtosecond laser pulse control of multidimensional vibrational dynamics: Computational studies on the pyrazine molecule*. J. Chem. Phys., 2006. **125**.
- [158] Turner, P. J. <http://linux.maruhn.com/sec/xmgr-semistatic.html>.

- [159] Bersuker, I. B. *Modern aspects of the Jahn-Teller effect theory and applications to molecular problems*. Chem. Rev., 2001. **101**, 1067–1114.
- [160] Woywood, C., Domcke, W., Sobolewski, A. L., & Werner, H.-J. *Characterization of the  $S_1$ - $S_2$  conical intersection in pyrazine using ab initio multiconfiguration self-consistent-field and multireference configuration-interaction methods..* J. Chem. Phys., 1994. **100**, 1400–1413.
- [161] Stock, G. *Classical description of non-adiabatic photoisomerization processes and their real-time detection via femtosecond spectroscopy*. J. Chem. Phys., 1995. **103**, 1561.
- [162] Ashfold, M. N. R., Bennett, C. L., & Dixon, R. N. *Dissociation dynamics of  $NH_3(\tilde{A}^1A_2')$* . Faraday Discuss. Chem. Soc., 1986. **82**, 163–175.
- [163] Yarkony, D. R. *Exploring molecular complexity: Conical intersections and  $NH_3$  photodissociation*. J. Chem. Phys., 2004. **121**, 628–631.
- [164] Biesner, J., Schneider, L., Schmeer, J., Ahlers, G., Xie, X., Welge, K. H., Ashfold, M. N. R., & Dixon, R. N. *State selective photodissociation dynamics of  $\tilde{A}$  state ammonia. I*. J. Chem. Phys., 1988. **88**, 3607–3616.
- [165] Bonhommeau, D. & Truhlar, D. G. *Mixed quantum/classical investigation of the photodissociation of  $NH_3(\tilde{A})$  and a practical method for maintaining zero-point energy in classical trajectories..* J. Chem. Phys., 2008. **129**, 014,302.
- [166] Li, Z. H., Valero, R., & Truhlar, D. G. *Improved direct diabaticization and coupled potential energy surfaces for the photodissociation of ammonia*. Theor. Chem. Acc., 2007. **118**, 9–24.
- [167] Nangia, S. & Truhlar, D. G. *Direct calculation of coupled diabatic potential-energy surfaces for ammonia and mapping of a four-dimensional conical intersection seam..* J. Chem. Phys., 2006. **124**, 124,309.

- [168] Hause, M. L., Yoon, Y. H., & Crim, F. F. *Vibrationally mediated photodissociation of ammonia: The influence of N-H stretching vibrations on passage through conical intersections..* J. Chem. Phys., 2006. **125**, 174,309.
- [169] Chapman, E. L. *Theoretical Studies on the Ultrafast Photodissociation of Molecules.* Ph.D. thesis, University of Birmingham, 2009.
- [170] Jäckle, A. & Meyer, H.-D. *Time-dependent calculation of reactive flux employing complex absorbing potentials: General aspects and application within MCTDH..* J. Chem. Phys., 1996. **105**, 6778.